BEYOND ΛCDM

Current and future constraints on alternative cosmological models

Natalie Beth Hogg

Institute of Cosmology and Gravitation
University of Portsmouth
2021

This thesis is submitted in partial fulfilment of the requirements for the award of the degree of Doctor of Philosophy of the University of Portsmouth.

For Andy Blower and Tim Nesbitt.

ABSTRACT

The widely accepted standard model of cosmology consisting of a cosmological constant, Λ, and cold dark matter, or ΛCDM, suffers from many well-known problems which motivate the study of alternative models. This thesis is an exploration of some of these alternatives, focusing in particular on the interacting vacuum scenario. In this scenario, vacuum energy and cold dark matter are allowed to exchange energy.

We perform a detailed study of models within the interacting vacuum scenario, using Markov chain Monte Carlo methods to constrain the parameter space using the latest observational data. When comparing the alternative models to ΛCDM, we find some cases which are weakly favoured over the standard cosmological model, although the tensions present within ΛCDM remain mostly unresolved.

We then move to forecasting future constraints on another fundamental aspect of cosmology: the distance duality relation. We create and use mock datasets of standard sirens, baryon acoustic oscillations and Type Ia supernovæ to forecast constraints on a violation of the distance duality relation due to photon–axion mixing, uncovering a potential smoking gun for modified gravity models with a particular screening phenomenology.

CONTENTS

LIST OF FIGURES

LIST OF TABLES

DECLARATION

Whilst registered as a candidate for the above degree, I have not been registered for any other research award. The results and conclusions embodied in this thesis are the work of the named candidate and have not been submitted for any other academic award.

Ethical review code: DC13-FB09-350F-F8FD-4CBD-44D3-2DF6-0455.
Word count: 44,721 words.

Natalie B. Hogg
Portsmouth, January 2021

DISSEMINATION

M. Martinelli, **N. B. Hogg**, S. Peirone, M. Bruni, D. Wands, 'Constraints on the interacting vacuum – geodesic CDM scenario'. arXiv: 1902.10694, *Monthly Notices of the Royal Astronomical Society*, 488, 3, 2019 [1].

N. B. Hogg, M. Bruni, R. Crittenden, M. Martinelli, S. Peirone, 'Latest evidence for a late time vacuum – geodesic CDM interaction'. arXiv: 2002.10449, *Physics of the Dark Universe*, 29, 100583, 2020 [2].

N. B. Hogg, M. Martinelli, S. Nesseris, 'Constraints on the distance duality relation with standard sirens'. arXiv: 2007.14335, *Journal of Cosmology and Astroparticle Physics*, 019, 12, 2020 [3].

F. Renzi, **N. B. Hogg**, M. Martinelli, S. Nesseris, 'Strongly lensed supernovæ as a self-sufficient probe of the distance duality relation'. arXiv: 2010.04155, submitted to *Physics of the Dark Universe*, 2020 [4].

ACKNOWLEDGEMENTS

Firstly, thanks to my supervisor Marco Bruni, for your trust and guidance and for continuously encouraging my confidence and independence over the past three years. While climbing the mountain that is a PhD, it has been an inordinate help to have someone who really knows the ropes leading the way, not only in matters of cosmology but also in mathematics, physics, geography, languages, politics and academia.

I am equally grateful to my second and third supervisors, David Wands and Rob Crittenden, for your invaluable input at many points during my PhD and for always keeping Marco and I on track. Thanks also to Carsten van de Bruck, for your generosity and enthusiasm which got me started in the field of dark energy in the first place, and to my examiners, David Bacon and Martin Kunz, for a very enjoyable viva and your valuable comments on this thesis.

I am grateful to Savvas Nesseris, Simone Peirone and Fabrizio Renzi for our fun and fruitful collaborations, and especially to Matteo Martinelli for teaching me everything I know about `CAMB` and `CosmoMC`, for mentoring me throughout my PhD, and demonstrating how efficiency, rigour and an incredible work ethic can be combined in research. Much of the work in this thesis would not have been realised without you.

I was lucky to travel extensively during my PhD and I gratefully acknowledge the financial support I was provided to do so by STFC and the EU COST-Action CANTATA. Thanks to the Lorentz Institute, Leiden for hosting my STSMs and the group at IFT UAM for hosting my (sadly curtailed) long-term attachment. Special thanks to Alvaro, Christian and Max for welcoming me into your office and the IFT guiris for teaching me the proper way to eat lunch in Spain.

There is a small but invaluable group of people in the ICG who keep everything running behind the scenes and without whom this thesis would literally not have been possible: to Jascha, Julie, Holly, Pippa, Toby and especially Gary, Georgia and Sharon for your unfailingly expeditious help with Sciama, your patience regarding FIN forms, and your forbearance in solving my myriad LTA problems respectively, my eternal gratitude.

Furthermore, I am indebted to everyone in the ICG for making it such a fun, friendly and stimulating environment to work in. Particular thanks to the denizens of the gravity meetings, from whom I learned a huge amount, and to all the occupants of DS 3.13 past and present for the camaraderie we shared, but especially Andrius and Maria, who were there from the beginning to the end.

Thanks also to Gui for being my relentless personal cheerleader; to Sam L and Michael for the questions, answers, football chats and our wonderful World Cup holiday; to Sam Y for the wordplay; to Minas for imparting all of your MCMC wisdom; to Mike for the poetry appreciation, LaTeX advice and much more besides; to Laura, for your extreme patience in the face of my attempts to speak Italian and for the walks, runs, aperitivi and smiles; to Bill, for ensuring massive neutrinos are always on my mind, for sharing my love of cosmology gossip and for enticing me out of my culinary comfort zone; and to Chris, for your willingness to listen to me complain about dark energy on a (very) regular basis, be it morning, noon or night, for all the laughs we shared and for your constant support, advice and encouragement.

I cannot overstate the equally great debt I owe to my friends in music. To every member of the UoP orchestra, the countless hours we spent together in rehearsals, concerts and deeply unprofessional pubs were a source of unreserved joy. I am especially grateful to Dan, Imogen and Matt for ensuring we never took ourselves too seriously, while still maintaining a rigorous forty hour practice schedule; to Tarek, for the crash course in Arabic, for tolerating my inevitably last minute page turns and for the warmth, skill and good humour with which you lead us from success to success; and finally to Colin, for your generally impeccable taste in repertoire (I'll forgive the G&S) but more importantly for the many, many beers over which we put the world to rights, one Thursday night at a time.

Finally, thank you to my family: Mum, Dad and James. Your support (both emotional and financial!) throughout all of my studies was indispensable. You can stop reading now!

Others taunt me with having knelt at well-curbs
Always wrong to the light, so never seeing
Deeper down in the well than where the water
Gives me back in a shining surface picture
Me myself in the summer heaven godlike
Looking out of a wreath of fern and cloud puffs.
Once, when trying with chin against a well-curb,
I discerned, as I thought, beyond the picture,
Through the picture, a something white, uncertain,
Something more of the depths – and then I lost it.
Water came to rebuke the too clear water.
One drop fell from a fern, and lo, a ripple
Shook whatever it was lay there at bottom,
Blurred it, blotted it out. What was that whiteness?
Truth? A pebble of quartz? For once, then, something.

ROBERT FROST

0

PREFACE

Questions about the Universe and our place within it have figured in the imagination of humanity for millennia. Some of the most spectacular surviving Palæolithic art, in the Lascaux cave system in southern France, depicts the Pleiades constellation clearly visible over the shoulder of an aurochs, in an image created by human hands more than 15,000 years ago [5]. However, cosmology as a physical science has only developed relatively recently, arguably with the inception of general relativity in the early 20$^{\text{th}}$ century, which provoked many questions about the behaviour and evolution of the Universe on the largest scales in space and time [6].

Hot on the heels of general relativity came a number of observational discoveries that quickly lent weight to the idea that the Universe is vast, populated by many galaxies distinct from our own, and expanding [7]. The notion of an expanding Universe naturally led to the question of how the Universe began, and so the hot Big Bang model of cosmology was developed, based on the simple principle that the Universe is homogeneous and isotropic [8, 9, 10].

The relic radiation from the Big Bang was first observed in 1964 as a uniform temperature across the whole sky, known today as the cosmic microwave background [11]. Since then, a further sixty years of scientific advances has left us in possession of the exquisite measurements of the cosmic microwave background made by the Planck satellite, which confirmed the postulated isotropy of the radiation to around one part in 100,000 [12].

However, the observational power we have at our disposal in this current era of precision cosmology continues to pose as many questions as it does answers. Just before the millennium, observations of distant supernovæ provided convincing evidence that the expansion of the Universe is apparently accelerating [13, 14]. In the simplest cosmological framework of spatial homogeneity and isotropy, this apparent acceleration is attributed to dark energy, in the form of a cosmological constant that becomes dominant at late times. But is the cosmological constant really the best explanation for the perceived accelerated expansion?

Our excellent precision in measuring the expansion rate of the Universe (quantified in the value of the Hubble parameter today, H_0) has revealed that measurements of H_0 made using different probes at high and low redshifts do not agree [15]. What is the reason for this tension?

Future measurements of all the different cosmological probes will yield even more precise constraints on the parameters of our cosmological models than current data is able to. How can we ensure we are not losing out on accuracy and becoming susceptible to bias when striving for ever more precise measurements?

This thesis is an attempt to answer these three questions.

In the standard model of cosmology, ΛCDM, the cosmological constant Λ is responsible for the late time accelerating expansion of the Universe. However, the cosmological constant explanation of dark energy is deficient in many aspects, which motivate us to consider alternative models, which must in turn be rigorously tested and constrained.

The majority of this thesis is devoted to a detailed study of the interacting vacuum scenario, an alternative type of dark energy in which the vacuum is free to interact with cold dark matter. In Chapter 3 we present the theoretical background to this scenario, followed by constraints on various models within the scenario from observational data. In Chapter 4, we extend this analysis to reconstruct the coupling between the vacuum and cold dark matter as a function of redshift, again using the latest observational data. We then move to an analysis of the Shan–Chen dark energy model cast into the framework of the interacting vacuum in Chapter 5.

We conclude the exposition of the novel research work presented in this thesis with Chapter 6, where we demonstrate how the distance duality relation can be probed using mock datasets of one of the most exciting future probes in cosmology: standard sirens. In this chapter, we also address the notion of biased detections that can arise when analysing non-standard cosmological models.

However, we begin by laying the foundations of physical cosmology in Chapter 1, covering the Friedmann–Lemaître–Robertson–Walker solution to the Einstein equations, observational probes in cosmology, the ΛCDM model and the theoretical and observational problems that model faces. We follow this with an explanation of our methodology in Chapter 2, in which we cover cosmological perturbation theory, statistical methods and the numerical codes used for the rest of the work described in the thesis.

Following the chapters containing the research work described above, we conclude the thesis in Chapter 7 with a summary of the main results, a discussion of their impact on the scientific community and some possible future directions for research in the field of dark energy.

Throughout this thesis, unless otherwise specified, we use units in which $c = \hbar = k_B = 1$.

1 COSMOLOGY

In this chapter, we review the fundamentals of physical cosmology that are relevant for the ideas discussed later in the thesis. We cover general relativity as the theory of gravity, the Friedmann–Lemaître–Robertson–Walker (FLRW) Universe and the ΛCDM model of dark energy and dark matter. We outline the main cosmological observables and describe how measurements of these observables help to constrain cosmological models. We explain the main problems with ΛCDM, and conclude the chapter with a discussion of alternative dark energy, dark matter and modified gravity models.

1.1 THE FLRW UNIVERSE

The cosmological principle states that on sufficiently large scales, the Universe is homogeneous and isotropic. A 4-dimensional spacetime with homogeneous and isotropic 3-dimensional subspaces is described by the FLRW metric, the line element for which can be written as

$$ds^2 = dt^2 - a(t)^2 \left[\frac{dr^2}{1 - Kr^2} + r^2 d\theta^2 + r^2 \sin^2\theta d\phi^2 \right], \tag{1}$$

where a is the cosmic scale factor, K is the spatial curvature of the Universe and t is cosmic time. The spatial curvature can either be zero (flat Universe), negative (open Universe) or positive (closed Universe). The parameter K thus takes a value of 0, -1 or 1.

At very early times, the Universe underwent a period of accelerated expansion, known as inflation [16, 17]. In the standard cosmological paradigm, the accelerated expansion is driven by a single scalar field slowly rolling down its potential. Despite its large size, the Universe is very homogeneous in temperature and is almost exactly spatially flat, two issues known as the horizon and flatness problems. Single field slow roll inflation is a mechanism by which the Universe can grow extremely large extremely rapidly, thereby solving these problems. Therefore, from now on, we set $K = 0$.

We will assume that gravity is described by Einstein's theory of general relativity [6], which has the field equations

$$G_{\mu\nu} \equiv R_{\mu\nu} - \frac{1}{2} R g_{\mu\nu} = 8\pi G T_{\mu\nu}, \tag{2}$$

where $g_{\mu\nu}$ is the metric on some 4-manifold $\mathbb{M}$ and has the pseudo-Riemannian Lorentzian signature $(1,3)$, $G_{\mu\nu}$ is the Einstein tensor, comprised of $R_{\mu\nu}$, the Ricci curvature tensor and R, the Ricci curvature scalar. The left hand side describes the geometry of spacetime and the right hand side describes the energy–momentum content of the Universe through the energy–momentum tensor $T_{\mu\nu}$. Newton's constant is represented by G.

The contracted Bianchi identity, $\nabla^\mu G_{\mu\nu} \equiv 0$, describes the covariant conservation of the Einstein tensor $G_{\mu\nu}$ and implies that the total energy–momentum tensor is also covariantly conserved, $\nabla^\mu T_{\mu\nu} = 0$. Using the perfect fluid form for the energy–momentum tensor, $T_{\mu\nu} = \mathrm{diag}(\rho, -P, -P, -P)$, we can identify an energy density $\rho \equiv T_{00}$ and a pressure $P \equiv -T_{ij}$.

1.2 COSMOLOGICAL DYNAMICS

Solving (2) with the spatially flat FLRW metric and the perfect fluid form of the energy–momentum tensor results in the equations which govern the background evolution of the Universe, the Friedmann equations:

$$H^2 \equiv \left(\frac{\dot{a}}{a}\right)^2 = \frac{8\pi G \rho}{3}, \tag{3}$$

$$\dot{H} = -4\pi G(P + \rho), \tag{4}$$

where H is the Hubble expansion scalar, ρ is the total energy density of the Universe's components and P the total pressure. A dot represents a derivative with respect to cosmic time. From these we can also derive the continuity equation,

$$\dot{\rho} = -3H(\rho + P). \tag{5}$$

We can define the equation of state for any given component,

$$w \equiv \frac{P}{\rho}, \tag{6}$$

and if we assume it to be constant, we can find the evolution of the energy density,

$$\frac{\dot{\rho}}{\rho} = -3\,\frac{\dot{a}}{a}\,(1+w), \tag{7}$$

$$\rho = a^{-3(1+w)}. \tag{8}$$

After the inflationary epoch, the scalar field that drove the accelerated expansion decayed into the radiation, matter and dark energy content of the Universe in a period known as reheating [18, 19, 20]. At this time, the Universe was radiation dominated. The equation of state for radiation is $w = 1/3$ which implies that $\rho \propto a^{-4}$ and hence $a \propto t^{\frac{1}{2}}$. From (4), $\ddot{a} < 0$, meaning that during radiation domination the Universe is expanding but slowing down.

The continued expansion and cooling of the Universe allowed the quarks to combine to form baryonic matter, and eventually the baryons to combine and form atomic nuclei in a process known as Big Bang nucleosynthesis [21]. Due to Compton scattering off the free electrons, the photons could not propagate freely during this time.

However, oscillations analogous to sound waves could propagate in the plasma, leading to a relative over-density in the plasma on the scale of the sound horizon. These baryon acoustic oscillations resulted in an increased amount of clustering in the matter content on that scale, visible as an imprint in the large scale structure of the late time Universe. We will discuss this further in section 1.5.

Eventually the Universe cooled sufficiently to allow for de-ionisation of the primordial plasma, thus allowing the photons to decouple from the electrons and freely stream across the Universe. This means that there is a fixed surface – the surface of last scattering – before which we cannot make optical observations of the Universe. Today, we observe the photons from the last scattering surface as the cosmic microwave background, which we will also discuss in more detail in section 1.5.

We can model the baryonic matter as a pressureless dust, with the equation of state $w = 0$. This means that $\rho \propto a^{-3}$ and $a \propto t^{\frac{2}{3}}$. Since radiation decays as a^{-4}, at early times the Universe transitioned from a period of radiation domination to a period of matter domination. The moment of matter–radiation equality and the transition to the matter dominated epoch occurred before the period of last scattering. Again, from (4), $\ddot{a} < 0$, so during matter domination the Universe is expanding but not accelerating. With the matter component now being the dominant component in the Universe, the first stars began

to form, followed by the formation of globular clusters, galaxies and galaxy clusters.

1.3 COLD DARK MATTER AND LATE TIME ACCELERATION

So far, we have only considered the presence of baryonic matter, which interacts electromagnetically as well as gravitationally. However, the presence of matter in the Universe which does not interact electromagnetically has been known since the early 1930s due to observations of the velocities of galaxies in the Coma cluster, which were found to be moving much faster than predicted by the virial theorem [22]. To properly satisfy the virial theorem, the mass of the galaxies in the cluster must be greater than their visible matter implies, meaning that there exists some unseen dark matter that only interacts gravitationally.

The notion that galaxies and galaxy clusters are virialised objects is of course an assumption, but further evidence for the presence of dark matter has been found by examining the rotation curves of individual galaxies (the rotation velocity does not decrease with radius, implying there is a large quantity of non-luminous matter in the halo of every galaxy) [23], X-ray emissions from galaxy clusters (by comparing the theoretical prediction from the hydrostatic equilibrium equations for the temperature and density of the ionised gas in clusters we see a discrepancy in the predicted and observed mass of the system) [24], the growth of large scale structure (perturbations in the pre-recombination photon–baryon fluid cannot grow until the surface of last scattering, meaning structure growth purely due to baryons does not match the growth we actually observe) [25] and finally the features we observe in the power spectrum of the cosmic microwave background, which we will discuss in more detail in section 1.5.

Little is known about the actual physical properties of the dark matter particle, and even the idea that is is a particle is unproven. However, cosmological observations have enabled some inferences to be made. For example, we know that the particle must be "cold", that is non-relativistic, from observations of large scale structure [26]. Observations of the cosmic microwave background [27] and Lyman-α forest [28] have also placed bounds on the mass and properties of the dark matter particle, and observations of the Bullet cluster can be used to constrain the dark matter self-interaction cross-section [29, 30]. Hence, in the Λ cold dark matter (CDM) model, the dark matter is considered to be a weakly interacting massive particle, or WIMP,

though many alternative ideas exist. We will discuss some of these ideas further in section 1.8.

Finally, we have known since 1998 that the late time expansion of the Universe is accelerating [13, 14]. This discovery was made by observing Type Ia supernovæ, which were found to be dimmer than expected in the expanding but decelerating Universe that is expected for the matter dominated scenario. We will discuss Type Ia supernovæ in more detail, along with other observational evidence for dark energy in section 1.5.

In order to have an accelerated expansion at late times i.e. $\ddot{a} > 0$, the Universe must be dominated by a component with negative pressure. From (4), this means $P < -\rho/3$, or $w < -1/3$. The simplest component that fulfils these criteria is the cosmological constant, Λ, which represents the vacuum energy of the Universe. Vacuum energy has the equation of state $w = -1$, leading to $\rho \propto a^0 = \text{const.}$ and in the simplest model of a Universe only containing vacuum energy (i.e. asymptotically into the future of a spatially flat ΛCDM Universe), $a \propto e^{tH}$, and hence accelerated expansion.

With the cosmological constant included, the Einstein field equations (2) become

$$R_{\mu\nu} - \frac{1}{2}Rg_{\mu\nu} + \Lambda g_{\mu\nu} = 8\pi G T_{\mu\nu}, \tag{9}$$

and the Friedmann equations in a spatially flat Universe (3), (4) become

$$H^2 = \frac{8\pi G\rho}{3} + \frac{\Lambda}{3}, \tag{10}$$

$$\dot{H} = -4\pi G(\rho + P) + \frac{\Lambda}{3}. \tag{11}$$

The cosmological constant Λ is thus the second part of the standard ΛCDM model.

It is convenient to define density parameters for the different components of the Universe. We define

$$\Omega_\mathrm{r} = \frac{8\pi G\rho_\mathrm{r}}{3H_0^2}, \tag{12}$$

$$\Omega_\mathrm{m} = \frac{8\pi G\rho_\mathrm{m}}{3H_0^2}, \tag{13}$$

$$\Omega_\mathrm{DE} = \frac{8\pi G\rho_\mathrm{DE}}{3H_0^2}, \tag{14}$$

where the subscripts r and DE refer to radiation and dark energy respectively. In ΛCDM, we refer to the sum of the baryonic and cold dark matter components as "matter", using the subscript m. Remembering that we are assuming there is zero spatial curvature, these density parameters sum to one,

$$\Omega_{\mathrm{r}} + \Omega_{\mathrm{m}} + \Omega_{\mathrm{DE}} = 1, \tag{15}$$

which, from (10) (and remembering that we have made the assumption that the dark energy fluid equation of state w_{DE} is constant), we can write

$$\frac{H(z)}{H_0} = \left[\Omega_{\mathrm{r}}(1+z)^4 + \Omega_{\mathrm{m}}(1+z)^3 + \Omega_{\mathrm{DE}}(1+z)^{3(1+w_{\mathrm{DE}})}\right]^{1/2}. \tag{16}$$

1.4 DISTANCES IN COSMOLOGY

In this thesis, we are interested in understanding the behaviour of the late time Universe, and in particular, the rate of acceleration through the value of the Hubble expansion scalar today, H_0. To do this, we must understand how photons propagate in general relativity and how distances can be measured in an expanding Universe.

In a curved spacetime described by general relativity, freely falling particles travel on geodesics. Since photons are massless, they travel on null geodesics, i.e. $ds^2 = 0$. Due to the assumption of isotropy, we can assume that the photons only propagate in the radial direction, implying

$$ds^2 = -dt^2 + a^2(t)dr^2 = 0, \tag{17}$$

$$dr^2 = \frac{dt^2}{a^2(t)}, \tag{18}$$

which can be integrated to find the distance which light can travel between some initial and final times t_i and t_f, known as the comoving distance,

$$d_c(t_i, t_f) = \int_{t_f}^{t_i} \frac{dt^2}{a^2(t)}. \tag{19}$$

The wavelength of light is stretched as the Universe expands, causing distant objects to appear reddened. This effect is quantified through the redshift,

$$z = \frac{\lambda_o}{\lambda_e} - 1, \tag{20}$$

where λ_o is the observed wavelength and λ_e is the emitted wavelength.

Under the assumptions of spatial flatness and the FLRW metric, the redshift is related to the cosmic scale factor via

$$1 + z = \frac{a_0}{a}. \tag{21}$$

Setting the value of the scale factor today to one, i.e. $a_0 = 1$, this means that

$$a = \frac{1}{1+z}. \tag{22}$$

We can hence write the comoving distance in terms of redshift and the Hubble parameter $H(z)$,

$$d_c(z) = \int_0^z \frac{dz'}{H(z')}. \tag{23}$$

The next important distance measure in cosmology is the luminosity distance, defined as

$$d_L^2 = \frac{L}{4\pi F}, \tag{24}$$

where L is the absolute luminosity of a source and F is the observed flux. The luminosity distance can be written in terms of the comoving distance,

$$d_L(z) = (1+z)d_c(z). \tag{25}$$

Finally, we define the angular diameter distance,

$$d_A = \frac{\Delta x}{\Delta \theta}, \tag{26}$$

where $\Delta\theta$ is the angle that subtends an object of known size Δx perpendicular to the line of sight. The angular diameter distance can also be written in terms of the comoving distance,

$$d_A(z) = \frac{d_c(z)}{1+z}. \tag{27}$$

The relationship between (25) and (27),

$$d_L(z) = (1+z)^2 d_A(z), \tag{28}$$

is known as the distance duality relation, or the Etherington reciprocity theorem, and holds under the conditions that photons propagate on null geodesics in a pseudo-Riemannian spacetime, and that photon number is conserved [31, 32]. It is also important to note that (25), (27) and (28) only hold in the stated forms under the assumption of spatial flatness.

1.5 OBSERVATIONAL EVIDENCE FOR DARK ENERGY

Nearly all of observational cosmology is based on detecting photons after they have travelled across the Universe, and inferring the properties and contents of the Universe from these photons. We can observe photons from the cosmic microwave background, from galaxies and from individual stars, typically when those stars reach their end of their lifetime in a supernova explosion. We will now discuss all of these observations in detail, focusing on how they allow us to constrain cosmic distances and the content of the Universe, and hence give us information about dark energy. For the majority of this discussion, we follow [33].

1.5.1 *The age of the Universe*

As we previously mentioned, the late time accelerated expansion of the Universe was confirmed in 1998 with observations of Type Ia supernovæ. However, even before that date, it was clear that a matter dominated model was not the correct description of the Universe, as the age of the oldest stars seemed to be well above the calculated age of the Universe.

The age of the Universe can be given in terms of (16) using $dt = -dz/[(1+z)H]$,

$$t_0 = \int_0^\infty \frac{dz}{H(z)(1+z)}. \tag{29}$$

For a Universe with zero spatial curvature, and neglecting the contribution from radiation as it is only important at very early times, and dark energy, as we want to understand the age of the Universe without it, we find

$$t_0 = \frac{2}{3} H_0^{-1}. \tag{30}$$

This means that, taking for example $H_0 = 70$ kms^{-1} Mpc^{-1}, $t_0 \approx 9$ gigayears. This is in conflict with the age of globular clusters, typically estimated to be greater than 11 gigayears (see e.g. [34]). The only way this age discrepancy can be resolved is by having a period of late time accelerated expansion.

1.5.2 *Type Ia supernovæ*

Supernovæ are among the brightest objects in the observable Universe, often outshining their own host galaxies at the peak of their explosions. The specific astrophysical properties of certain types of supernovæ mean we are able to probe cosmic distances with them, allowing a Hubble diagram to be constructed and H_0 to be constrained. Detailed explanations of all types of supernovæ and their astrophysical properties can be found in [35]. We focus here on a description of the supernova class most commonly used for cosmology, Type Ia.

A Type I supernova is classified as such by the absence of hydrogen in its spectrum and it is classified as a Type Ia by the presence of a silicon absorption line [36, 37]. The progenitor systems of Type Ia supernovæ are generally believed to fall into two categories: single degenerate, which are binary systems composed of a white dwarf and a companion red giant, and double degenerate, a binary system of two white dwarfs [38, 39]. Let us first consider the single degenerate case.

A red giant is a star that has exhausted the supply of hydrogen in its core, and thus hydrogen fusion begins in a shell surrounding the degenerate core. The core contracts and the outer layers of the atmosphere expand in compensation, thus maintaining the gravitational and thermal equilibrium of the star. As the outer layers expand, they begin to overflow the Roche lobe, and material from the atmosphere of the red giant begins to accrete onto the white dwarf. Eventually the additional mass added to the white dwarf means that the electron degeneracy pressure that supports it against gravity is overcome, and the supernova explosion occurs.

Since the limit at which the electron degeneracy pressure fails is known to be the Chandrasekhar limit, the peak luminosity of these supernovæ should be the same, no matter where they are in the Universe. Simplistically speaking, this allows their absolute magnitude to be standardised, and the luminosity distances to them to be measured with good accuracy. For this reason, Type Ia supernovæ are referred to as "standardisable candles".

Moving beyond the simple picture of standardisability, the absolute magnitude of a Type Ia supernova can actually only be obtained via the correlation of apparent magnitude with the width of the light curve and the colour of the supernova at maximum brightness [40, 41]. Other systematics that could affect the standardisability include the properties of the host galaxy of the supernovæ [42, 43, 44] and

the possible redshift dependency of the supernova luminosity on its surroundings, which can be modelled as depending on the star formation rate [45, 46] or the metallicity of the environment [47].

Furthermore, in the double degenerate case, the merging of two white dwarfs would cause their combined masses to exceed the Chandrasekhar limit (see e.g. [48]). If the majority of Type Ia supernovæ are the result of double degenerate progenitor systems, then their standardisability is also less certain, as the lack of an upper mass limit means there is no limit on their peak luminosity. A further complication common to both cases is the randomness of supernovæ in sky location and time, meaning it is extremely difficult to locate and observe a supernova before it occurs. This makes determining the role of environment on the supernovæ even more challenging.

However, in the rest of this thesis we will assume that the standardisability questions are insignificant and therefore the absolute magnitude can be reliably found in the most basic way described. The luminosity distance is then accessed using the distance modulus,

$$m(z) - M = 5 \log_{10} d_L(z) - 5, \tag{31}$$

where $m(z)$ is the apparent magnitude of the supernova, M is the absolute magnitude and $d_L(z)$ is the luminosity distance in parsecs. The redshift of the supernova can be found by observing the wavelength of its light and the shift of various absorption lines in its spectra, and with a sufficient number of supernova observations the dependence of the observed luminosity on redshift can be found. For large supernova catalogues such as Pantheon, this is compared to the theoretical distance in spatially flat ΛCDM (25) and the values of cosmological parameters such as Ω_m and Ω_Λ are inferred [49].

In this way, the late time accelerating expansion of the Universe was discovered by [13] and [14]. In Figure 1, we reproduce the Hubble diagram from [14], in which it was found that the cosmological constant model was favoured at the 99% confidence level and the matter density parameter today is $\Omega_m = 0.28^{+0.09}_{-0.08}$. Thus we have our second significant piece of evidence in favour of a dominant dark energy component in the Universe.

1.5.3 *The cosmic microwave background*

The cosmic microwave background, or CMB, is the oldest part of the optical sky, comprising the first photons to decouple from the primordial plasma and freely stream across the Universe. It was discovered

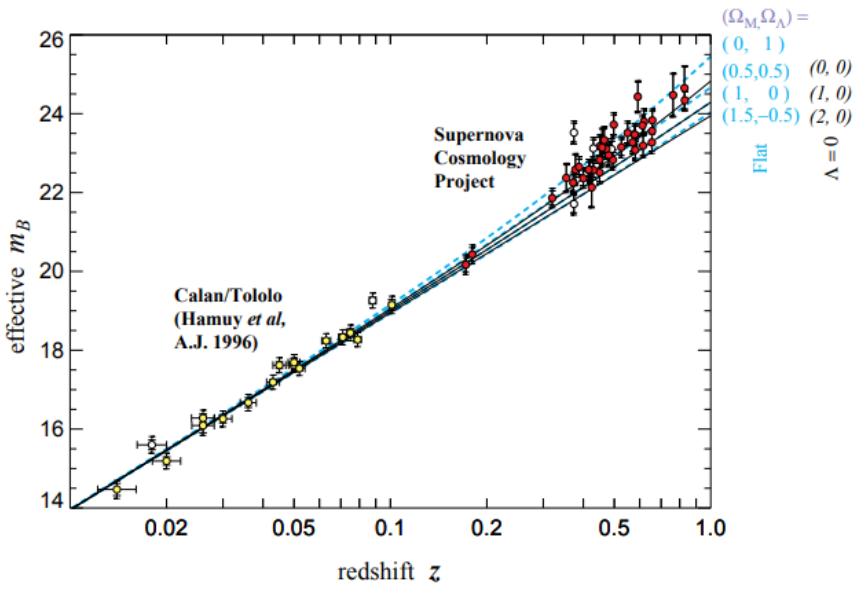

Figure 1: The Hubble diagram from [14], showing the effective apparent luminosity as a function of redshift. The solid lines show the theoretical predictions for various cosmological models with non-zero spatial curvature but no cosmological constant, and the dashed lines show the theoretical predictions for various flat models with a cosmological constant.

in 1964 by Penzias and Wilson [11], who observed the CMB as an almost uniform temperature across the whole sky. This observation was followed three decades later by the COBE satellite [50], which discovered small temperature anisotropies in the CMB, more precise measurements of which have been made by BOOMERanG [51], MAXIMA [52], WMAP [53] and most recently, Planck [12]. These anisotropies are mainly sourced by scalar perturbations in the photon–baryon fluid. We will discuss the computation and evolution of these perturbations in more detail in Chapter 2. Here we will explain how the presence of dark energy in the Universe affects the CMB anisotropies.

The main effect of dark energy on the CMB is the alteration of the position of the acoustic peaks in the power spectrum due to modification of the angular diameter distance (the other contribution comes from the integrated Sachs–Wolfe effect, which describes the evolution of gravitational potential wells as photons fall into and climb out of them and is only relevant on very large scales [54]). Following [33], we can define a temperature perturbation

$$\Theta(x,\tau) \equiv \frac{\delta T}{T}, \tag{32}$$

where x is position and τ the conformal time, defined as

$$\tau = \int_0^t \frac{dt'}{a(t')}, \tag{33}$$

and T is the average CMB temperature, $T = 2.725\text{K}$. Since we observe the CMB across the whole sphere of the sky, we expand the temperature perturbation in terms of spherical harmonics,

$$\Theta(x,\tau) = \sum_{\ell=1}^{\infty} \sum_{m=-\ell}^{\ell} a_{\ell m} Y_{\ell m}, \tag{34}$$

from which we can express the multipole cross-correlation function in the Fourier space k as

$$C_\ell = \frac{2}{\pi} \int_0^\infty dk\, k^2 |\Theta_\ell(k)|^2. \tag{35}$$

According to the Wiener–Khinchin theorem, the Fourier transform of the correlation function is the power spectrum [55, 56], so C_ℓ is the CMB power spectrum.

There are actually six power spectra potentially accessible to CMB observations: the power spectra arising from the temperature–temperature (TT), E-mode–E-mode polarisation (EE) and B-mode–B-mode polarisation (BB) autocorrelations and the power spectra

arising from the temperature–E mode (TE), temperature–B-mode (TB) and E-mode–B-mode (EB) cross-correlations. However, since the T and E-modes are parity even and the B-mode is parity-odd, the TB and EB cross-correlations should vanish if the CMB fluctuations are parity invariant [57, 58]. Furthermore, since the BB spectra are very subdominant to TT in terms of the power, we use the constraints coming from the TT, EE and TE spectra only in the work reported in Chapters 3, 4 and 5.

However, the B-mode itself is extremely interesting in its own right. Scalar perturbations can only create E-mode polarisations, meaning that any primordial B-modes must have been created by tensor perturbations, which could have only been present in the early Universe if they were sourced during inflation. Detection of primordial B-modes would therefore represent a huge leap forward in our understanding of the very early Universe, but efforts in this direction have so far been hampered by the secondary B-mode signals generated by weak lensing of the CMB photons as they propagate through the Universe, as well as other foregrounds such as galactic dust [59, 60].

In general, the scalar perturbations can be thought of as analogous to sound waves propagating in the primordial plasma, which cause areas of rarefaction and compression. These in turn correspond to peaks and troughs in the CMB power spectrum. The position of the peaks depends on the contents and evolution of the Universe, and we are particularly interested on the effect of dark energy on the CMB peaks.

As shown in [33], the comoving wavelength corresponding to the acoustic peaks can be approximated as $\lambda_c = 2\pi/k = 2r_s/n$, where r_s is the sound horizon and n are integers. The characteristic angle for the peak locations can then be defined as

$$\theta_{\mathrm{MC}} \equiv \frac{r_s(z_{\mathrm{rec}})}{d_A^{\mathrm{com}}(z_{\mathrm{rec}})}, \tag{36}$$

where z_{rec} is the redshift of the recombination epoch when photons decoupled from the electrons (more specifically, at recombination, the majority of the electrons combined with the atomic nuclei produced during Big Bang nucleosynthesis, but the photons continued to be scattered off the remaining free electrons; this time is not to be confused with drag epoch when photons decoupled completely from the remaining electrons and began to freely stream across the Universe, which occurred approximately $z = 80$ later) and d_A^{com} is the comov-

ing angular diameter distance, defined in terms of the proper angular diameter distance (27) as

$$d_A^{\mathrm{com}}(z) = (1+z)d_A(z). \tag{37}$$

The specific multipole ℓ which corresponds to the angle θ_{MC} is given by

$$\ell_A = \frac{\pi}{\theta_{\mathrm{MC}}}. \tag{38}$$

The comoving angular diameter distance can be expressed as

$$d_A^{\mathrm{com}}(z_{\mathrm{rec}}) = \frac{c}{H_0}\frac{1}{\sqrt{\Omega_{\mathrm{m},0}}}\mathcal{R}, \tag{39}$$

where $\mathcal{R}$ is the CMB shift parameter, which in a spatially flat Universe is given by

$$\mathcal{R} = H_0\sqrt{\Omega_{\mathrm{m},0}}\int_0^{z_{\mathrm{rec}}}\frac{dz}{H(z)}, \tag{40}$$

and it can be shown that the multipole ℓ_A is directly proportional to $\mathcal{R}$. It is also clear from (40) that the CMB shift parameter is altered according to the expansion history of the Universe from the epoch of recombination to the present. With dark energy present in the Universe, the value of $\mathcal{R}$ is different compared to in a matter dominated Universe, thereby changing the position of the acoustic peaks ℓ_A.

This effect can be seen by comparing the predicted CMB temperature–temperature power spectrum for ΛCDM with the Planck 2018 observations, as shown in Figure 2 (reproduced from [61]). The prediction for the peak positions and amplitudes in a Universe with dark energy represented by a cosmological constant almost perfectly matches the observational data.

Let us briefly depart from our dark energy theme for a moment to remark on the superb constraints the Planck satellite observations have placed on other cosmological parameters, and in particular, the predictions made by single field slow roll inflationary models. We reproduce a summary table from [12] in Table 1 which elucidates these constraints. Note that the statement in the table that the scalar perturbations are Gaussian could be modified to "very close to Gaussian". The non-linearity of general relativity and the fact that the accelerated expansion during inflation is not perfectly exponential even in single field slow roll inflationary models implies a small degree of non-Gaussianity.

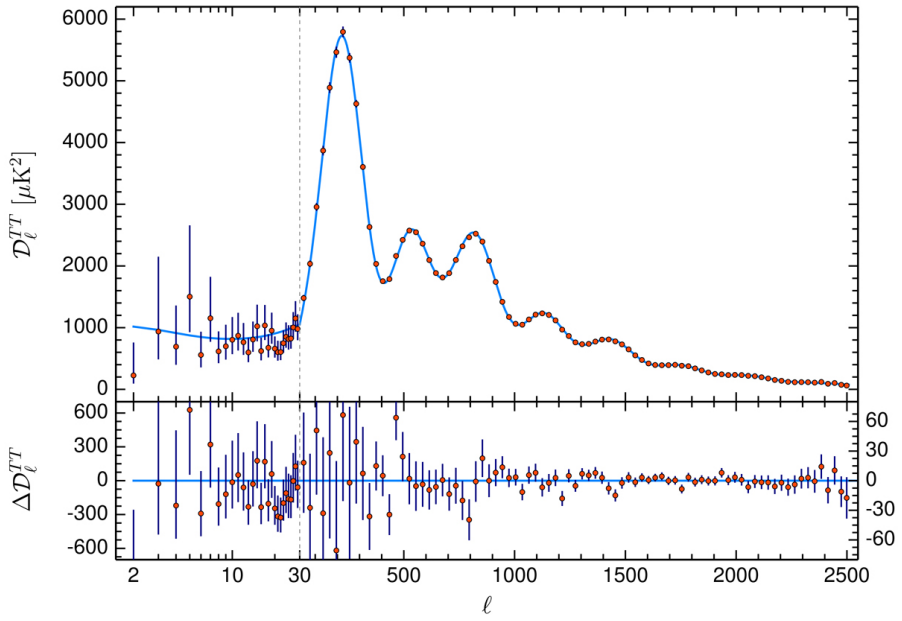

Figure 2: The CMB temperature–temperature power spectrum from [61]. The theoretical prediction is given by the blue line and the binned observational data is shown by the red points.

Prediction	Measurement
A spatially flat Universe	$\Omega_K = 0.0007 \pm 0.0019$
with a *nearly* scale-invariant spectrum,	$n_s = 0.967 \pm 0.004$
which is almost a power law,	$\frac{dn}{d\ln k} = -0.0042 \pm 0.0067$
dominated by scalar perturbations,	$r_{0.002} < 0.065$
which are Gaussian	$f_{\mathrm{NL}} = -0.9 \pm 5.1$
and adiabatic,	$\alpha_{-1} = 0.00013 \pm 0.00037$
with negligible topological defects	$f < 0.01$.

Table 1: Planck 2018 results for the predictions of the simplest inflationary models, reproduced from [12] .

1.5.4 *Baryon acoustic oscillations*

Before recombination, the photons and baryons were tightly coupled. This means that the same sound waves that resulted in the CMB temperature anisotropies also left an imprint in the baryon perturbations. The peak of the baryon acoustic oscillations, or BAO, was first detected at $100h^{-1}$ Mpc [62], where h is the Hubble parameter in units of 100 kms^{-1} Mpc^{-1}. From the location of this peak, we have yet more evidence of a dominant dark energy component in the Universe, as we will now explain.

The epoch when the photons were released from the Compton scattering, or drag, of the baryons is known as the drag epoch. The sound horizon at $z = z_{\text{drag}}$ is

$$r_s(z_{\text{drag}}) = \int_0^{\tau_{\text{drag}}} d\tau \; c_s(\tau), \tag{41}$$

where $c_s(\tau)$ is the sound speed of the photon–baryon plasma,

$$c_s^2 = \frac{\delta P_\gamma}{\delta\rho_\gamma + \delta\rho_b}, \tag{42}$$

where a subscript γ refers to photon quantities, a subscript b refers to baryon quantities and τ is conformal time.

The angular and redshift distributions of galaxies in redshift space are observed as a power spectrum $P(k_\perp, k_\parallel)$, where $k_\perp$ and $k_\parallel$ are wavenumbers perpendicular and parallel to the line of sight respectively. As shown in [33], from the power spectrum it is possible to obtain the quantities

$$\theta_{\text{BAO}} = \frac{r_s(z_{\text{drag}})}{(1+z)d_A^{\text{com}}(z)}, \tag{43}$$

$$\delta z_{\text{BAO}} = \frac{r_s(z_{\text{drag}})H(z)}{c}, \tag{44}$$

where $d_A^{\text{com}}(z) = (1+z)d_A(z)$ as previously described in (37). The angle θ_{BAO} corresponds to observations perpendicular to the line of sight and δz_{BAO} corresponds to observations made along the line of sight.

The current BAO data is insufficient to measure these two distances separately, but a combined distance scale can be obtained from the spherically averaged power spectrum,

$$[\theta_{\text{BAO}}^2 \delta z_{\text{BAO}}]^{1/3} \equiv \frac{r_s(z_{\text{drag}})}{[(1+z)^2 d_A^2(z) c/H(z)]^{1/3}}, \tag{45}$$

or as a related effective distance,

$$d_V(z) \equiv \left[(1+z)^2 d_A^2(z) \frac{cz}{H(z)}\right]^{1/3}. \tag{46}$$

We can thus compare predictions for the distance scale $d_V(z)$ to observational data, finding once again that a dark energy dominated Universe is favoured over a matter dominated one (see e.g. [63, 64]).

1.6 OTHER OBSERVATIONAL PROBES

There are many other observational probes in cosmology that can be used to probe not only the dark energy content but also the dark matter density and its overall growth into the large scale structure we observe in the late time Universe. We will now give a brief overview of the most important of these, some of which were used in the research work detailed in Chapters 3, 4, 5 and 6, namely redshift space distortions, gravitational lensing and gravitational waves.

1.6.1 *Redshift space distortions*

The distances to galaxies are generally measured using their redshifts. In a perfectly homogeneous Universe, the redshift to a galaxy would be an accurate measure of the radial distance from the observer, and the mapping from real space to redshift space would be an identity [65].

However, the Universe is not perfectly homogeneous. Inhomogeneous structure growth induces peculiar velocities in the galaxies, which in turn distort the mapping from real space to redshift space, leading to an apparent increase in large scale clustering in the radial direction compared to the transverse direction. These are called redshift space distortions (RSD) (see [66] for a review).

The linear growth rate of structure is given by

$$f(z) \equiv \frac{d\ln D}{d\ln a}, \tag{47}$$

where D is the amplitude of the linear growing mode [67]. The anisotropic clustering seen in the redshift space distortions is correlated with the structure growth rate f, meaning that redshift space distortions can be used as a probe of the quantity $f\sigma_8$, the growth rate multiplied by the amplitude of the velocity power spectrum on the scale of 8 h^{-1} Mpc [68].

More formally, the quantity σ_8 is defined as

$$\sigma_8^2 = \int_0^\infty W^2(kR)P(k)\frac{1}{k}dk, \tag{48}$$

where W is a top hat filter function in the Fourier space k,

$$W(kR) = 3\left[\frac{\sin(kR)}{(kR)^3} - \frac{\cos(kR)}{(kR)^2}\right], \tag{49}$$

$P(k)$ is the matter power spectrum and R is the radius defined by 8 h^{-1}Mpc [18]. A related parameter, S_8, is often quoted instead of σ_8, which is defined as $S_8 = \sigma_8\sqrt{\Omega_m/0.3}$.

Note that in the interacting dark energy models studied later in this thesis, the growth rate picks up an additional term due to the coupling between dark energy and dark matter, meaning that redshift space distortions are no longer a direct probe of structure growth in these models. We will discuss this point further in Chapter 3.

1.6.2 *Gravitational lensing*

In general relativity, massive objects curve spacetime and act as gravitational lenses, meaning that the geodesics that photons travel on also follow curved paths, making them longer than in flat spacetime [69, 70]. This bending of the light's path gives rise to several observable phenomena:

- Multiple images of the source object can appear to the observer due to the light from the source travelling along different paths around the lens mass;
- The different lengths of the various paths taken by the light from the source around the lens mass means the images of the source appear to the observer at different times, with a measurable quantity called the "time delay" between them;
- Photons are not created or destroyed during lensing so the surface brightness of the source object remains unchanged. However, the apparent size of the source is not conserved, due to the light from each side of the source object taking different paths around the lens. This means that the source can appear brighter or dimmer, in a process respectively called magnification or demagnification.

Observations of strong lensing time delays lead directly to constraints on cosmology, as the quantity $\Delta t H_0$, where Δt is the time delay, depends only on the mass profile of the lens and the relative redshifts to

the source and lens [71]. Single galaxy lenses tend to be relied on for cosmological applications, as they are abundant in the sky and have relatively simple mass profiles. For ease of detection, a luminosity comparable to a galaxy is preferred for the source object, which has led to lensed quasars being the main strong lensing probe of cosmology, with great success [72, 73, 74, 75, 76], although strongly lensed Type Ia supernovæ are a promising future probe (see e.g. [4]). We will discuss the strongly lensed quasar constraints on H_0 in more detail in section 1.7.

A weaker form of gravitational lensing occurs when very distant background galaxies are lensed by foreground galaxy clusters. While generally not visible to the eye, the shear introduced by the cluster potential acts to align the background galaxies, which becomes apparent after averaging over many images [77]. This weak lensing signal can be combined with cluster abundances to constrain structure growth, as done by the Dark Energy Survey, which recently reported a measure of $S_8 = 0.65 \pm 0.04$ [78]. Weak lensing can therefore be used when constraining interacting dark energy models that predict a different structure growth to ΛCDM, as we will see in Chapter 4.

1.6.3 *Gravitational waves*

We have already mentioned anisotropies in the CMB which are sourced by scalar perturbations, which we will discuss in more detail in Chapter 2. Besides these scalar modes, and vector modes which in standard inflationary models decay rapidly and hence play no part in cosmology on linear scales, the propagation of tensor modes (either sourced during inflation, or at later times by the merging of compact objects) can be observed as gravitational waves.

In general relativity and in a vacuum, gravitational waves propagate according to the wave equation

$$h_A''(\tau, k) + 2\mathcal{H}h_A'(\tau, k) + k^2 h_A(\tau, k) = 0, \tag{50}$$

where primes denote derivatives with respect to conformal time, $h_A(\tau, k)$ are the Fourier modes of the gravitational wave amplitude, $\mathcal{H}$ the conformal Hubble parameter $\mathcal{H} = aH$ and the index $A = +, \times$ represent the two polarisations of the gravitational waves [79].

Gravitational waves sourced by the merging of two black holes were first detected in 2015 by the LIGO–Virgo collaboration [80]. This detection confirmed the prediction by general relativity of the existence of gravitational waves. The subsequent observation two years later

of a binary neutron star merger with an electromagnetic counterpart was even more important for cosmology. It allowed extremely tight constraints to be placed on the tensor speed, thus ruling out theories of modified gravity which predicted a tensor speed different to that of light [81, 82, 83].

Furthermore, gravitational waves observed with an electromagnetic counterpart can be used as "standard sirens" to construct a Hubble diagram and obtain distance ladder independent measurements of the value of the Hubble parameter today, H_0 [84]. This is because the gravitational wave amplitude is inversely proportional[1] to the luminosity distance to the gravitational wave source [79],

$$h_A \propto \frac{1}{d_L(z)}, \tag{51}$$

and the redshift can be found using the electromagnetic counterpart, meaning the measurement of H_0 can be made via combining (23) and (25) to express the luminosity distance as

$$d_L(z) = (1+z)\int_0^z \frac{c}{H(z')dz'}, \tag{52}$$

where $H(z)$ can be found from (16) in the spatially flat ΛCDM model.

To date, there has only been a single confirmed observation of a compact object merger with an electromagnetic counterpart, making the constraint on H_0 uncompetitive with other probes: $H_0 = 70.0^{+12.0}_{-8.0}$ kms^{-1} Mpc^{-1} [84]. Future observations could yield tens or hundreds more measurements of H_0 from standard sirens, meaning that they will eventually become an excellent probe of the cosmic expansion history and hence ΛCDM or alternatives to it. We discuss a related application of standard sirens in Chapter 6.

1.7 PROBLEMS WITH ΛCDM

The ΛCDM model has survived many challenges in its twenty year lifespan, in part due to its simplicity. From a statistical standpoint, it is generally difficult for more complex models to be preferred by the data, as the information gained from any additional parameters introduced in an alternative model is usually insufficient to justify their inclusion. The six parameter ΛCDM model, described by the cold dark

1 In practice, terms from the antenna pattern functions of the gravitational wave detector and the chirp mass of the merging compact objects will also appear in this expression. We give more details on this in Chapter 6 and Appendix A. The specific expression is given in (225).

matter and baryon energy densities, $\Omega_c h^2$ and $\Omega_b h^2$, the amplitude and spectral tilt of the primordial power spectrum, A_s and n_s, the optical depth at reionisation, $\tau_{\rm op}$, and the angular size of the sound horizon at recombination, $\theta_{\rm MC}$, remains the cosmological model to beat, and one against which all alternatives must be measured and compared.

The outlook may therefore seem bleak for alternative dark energy models such as those that are the focus of this thesis. However, the idea of using the cosmological constant as dark energy has long faced issues from a quantum field theory standpoint as well as a cosmological one, and observational tensions present within the framework of ΛCDM also motivate the continued study of possible alternatives. These problems are the cosmological constant problem, the coincidence problem, the H_0 tension and the σ_8 tension, and we will now discuss each of these in turn.

1.7.1 *The cosmological constant problem*

Well before the late time acceleration was discovered and attributed to the cosmological constant, the problem of the "vacuum catastrophe" was known [85, 86]. In simple terms, quantum field theory predicts the vacuum energy to have a very large value, obtained by summing the zero-point energies of every degree of freedom of all quantum fields present in the Universe, up to some cut-off scale, which should have correspondingly large gravitational effects.

However, these large gravitational effects have not been observed. The upper limit from observations on the size of the vacuum energy is completely in conflict with the prediction from quantum field theory, at the level of 120 orders of magnitude. The problem can be eased somewhat – perhaps down to forty or sixty orders of magnitude – if a different cut-off scale for the zero-point energy summation is chosen [87], but this is still extremely unsatisfactory.

It is not clear if the solution to the cosmological constant problem will come from quantum field theory or cosmology. A cosmological solution would entail introducing a "bare" cosmological constant which effectively cancels the contributions from all fields except the observed cosmological constant, or perhaps eliminating the observed cosmological constant entirely, attributing the late time acceleration to a new component such as a scalar field [88]. We will discuss this point in more detail in section 1.8.

1.7.2 *The coincidence problem*

The coincidence problem highlights the apparent issue with the matter and dark energy densities being roughly the same at present, despite evolving at different rates, as we discussed in section 1.2. This problem is generally considered to be less troublesome than the cosmological constant problem [89, 90, 91] and whether one believes it is a true problem with our cosmological model or is simply just a coincidence is largely dependent on how distasteful one finds anthropic arguments.

In brief, the anthropic principle posits that, since we are here to observe the Universe in its current state, the values of physical quantities (such as the dark matter and dark energy densities) in that state are what they are due to the requirement that carbon-based life must be able to evolve under those conditions [92]. This idea was summarised in a neat paraphrase of Descartes by Carter: *cogito ergo mundus talis est*[2] [93].

However, the anthropic principle is not a natural bedfellow of the Copernican principle, the bedrock of observational cosmology which states that we do not occupy a privileged position in the Universe. So, if we do not dismiss the coincidence problem as a mere coincidence, it can be used to motivate alternative dark energy models. In particular, dynamical dark energy models, in which the energy density of dark energy is not constant but changes over time, are useful due to their ability to provide a natural explanation to the apparently coincidentally similar values of the matter and dark energy densities. We will discuss this type of model further in section 1.8.

1.7.3 *Tensions*

The H_0 tension has become the most notorious problem in cosmology in recent years and is the single biggest motivator for the investigation of alternative models of dark energy. The value of H_0 can be obtained from measurements of the luminosity distances to Type Ia supernovæ, a method which generally requires the construction of the distance ladder if independence from a cosmological model is desired. The first rung on the ladder is found by measuring parallax distances to Cepheid variable stars in the Milky Way. These stars have a well-known relationship between their variability period and

2 "I think, therefore the world is such as it is."

their luminosity, meaning that they can be used to constrain the distances to Cepheid variable stars in other galaxies. By measuring the distance to a Cepheid in a galaxy that also hosts a Type Ia supernova, the absolute magnitude of the supernova can be calibrated. This calibration thus allows for standardisation of the magnitudes of more distant supernovæ in the Hubble flow. This method results in a value of $H_0 = 74.03 \pm 1.42$ kms^{-1} Mpc^{-1}, as reported by the Supernova H_0 Equation of State (SH_0ES) collaboration [94].

This result is completely at odds with the value of H_0 derived from the Planck 2018 measurements of the CMB temperature anisotropies in the context of spatially flat ΛCDM, which found $H_0 = 67.4 \pm 0.5$ kms^{-1} Mpc^{-1} [61]. Critically, a cosmological model must be assumed to derive this value, so the immediate question that springs to mind is whether this 4.4σ tension in measurements of H_0 is because something is wrong with the spatially flat ΛCDM model.

The Cepheid-anchored supernovæ and the CMB are not the only ways of measuring H_0. In Figure 3 we plot a large number of the most up-to-date H_0 constraints from a variety of different probes, divided into so-called "early" and "late" types, the former all being derived from measurements of the distance to the sound horizon (thus also sometimes referred to as "geometric" or "indirect"), and most of the latter being derived from measurements of the luminosity distances to Type Ia supernovæ in the Hubble flow, calibrated via various methods.

Besides the Planck 2018 result which we have already mentioned, the other early probes included on this plot are:

- The 6dF galaxy survey [96], the Sloan Digital Sky Survey (SDSS) Data Release 7 [97] and the Baryon Oscillation Spectroscopic Survey (BOSS) Data Release 12 [63] galaxy BAO plus the Dark Energy Survey (DES) Year 1 clustering and weak lensing result as reported in [98] plotted in light blue and denoted as DES + BAO ($H_0 = 67.4^{+1.1}_{-1.2}$ kms^{-1} Mpc^{-1});
- The same galaxy BAO measurements plus the void–galaxy cross-correlation as reported in [99] plotted in olive green and denoted as BAO + voids ($H_0 = 72.3 \pm 1.9$ kms^{-1} Mpc^{-1});
- The same galaxy BAO and void measurements plus the Lyα BAO measured by the extended Baryon Oscillation Spectroscopic Survey (eBOSS) in Data Release 14 [64, 100, 101] from [102] plotted in grey and denoted as BAO + voids + Lyman-α ($H_0 = 69.0 \pm 1.2$ kms^{-1} Mpc^{-1}).

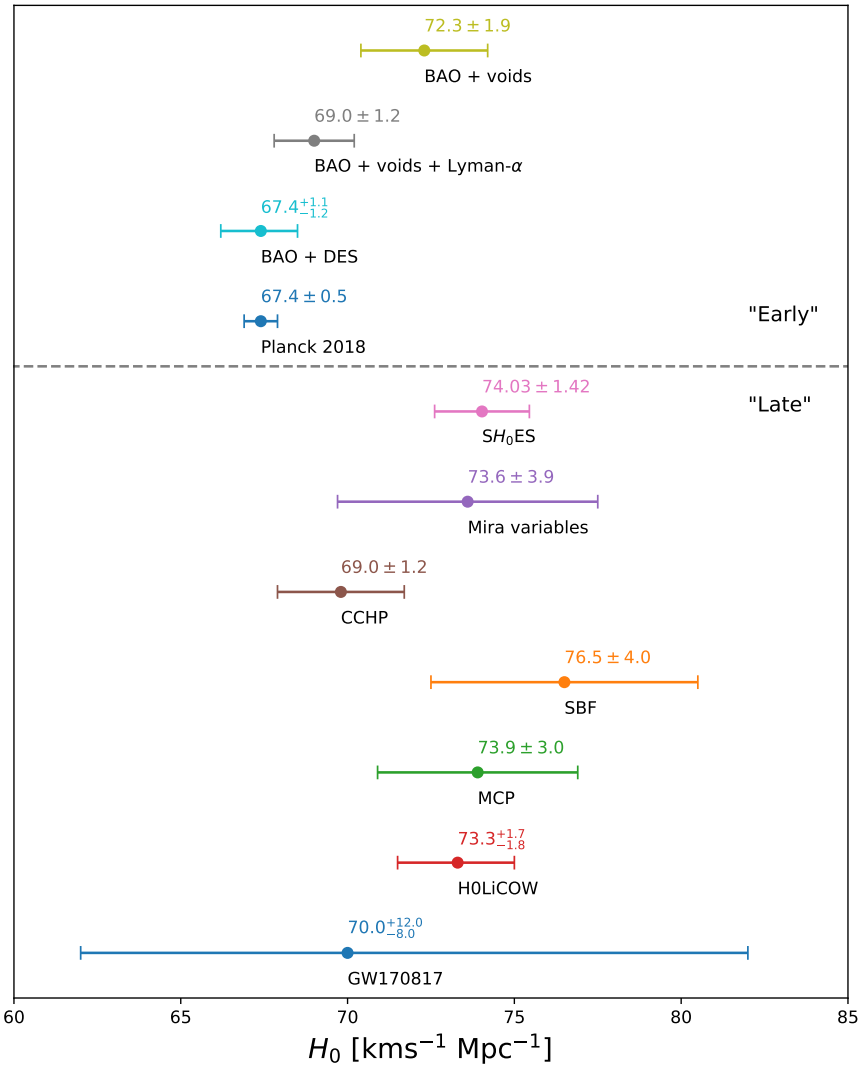

Figure 3: Various probes of H_0 (specific details provided in text). Plot design inspired by Figure 1 of [95].

As can be seen in Figure 3, the majority of the early probes are in agreement with the Planck value of H_0 and thus are in tension with the SH_0ES measurement. The exception to this is the BAO plus voids combination. As explained in [102], the galaxy BAO alone provides a constraint of $H_0 = 73.7^{+3.0}_{-3.9}$ kms^{-1} Mpc^{-1}: high compared to Planck, but with large uncertainties. The addition of the void–galaxy cross-correlation measurement reduces this uncertainty, yielding the BAO plus voids result shown in the figure, which is consistent with the SH_0ES measurement and in 2.5σ tension with Planck. However, the addition of either the Lyman-α BAO or the DES clustering and weak lensing measurement brings the overall BAO constraint back in line with Planck. This is because of the degeneracy between H_0 and the matter density parameter Ω_m; both the Lyman-α BAO and the DES clustering favour a lower value of Ω_m, thus resulting in a lower overall value of H_0. A more detailed discussion of the various BAO constraints on H_0 can be found in [103].

Apart from the SH_0ES result that we have already explained, some other probes which rely on the construction of a distance ladder to obtain a value of H_0 are:

- Type Ia supernovæ calibrated using Mira variable stars. Mira variables are asymptotic giant branch stars, and an oxygen-rich subclass of these stars has a well-defined period–luminosity relation which allows them to replace the Cepheids in the distance ladder [104, 105], plotted in purple ($H_0 = 73.6 \pm 3.9$ kms^{-1} Mpc^{-1});
- Type Ia supernovæ calibrated using tip of the red giant branch (TRGB) stars. Due to a runaway helium fusion reaction that occurs at a well-known point in the lifetime of red giant stars, there is a stark discontinuity in the red giant branch of the Hertzsprung–Russell diagram at a fixed luminosity [106]. Stars at this point can therefore be used as calibrators for the supernovæ in place of the Cepheids, as shown by the Carnegie–Chicago Hubble Program (CCHP) [107], plotted in brown ($H_0 = 69.0 \pm 1.2$ kms^{-1} Mpc^{-1});
- Infrared observations of surface brightness fluctuations (SBF) of early type galaxies [108]. Since galaxies are composed of a finite number of stars, the surface brightness naturally fluctuates from point to point. An average of the surface brightness can be found and observed as an apparent magnitude. The absolute magnitude of the equivalent galaxy can be determined via Cepheid calibration or stellar population models, and hence

a luminosity distance and H_0 can be found [109, 110]. This constraint is plotted in orange ($H_0 = 76.5 \pm 4.0$ kms^{-1} Mpc^{-1}).

It is clearly apparent that the method used to calibrate the supernovæ in the Hubble flow has a large effect on the resulting value of H_0 – so much so that it is tempting to write off the tension as a systematic error, or perhaps being due to Cepheids not having such a consistent period–luminosity relation as previously thought. This idea is especially tempting due to the finding that the SBF result varied (albeit within the error bars) depending on if the galaxy luminosities were calibrated using Cepheids, TRGB stars or stellar population models [95]; see also [111]. Another attempt to resolve the tension along these lines involved anchoring the distance ladder to the BAO rather than the Cepheids, thus creating an inverse distance ladder. This method yielded $H_0 = 67.8 \pm 1.3$ kms^{-1} Mpc^{-1} [112].

However, this idea of recalibrating the distance ladder provides an unsatisfactory resolution to the tension, as there exist a number of late Universe probes that are independent of the distance ladder and yet still find a value of H_0 that is in agreement with SH_0ES and in tension with Planck. These are:

- Measurements of geometric distances using very long baseline interferometry observations of water masers in the accretion disks of supermassive black holes by the Megamaser Cosmology Project (MCP) [113], plotted in green ($H_0 = 73.9 \pm 3.0$ kms^{-1} Mpc^{-1});
- Measurements of time delay distances from observations of systems of strongly lensed quasars by the HoLiCOW collaboration [76], plotted in red ($H_0 = 73.3^{+1.7}_{-1.8}$ kms^{-1} Mpc^{-1});
- The observation of a gravitational wave event with an electromagnetic counterpart, i.e. a standard siren, by the LIGO–Virgo collaboration [84], plotted in dark blue ($H_0 = 70.0^{+12.0}_{-8.0}$ kms^{-1} Mpc^{-1}).

The standard siren event cannot really be claimed as evidence for a higher value of H_0 as the error bars are so large it is compatible with all the other probes described above. However, in the era of third generation detectors, hundreds or even tens of hundreds of standard siren events are expected to be detected, thus making this an extremely promising window onto the tension. We discuss further precision cosmology applications of standard sirens in Chapter 6, where we create mock standard siren datasets in order to forecast future constraints on the distance duality relation.

The error bars on the water maser constraint are also large enough to make this result tension-ambiguous, though these results will naturally improve over time too, as more maser host galaxies are identified and studied. The most convincing late time, distance ladder independent probe of H_0 therefore comes from the strongly lensed quasars observed by the HoLiCOW collaboration. This value of H_0 is in excellent agreement with SH_0ES and in combination, the late time probes are in a staggering $\sim 6\sigma$ tension with the early time probes previously discussed [95].

It seems unlikely that this tension will be explained by systematic errors in one or other of the datasets. We therefore turn to another explanation: that ΛCDM is not the correct cosmological model and by employing an alternative model of dark energy we could reconcile the early and late time measurements of the Hubble parameter[3]. In the interacting dark energy models we study in Chapters 3, 4 and 5, the H_0 tension can be resolved due to the exchange of energy between dark energy and dark matter. If the dark energy component grows at the expense of the dark matter, this can result in a higher value of H_0 at late times. Many other possible ways of resolving the tension are discussed in detail in [15]; we will cover a few of these in section 1.8.

There is another tension in cosmology, again between early and late probes, in measurements of the σ_8 parameter, which is a proxy for the amount of clustering, or structure growth, on the approximate scale of galaxy clusters [115]. The value inferred from the Planck CMB measurement is $S_8 = 0.832 \pm 0.013$ [61], which is in a roughly 2σ tension with measurements of σ_8 coming from galaxy clusters and weak lensing. For example, the Kilo Degree Survey (KiDS) weak lensing constraint is $S_8 = 0.766^{+0.020}_{-0.014}$ [116] and the DES value previously mentioned is even lower, $S_8 = 0.65 \pm 0.04$ [78]. Interacting dark energy models are also able to resolve the σ_8 tension, though typically the H_0 tension will be made worse if the σ_8 tension is resolved, due to the direction of the degeneracy in the H_0–Ω_m plane. We will discuss this point further in Chapter 3.

In summary, the cosmological constant problem, the coincidence problem and the H_0 and σ_8 tensions provide convincing reasons to study alternative models of dark energy. In the next section, we will describe some of the main alternatives to ΛCDM that have been proposed in the literature.

3 A third distinct possibility is that we are living in a local void, meaning that the observed acceleration is merely apparent rather than real (see e.g. [114]).

1.8 ALTERNATIVES TO ΛCDM

For the reasons described above, we wish to examine alternative models to ΛCDM and in particular, alternative models for dark energy. In this section we will discuss one of the most studied alternatives to the cosmological constant, quintessence, as well as giving an overview of modified gravity and dark matter models.

1.8.1 *Dark energy models*

To begin with, we remain within the framework of general relativity, but assume that there is some mechanism that sets the cosmological constant equal to zero [117]. This then gives us the freedom to insert a new dark energy model that can explain the observed late time acceleration.

One of the first alternatives to the cosmological constant to be considered was a dynamical scalar field, essentially the same mechanism proposed to drive the period of inflation in the very early Universe. In fact, cosmological scalar fields were already being considered in the pre-dark energy era in an attempt to solve the cosmological constant problem [118, 119], so it is a natural extension to use them as a driver for the accelerated expansion. This was first proposed in the class of dark energy models known as quintessence [120, 121, 122]. Dynamical dark energy models have also been employed to resolve the coincidence problem [123, 124].

Following [125], a general quintessence model is described by the action

$$S = \int d^4x\sqrt{-g}\left[-\frac{1}{2}(\nabla\phi)^2 - V(\phi)\right], \tag{53}$$

where $(\nabla\phi)^2 = g^{\mu\nu}\partial_\mu\phi\partial_\nu\phi$ and $V(\phi)$ is the potential of the field. In the spatially flat FLRW background we are using throughout this thesis, variation of the action (53) with respect to ϕ yields the Klein–Gordon equation for the scalar field,

$$\ddot{\phi} + 3H\dot{\phi} + \frac{dV}{d\phi} = 0, \tag{54}$$

where dots represent derivatives with respect to cosmic time. The energy density and pressure of the field are given by

$$\rho_\phi = \frac{1}{2}\dot{\phi}^2 + V(\phi), \tag{55}$$

$$P_\phi = \frac{1}{2}\dot{\phi}^2 - V(\phi), \tag{56}$$

so that the equation of state for the scalar field is given by

$$w_\phi = \frac{P_\phi}{\rho_\phi} = \frac{\dot{\phi}^2 - 2V(\phi)}{\dot{\phi}^2 + 2V(\phi)} \tag{57}$$

and the Friedmann equations can be rewritten as

$$H^2 = \frac{1}{3}\left[\frac{1}{2}\dot{\phi}^2 + V(\phi)\right], \tag{58}$$

$$\frac{\ddot{a}}{a} = -\frac{1}{3}\left[\dot{\phi}^2 - V(\phi)\right]. \tag{59}$$

For accelerated expansion to occur, we recall that we need the equation of state of the dark energy component to be such that $w_{\rm DE} < -1/3$. From (57), we can see that for quintessence this condition means that $\dot{\phi}^2 < V(\phi)$; in other words, the form of the scalar field potential determines whether or not accelerated expansion occurs.

This situation is exactly analogous to the conditions required for inflation to occur in the very early Universe: the scalar field must be slowly rolling. We can quantify this statement by introducing the slow roll parameters (see e.g. [126]),

$$\epsilon \equiv \frac{1}{\kappa^2}\left(\frac{V_{,\phi}}{V}\right)^2, \tag{60}$$

$$\eta \equiv \frac{V_{,\phi\phi}}{\kappa^2\phi}, \tag{61}$$

where $\kappa = 8\pi G$. When $\epsilon \ll 1$ and $|\eta| \ll 1$, the evolution of the scalar field is sufficiently slow for acceleration to occur. A quintessence-like model with a scalar field that decays away faster than radiation has been proposed as a possible solution to the H_0 tension due to its ability to reduce the size of the sound horizon at recombination, thereby ensuring a higher value of H_0 is inferred from CMB data [127]. This type of model is generally referred to as early dark energy.

However, no matter the choice of potential, it is expected that the scalar field will couple to the matter field, resulting in a fifth force felt

by the particles in addition to gravity, hence the name quintessence. The presence of such a fifth force is very strongly constrained by laboratory and solar system scale tests [128], so it is necessary to introduce some mechanism by which these models can evade the constraints and still be used as an explanation for the late time cosmic acceleration. This is typically achieved via a screening mechanism.

The most well-known examples of screening mechanisms are the chameleon mechanism [129, 130], which is active in regions of large Newtonian potential i.e. close to massive objects; the k-mouflage mechanism [131], which is active in regions of large acceleration in k-essence models in which the potential of the scalar field is a function of the scalar field and its kinetic energy; and the Vainshtein mechanism [132], which is active in regions of high density, typically in the Galileon and massive gravity theories of modified gravity [133]. All these mechanisms act to screen away the effects of the fifth force in the regions where its existence is most constrained.

It is clear that the introduction of additional scalar fields to act as the dark energy can be difficult due to the question of fifth forces and screening. This motivates us to consider a much simpler alternative to ΛCDM: the interacting vacuum scenario [134, 135, 136]. In this scenario, the vacuum is still used to drive the accelerated expansion, but it is allowed to exchange energy with the cold dark matter component. This scenario is the main focus of this thesis, and we will discuss both the theoretical aspects of the model and the observational constraints on it in great detail in Chapters 3, 4 and 5.

1.8.2 *Modified gravity models*

There exists the possibility that the accelerating expansion in the late time Universe is not caused by some additional dark energy component, but is in fact a result of the gravitational theory. The distinction between dark energy and modified gravity models is not always clear (or necessary), as within the framework of general relativity it depends on whether some exotic component with negative pressure is included in the energy–momentum tensor on the right hand side of the Einstein field equations (2) (typically called dark energy) or whether a modification is made to the Einstein tensor on the left hand side of the field equations (typically called modified gravity) [133].

We take as an example of modified gravity the most general four dimensional Lorentz invariant scalar-tensor theory that produces

second-order equations of motion[4], given by the Horndeski action [139],

$$S = \int d^4x\sqrt{-g}\left[\sum_{i=2}^{5}\mathcal{L}_i + \mathcal{L}_m\right], \tag{62}$$

where the Lagrangian densities $\mathcal{L}_i$ are

$$\mathcal{L}_2 = G_2(\phi, X), \tag{63}$$

$$\mathcal{L}_3 = G_3(\phi, X)\Box\phi, \tag{64}$$

$$\mathcal{L}_4 = G_4(\phi, X)R + G_{4,X}(\phi, X)[(\Box\phi)^2 - (\nabla_\mu\nabla_\nu\phi)^2], \tag{65}$$

$$\mathcal{L}_5 = G_5(\phi, X)G_{\mu\nu}\nabla^\mu\nabla^\nu\phi - \frac{1}{6}G_{5,X}(\phi, X)[(\Box\phi)^3 - 3\Box\phi(\nabla_\mu\nabla_\nu\phi)^2 + 2(\nabla_\mu\nabla_\nu\phi)^3], \tag{66}$$

where $X = -\frac{1}{2}\partial_\mu\phi\partial^\mu\phi$, R is the Ricci scalar, $G_{\mu\nu}$ is the Einstein tensor, and ϕ is the additional scalar field of the Horndeski theory. Minimally coupled matter fields are contained in $\mathcal{L}_m$. The action is simplified by the binary neutron star merger constraint on the tensor speed, which implies that $G_{4,X} = G_5 \approx 0$.

Many of the most well-studied modified gravity theories, such as the cubic Galileon and Brans–Dicke theories, as well as general relativity itself, arise from the Horndeski action in the relevant limits. What is common to all of these modified gravity theories, and what distinguishes them from general relativity, is that they admit new degrees of freedom in the gravitational sector. These in turn couple to the standard matter particles, resulting in a fifth force felt by the particles in addition to gravity, which as we discussed in the context of quintessence must be screened away in order to evade stringent small scale tests of gravity. We will discuss the effects of screened and unscreened modified gravity on constraints on the distance duality relation using standard sirens in Chapter 6.

1.8.3 *Dark matter models*

Finally, since this thesis is primarily concerned with dark energy, we have so far given no consideration to what the cold dark matter might physically be. The most widely accepted dark matter model is that of

4 Higher order equations of motion are not generally desired, as they result in ghost degrees of freedom, i.e. negative energy densities, due to Ostrogradsky's theorem [137, 138].

a weakly interacting massive particle, or WIMP, the proven existence of which would necessitate an extension to the standard model of particle physics. Various alternatives to WIMPs have been proposed in the literature, as either part or all of the dark matter in the Universe, the main contenders being primordial black holes (black holes formed from the collapse of over-densities in the early Universe [140]), and axions (another hypothetical elementary particle initially proposed to provide a solution to the strong CP problem [141, 142]).

The allowed mass ranges for primordial black holes are increasingly constrained (see e.g. [143]), but efforts to directly detect axions recently gained interest due to the observation of excess electronic recoil by the XENON1T experiment, which was attributed to the presence of solar axions with a significance of 3.5σ [144]. However, it was very quickly noted that astrophysical constraints on solar axions are incompatible with the XENON1T excess [145], and that the detection could be due to previously unaccounted-for β decays of tritium in the detector [146]. The significance of the solar axion fit decreases to 2.1σ if the tritium component is considered.

In the rest of this thesis, we exploit the fact that no particle model of dark matter has been confirmed or ruled out, allowing us to consider the phenomenology of a model of dark energy which exchanges energy with the dark matter without having to worry about the microphysical properties or effects of such a model.

1.9 SUMMARY

In this chapter, we began by introducing the FLRW solution to the Einstein field equations for general relativity and then moved to a discussion of the observational evidence for a period of late time accelerated expansion, attributed to dark energy, along with a dominant form of matter which only interacts gravitationally, cold dark matter. We the discussed the theoretical and observational problems with the concordance model of the cosmological constant plus cold dark matter, ΛCDM, and detailed some of the possible alternatives to this model. The next important question we must answer is how to test whether these models explain our observations, and if they do, how well they fit the observational data with respect to ΛCDM.

2

METHODOLOGY

You can measure a programmer's perspective by noting his attitude on the continuing vitality of FORTRAN.

ALAN PERLIS

Oh, boys, can't you code it,
And program it right?
Nothing ever happens in this life of mine,
I'm hauling up the data on the Xerox line.

STAN ROGERS

In this chapter, we will detail the methodology of the work presented in subsequent chapters. In all of the research presented in this thesis, we used the Boltzmann code `CAMB` and the Bayesian parameter inference code `CosmoMC` to analyse and constrain our alternative cosmological models. We therefore give an overview of the perturbation equations computed in the synchronous gauge by `CAMB`, then introduce Bayesian statistics, Monte Carlo sampling methods and model comparison techniques.

2.1 BOLTZMANN CODES

Up to this point, we have assumed that the Universe and its contents are completely homogeneous. However, this is not really true. We observe over-densities in the Universe today in the form of planets, stars and galaxies, and can therefore infer that there must have been small perturbations in the early Universe which grew over time into these larger objects.

However, the study of how the matter species and their perturbations evolve is rather complex. For this reason, a number of numerical codes have been developed to expedite such analyses, beginning with `COSMICS` [147] and followed by `CMBFAST` [148], `CMBEASY` [149], and more recently, `CAMB` [150, 151] and `CLASS` [152, 153]. These codes are known as Boltzmann solvers, as they are designed to solve the Boltzmann equation and the fluid equations of motion for all the matter species

in the Universe. As the work presented later in Chapters 3, 4, 5 and 6 was all carried out using CAMB, we focus on the specific workings of that code, although the equations solved are the same as in CLASS.

It is worth briefly commenting here on the choice of code. The two codes CAMB and CLASS are both designed to do the same thing, though the implementation differs in a number of ways. The CLASS code was developed much more recently (the first public version was released in 2011, while CAMB was made public in 2000), and is designed in a more modular way in comparison to the original Fortran 90 version of CAMB, thus supposedly allowing for easier modification. The source code is also written in C, rather than Fortran, which some users may find more accessible, though this point is irrelevant if no hardcore modifications to the base code are needed, as both now ship with user-friendly Python wrappers. Ultimately the choice between the two comes down to personal preference (or prejudice).

2.1.1 *Perturbation equations*

The purpose of a Boltzmann code is to solve the Einstein and fluid equations, or Boltzmann equation, depending on the regime in question – at late times, the fluid equations suffice, but at early times, when collisions between the different components become important, the Boltzmann equation must be used.

The exact form these equations take depends on the choice of gauge, i.e. the mapping from some fictitious smooth background spacetime to the real inhomogeneous Universe. In CAMB, the covariant equations are propagated in a frame in which the cold dark matter velocity is zero, which we refer to as the synchronous comoving gauge [154]. We consider small perturbations to the background metric (denoted with a bar, $\bar{g}_{\mu\nu}$) such that $\delta g_{\mu\nu} \ll \bar{g}_{\mu\nu}$,

$$g_{\mu\nu} = \bar{g}_{\mu\nu} + \delta g_{\mu\nu}, \tag{67}$$

and in a spatially flat FLRW background, following [155], the line element of the linearly-perturbed metric in the synchronous gauge is given by

$$ds^2 = a^2(\tau)[-d\tau^2 + (\delta_{ij} + h_{ij})dx^i dx^j], \tag{68}$$

where τ is the conformal time. It is usual to decompose these into the scalar, vector and tensor parts, as at linear order the Einstein equations for the different components do not mix and can therefore be

treated separately. The decomposition of the metric perturbation h_{ij} can be written as

$$h_{ij} = h\delta_{ij} + h_{ij}^{\parallel} + h_{ij}^{\perp} + h_{ij}^{\mathrm{T}}. \tag{69}$$

Continuing to follow [155], the $h_{ij}^{\parallel}$ and $h_{ij}^{\perp}$ terms can be rewritten in terms of a scalar μ and a divergence-free vector $\vec{A}$,

$$h_{ij}^{\parallel} = \left(\partial_i\partial_j - \frac{1}{3}\delta_{ij}\nabla^2\right)\mu, \tag{70}$$

$$h_{ij}^{\perp} = \partial_i A_j + \partial_j A_i. \tag{71}$$

The scalar mode of the metric perturbations is characterised by h and μ, while A_i and h_{ij}^{T} are the vector and tensor modes respectively. With our gauge choice in hand, we can write down the linearised form of the Einstein equations (2) in the Fourier space k, introducing $h(k,\tau)$ and $\eta(k,\tau)$ as the Fourier transforms of $h(x^i,\tau)$ and $\mu(x^i,\tau)$, where x^i is the comoving position, related to the proper position $\vec{r}$ by $d\vec{x} = d\vec{r}/a(\tau)$. The Einstein equations thus become

$$k^2\eta - \frac{1}{2}\frac{\dot{a}}{a}\dot{h} = 4\pi G a^2 T_0^0, \tag{72}$$

$$k^2\dot{\eta} = 4\pi G a^2(\bar{\rho}+\bar{P})\theta, \tag{73}$$

$$\ddot{h} + 2\frac{\dot{a}}{a}\dot{h} - 2k^2\eta = -8\pi G a^2 \delta T_i^i, \tag{74}$$

$$\ddot{h} + 6\ddot{\eta} + 2\frac{\dot{a}}{a}\left(\dot{h} + 6\dot{\eta}\right) - 2k^2\eta = -24\pi G a^2(\bar{\rho}+\bar{P})\sigma, \tag{75}$$

where the fluid velocity divergence θ and the anisotropic stress σ are defined as

$$(\bar{\rho}+\bar{P})\theta \equiv ik^j\delta T_j^0, \tag{76}$$

$$(\bar{\rho}+\bar{P})\sigma \equiv -(\hat{k}_i\hat{k}_j - \frac{1}{3}\delta_{ij})\Sigma_j^i, \tag{77}$$

and $\Sigma_j^i \equiv T_j^i - \delta_j^i T_k^k/3$ is the traceless component of T_j^i, $\hat{k}$ is the unit vector in the direction of $\vec{k}$ and the energy–momentum tensor decomposed to linear order takes the following form:

$$T_0^0 = -(\bar{\rho}+\delta\rho), \tag{78}$$

$$T_i^0 = -T_0^i = (\bar{\rho}+\bar{P})v_i, \tag{79}$$

$$T_j^i = (\bar{P}+\delta P)\delta_j^i + \Sigma_j^i, \tag{80}$$

where v_i is the velocity of the fluid ($dx^i/d\tau$) and dots represent derivatives with respect to conformal time.

As mentioned in Chapter 1, the conservation of energy–momentum is a consequence of the Einstein equations via the Bianchi identity. As shown in [155], the perturbed part of the energy–momentum conservation equations in the Fourier space k implies

$$\dot{\delta} = -(1+w)\left(\theta + \frac{\dot{h}}{2}\right) - 3\frac{\dot{a}}{a}\left(\frac{\delta P}{\delta \rho} - w\right)\delta, \tag{81}$$

$$\dot{\theta} = -\frac{\dot{a}}{a}(1-3w)\theta - \frac{\dot{w}}{1+w}\theta + \frac{\delta P/\delta\rho}{1+w}k^2\delta - k^2\sigma, \tag{82}$$

where w is the equation of state of the fluid, $w \equiv P/\rho$ and $\delta = \delta\rho/\rho$ is the density contrast. These equations are valid for a single uncoupled fluid; for example, in the tight-coupling limit of the photon–baryon fluid in the early Universe.

The benefit of the choice of synchronous gauge for this work is made apparent when we consider the solution of (82) for cold dark matter. Cold dark matter, when uncoupled from other components, is pressureless and has zero anisotropic stress. From (82) this implies that in this gauge, with the residual gauge freedom of the initial condition for the velocity removed by setting $\theta(\tau = 0) = 0$, the velocity of the cold dark matter fluid is always zero.

Typically, if a coupling is introduced between the cold dark matter and the dark energy fluid this would result in a non-zero cold dark matter fluid velocity. In Chapters 3, 4 and 5, we consider what we call the geodesic CDM scenario, meaning that the interaction term between the components is fixed in such a way that there is no additional acceleration on to the cold dark matter, thus ensuring the fluid velocity remains zero. This choice further means that, in the synchronous gauge, the dark energy component, in this case treated as vacuum energy, remains unperturbed. This greatly simplifies the numerical analysis performed. We will discuss this point in greater detail in Chapter 3.

2.1.2 *The Boltzmann equation*

We have so far assumed that we are dealing with a single fluid that does not interact with any others, or that we can take an average over all fluids. However, there are certain regimes in which microphysics becomes important, and we must consider the behaviour of individual particles rather than fluid elements. To do this, we must use the Boltzmann equation, which describes the evolution of the phase-space distribution of the particles over time.

The phase-space distribution function is the product of the particle number density and the particle momentum probability distribution function [77], which is given by [155] as

$$f(x^i, p_j, \tau) = dx^1 dx^2 dx^3 dp_1 dp_2 dp_3 = dN, \tag{83}$$

where x^i are positions and p_i the conjugate momenta, related to the proper momentum P_i via $p_i = a(\delta_{ij} + \frac{1}{2}h_{ij})P^j$. However, it is common to eliminate the metric perturbations from this definition by replacing p_j with the comoving 3-momentum $q_j \equiv aP_j$. As shown in [155], we can further write this quantity in terms of its magnitude and direction, $q_j = qn_j$, where $n^i n_i = \delta_{ij} n^i n^j = 1$, allowing us to rewrite the phase-space distribution function as $f(x^i, q, n_j, \tau)$. We can now give the expression for the energy–momentum tensor written in terms of the distribution function and the components of the 4-momentum,

$$T_{\mu\nu} = \int dp_1 dp_2 dp_3 \sqrt{-g} \frac{p_\mu p_\nu}{p^0} \left[f_0(q)(1 + \Psi(x^i, q, n_j, \tau)) \right], \tag{84}$$

where we have split the phase-space distribution into a background and perturbed part. This yields

$$T^0_0 = -a^{-4} \int q^2 \, dq \, d\Omega \, \sqrt{q^2 + m^2 a^2} f_0(q)(1 + \Psi), \tag{85}$$

$$T^0_i = a^{-4} \int q^2 \, dq \, d\Omega \, q n_i f_0(q) \Psi, \tag{86}$$

$$T^i_j = a^{-4} \int q^2 \, dq \, d\Omega \, \frac{q^2 n_i n_j}{\sqrt{q^2 + m^2 a^2}} f_0(q)(1 + \Psi), \tag{87}$$

where $d\Omega$ is the solid angle associated with direction n_i. Finally, as shown by [155], the Boltzmann equation in the Fourier space k, which gives the evolution of the phase-space distribution perturbation Ψ, is given by

$$\frac{\partial \Psi}{\partial \tau} + \frac{iq}{E}(\vec{k} \cdot \hat{n})\Psi + \frac{d \ln f_0}{d \ln q} \left[\dot{\eta} - \frac{\dot{h} + 6\dot{\eta}}{2} (\hat{k} \cdot \hat{n})^2 \right] = \frac{1}{f_0} \left(\frac{\partial f}{\partial \tau} \right)_C, \tag{88}$$

where $E = \sqrt{q^2 + a^2 m^2}$ is the comoving energy and f_0 is the Fermi–Dirac distribution for fermions (plus sign) and the Bose–Einstein distribution for bosons (minus sign), given by

$$f_0 = \frac{g_s}{h^3_{\mathrm{Pl}}} \frac{1}{e^{E/k_{\mathrm{B}}T_0} \pm 1}, \tag{89}$$

where g_s is the number of spin degrees of freedom, T_0 is the temperature today, h_{Pl} is the Planck constant and k_{B} is the Boltzmann constant.

The $\left(\frac{\partial f}{\partial \tau}\right)_C$ term in (88) is the collision term that takes into account the scattering physics between the different components under consideration.

The overall purpose of CAMB is to use the equations defined above to compute the CMB power spectra, lensing and matter power spectra, transfer functions and background cosmological functions like $H(z)$. A detailed presentation of the exact form of the equations used by CAMB can be found in Chapter 6 of [156], while the most up-to-date documentation for the code itself can be found at https://camb.info/.

Depending on the cosmological model that is being analysed, modifications may need to be made to the equations in CAMB. This is the case for the interacting vacuum dark energy model we study in Chapters 3, 4 and 5, where we introduce a coupling between the vacuum and cold dark matter. We present the details of the CAMB implementation of this model in Chapter 3.

2.2 PARAMETER INFERENCE

It is usual that an alternative dark energy model will have additional parameters with respect to ΛCDM, typically to control the behaviour of the new dark energy component, or the coupling between the dark energy and dark matter components in the case of interacting models. Once the alternative model is implemented in CAMB, the initial values[1] of these additional parameters must be chosen in order to run the code.

The question then becomes how best to choose the initial value when very little about the physical behaviour of the model is known. To answer this question, we can use a statistical method known as parameter inference, which allows observational data to inform us what the most likely value of that parameter is. To further explain this, we will introduce Bayesian statistics and then the most common Monte Carlo sampling methods and codes used for parameter inference. Another benefit of these methods is they typically allow for a quantitative model comparison to be done, meaning that we can determine whether our alternative model is preferred over ΛCDM by the data. We will discuss model comparison methods in the final section of this

1 Note that we use the term "initial" but the value given to CAMB is in fact that parameter's value today, as CAMB evolves the equations backwards in time.

chapter. An in-depth treatment of everything discussed in this section can be found in [157] and [158].

2.2.1 *The Bayesian approach*

Statistical methods over the past two centuries have largely been informed by the frequentist approach, which views the probability of an event as the fraction of times that event will occur given infinitely many repeated trials. This is contrasted by the Bayesian approach, in which probability indicates the plausibility of something being true. The main ideological difference between the two is that in the Bayesian approach, our prior knowledge or beliefs inform our expectation of an outcome, whereas in the frequentist context, priors are not explicitly taken into account.

There is no one true or correct approach, although the best choice of method for different applications is widely debated. In general, if the observed data is good enough, both approaches should draw the same conclusions. However, in cosmology we are often at the limit of what information we can gain from data and so prior information and understanding of the dependence of a result on the prior assumptions becomes important[2]. Hence, throughout this thesis, we will follow the Bayesian approach, making our prior choices explicit.

In general, we can denote the probability of two events A and B occurring by $P(A)$ and $P(B)$. We can write down the conditional probability $P(A|B)$ which is the probability of A occurring given that B has happened, and the joint probability of A and B happening, $P(A, B)$. The conditional probability, $P(A|B)$, is formally defined as

$$P(A|B) \equiv \frac{P(A, B)}{P(B)}, \tag{90}$$

from which we can write

$$P(A|B)P(B) = P(B|A)P(A) = P(A, B), \tag{91}$$

which immediately yields Bayes' theorem [160],

$$P(A|B) = \frac{P(B|A)P(A)}{P(B)}. \tag{92}$$

The essence of Bayesian parameter inference is contained in (92).

2 For a concrete example of how a prior choice can affect a result, see e.g. section VIII C of [159].

In a real-world scenario, we have a posterior distribution of a parameter θ given some data D and a model M, $P(\theta|D, M)$, which is given by the likelihood function, $P(D|\theta, M)$ multiplied by the prior probability distribution $P(\theta|M)$ and normalised by the Bayesian evidence, $P(D|M)$,

$$P(\theta|D, M) = \frac{P(D|\theta, M)P(\theta|M)}{P(D|M)}. \tag{93}$$

We are generally interested in calculating the expectation value of a parameter, or a set of parameters, from the posterior distribution,

$$\langle f(\theta) \rangle = \int d\theta f(\theta) P(\theta|D, M). \tag{94}$$

As discussed in [158], this integral can be evaluated numerically to the highest precision allowed by the computer being used. The simplest way to do this for when the number of parameters (equivalently referred to as dimensions) n is greater than one is to sum over an evenly spaced grid in parameter space. The grid must be large enough in volume to cover all the regions in which $f(\theta)P(\theta|D, M)$ is non-zero, with some width w_i in each direction. The grid will also have some resolution Δ_i in each direction, dependent on the smoothness of $f(\theta)$ and $P(\theta|D, M)$. The number of points required in the grid is then given by

$$G = \prod_1^n \left(\frac{w_i}{\Delta_i} \right), \tag{95}$$

which, if all dimensions contain a similar amount of structure, can be approximated as

$$G \approx \left(\frac{w_1}{\Delta_1} \right)^n. \tag{96}$$

The exponential scaling with the number of dimensions makes the grid method prohibitively slow when the number of dimensions gets too large. For all the applications considered in this thesis, we have a sufficiently large number of parameters in the problem that we cannot use a grid method[3], but must instead approximate the posterior distribution using a sampling technique.

3 The limit above which it becomes sensible to use a sampling method rather than calculate the integral directly is around five parameters.

2.2.2 *Monte Carlo sampling methods*

The term "Monte Carlo method" refers to an experiment which yields results via repeated random sampling[4]. The first step that any Monte Carlo method used for drawing from a probability distribution relies on is the assumption that from a set of samples $\{\theta_i\} \subseteq \{\theta\}$, we can infer the properties of the full distribution. This means we only have to calculate $P(f(\theta)|\{\theta_i\})$ rather than $P(f(\theta)|P(\theta))$. If we are only interested in the expectation values $\langle f(\theta)\rangle$, the central limit theorem states that, as long as the distribution $f(\theta_i)$ has finite variance, the distribution over different sets of samples of any sum $\sum_i f(\theta_i)$ will tend to a normal distribution for large numbers of independent samples. This means that from $\{\theta_i\}$ we can estimate $\langle f(\theta)\rangle$ using the estimator

$$E_f \equiv \frac{1}{n_s}\sum_{i=1}^{n_s} f(\theta_i), \tag{97}$$

where n_s is the number of samples. The expected value of the estimator is then the true expectation value,

$$\langle E_f\rangle = \langle f(\theta)\rangle. \tag{98}$$

For a large number of independent samples, $P(E_f)$ tends to the normal distribution $N(\langle f(\theta)\rangle, \sigma_E^2)$, where $\sigma_E = \sigma_f/\sqrt{n_s}$ and σ_f is the true variance of $f(\theta)$.

Given some distribution of interest, we will now describe how to generate the samples. For low dimensional problems a direct sampling technique can be used[5], of which a detailed description can be found in [158]. However, even these methods are insufficient for the work discussed later in this thesis, so we must consider more powerful techniques better suited to very high dimensional problems, the majority of which are based on constructing Markov chains. For this reason, this technique is commonly known as "MCMC" – Markov chain Monte Carlo.

A Markov chain is defined by the concept of "memoryless-ness". An ideal Markov chain is a sequence of points in parameter space for which the current position θ_i only depends on the point exactly previous to that one, θ_{i-1}. We can define the transition probability $T(\theta_i, \theta_{i+1})$ that determines the probability of the chain moving from

4 They are named as such after the casino in the Monégasque city of the same name, where random chance prevails [161].

5 A direct sampling technique generates exactly independent samples, as opposed to the Markov chain-based methods we will go on to discuss, in which the samples only become independent as the sampling progresses.

θ_i to θ_{i+1}. The probability of arriving at a given point must be equal to the probability at that point to ensure that the chain has the correct asymptotic distribution,

$$P(\theta_j) = \int d\theta_i P(\theta_i) T(\theta_i, \theta_j). \tag{99}$$

The way to ensure this is to use a transition probability that satisfies the detailed balance condition, which means that the probability of going from θ_i to θ_{i+1} must be the same as the probability of going from θ_{i+1} to θ_i, i.e.

$$P(\theta_{i+1}) T(\theta_{i+1}, \theta_i) = P(\theta_i) T(\theta_i, \theta_{i+1}). \tag{100}$$

The choice of the transition probability $T(\theta_i, \theta_{i+1})$ thus determines the type of sampling method. We will focus on the method used by the code `CosmoMC`, as this is the code used in subsequent chapters of this thesis for parameter inference. The `CosmoMC` code [162, 163] employs the Metropolis–Hastings algorithm [164, 165] to construct a Markov chain that satisfies the detailed balance condition. The Metropolis–Hastings algorithm uses a proposal distribution to select the next possible point in the chain. This point is then either rejected, in which case the chain does not move and a new proposed point is selected, or is accepted with some probability.

Following [158], the proposal distribution $s(\theta_i, \theta_{i+1})$ can be chosen so that it is easy to sample from, and it is commonly chosen to resemble the expected posterior distribution in order to speed up the sampling process. The acceptance probability is given in terms of the proposal distribution as

$$a(\theta_i, \theta_{i+1}) = \min\left\{1, \frac{P(\theta_{i+1}) s(\theta_{i+1}, \theta_i)}{P(\theta_i) s(\theta_i, \theta_{i+1})}\right\}, \tag{101}$$

and the transition probability is thus

$$T(\theta_i, \theta_{i+1}) = a(\theta_i, \theta_{i+1}) s(\theta_i, \theta_{i+1}). \tag{102}$$

The proposal distribution must be a function of the current position only, otherwise the resulting chain will not be Markovian. This requirement can be circumvented by having a "burn in" stage at the beginning of the sampling, during which the choice of sample may be informed by the past history. This allows for the proposal distribution to be improved before the main sampling begins. Once the burn in stage is complete, the proposal distribution must be fixed, and the samples collected during the burn in phase should be discarded before the final chain is analysed.

The time taken to produce a fixed number of samples using the Metropolis–Hastings method scales linearly with the number of dimensions. Besides refining the proposal distribution during the burn in phase, the speed of sampling can be improved by using a covariance matrix generated from samples of a previous chain to inform the proposal distribution.

The main drawback of Metropolis–Hastings sampling is that it is very sensitive to degeneracies in parameter space and struggles to explore complicated posterior distributions as it is designed to find the peak of the posterior distribution and steps in the chain away from the peak are disfavoured. In cosmology, we are fortunate that we do not expect multimodal distributions to appear very often, but we do commonly see degeneracies. An example that we discuss in detail in Chapter 6 is a degeneracy between the matter density parameter Ω_m and a model parameter which controls violation of the distance duality relation (given in (28)) that is evident when using baryon acoustic oscillation data to constrain these parameters (for a very clear example, see Figure 1 of [166]). In this case, the degeneracy can be broken by adding a dataset that is sensitive to both parameters, such as Type Ia supernovæ.

However, if we don't have additional degeneracy-breaking data available, or we suspect that the posterior distribution may have multiple peaks, it may be sensible to consider an alternative sampling method, such as nested sampling [167]. Nested sampling can effectively explore multimodal distributions, as rather than constructing a Markov chain, the sampling proceeds by exploring nested contours of equal likelihood, ordered from least likely to most likely. For a detailed explanation of nested sampling, see Chapter 1 of [158]. The nested sampling code `polychord` is available for use with `CAMB` in the `CosmoChord` package [168, 169]. A comparison of Metropolis–Hastings, nested sampling and a third method, affine-invariant ensemble sampling (on which the popular code `emcee` is based [170]) can be found in [171].

Another advantage of nested sampling is that the Bayesian evidence (the denominator of (93)) is the main output, rather than the posterior distribution, allowing for quantitative comparison of different models. However, it is still possible to compare models even when the evidence is not available, as we will now discuss.

2.2.3 *Model comparison*

The most basic way to compare the results of a parameter inference analysis is to perform a χ^2 goodness-of-fit test. The χ^2 distribution is the distribution expected from the sum of the square of a number[6] n of Gaussian distributed variables x,

$$f(x,n) = \frac{1}{\Gamma(n/2)2^{n/2}} x^{n/2-1} \exp^{-x/2}. \tag{103}$$

Under the assumption that the errors on our data[7] are Gaussian, a "goodness of fit" statistic, known as the χ^2 statistic, can be defined as

$$\chi^2 = \sum_{i=1}^{n} \frac{(y_i - g(x_i))^2}{\sigma_i^2}, \tag{104}$$

or in the case of correlated errors,

$$\chi^2 = \sum_{i,j} (y_i - g(x_i)) C_{ij}^{-1} (y_j - g(x_j)), \tag{105}$$

where the data are $[x_i, y_i]$, the errors are σ_i, a model for the data is given by $g(x)$ and C_{ij} is the covariance matrix of the errors. This should be distributed as a χ^2 distribution, (103), with degrees of freedom given by $n = d - p$, where d is the number of data points and p the number of parameters in the model.

To understand if a model is a good fit to the data using the χ^2 statistic, it is common to calculate the reduced χ^2,

$$\chi^2_{\mathrm{r}} = \frac{\chi^2}{d-p}. \tag{106}$$

The expected result for a good fit is one. If $\chi^2_{\mathrm{r}} \ll 1$, it indicates that the data error bars were overestimated, whereas if $\chi^2_{\mathrm{r}} \gg 1$, it generally indicates that the model is a poor fit to the data.

In the context of comparing alternative dark energy models to ΛCDM, we can generate two MCMC runs, one in ΛCDM, and one in our alternative cosmology. We can then calculate the difference between the χ^2 statistics for the two models, i.e.

$$\Delta\chi^2 = \chi^2_{\Lambda\mathrm{CDM}} - \chi^2_{\mathrm{alternative}}, \tag{107}$$

6 Also referred to as degrees of freedom.

7 By data we here mean the samples obtained from our sampling of the posterior distribution of the model.

along with the difference in degrees of freedom,

$$\Delta n = n_{\Lambda\text{CDM}} - n_{\text{alternative}}. \tag{108}$$

The $\Delta\chi^2$ can then be compared with a χ^2 table to determine the significance. If the value is significant, it indicates that the alternative model is a better fit than ΛCDM. It is very important to note that this approach is only valid for nested models, i.e. situations in which the additional parameters of the alternative model can be fixed in such a way to completely recover ΛCDM. All the alternative dark energy models considered in this thesis are nested models of ΛCDM.

If the models under consideration are not nested, another approach is necessary. We can instead use information criteria to compare our models. The most well-known are the Akaike information criterion [172], Bayesian or Schwarz information criterion [173] and the deviance information criterion [174, 175]. A benefit of the information criteria is that they penalise complexity, which is generally desired from an Ockham's razor standpoint[8].

The Akaike information criterion is given by

$$\text{AIC} = 2n - 2\ln(\mathcal{L}), \tag{109}$$

where n is the number of parameters and $\mathcal{L}$ the maximised value of the likelihood function. A model with a smaller AIC is considered preferred by the data. The Bayesian information criterion is very closely related, albeit with a stronger penalty term,

$$\text{BIC} = n\ln(n) - 2\ln(\mathcal{L}). \tag{110}$$

Finally, the deviance information criterion is given by

$$\text{DIC} = \chi^2_{\text{eff}}(\hat{\theta}) + 2p_D, \tag{111}$$

where $\chi^2_{\text{eff}}(\hat{\theta}) = -2\ln\mathcal{L}(\hat{\theta})$, $\hat{\theta}$ is the parameter vector at the best fit and $p_D = \overline{\chi^2_{\text{eff}}(\theta)} - \chi^2_{\text{eff}}(\hat{\theta})$, where the bar denotes the average taken over the posterior distribution. This estimator accounts for both the goodness of fit through $\chi^2_{\text{eff}}(\hat{\theta})$ and for the Bayesian complexity of the model, p_D, which disfavours models with extra parameters. We make use of the deviance information criterion to compare alternative dark energy models to ΛCDM in Chapter 3 and Chapter 5.

While the χ^2 statistic is generally viewed as part of the frequentist paradigm, and the information criteria as neither frequentist or

8 Simply put, simpler models are better.

Bayes factor	Interpretation
$\lvert\log B_{12}\rvert < 1$	Not worth more than a bare mention
$1 < \lvert\log B_{12}\rvert < 2.5$	Weak
$2.5 < \lvert\log B_{12}\rvert < 5$	Significant
$5 < \lvert\log B_{12}\rvert$	Strong

Table 2: The Jeffreys scale, originally given in [177] and modified for cosmological applications in [158].

Bayesian (they have no dependence on significance levels or on priors), a truly Bayesian model comparison can be done by comparing the Bayesian evidence for each model, given by the denominator of (93). If the samples are obtained using the nested sampling method previously described, then the evidence is immediately available. However, if a Metropolis–Hastings method is used, the evidence can be estimated from the chains, provided the dimensionality is not too high, for example by using the `MCEvidence` code [176].

Once the Bayesian evidence has been obtained for two different models, a quantity called the Bayes factor can be calculated,

$$\log B_{12} = \log\left[\frac{P(D|M_1)}{P(D|M_2)}\right], \tag{112}$$

$$= \log[P(D|M_1)] - \log[P(D|M_2)], \tag{113}$$

where M_1 and M_2 are the models to be compared. To interpret the resulting Bayes factor values, the Jeffreys scale, shown in Table 2, can be used. This is the method of model comparison we employ in Chapters 4 and 5.

2.3 SUMMARY

In this chapter, we have given an overview of cosmological perturbation theory in the synchronous gauge and the Boltzmann equation to explain how the Boltzmann code `CAMB` works. This code allows for products such as CMB power spectra to be calculated for alternative dark energy models such as the interacting vacuum model studied in subsequent chapters of this thesis. We have discussed how we can constrain alternative models using various sampling methods, focusing on the Metropolis–Hastings approach as implemented in the `CosmoMC` code used later in this thesis. Finally, we have described three ways in which the resulting model constraints can be compared to each other or to ΛCDM, to address the question of which is a

better description of reality. We now move to the results of the research covered in this thesis: a thorough investigation of the interacting vacuum dark energy scenario, and an examination of the ability of future standard siren observations to probe the distance duality relation.

3

CONSTRAINTS ON THE INTERACTING VACUUM

> *'Is there any other point to which you would wish to draw my attention?'*
> *'To the curious incident of the dog in the night-time.'*
> *'The dog did nothing in the night-time.'*
> *'That was the curious incident,' remarked Sherlock Holmes.*
>
> ARTHUR CONAN DOYLE

In this chapter, we introduce the interacting vacuum dark energy scenario, motivated by the problems with ΛCDM previously discussed in Chapter 1. We show how the interaction is introduced between the vacuum and cold dark matter energy–momentum tensors and how the interacting term arises in the linear perturbations of the theory. The interaction can act for the entire history of the Universe, or switch on at a certain time. It can also remain constant or vary with time. We study various combinations of these choices, constraining the relevant cosmological and model parameters using the parameter inference method of Metropolis–Hastings MCMC described in Chapter 2. This chapter is based on [1].

3.1 INTRODUCTION

The idea of a decaying vacuum energy as been afforded a great deal of study in the literature (see, for example, [178, 179, 180, 181, 182, 134]). Many other dynamical and interacting dark energy models have also been investigated, often with the conclusion that not only can cosmological tensions be relieved in such models, but they may even be favoured over ΛCDM (see, for example, [135, 183, 184, 185, 186, 187, 188, 189, 190] for more details).

The specific scenario we here consider retains general relativity as the description of gravity, while allowing for a possible exchange of energy between cold dark matter (CDM) and the vacuum, i.e. a dark energy with an equation of state parameter $w = -1$ [8, 10]. This scenario does not introduce any additional dynamical degrees of freedom with respect to ΛCDM [134]. The interaction allows for the energy density of the vacuum, V, to change, while cold dark matter can

freely cluster under the sole action of gravity i.e. cold dark matter remains geodesic, as in ΛCDM.

We investigate the possibility of such an interaction by choosing a simple parameterisation and studying its behaviour as a function of redshift. In the synchronous comoving gauge and under the assumption of geodesic cold dark matter, the interaction is described by a single background function $Q(z)$ which we model as $Q = q_{\rm V} HV$, where $q_{\rm V}$ is a dimensionless function. Based on this, we consider five different cosmologies, with the aim of reconstructing $q_{\rm V}$ with step functions in different redshift bins, using the values $q_{\rm V}$ has in each bin as parameters. In particular, the four bin case is essentially model-independent.

The first two cosmologies, which we name *Cfix*, consider a physical scenario in which we have a ΛCDM evolution in the past up to a fixed transition redshift $z_{\rm trans}$. At z lower than $z_{\rm trans}$, the interaction switches on and the vacuum energy starts to evolve. The two cases differ in the redshift of the transition: in the first we assume that the interaction starts at high redshift, with $z_{\rm trans} = 3000$; in the other we assume $z_{\rm trans} = 0.9$, in order to compare with the same case considered by [135]. For these two *Cfix* cases we sample over the usual cosmological parameters, with the addition of the single interaction parameter, $q_{\rm V}$.

The third case, *Cvar*, is similar to the first two, but we additionally sample over the transition redshift, $z_{\rm trans}$. The fourth case, which we call *seeded vacuum energy* or *SVE*, mimics a physical scenario in which the coupling causes the vacuum energy to suddenly grow from zero up to a 'seed' value at $z_{\rm trans}$. At lower redshifts, the interaction then behaves as in the previous three cases i.e. with a constant $q_{\rm V}$, and the vacuum evolves accordingly. Therefore this case, like the third, has two free parameters: $q_{\rm V}$ and $z_{\rm trans}$. The fifth case we consider is the model-independent scenario in which we allow the interaction to evolve in four redshift bins, using four different values of the interaction strength $q_{\rm V}$. We call this the *4bins* case.

3.2 COLD DARK MATTER – VACUUM ENERGY INTERACTION

In this section we outline the theoretical framework for the interacting vacuum scenario, beginning with a summary of the general covariant theory and progressing to the details of the scenario in an FLRW background with perturbations.

3.2.1 *Covariant theory of the interacting vacuum*

In ΛCDM, the cosmological constant Λ represents the vacuum energy of the Universe, and in a classical sense, this vacuum energy can be treated as a non-interacting perfect fluid with an equation of state parameter $w = -1$, as was realised by Lemaître [8, 10]. The energy–momentum tensor of a perfect fluid is

$$T^{\mu}_{\nu} = P\delta^{\mu}_{\nu} + (\rho + P)u^{\mu}u_{\nu}, \tag{114}$$

where ρ is the energy density, P the pressure and u^{μ} the 4-velocity of the fluid. We define the energy–momentum tensor of the vacuum as

$$\check{T}^{\mu}_{\nu} = -V\delta^{\mu}_{\nu}, \tag{115}$$

and by comparison with (114) we can identify $V = -\check{P} = \check{\rho}$, i.e. V is the vacuum energy density. This means that the equation of state parameter $w = P/\rho$ is equal to -1, as it is for the cosmological constant Λ. Moreover, this form of the vacuum energy–momentum tensor leaves the vacuum 4-velocity undefined and any 4-vector is an eigenvector of $\check{T}^{\mu}_{\nu}$. Therefore all observers measure the same vacuum energy density V; in other words, the vacuum energy is boost invariant. In the following, u^{μ} therefore denotes the 4-velocity of cold dark matter.

Denoting the energy–momentum tensor of cold dark matter with T^{μ}_{ν} and its energy density with ρ_c,

$$T^{\mu}_{\nu} = \rho_c u^{\mu}u_{\nu}, \tag{116}$$

we can introduce an interaction between cold dark matter and the vacuum energy in the following way:

$$\nabla_{\mu}T^{\mu}_{\nu} = -Q_{\nu}, \tag{117}$$
$$\nabla_{\mu}\check{T}^{\mu}_{\nu} = -\nabla_{\nu}V = Q_{\nu}, \tag{118}$$

where the interaction 4-vector Q^{ν} represents the energy–momentum flow between vacuum and cold dark matter.

If $T^{\mu\nu}_{\text{tot}} = T^{\mu\nu} + \check{T}^{\mu\nu}$ is the total energy–momentum tensor, then the form of the interaction in (117) and (118) ensures the total conservation equation $\nabla_{\mu}T^{\mu\nu}_{\text{tot}} = 0$, which, as we mentioned in Chapter 1 follows from the contracted Bianchi identity $\nabla_{\mu}G^{\mu\nu} \equiv 0$ in Einsteinian gravity. We note that this scenario reduces to the standard ΛCDM case when $Q^{\nu} = 0$, as this implies $V =$ constant.

We can project the interaction 4-vector in two parts parallel and orthogonal to the cold dark matter 4-velocity:

$$Q^\mu = Qu^\mu + f^\mu, \tag{119}$$

where, in the frame of observers comoving with the cold dark matter, Q represents the energy flow, and f^μ the momentum exchange between cold dark matter and the vacuum; f^μ is orthogonal to u^μ i.e. $f^\mu u_\mu = 0$.

Following [135] and [191], we consider the simplest case of interaction: a pure energy exchange in the cold dark matter frame wherein $f^\mu = 0$, and so $Q^\mu = Qu^\mu$. The 4-force, f^μ, is related to the 4-acceleration $a^\mu = u^\alpha \nabla_\alpha u^\mu$ by

$$f^\mu = a^\mu \rho_c. \tag{120}$$

Since we set $f^\mu = 0$, it follows that $a^\mu = 0$, meaning there is no acceleration of the cold dark matter due to the interaction and hence the cold dark matter remains geodesic. We may call this interacting scenario the *geodesic CDM scenario* (see also [192]). It follows from this geodesic cold dark matter assumption that the effective sound speed of matter perturbations is zero and hence the Jeans length is also zero, meaning that there is no damping of matter perturbations on scales smaller than the Jeans length. However, the interaction will still affect structure growth, as discussed below in subsection 3.2.3.

A second important consequence of the assumption of pure energy exchange is that, following (118), the cold dark matter 4-velocity u^μ consequently defines a potential flow and the cold dark matter fluid is thus irrotational [193]. This is a sufficient approximation of the behaviour of cold dark matter at early times and on large scales, in a linear regime where only scalar perturbations are relevant for structure formation, but at late times it is expected that non-linear structure growth will lead to vorticity.

At late times, dark matter haloes are rotationally supported and in this non-linear regime, a gravito-magnetic frame-dragging vector field is generated [194]. Dark matter composed of a purely irrotational fluid would have strong observational signatures (in particular, the rapid formation and growth of supermassive black holes [195]), so our assumption of the pure energy exchange which allows cold dark matter to remain geodesic must break down below some length scale.

3.2.2 *Flat FLRW background*

In a spatially flat FLRW background, (117) and (118) reduce to the coupled energy conservation equations,

$$\dot{\rho}_c + 3H\rho_c = -Q, \tag{121}$$
$$\dot{V} = Q, \tag{122}$$

where H is the Hubble expansion function and Q is the interaction term.

3.2.3 *Linear perturbations*

We now consider the linear, scalar perturbations about the FLRW metric. With the inclusion of these, the line element in a general gauge becomes

$$\begin{aligned} ds^2 = &-(1+2\phi)dt^2 + 2a\partial_i B dx^i dt \\ &+ a^2[(1-2\psi)\delta_{ij} + 2\partial_i\partial_j E]dx^i dx^j. \end{aligned} \tag{123}$$

The perturbed energy density of cold dark matter is given by $\rho_c + \delta\rho_c$, and the perturbed 4-velocity of matter is

$$u^\mu = [1-\phi,\ a^{-1}\partial^i v], \tag{124}$$
$$u_\mu = [-1-\phi,\ \partial_i\theta], \tag{125}$$

where

$$\partial^i v = a\frac{\partial x^i}{\partial t}, \tag{126}$$
$$\theta = a(v+B). \tag{127}$$

In the geodesic CDM scenario, where in (119) $f^\mu = 0$, the perturbed energy conservation equations for cold dark matter and the vacuum become

$$-\delta Q - Q\phi = \delta\dot{\rho}_c + 3H\delta\rho_c - 3\rho_c\dot{\psi} + \rho_c\frac{\nabla^2}{a^2}(\theta + a^2\dot{E} - aB), \tag{128}$$
$$\delta\dot{V} = \delta Q + Q\phi, \tag{129}$$

and the momentum conservation equations become

$$\dot{\theta} + \phi = 0, \tag{130}$$
$$-\delta V = Q\theta. \tag{131}$$

Considering that we are interested in the geodesic CDM scenario, with the interaction consisting of a pure energy exchange in the cold dark matter frame, i.e. $Q^\mu = Qu^\mu$, the cold dark matter 4-velocity u^μ acquires a central role, and it is therefore useful to consider a velocity-orthogonal slicing where u^μ coincides with the normal to the constant-time hypersurfaces [196, 197].

In this case the spatial components of u_μ in (125) vanish, and so $\theta = 0$, which then implies $v + B = 0$ from (127). The main convenience of this time-slicing with $\theta = 0$ is that the vacuum is spatially homogeneous on these hypersurfaces, $\delta V = 0$, which follows from (131). In this slicing, we can then specify a gauge.

As previously described in Chapter 2, a convenient choice of gauge for the numerical analysis discussed later is the synchronous gauge comoving with the 4-velocity of cold dark matter, fixed by setting $\phi = v = B = 0$. With this choice, (130) becomes an identity, (131) again implies $\delta V = 0$ and (129) therefore gives $\delta Q = 0$: both the interaction and the vacuum are spatially homogeneous with this gauge choice. The interaction therefore does not explicitly appear in the perturbation equations (128), (129) and it is not necessary to evolve the vacuum perturbations once this choice of gauge is made[1].

However, it is usual to use the density contrast $\delta_c = \delta\rho_c/\rho_c$ to describe matter perturbations. In doing so, the interaction is reintroduced via the evolution of ρ_c from (121). We find that δ_c evolves as

$$\dot{\delta}_c = \frac{Q}{\rho_c}\delta_c + 3\dot{\psi} - \nabla^2\dot{E}. \tag{132}$$

This point cannot be stressed enough, as it shows that the interaction has an effect on the perturbations and not just the background. This has important implications for cosmological structure growth, as we will further describe in subsection 3.2.4.

One may feel that the discussion of perturbations in cold dark matter and the vacuum only is too idealised, especially considering that in our numerical analysis described in section 3.4, we make use of the Boltzmann code `CAMB` [150, 151] in which baryons and radiation are also included. In such a multi-component case, a common gauge choice is that of the total matter gauge, with a 4-velocity chosen to be the eigenvector of the total energy–momentum tensor [196]. In such a gauge the cold dark matter would have a peculiar velocity and both the vacuum and the interaction would be inhomogeneous. However,

1 We emphasise that the vacuum *is* perturbed in a general spacetime sense; it is only homogeneous in the frame of observers comoving with the geodesic cold dark matter, where $\delta V = 0$.

CAMB works in the synchronous gauge comoving with cold dark matter and therefore the perturbation equations of the other components remain unchanged when one modifies CAMB from its basic ΛCDM version. This greatly simplifies the analysis of the geodesic CDM scenario we consider in this thesis.

3.2.4 *Redshift space distortions in interacting cosmologies*

An interacting scenario such as the one described above has a non-trivial effect on the growth of structure, as we will now explain. The peculiar velocities of galaxies, $\vec{v}$, cause a stretching and squashing in their shapes when plotted in redshift space. In ΛCDM, where there is no interaction, these redshift space distortions constrain structure growth because the divergence of the peculiar velocity field, $\nabla \cdot \vec{v}$, is related to the time derivative of the density contrast,

$$\dot{\delta}_c = -\frac{1}{a}\nabla \cdot \vec{v}\,. \tag{133}$$

One can write this time derivative in terms of a growth factor f as

$$\dot{\delta}_c = -\delta_c H f, \tag{134}$$

where f is defined as

$$f \equiv \frac{d\ln D}{d\ln a}, \tag{135}$$

and where D is the amplitude of the linear growing mode [67]. These distortions therefore allow a constraint to be placed on the growth rate of structure in the form of $f\sigma_8$, where σ_8 is the amplitude of the linear matter power spectrum on a scale of $8h^{-1}$Mpc. Equation (133) can be interpreted in relativistic perturbation theory as relating δ_c in the synchronous comoving gauge of the previous section to $\nabla \cdot \vec{v}$ in the Newtonian–Poisson gauge [196, 197].

However, in the interacting vacuum scenario, the interaction enters into the equation for the evolution of the density contrast, (132). Relating the $\nabla \cdot \vec{v}$ term with the metric perturbations in the synchronous comoving gauge gives

$$\nabla \cdot \vec{v} \equiv -a(3\dot{\psi} - \nabla^2\dot{E}), \tag{136}$$

and so

$$\nabla \cdot \vec{v} = -a\dot{\delta}_c + \frac{aQ\delta_c}{\rho_c}, \tag{137}$$

$$\nabla \cdot \vec{v} = -a\delta_c H f_i, \tag{138}$$

where f_i is the modified growth rate in the interacting vacuum cosmology,

$$f_i = f - \frac{Q}{H\rho_c}. \tag{139}$$

This means that in the interacting vacuum scenario, the redshift space distortions that we observe place a constraint on a new parameter that we may call $f_i\sigma_8$. This has been studied in [193], and a similar effect in a cosmology with a scalar field that conformally and disformally couples to dark matter was noted in [198].

An unmodified version of the code `CAMB` would compute the parameter $f\sigma_8$ as written in Equation 33 of [199],

$$f\sigma_8(z) \equiv \frac{\left[\sigma_8^{(\mathrm{vd})}(z)\right]^2}{\sigma_8^{(\mathrm{dd})(z)}}, \tag{140}$$

where $\sigma_8^{(\mathrm{vd})}$ is the smoothed density-velocity correlation and $\sigma_8^{(\mathrm{dd})}$ the smoothed density autocorrelation. The peculiar velocity in (140) is the Newtonian–Poisson gauge velocity of the baryons and cold dark matter. However, as we will explain in section 3.4, we modify `CAMB` to include our interacting scenario. It follows that the modified `CAMB` actually computes the right hand side of (140), which we may interpret as the parameter $f_i\sigma_8$. We can therefore safely use redshift space distortion data when attempting to constrain the interaction strength. However, this is not a direct constraint on the growth factor, f.

3.3 COUPLING FUNCTION RECONSTRUCTION

In order to constrain the interaction with available data, we write the covariant coupling in (119) as

$$Q = -q_{\mathrm{V}}\frac{1}{3}\Theta V, \tag{141}$$

where $\Theta = \nabla_\mu u^\nu$ is the expansion scalar and q_{V} is a dimensionless function that represents the strength of the coupling. In an FLRW background, (141) reduces to

$$Q(z) = -q_{\mathrm{V}}(z)H(z)V(z), \tag{142}$$

and hence the energy conservation equations (121) and (122) become

$$\dot{\rho}_c + 3H\rho_c = q_{\mathrm{V}}(z)H(z)V(z), \tag{143}$$

$$\dot{V} = -q_{\mathrm{V}}(z)H(z)V(z). \tag{144}$$

Now that we have the differential equations written in terms of the dimensionless coupling $q_V(z)$, we need to model the evolution of this function in redshift in terms of some numerical parameter that we will later constrain with cosmological data.

In this chapter, however, we are aiming to reconstruct the coupling rather than test specific models, adopting an agnostic standpoint regarding q_V and letting the data to tell us what this function is likely to be. The simplest way to proceed is to use step functions[2], approximating the coupling function q_V with one or more constant values of q_V in a series of redshift bins.

We focus on two main cases: the first is based on a single redshift bin, the second on four. Thus, in the first case we consider a single step function, with a fixed constant value q_V from $z = 0$ to a transition redshift z_{trans}, after which $q_V = 0$, the coupling vanishes and V is constant at higher redshifts. We will elaborate on four variants of this single step function reconstruction scenario in section 3.5, discussing two cases where z_{trans} is kept fixed, a case where we sample over z_{trans} and a case where we assume $V = 0$ for $z > z_{trans}$.

Finally, going beyond the single step function reconstruction, we want to account for a dynamical interaction q_V with no *a priori* assumption of any specific model for its time evolution: to this end, we consider a binned reconstruction of the function $q_V(z)$, based on several step functions.

It is worth stressing here that z_{trans} is a purely phenomenological parameter, used to implement the step function reconstruction. A true physical model producing an interaction between dark components might indeed imply that such a coupling is active throughout the whole history of the Universe, which would effectively correspond to $z_{trans} = \infty$. However, given our choice of $Q \propto V(z)$, even if the coupling is active at all times it will be effectively vanishing when the vacuum energy becomes negligible. Choosing a z_{trans} corresponding to an era where $V(z) \ll \rho_c(z)$ therefore mimics a model in which the coupling is always active and also allows us save computational time, as it only requires solving the differential equations presented in section 3.2 up to z_{trans} (see subsection 3.3.1).

At the same time, the physical model might imply that the coupling only becomes active when certain conditions are satisfied. Having a

2 Notice that adopting a step function reconstruction for q_V introduces discontinuities in $\dot{\rho}_c$ and $\dot{V}$ in (143) and (144) at the boundaries of the redshift bins; however this is not a problem, as the resulting ρ_c and $V(z)$ are continuous. In practice, we adopt a smoothed version of the step function reconstruction, so that even $\dot{\rho}_c$ and $\dot{V}$ are continuous, see subsection 3.3.2.

low $z_{\rm trans}$ can in principle phenomenologically mimic such a model and obtaining the value of $z_{\rm trans}$ that is preferred by the data would allow us to understand if models with a coupling that is not active at all times are preferred with respect to those in which the transfer of energy between the components is always active.

In the next three subsections, we describe the three main physical scenarios and their implementation through a step function reconstruction; namely a constant $q_{\rm V}$ up to $z_{\rm trans}$ followed by $V =$ constant, a varying $q_{\rm V}(z)$ represented by multiple bins and in which $V =$ constant after the final bin and finally a constant $q_{\rm V}$ up to the transition redshift $z_{\rm trans}$, after which $V = 0$. We then illustrate the effect of the coupling on the cosmological evolution.

3.3.1 *Constant $q_{\rm V}$ interaction*

With the reconstruction of $q_{\rm V}$ in mind, we elaborate on the five different possibilities, all based on assuming that in some redshift range $q_{\rm V}$ is constant in time, i.e. $q_{\rm V}(z) = q_{\rm V}$. Then, in each bin the interaction between dark matter and vacuum energy scales with redshift as $Q(z) \propto H(z)V(z)$. Such an interaction is a sub-case of the linear couplings considered by [200], and it greatly simplifies the solutions for ρ_c and V, which can be now obtained analytically from equations (143) and (144).

Setting initial conditions at $z = 0$ gives

$$\rho_c(z) = \rho_c^0 a^{-3} + V_0 \frac{q_{\rm V}}{q_{\rm V} - 3} \left(a^{-3} - a^{-q_{\rm V}}\right), \tag{145}$$

$$V(z) = V_0 a^{-q_{\rm V}}, \tag{146}$$

where ρ_c^0 and V_0 are the present values of the energy density of cold dark matter and vacuum, respectively. Furthermore, the equations for matter perturbations δ_c follow (132). Note that for $q_V = 3$ the solution is not divergent but has a logarithmic behaviour.

Analytical expressions similar to (145) and (146) can be found in different redshift bins, in a way that guarantees the continuity of ρ_c and V across bin boundaries.

It is worth noticing at this point that the choice of a constant $q_{\rm V}(z)$ is a strong assumption that has to be taken with a pinch of salt: it conveniently simplifies the equations but can give an unphysical model[3];

3 For instance, in an over-simplified model based on a negative constant $q_{\rm V}$ at all times the cold dark matter density ρ_c would become negative at some point.

we use it here only to give a phenomenological representation of a generic interaction in various redshift ranges, up to $z = 0$.

Hence, a first step we can take towards a more general description of the coupling is to consider a single step function reconstruction for $q_V(z)$, i.e. a q_V that remains constant up to a certain redshift z_{trans} and vanishes for higher redshifts; this corresponds to a cosmology equivalent to ΛCDM in the distant past, undergoing a transition at z_{trans} where the coupling is turned on and densities and perturbations start to scale as in the constant q_V case.

3.3.2 *Binned reconstruction*

In order to allow for a variation in redshift of the coupling function $q_V(z)$, we reconstruct its evolution using a number of redshift bins N, with the i^{th} bin being enclosed in the range $[z_{i-1}, z_i]$, with $z_0 = 0$ and $i = 1, ..., N$. For each of these bins the value at the centre of the range ($\bar{z}_i$) is $q_i = q_V(\bar{z}_i)$ and we assume the function to take this constant value within the entire redshift bin. With this choice, we can generally reconstruct the value of the function at any point as

$$q_V(z) = q_1 + \sum_{i=1}^{N-1} (q_{i+1} - q_1) \left[\theta_H(z - z_i) - \theta_H(z - z_{i+1})\right] \tag{147}$$

or, equivalently,

$$q_V(z) = q_1 + \sum_{i=1}^{N-1} (q_{i+1} - q_i) \left[\theta_H(z - z_i)\right] \tag{148}$$

where θ_H is the Heaviside function. We choose however to adjust this reconstruction by introducing a smoothing at the border of the bins, controlled by the parameter s, substituting the Heaviside functions with smooth steps based on hyperbolic tangent functions. This allows us to avoid sharp transitions between values of the function $q_V(z)$, which could lead to numerical problems. Given that no derivatives of the coupling enter our equations, this should not be an issue in our case, but even so, we rewrite the reconstructed function as

$$q_V(z) = q_1 + \sum_{i=1}^{N-1} \frac{q_{i+1} - q_i}{2} \left[1 + \tanh\left(s \frac{z - z_i}{z_i - z_{i-1}}\right)\right]. \tag{149}$$

Using (148) in equations (143) and (144) gives analytic expressions similar to (145) and (146) in each bin, matched at the bin boundaries; using (149) gives a smoothed version of the same $q_V(z)$. With

this, we numerically obtain the densities ρ_c and V such that their derivatives $\dot{\rho}_c$ and $\dot{V}$ are continuous through the bin boundaries. We have checked that the numerical and analytical solutions for ρ_c and V match extremely well.

3.3.3 *Seeded vacuum energy*

In the cosmology described above, there is a standard ΛCDM evolution at high redshifts until the coupling switches on at $z_{\rm trans}$ and the vacuum and cold dark matter energies can begin to interact. Instead, in the *seeded vacuum energy* case, or *SVE*, we have designed a reconstruction that mimics a physical scenario in which for $z > z_{\rm trans}$ we have a pure cold dark matter (Einstein–de Sitter) evolution, rather than ΛCDM. In this scenario the coupling causes the vacuum energy to suddenly grow from zero up to a 'seed' value at $z_{\rm trans}$, a kind of fast transition; cf. [201, 202] for a similar idea for unified dark matter models. Then, at lower redshifts, the interaction is characterised as in the previous cases, i.e. with a constant $q_{\rm V}$, and the vacuum evolves accordingly. The free parameter, $z_{\rm trans}$ allows this rapid growth of vacuum to a non-zero value to occur even at very late times.

In practice, this setup is achieved by some reverse engineering in `CAMB`. Since the coupling function Q is proportional to V, if V remained practically zero for the entire cosmic history we would never have any interaction. Instead, we 'seed' the growth of vacuum by inducing a sudden spike in its density at $z_{\rm trans}$. The vacuum energy V can then grow to a finite value and the transfer of energy between the vacuum and cold dark matter via the coupling can begin.

3.3.4 *Effects of the coupling*

As mentioned in Chapter 1, we are interested in the ability of these models to ease the tensions between low and high redshift observations. In particular we focus on the tension between the local determination of H_0 and that inferred from CMB measurements of the angular size of the sound horizon at recombination, $\theta_{\rm MC}$. In Figure 4 we show the $H(z)$ obtained for three different values of $q_{\rm V}$ and the same value of $\theta_{\rm MC}$, also highlighting the resulting value of H_0, while the other cosmological parameters, i.e. the densities $\Omega_b h^2$ and $\Omega_c h^2$, primordial power spectrum amplitude and tilt A_s and n_s and the optical depth $\tau_{\rm op}$, are fixed to the best fit of Planck 2015 [199]. We find that starting from the Planck value of $\theta_{\rm MC}$, a positive $q_{\rm V}$ leads

to higher values of H_0 with respect to ΛCDM, thus moving in the direction required to ease the tension.

Figures 5, 6 and 7 illustrate different aspects of the same three cosmologies. Given the definition of Q in (142), a negative value for q_V implies that cold dark matter is decaying into the vacuum, thus with the values of the density parameters $\Omega_c h^2$ and $\Omega_b h^2$ fixed at $z = 0$ we end up with a higher matter density in the past (see Figure 5). However, because the cosmologies shown here have the same present value of the matter density $\Omega_c h^2$, they will have significantly different matter abundances at early times; this impacts other observables, e.g. CMB power spectra which are significantly affected by the amount of matter (see Figure 6). Therefore if the only free parameters considered are q_V and H_0 one would expect a positive correlation between the two, but it is crucial not to neglect the effect of matter abundance on predictions for cosmological probes and the resulting degeneracy of $\Omega_c h^2$ with q_V and H_0.

In Figure 7 the effect of the coupling on the evolution of perturbations is shown through its effect on the matter power spectrum $P(k, z)$; we can see that a positive value of q_V suppresses the amplitude of $P(k, z)$, while on the contrary this is increased by a negative q_V. We stress that even though the results we comment on here refer to a case with constant q_V up to $z = 1$ and vanishing at higher redshifts, the same qualitative behaviour also holds for different choices of the redshift evolution of q_V.

3.4 DATA AND ANALYSIS METHOD

We want to compare the predictions of the interacting vacuum scenario with recent cosmological data. For this analysis we consider the Planck 2015 measurements of the CMB temperature and polarisation [203, 199]. For the Planck likelihood, we also vary the nuisance parameters that are used to model foregrounds as well as instrumental and beam uncertainties. We note that at the time of writing[4], the new Planck 2018 likelihood was not publicly available, but given the similarities between the Planck 2015 and 2018 results we do not expect that our results would change significantly were we to use the 2018 data presented in [61].

4 We remind the reader that this chapter is based on the published paper [1], which was written prior to the Planck 2018 likelihood being made public, but in subsequent chapters based on later papers, we do use the Planck 2018 likelihood. The two likelihoods are sufficiently similar that we do not anticipate that the results presented in this chapter would change if the analysis was repeated with the newer likelihood.

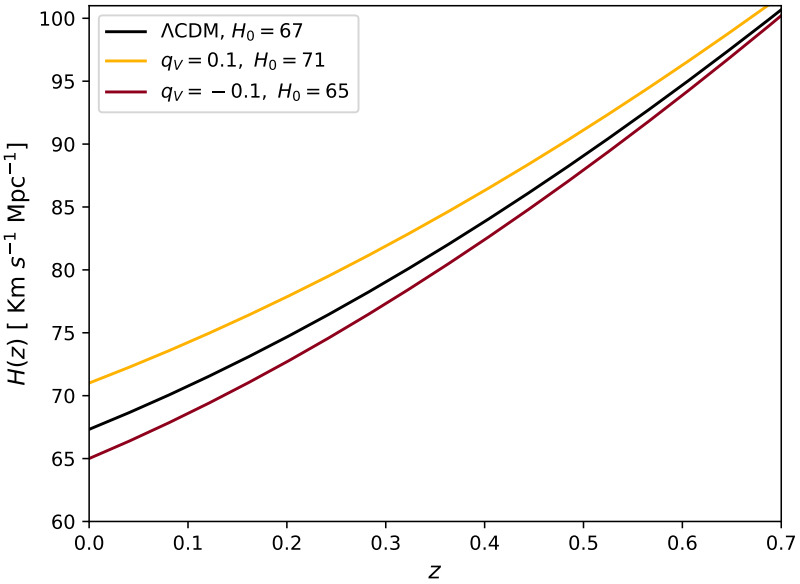

Figure 4: The evolution of the Hubble function $H(z)$ for three cosmologies resulting in the same angular size of the sound horizon at recombination. Except for q_V and H_0, whose values are shown in the label, all the other primary parameters are fixed to the Planck 2015 best fit.

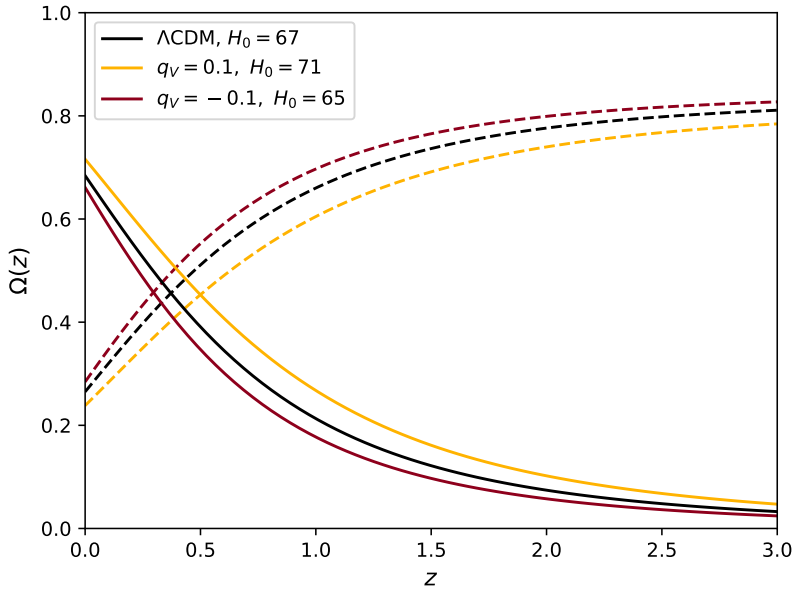

Figure 5: The evolution of the matter (dashed lines) and vacuum density (solid lines) parameters as a function of redshift, for a small positive and negative coupling. The ΛCDM case is shown in blue. Except for q_V and H_0, whose values are shown in the label, all the other primary parameters are fixed to the Planck 2015 best fit.

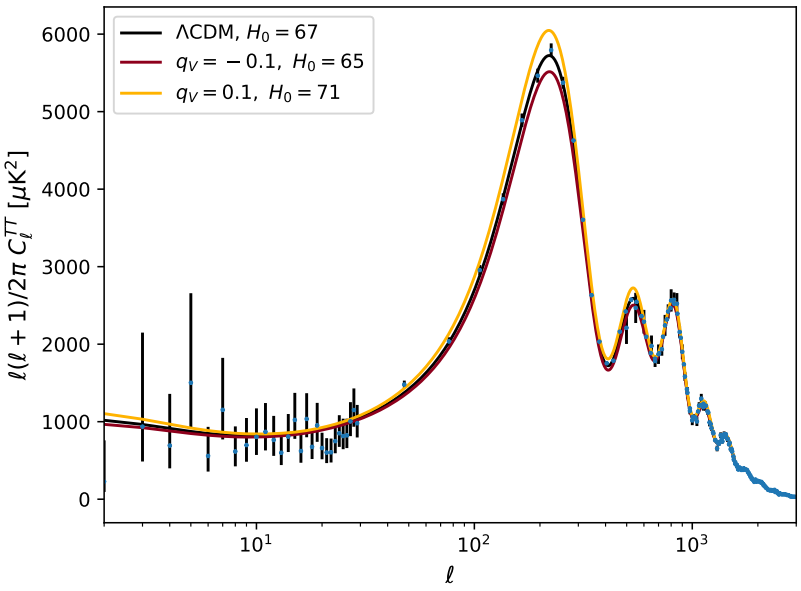

Figure 6: The CMB temperature–temperature power spectrum for three cosmologies resulting in the same angular size of the sound horizon at recombination. Except for q_V and H_0, whose values are shown in the label, all the other primary parameters are fixed to the Planck 2015 best fit. The data points are the TT observations of Planck 2015.

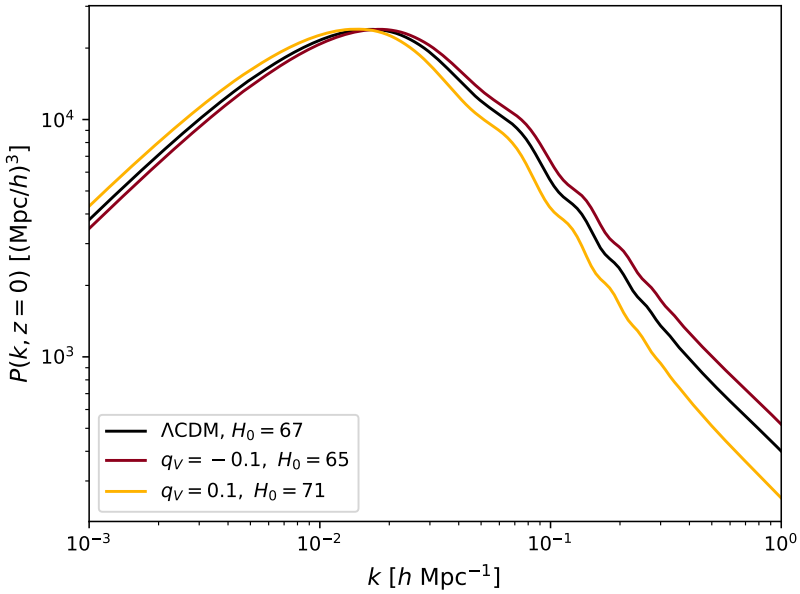

Figure 7: The matter power spectrum at $z = 0$ for three cosmologies resulting in the same angular size of the sound horizon at recombination. Except for q_V and H_0, whose values are shown in the label, all the other primary parameters are fixed to the Planck 2015 best fit. The ΛCDM case is plotted in blue.

Quantity	z_{eff}	Measurement	Source
d_v	0.106	$457 \pm 27 (r_s/r_{s,\text{fid}})$ Mpc	[96]
d_v	0.15	$(664 \pm 25)(r_s/r_{s,\text{fid}})$ Mpc	[97]
d_v	0.32	$(1270 \pm 14)(r_s/r_{s,\text{fid}})$ Mpc	[63]
d_v	0.57	$(2033 \pm 21)(r_s/r_{s,\text{fid}})$ Mpc	[63]
$f\sigma_8$	0.32	0.392	[63]
$f\sigma_8$	0.57	0.445	[63]

Table 3: This table lists the BAO and $f\sigma_8$ data points used in our analysis. The parameter d_v is a distance scale, defined as $d_v(z) = \left[(1+z)^2 d_A^2(z) \frac{cz}{H(z)}\right]^{1/3}$, d_A being the angular diameter distance [96], and $f\sigma_8$ is the value of the linear growth rate f multiplied by σ_8, the amplitude of the linear matter power spectrum on a scale of $8h^{-1}$ Mpc.

In addition to the Planck CMB data, we utilise the BAO measurement from the 6dF Galaxy Survey [96], the BAO scale measurement from the SDSS DR7 Main Galaxy Sample [97] and the combined BAO and RSD data from the SDSS DR12 consensus release [63] (data points listed in Table 3), together with the JLA Type Ia supernovæ sample [44]. We refer to the combined datasets as Planck + Low-z, with Low-z referring to the combination of all dataset at redshifts lower than recombination.

3.4.1 *Implementation in CAMB*

Now that we have chosen our methods of reconstruction, we need to obtain predictions for the cosmological observables. In order to do so we use the Einstein–Boltzmann Code for the Anisotropies in the Microwave Background (CAMB); we modify the code so that it uses the $\rho_c(z)$ and $V(z)$ of our model rather than those computed internally within the ΛCDM framework. We therefore add a new module which solves the differential equations (143) and (144), with q_V computed at each redshift according to the methods described in section 3.3. We use a Runge–Kutta algorithm, starting from the present day with initial conditions

$$\begin{aligned} \rho_c^0 &= 3H_0^2\Omega_c, \\ V_0 &= 3H_0^2\Omega_\Lambda, \end{aligned} \tag{150}$$

and then evolving the equations backwards in time. To solve the equations for cold dark matter perturbations we make use of the routines

present in CAMB, modifying the equation for cold dark matter with the extra source term proportional to q_V described in (132).

On top of this, we make use of the MCMC sampler CosmoMC [162, 163] to sample the parameter space and compare our predictions with the cosmological data mentioned above. The six sampled parameters are therefore those of the minimal ΛCDM: the baryon and cold dark matter densities at present day, $\Omega_b h^2$ and $\Omega_c h^2$; the optical depth, τ_{op}; the primordial power spectrum amplitude and tilt, A_s and n_s, and the Hubble constant H_0.

Furthermore, we also consider additional parameters depending on the specific cosmology we investigate:

- *Cfix*: the constant coupling q_V with uniform prior $[-6, 3]$, controlling the evolution of the densities up to a fixed $z_{trans} = 3000$, with standard ΛCDM evolution at higher redshifts. We also consider a variation on this in which $z_{trans} = 0.9$, to compare directly with [135].
- *Cvar*: the constant coupling q_V and the varying z_{trans} with uniform priors $[-6, 3]$ and $[0.1, 10]$ respectively. At redshifts higher than z_{trans} the coupling is turned off and we then have standard ΛCDM evolution. In order to test the stability of the results changing the prior choice, we also explored a logarithmic prior on z_{trans}, including also higher values of this parameter, finding no significant differences in our results. We choose therefore to only present the results obtained with the uniform prior.
- *SVE*: a constant q_V and the varying transition redshift z_{trans}. At redshifts higher than the transition redshift, cold dark matter evolves in the standard way while $V(z)$ smoothly transitions to zero from its value at z_{trans} according to the solution of the differential equations. For these parameters we also use the uniform priors $[-6, 3]$ and $[0.1, 10]$ respectively.
- *4bins*: $N = 4$ low redshift bins q_i, with uniform priors $[-6, 3]$, used to reconstruct the evolution in time of the coupling function $q_V(z)$, with a return to standard ΛCDM for redshifts higher than the last bin. The number and redshift of the considered bins ($z_i \in \{0.3, 0.9, 2.5, 10\}$) are chosen in order to compare our results with that from previous work by [135].

The choice of the prior range $[-6, 3]$ for the q_V parameters arises from the fact that ρ_c in (145) becomes singular when $q_V = 3$. While higher values of the coupling are theoretically possible, we choose to limit the parameter space to the non-pathological part, in order to avoid

Parameter	Prior range
$\Omega_b h^2$	$[0.005, 0.1]$
$\Omega_c h^2$	$[0.001, 0.99]$
H_0	$[50, 100]$
$\tau_{\rm op}$	$[0.01, 0.8]$
$\log 10^{10} A_s$	$[2.0, 4.0]$
n_s	$[0.8, 1.2]$
$q^i_{\rm V}$	$[-6, 3]$
$z_{\rm trans}$	$[0.1, 10]$

Table 4: Prior ranges on the cosmological parameters sampled in our analysis. The prior range on $z_{\rm trans}$ refers to the *Cvar* and *SVE* cases, while in the rest of the analysis this parameter is fixed.

issues with the sampling. Indeed, we find that this prior is sufficiently broad as to have no effect on our results. A summary of the priors used on all parameters can be found in Table 4.

3.5 RESULTS

In this section we present the results of our investigation, beginning with the two *Cfix* cases where the interaction is characterised by a constant parameter $q_{\rm V}$ up to a transition redshift, moving to the cases where the transition redshift $z_{\rm trans}$ is allowed to vary (*Cvar* and *SVE*) and finally the *4bins* case. We remark again that any integration is performed with initial values set today at $z = 0$. In particular a non-zero value for the vacuum V_0 is set as in (150).

In Table 5 we summarise results for the five cases; we report the marginalised constraints on the primary parameters sampled in our analysis, adding also the combination of derived parameters $\sigma_8 \Omega_{\rm m}^{1/2}$, useful to assess the status of the tensions between high and low redshift probes.

Parameter	Case	Planck	Planck + Low-z
$\Omega_b h^2$	*Cfix*	0.02226 ± 0.00022	0.02235 ± 0.00015
	Cfix ($z_{\rm trans} = 0.9$)	$0.02226^{+0.00014}_{-0.00020}$	0.02235 ± 0.00014
	Cvar	0.02222 ± 0.00015	0.02234 ± 0.00014
	SVE	0.02224 ± 0.00016	0.02235 ± 0.00015
	4bins	0.02224 ± 0.00015	0.02226 ± 0.00016

$\Omega_c h^2$	*Cfix*	0.131 ± 0.040	$0.122^{+0.011}_{-0.0089}$
	Cfix ($z_{\mathrm{trans}} = 0.9$)	$0.118^{+0.025}_{-0.038}$	0.130 ± 0.015
	Cvar	$0.153^{+0.047}_{-0.031}$	0.124 ± 0.012
	SVE	$0.150^{+0.049}_{-0.024}$	0.124 ± 0.011
	4bins	$0.132^{+0.031}_{-0.056}$	$0.117^{+0.020}_{-0.045}$
τ_{op}	*Cfix*	$0.080^{+0.021}_{-0.017}$	0.077 ± 0.017
	Cfix ($z_{\mathrm{trans}} = 0.9$)	$0.080^{+0.018}_{-0.015}$	0.078 ± 0.016
	Cvar	0.080 ± 0.017	0.077 ± 0.016
	SVE	0.079 ± 0.016	0.076 ± 0.017
	4bins	0.081 ± 0.017	0.074 ± 0.017
$\log 10^{10} A_s$	*Cfix*	$3.094^{+0.039}_{-0.032}$	3.084 ± 0.033
	Cfix ($z_{\mathrm{trans}} = 0.9$)	$3.094^{+0.029}_{-0.033}$	3.087 ± 0.032
	Cvar	3.094 ± 0.034	3.084 ± 0.031
	SVE	3.093 ± 0.032	3.084 ± 0.033
	4bins	3.098 ± 0.032	3.082 ± 0.034
n_s	*Cfix*	$0.9647^{+0.0048}_{-0.0062}$	0.9681 ± 0.0043
	Cfix ($z_{\mathrm{trans}} = 0.9$)	$0.9658^{+0.0042}_{-0.0062}$	0.9684 ± 0.0040
	Cvar	0.9643 ± 0.0047	0.9679 ± 0.0041
	SVE	0.9646 ± 0.0048	0.9682 ± 0.0043
	4bins	0.9644 ± 0.0045	0.9655 ± 0.0047
H_0	*Cfix*	$62.3^{+3.2}_{-6.2}$	67.54 ± 0.80
	Cfix ($z_{\mathrm{trans}} = 0.9$)	67.05 ± 2.1	67.26 ± 0.86
	Cvar	$62.2^{+4.9}_{-5.5}$	67.50 ± 0.81
	SVE	61.9 ± 5.2	67.46 ± 0.86
	4bins	64.0 ± 4.8	67.33 ± 0.80
$\sigma_8 \Omega_{\mathrm{m}}^{1/2}$	*Cfix*	$0.4652^{+0.0075}_{-0.022}$	$0.452^{+0.011}_{-0.014}$
	Cfix ($z_{\mathrm{trans}} = 0.9$)	0.4752 ± 0.037	0.446 ± 0.017
	Cvar	$0.4614^{+0.0088}_{-0.021}$	$0.451^{+0.012}_{-0.015}$
	SVE	$0.461^{+0.012}_{-0.025}$	0.450 ± 0.016
	4bins	$0.481^{+0.064}_{-0.076}$	0.482 ± 0.055
q_{V}	*Cfix*	$0.52^{+0.65}_{-0.77}$	0.04 ± 0.10
	Cfix ($z_{\mathrm{trans}} = 0.9$)	0.059 ± 0.39	0.14 ± 0.19
	Cvar	0.59 ± 0.53	$0.07^{+0.11}_{-0.14}$
	SVE	0.62 ± 0.60	0.06 ± 0.12
q_1	*4bins*	$0.0^{+1.2}_{-1.5}$	$-0.42^{+0.51}_{-1.0}$

q_2	*4bins*	$0.3^{+1.9}_{-1.2}$	$0.88^{+0.82}_{-0.66}$
q_3	*4bins*	> -2.7	$-0.62^{+1.3}_{-0.91}$
q_4	*4bins*	unconstrained	unconstrained
	Cfix	–	–
	Cfix ($z_{\rm trans} = 0.9$)	–	–
$z_{\rm trans}$	*Cvar*	unconstrained	unconstrained
	SVE	> 1.7	> 1.4

Table 5: Marginalised values of the parameters and their 68% confidence level bounds, obtained using Planck and Planck + Low-z. When only upper or lower bounds are found, we report the 95% confidence level limit.

3.5.1 *Cfix case*

As a baseline result, we report the constraints obtained assuming a constant value $q_{\rm V}$ for the coupling, up to a fixed redshift $z_{\rm trans} = 3000$. At higher redshifts, the interaction is turned off ($q_{\rm V}(z > z_{\rm trans}) = 0$) and the vacuum assumes a constant value $V = V(z = z_{\rm trans})$. This choice is made so that the interaction affects the evolution of cold dark matter and vacuum only after the last scattering surface; however, given our choice of $Q \propto V$, the interaction is negligible during the matter dominated era.

In Figure 8 we show the 2D joint marginalised contours of $q_{\rm V}$ with H_0, $\Omega_{\rm m}$ and $\Omega_{\rm c}h^2$. We point out that the constraints placed by Planck on $q_{\rm V}$ and H_0 are strongly degenerate. This effect is due to the change in the Universe's expansion history caused by the interaction: we find that a larger H_0 requires a smaller coupling parameter $q_{\rm V}$ in order to recover the same expansion history. A similar degeneracy is also present between $q_{\rm V}$ and $\Omega_{\rm m}$. In general, the CMB data prefer positive values of $q_{\rm V}$. Negative values of $q_{\rm V}$ imply that we would have a smaller cold dark matter density at late times (see bottom bottom panel of Figure 8), which would boost the amplitude of the acoustic peaks in the CMB temperature–temperature power spectrum by such an amount that the change could not be compensated for by equivalent changes in the other cosmological parameters.

We find that the Planck data alone allow for the coupling $q_{\rm V}$ to be non-vanishing; however, the ΛCDM limit of this model is within the 68% confidence level region. The degeneracies between $q_{\rm V}$, H_0 and $\Omega_{\rm m}$ are broken when the Low-z datasets are added to Planck. This is because

the data directly probe the redshift range where the interaction is primarily effective. The combination of the Planck and Low-z data does not allow q_V to greatly deviate from zero and the cosmology is therefore very similar to ΛCDM.

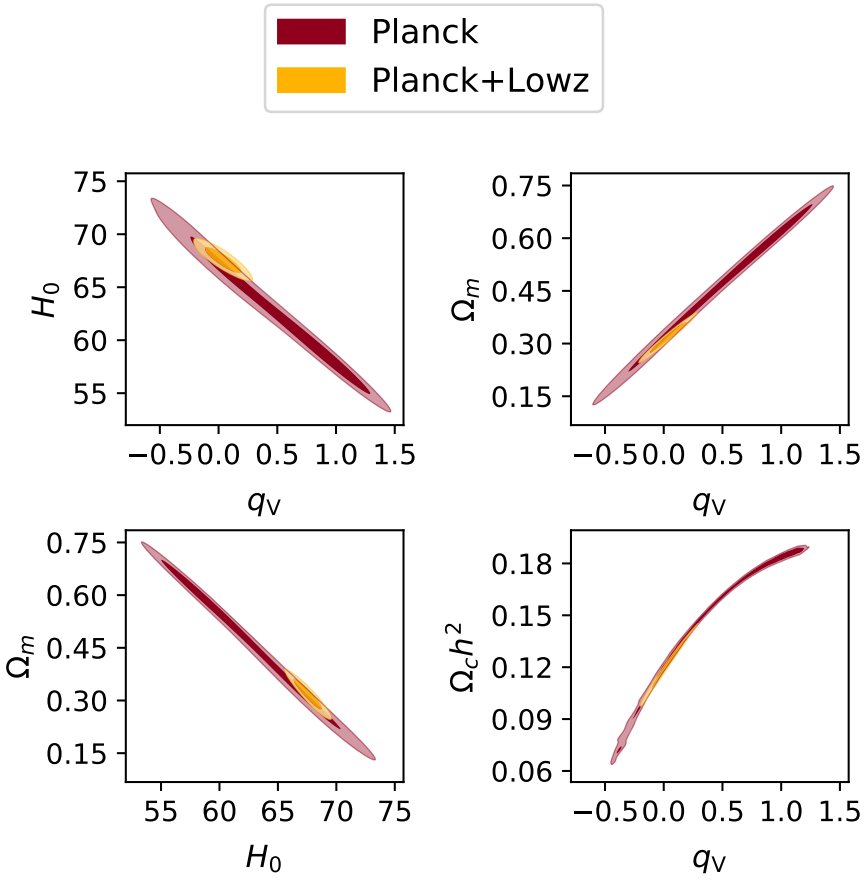

Figure 8: *Cfix* case with $z_{trans} = 3000$: 68% and the 95% confidence level marginalised contours on H_0, $q_V = q_V(z \leq 3000)$ and Ω_m as obtained in the analysis with the Planck (red) and Planck + Low-z (yellow) datasets.

3.5.2 *Cfix with low transition redshift*

We now consider a *Cfix* case in which we set the transition redshift to $z_{trans} = 0.9$. This allows us to make a direct comparison with the so-called q_{34} case presented in [135], in which it was found that a null interaction was excluded at the 99% confidence level.

This *Cfix* case should be seen as a simple single step function reconstruction of an interaction that is negligible for $z > z_{trans} = 0.9$. It is

a single parameter reconstruction where, as in [135] and in comparison to our *4bins* case of section 3.5.5, the first two bins are grouped together, with no interaction for $z > z_{\rm trans} = 0.9$. Note that in [135] the $z_{\rm trans} = 0.9$ value was also chosen because it was the best fit value resulting from a two parameter analysis, similar to our *Cvar* case in the next section.

Our results for this case are similar to that of the *Cfix* case with $z_{\rm trans} = 3000$. However, in this case, the CMB bound on $q_{\rm V}$, and consequently the bound on the degenerate cosmological parameters, is less broad and more directly centred on $q_{\rm V} = 0$ with respect to the $z_{\rm trans} = 3000$ case; this is due to the fact that the coupling is active for less time and therefore values of $q_{\rm V}$ that are significantly different from zero cannot be compensated by changes in $\Omega_c h^2$. This result differs from that found by [135] in that we do not exclude the ΛCDM limit of $q_{\rm V} = 0$ at any confidence level. The marginalised 2D joint distributions for the relevant parameters in this case are shown in Figure 9.

3.5.3 *Cvar case*

In Figure 10 we show the results of the case where the transition redshift $z_{\rm trans}$ is allowed to vary. In this case we also find the ΛCDM limit to be a good fit to the data, both in the Planck and Planck + Low-z combinations respectively, as reported in Table 5. We find an evolution similar to both *Cfix* cases, with the inclusion of the Low-z dataset breaking the degeneracies between $q_{\rm V}$ and the cosmological parameters in the Planck result. With both Planck alone and Planck+Low-z, we find that $z_{\rm trans}$ is unconstrained, in contrast to a similar analysis in [135]. For values of this parameter that correspond to the matter dominated era, this *Cvar* case effectively reduces to the *Cfix* one, as $V(z)$ and consequently $q_{\rm V}$ become negligible. For low values of $z_{\rm trans}$ this case becomes extremely similar to ΛCDM, with $z_{\rm trans} = 0$ acting as another ΛCDM limit of the model for any value the coupling can take.

3.5.4 *SVE case*

In Figure 11, we show the results for the *SVE* cosmology. The first thing to notice is that this case is analogous to *Cvar* when $z_{\rm trans}$ takes high values, with both data combinations favouring positive values of the coupling, i.e. a decay of vacuum energy density into cold dark

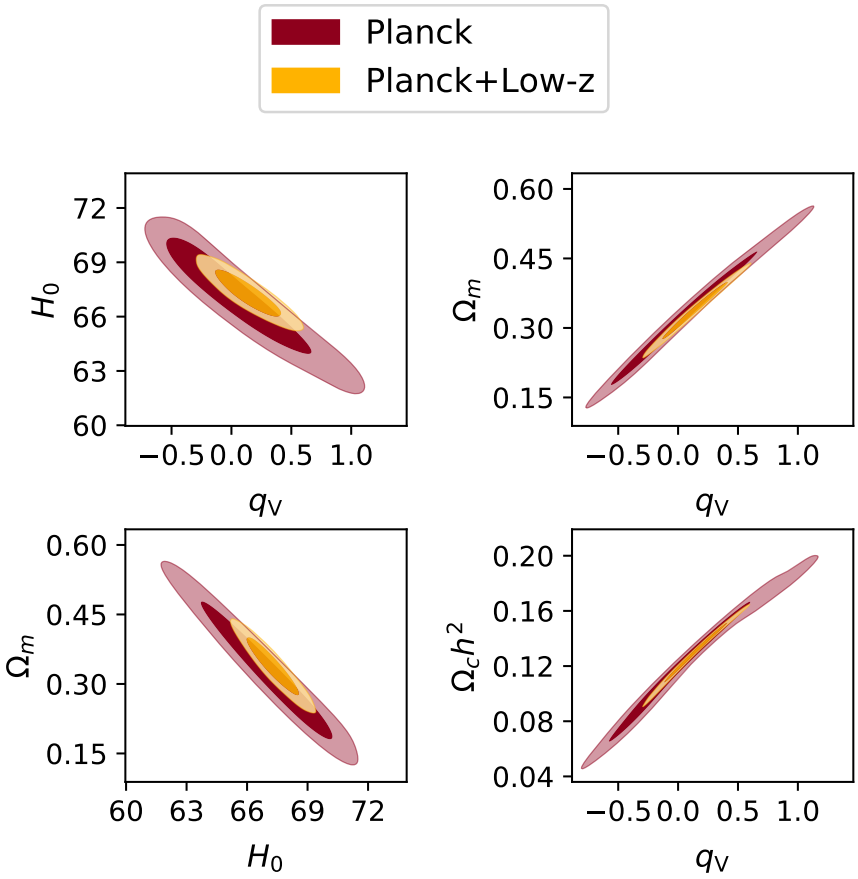

Figure 9: *Cfix* case with $z_{\rm trans} = 0.9$: 68% and the 95% confidence level marginalised contours on H_0, $q_{\rm V} = q_{\rm V}(z \leq 0.9)$, $\Omega_{\rm m}$ and $\Omega_c h^2$ as obtained in the analysis with the Planck (red) and Planck + Low-z (yellow) datasets.

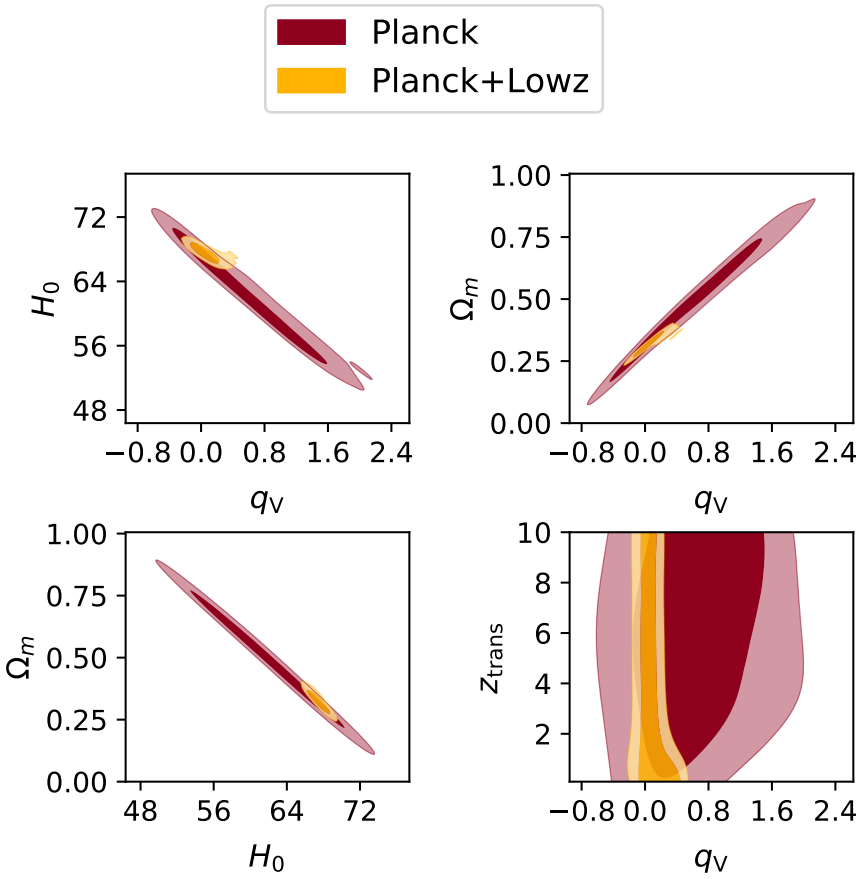

Figure 10: *Cvar* case: 68% and the 95% confidence level marginalised contours on H_0, $q_V = q_V(z \leq z_{trans})$, z_{trans} and Ω_m as obtained in the analysis with the Planck (red) and Planck + Low-z (yellow) datasets.

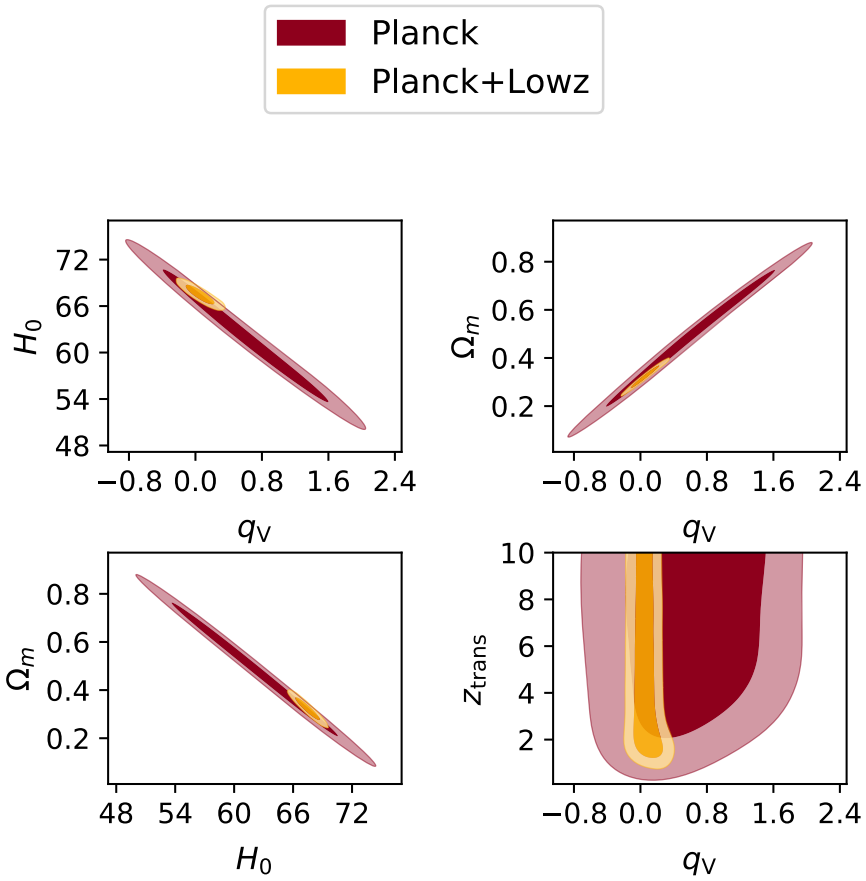

Figure 11: *SVE* case: 68% and the 95% confidence level marginalised contours on H_0, $q_V = q_V(z \leq z_{trans})$, z_{trans} and Ω_m as obtained in the analysis with the Planck (red) and Planck + Low-z (yellow) datasets.

matter. This is due to the fact that in *Cvar*, even though $V(z)$ does not vanish, it becomes negligible in the past following the ΛCDM evolution (see Figure 15) and the difference between the two models effectively vanishes. The situation is different for low transition redshifts; while in the *Cvar* case the model approaches ΛCDM, in *SVE*, low values of this parameter are significantly disfavoured. This is because for $z_{trans} \lesssim 2$, a vanishing $V(z)$ affects both the predictions for Low-z and for CMB, through its impact on CMB lensing and ISW effect. In the *Cvar* case z_{trans} was unconstrained, while here we find a lower limit at 95% confidence level of $z_{trans} = 1.8$ (Planck) and $z_{trans} = 1.4$ (Planck+Low-z).

3.5.5 *4bins case*

In this case, we aim to update the work of [135], in which the coupling consists of $N = 4$ bins in redshift, with transitions at $z = 0.3,\ 0.9,\ 2.5$ and 10 and values q_i with $i = 1, ..., 4$, thus allowing for a general evolution in redshift of the coupling function $q_{\rm V}(z)$. In Figure 12 and Table 5 we show the results obtained from the cosmological analysis with this four bins setup, considering both the Planck and Planck + Low-z datasets.

The first thing to note is that the high redshift bin q_4 is not constrained by either dataset. This is due to the fact that most of the Low-z data lie at redshifts lower than those affected by this parameter and therefore any constraining power would come from the effect of the coupling in this redshift bin on CMB power spectra predictions. However, we see that the Planck data is also unable to place any bounds on the value of q_4, nor an upper bound on the value of q_3.

While ΛCDM is also a good fit to the data in this case, in general we find that the allowed range for the amplitude of the interaction in each redshift bin is larger than in the *Cfix* and *Cvar* cases. This is expected, as the values of q_i can be compensated for by the overall evolution of $q_{\rm V}(z)$ and therefore by the $q_{j\neq i}$ parameters. This induces an anti-correlation between the values of the coupling in neighbouring bins. Once again, this degeneracy is significantly reduced when the Low-z data are included, as these datasets are more efficient in constraining the values of q_i in each redshift bin rather than the average effect of the interaction.

However, while in the *Cfix* and *Cvar* cases the inclusion of Low-z produces tight posteriors centered on the ΛCDM limit, in the *4bins* case the first bin posterior is slightly shifted to negative values (with $q_1 = 0$ still within the 68% confidence interval) and the second bin posterior is shifted towards positive values: this is due to the aforementioned anti-correlation. While still in agreement with a constant $q_{\rm V}(z) = 0$ cosmology, the Planck+Low-z dataset allows for a model with an oscillatory amplitude of vacuum energy–cold dark matter interaction at low redshifts (See subsection 3.6.3 for further discussion). This is in contrast to the results of many similar works. We will expand on this point in section 3.7.

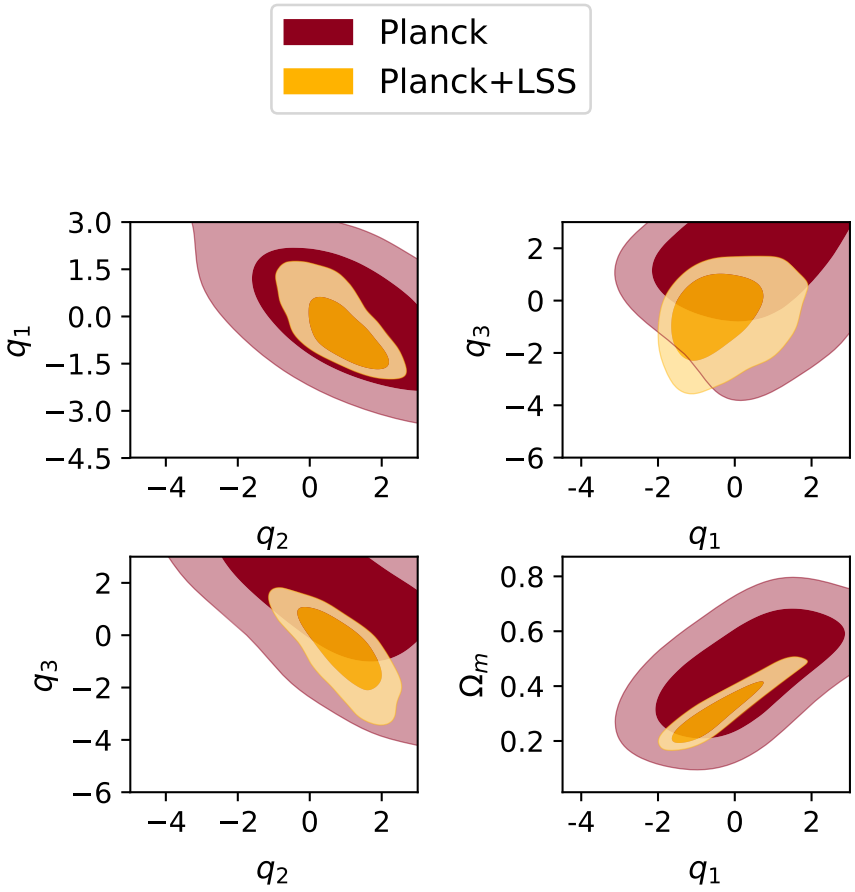

Figure 12: *4bins* case: 68% and the 95% confidence level marginalised contours on q_i, $i = 1, ..., 3$ and Ω_m as obtained in the analysis with the Planck (red) and Planck + Low-z (yellow) datasets.

3.5.6 *Evolution of $f\sigma_8$*

From these results, we can also examine how the interaction in each case affects the evolution of the $f\sigma_8$ parameter as computed by the modified `CAMB`, keeping in mind that in our interacting scenario this parameter does not directly constrain the growth factor, i.e. it rather represents $f_i\sigma_8$, as discussed in subsection 3.2.4. In Figure 13, we plot the $f\sigma_8$ prediction for each case, using the mean posterior values of q_V from the Planck+Low-z runs to obtain its evolution as a function of redshift. For illustrative purposes, we plot these predictions along with data points from various collaborations: 2dFGRS [204], 6dFGRS [205], WiggleZ [206], SDSS LRG [207], BOSS CMASS [208] and VIPERS [209].

This plot shows how the similar values of q_V obtained for *Cfix*, *Cvar* and *SVE* lead to similar evolution histories for $f\sigma_8$, with the small positive values of q_V in these cases leading to a suppression of this quantity with respect to ΛCDM. Growth is suppressed with a positive coupling because our implementation in `CAMB` works by starting with the values of cosmological parameters at $z = 0$ and evolving them backwards in time. This means that, with a positive q_V, we need less matter in the past to reach the correct value of Ω_m today; in addition, $q_V > 0$ implies a negative contribution of the coupling to $\dot{\delta}$ in (132); the net result is that the growth is suppressed. The *4bin* case instead sees an enhancement of $f\sigma_8$ with respect to ΛCDM: this is due to the overall negative value of the coupling across the 4 redshift bins.

Note that for $q_V \neq 0$, Figure 13 is effectively a plot of $f_i\sigma_8$, and $f_i > f$ for $q_V > 0$ (see (139)). In practice, the suppression of the growth implies a σ_8 small enough to produce a smaller $f_i\sigma_8$, and vice versa for $q_V < 0$.

3.6 DISCUSSION

In this section we discuss our results, presenting a rough model comparison analysis in order to estimate the statistical preference of our models with respect to ΛCDM. Moreover, we focus on the effects on the tensions in the values of H_0 and σ_8 in the different interacting cases presented above. We also describe how the $q_V(z)$ function can be reconstructed using Gaussian processes.

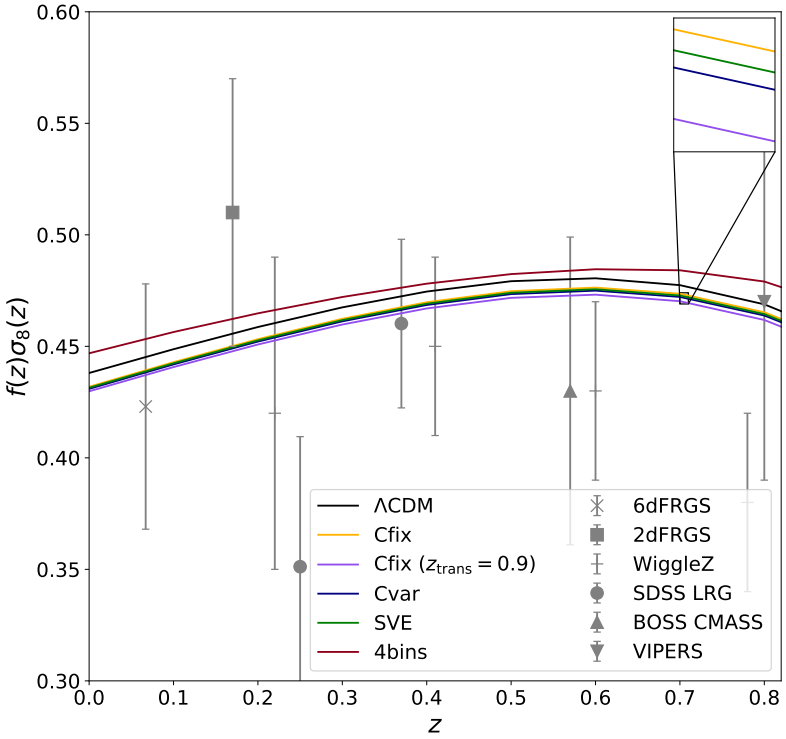

Figure 13: The predictions for $f\sigma_8$ for ΛCDM (plotted in black) and the interacting cosmologies studied in this chapter. For illustrative purposes, we plot these together with data from various collaborations (see text for details).

3.6.1 *Model comparison*

In all our results we find a good agreement between the ΛCDM limit of the interacting models investigated and the constraints obtained through the analysis of cosmological data. We therefore expect that there is no significant statistical preference for the extended model over ΛCDM. However, we will quantify this preference by making use of the deviance information criterion (DIC) [175], which, as we explained in Chapter 2 is given by

$$\mathrm{DIC} \equiv \chi^2_{\mathrm{eff}}(\hat{\theta}) + 2p_D\,, \tag{151}$$

where $\chi^2_{\mathrm{eff}}(\hat{\theta}) = -2\ln\mathcal{L}(\hat{\theta})$, $\hat{\theta}$ is the parameter vector at the best fit and $p_D = \overline{\chi^2_{\mathrm{eff}}(\theta)} - \chi^2_{\mathrm{eff}}(\hat{\theta})$, where the bar denotes the average taken over the posterior distribution. In order to compare ΛCDM with the models explored here, we compute:

$$\Delta\mathrm{DIC} = \mathrm{DIC}_{\mathrm{V}} - \mathrm{DIC}_{\Lambda\mathrm{CDM}}. \tag{152}$$

From this definition it follows that a negative ΔDIC would support the extended model, while a positive one would support ΛCDM.

In Table 6 we show the values obtained for this estimator in all the cases analysed in this chapter. We find that when analysing only CMB data, all the models except for *Cfix* are slightly preferred with respect to ΛCDM. However, all the cases have a Δ DIC close to zero, showing that the preference of the extension over the standard model (or vice versa) is inconclusive in all cases, if we set $\Delta\mathrm{DIC} = 5$ as the threshold for a moderate preference [210]. When analysing the Planck+Low-z case, we find that all cases have a small positive Δ DIC, indicating that ΛCDM is marginally preferred over the extended model. This comes from the fact that adding the Low-z datasets significantly shrinks the constraints around the ΛCDM limit of the model, thus disfavouring the extended case which, at this point, effectively reproduces a ΛCDM cosmology with the addition of extra parameters.

3.6.2 *Effects on cosmological tensions*

As we highlighted in Chapter 1, one of the motivations to explore the coupling scenarios discussed in this thesis is to attempt to solve the tensions that exist between different observations, i.e. the discrepancies between low and high redshift measurements of the present day expansion rate of the Universe and of the clustering of matter. In Figure 14 we plot the H_0 versus Ω_{m} and σ_8 versus Ω_{m} 2D marginalised

Parameter	Planck	Planck+Low-z
Cfix	1.1	3.8
Cfix ($z_{\rm trans} = 0.9$)	-1.2	0.4
Cvar	-0.5	2.6
SVE	-1.3	1.3
4bins	-1.6	3.1

Table 6: ΔDIC values for the different models analysed, both when using Planck data alone and when combining them with the Low-z datasets.

contours for every case considered, obtained using the Planck 2015 dataset, comparing them with the constraints used assuming ΛCDM, in order to examine the effects of the interaction on the H_0 and σ_8 tensions.

We firstly note that for both of these combinations, the contours obtained for the *Cfix*, *Cvar* and *SVE* are very similar, showing that changing the behaviour of $V(z)$ after $z_{\rm trans}$ (from standard ΛCDM evolution to vanishing $V(z)$) has no significant effect if $z_{\rm trans}$ is already in an epoch where vacuum energy is negligible. In Figure 15, we have plotted the ratio of the vacuum to cold dark matter energy densities, for both a small positive and negative coupling and with two transition redshifts, $z_{\rm trans} = 0.9$ and 10. The sign of the coupling and the transition redshift value have limited effect, as for each of the four values shown, the density ratio reaches $1/100$ and 1 at very similar redshifts. The *4bins* case instead yields broader constraints with respect to the other cases, an effect which is due to the higher number of coupling parameters and their degeneracies with the standard cosmological ones.

The top panel of Figure 14 shows how the coupling scenarios are able to apparently ease the tension between the local measurements of H_0 (grey band) and the Planck measurement. However, this is only due to the extreme degeneracy between H_0, $\Omega_{\rm m}$ and $q_{\rm V}$ that we highlighted in section 3.5; the mean values obtained for H_0 are actually lower than those found by Planck assuming ΛCDM, and the tension is eased only because of the much larger error bars. In [127] it was proposed that this tension could be relaxed with an early dark energy component, affecting the evolution of the Universe at $z \gtrsim 3000$; while not explored here, a high redshift coupling between cold dark matter and vacuum energy could in principle be used to mimic the effect of such a component. We explore this point further in Chapter 5.

In the bottom panel of Figure 14, we instead highlight how reconciling the tension in σ_8 is less feasible in this model. The errors on the cosmological parameters are once again enlarged by the degeneracies introduced by the coupling. This leads to lower values of σ_8 being allowed, but these lower values subsequently necessitate higher values of Ω_m in compensation, which are then disfavoured by the Low-z data.

3.6.3 *Gaussian process reconstruction*

We can use Gaussian processes to attempt to reconstruct the q_V function for the four bin case. Gaussian processes have been widely used in cosmology to reconstruct smooth functions from observational data, particularly for functions such as $H(z)$ and the dark energy equation of state $w(z)$ (see, for example, [212, 213, 214, 215]). Since we do not expect the q_V function to vary rapidly, the Gaussian process approach is suitable to use in this case too. We use the Gaussian process regressor available in the Python library `george`[5].

The Gaussian process regression works by using a covariance function, or kernel, to relate the function values at two points, x and $\tilde{x}$, to each other. The advantage of using Gaussian processes over a basic spline or parametric fit is that it not only allows us to consider a much wider range of possible fitting functions for q_V but it also means we can potentially inform our choice of kernel based on the underlying physical processes at work.

There has been some debate in the literature about the appropriate choice of kernel for various problems, with no clear-cut answer yet. For example, [216] found that the Matérn class of kernels, and especially the Matérn ($\nu = 9/2$) kernel was the most successful at reconstructing $w(z)$ using supernova data. The Matérn class of kernels have the following general form

$$k(x, \tilde{x}) = \sigma^2 \frac{2^{1-\nu}}{\Gamma(\nu)} \left(\frac{\sqrt{2\nu(x-\tilde{x})^2}}{\ell} \right)^{\nu} \times K_\nu \left(\frac{\sqrt{2\nu(x-\tilde{x})^2}}{\ell} \right), \quad (153)$$

where $\Gamma(\nu)$ is the gamma function, K_ν is a modified Bessel function and ν controls the shape of the covariance function, tending to the Gaussian limit as $v \to \infty$. The hyperparameters ℓ and σ correspond to the approximate length scale over which the function varies and the magnitude of these variations respectively.

5 https://github.com/dfm/george

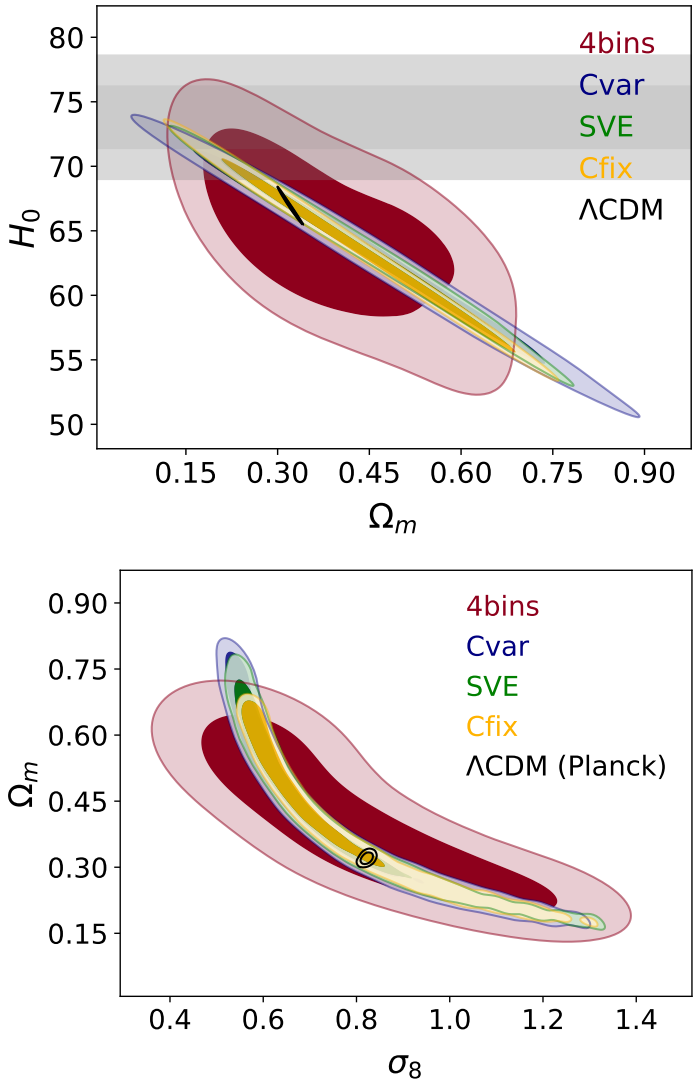

Figure 14: 68% and 95% confidence levels on the H_0 – Ω_m plane (top panel) and Ω_m – σ_8 plane (bottom panel) for the 4 cosmologies considered: *Cfix* (yellow contours), *var* (dark blue contours), *4bins* (red contours) and *SVE* (green contours), with the ΛCDM Planck alone case plotted in black. The grey bands in the top panel show the 68% and 95% confidence level on H_0 as obtained in [211]. These results are obtained with the analysis of the full Planck dataset.

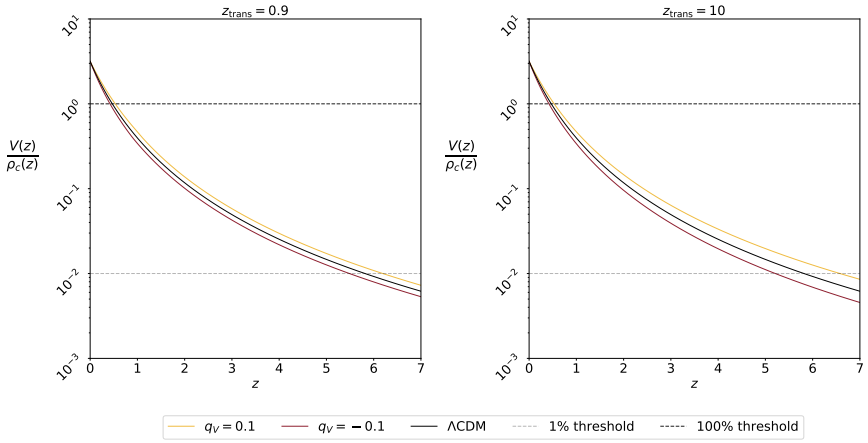

Figure 15: Ratio of the vacuum to cold dark matter energy density for a small positive and negative coupling with two different transition redshifts. The ΛCDM case is plotted in dark blue.

In the course of our analysis we investigated the results given by all the basic kernels provided by `george`, none of which resulted in a function that excludes ΛCDM at any confidence level, but as kernels can be added or multiplied in almost any combination, we did not test every possibility exhaustively. We therefore present the reconstruction given by the squared exponential kernel, the simplest of the Matérn class kernels, recovered from (153) when $\nu \to \infty$,

$$k(x, \tilde{x}) = \sigma^2 \exp\left(-\frac{(x-\tilde{x})^2}{2\ell^2}\right). \tag{154}$$

This reconstruction is shown in Figure 16. For comparison, we also show the reconstruction using the 2nd and 3rd order polynomial kernels provided by `george` in Figure 17. The data points in both cases come from the Planck + Low-z runs, in which we can clearly see the oscillatory behaviour of the coupling mentioned earlier.

The hyperparameters ℓ and σ that appear in the kernels described above can be optimised by maximising the log-likelihood of the functions they produce. However, with this optimisation implemented, our Gaussian process regressions all collapsed to be exactly equal to zero for all redshifts. This is because we have very little data with which to inform the Gaussian process and the Gaussian process always returns to its baseline of zero when it has insufficient information. We therefore conclude that the Gaussian process approach will be better suited to reconstructing a case with a greater number of redshift bins. Such a case is the focus of Chapter 4.

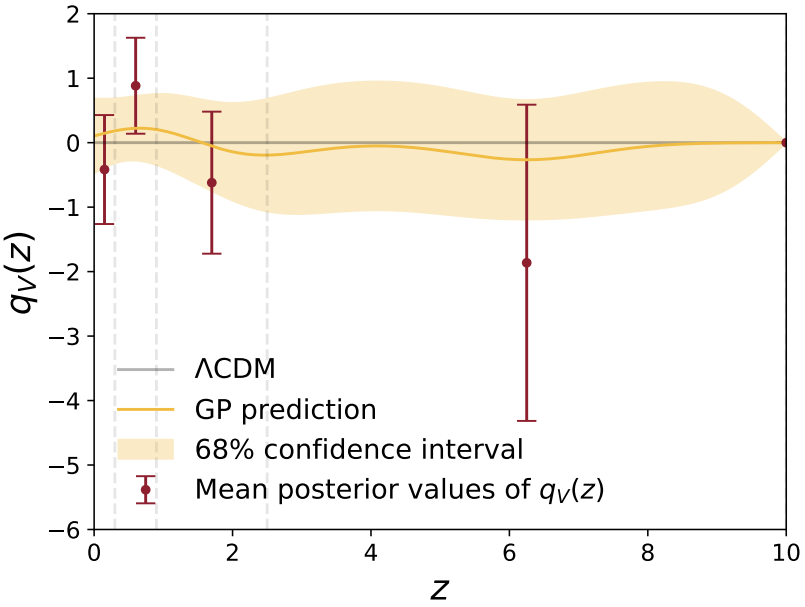

Figure 16: Gaussian process reconstruction of q_V using the squared exponential kernel, with data points as provided by the analysis of the *4bins* cosmology. The grey dashed lines indicate the boundaries of each redshift bin.

3.7 COMMENT ON OTHER RESULTS

Finally, we note that there has been an extensive treatment in the literature of a similar interacting vacuum scenario to that studied in this chapter [187, 217, 218, 219, 220], upon which we would like to comment.

Firstly, all of the aforementioned works appear to use a single bin case, akin to what we call *Cfix*, which implies the interaction parameter q_V has been constant throughout the entire cosmic history. This is sufficient for a basic analysis, but carries some important physical implications. If the interaction remains constant for the entire cosmic history (and is found to favour a decay of cold dark matter into the vacuum) it implies that eventually the energy density of cold dark matter must become negative, as we have pointed out at the end of subsection 3.3.1. While the phenomenology of such a scenario may still be interesting when studying the Universe's history, the unphysicality of the model is motivation enough to instead consider the effects of a dynamical interaction, as we have done in this chapter.

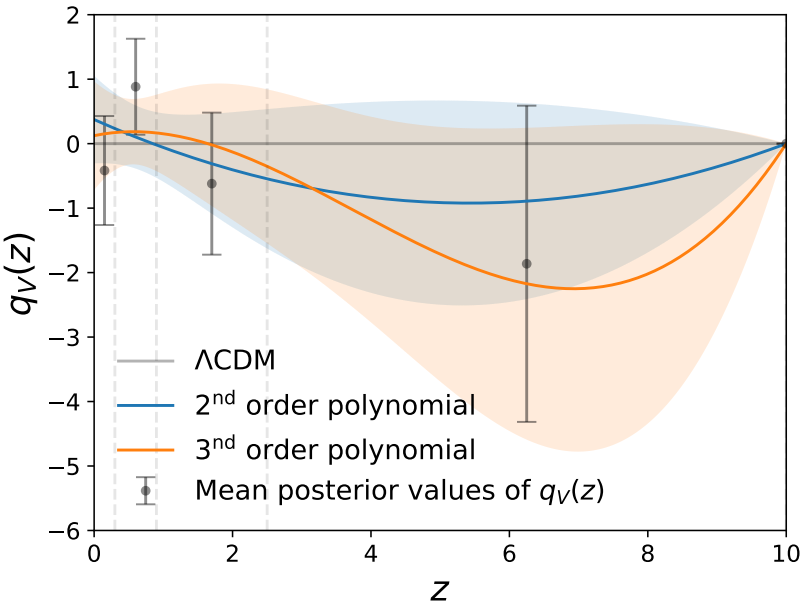

Figure 17: Gaussian process reconstruction of q_V using three different kernels, with data points as provided by the analysis of the *4bins* cosmology. The grey dashed lines indicate the boundaries of each redshift bin and the shaded regions denote the 68% confidence intervals of the Gaussian process reconstruction.

Secondly, in [219], the effect of the interaction on perturbations in the matter energy density are not clearly taken in to account. As we have shown, the interaction enters into the equation for the density contrast (132) and it is necessary to modify `CAMB` accordingly. The presence of the coupling in this equation means that the interaction will have some effect on cosmological structure growth, which is also clear from the matter power spectrum for the *Cfix* case, as shown in Figure 7. While an analysis of the background cosmology is instructive, we consider the work in this chapter to be an improvement, as we also take into account the effect of the coupling at the level of the perturbations.

Furthermore, [217] and [218] forgo a complete MCMC parameter inference with the full Planck CMB likelihood, choosing instead to use only the compressed likelihood. We believe our full analysis that takes the complete, uncompressed data into account has produced a more reliable result. However, we note that the novel use of the bispectrum as a potential tracer of the dynamics of dark energy was investigated in [218] and subsequently expanded on in [188] using the well-known XCDM, CPL and ϕCDM parameterisations (in this work the authors also used the full Planck likelihood). Such an idea was also proposed by [193], but we emphasise that the original `arXiv` version of [218] preceded [193]. It was indeed found in [188] that the bispectrum enhances the dynamical dark energy signal, so an interesting avenue of future investigation would be to use the bispectrum data when constraining the interacting vacuum scenario. A careful consideration of the effect of the interaction on the bispectrum measurements would be needed, however.

The work of [187] also examined the same interacting scenario, but in addition to varying the interaction strength along with the six standard cosmological parameters in ΛCDM, they also varied the sum of the neutrino masses, $\sum m_\nu$, and the effective number of relativistic degrees of freedom, $N_{\rm eff}$. It was found in that work that the use of the combination of Planck+BAO+JLA data (exactly equivalent to the Planck+Low-z combination used in this chapter) resulted in finding no suggestion of an interaction. However, the inclusion of galaxy cluster count data from Planck [221] and CFHTLenS [222] resulted in finding a non-zero interaction at the 99% confidence level.

In [220], the authors again tested the same interacting scenario, but with yet another combination of datasets: Planck 2015 with the KiDS weak lensing survey [223] and the 2016 Hubble Space Telescope measurement of H_0 [224]. In this work, the authors found compelling statistical evidence for an interaction and were also able to simultan-

eously relax the H_0 and σ_8 tensions. This again indicates the strong effects that different datasets can have and demonstrates the need for awareness of possible systematics when choosing and combining datasets. In particular, when using weak lensing data, it important to make a conservative cut of the non-linear scales in these datasets, unless the non-linear theory for perturbations is known.

Finally, we would like to address some differences between the results presented in this chapter and that done by [135]. In [135], it was found that a late-time interaction in a single low redshift bin of $z \leq 0.9$ was favoured over the null interaction case, with ΛCDM being excluded at 99% confidence level. As described in subsection 3.5.2, we replicated this case, *Cfix* with $z_{\text{trans}} = 0.9$, albeit using more up-to-date datasets (the Planck 2015 likelihood and newer BAO, RSD and Type Ia supernovæ data), as well as a broader prior on the parameter q_{V} that includes positive values, but found no significant deviation from ΛCDM at all.

Similarly, when replicating the four bin case, also analysed by [135], we found no significant deviation from ΛCDM at low redshift, in contrast to the 95% confidence level difference reported in that work. We can possibly attribute this to the simple lack of evidence for an interaction in the newer observational datasets used in the work presented in this chapter. Our finding that the null interaction scenario (i.e. ΛCDM) is always well within the 95% confidence region for q_{V} is in agreement with the recent work by [225].

3.8 SUMMARY

In this chapter, we have considered the possibility of an interaction in the dark sector, represented as a pure energy exchange between vacuum and cold dark matter. We have investigated constraints on this scenario, by making a simple binned parameterisation of the coupling function in redshift, using the latest cosmological datasets to place constraints on the coupling in each bin.

We investigated a number of different cases under the umbrella scenario of the interacting vacuum, namely the cases with a single bin and either a fixed or varying transition redshift (*Cfix* and *Cvar*); a case in which the vacuum energy is zero at early times, only growing after the interaction switches on, and lastly, in a model-independent way, a four bin case to replicate the work of [135].

In all the cases we studied, we found that the ΛCDM case, corresponding to no interaction in our scenario, is always well within the 95% confidence regions of our parameter estimation. At the same time the interacting scenario remains a viable alternative to ΛCDM, and only future data will be able to settle the case. We also note that our analysis is restricted to linear scales, while it is entirely possible that in extending the interacting vacuum scenario to non-linear scales more stringent constraints will be found, cf. [226]. Our findings are in contrast to a number of recent works mentioned in the previous section, but we have described the differences in our approach and contest that these are sufficient to explain the different results.

In the next chapter, we continue our analysis of the interacting vacuum scenario, increasing the number of bins used for the coupling function, thus allowing us to improve the reconstruction of the interaction as a function of redshift.

4

RECONSTRUCTING THE INTERACTION

Simplicity does not precede complexity, but follows it.

ALAN PERLIS

In this chapter, we perform a reconstruction of the coupling function between vacuum energy and geodesic cold dark matter using the latest observational data. We bin the interaction in seventeen redshift bins but use a correlation prior to prevent rapid, unphysical oscillations in the coupling function. This prior also serves to eliminate any dependence of the reconstruction on the binning method. We use two different forms of the correlation prior, finding that both give similar results for the reconstruction of the dark matter – dark energy interaction. Calculating the Bayes factor for each case, we find no meaningful evidence for deviation from the null interacting case, i.e. ΛCDM, in our reconstruction. This chapter is based on [2].

4.1 INTRODUCTION

In the previous chapter, we investigated whether a simple form of an interaction between cold dark matter and the vacuum could relieve the tensions present in ΛCDM, testing the interaction acting in a single redshift bin and reconstructing the interaction using four redshift bins. We found that, while the interacting scenario does not manage to relieve cosmological tensions, it is not ruled out by current observational data.

In this chapter, we continue that investigation by increasing the number of redshift bins used in our reconstruction, thereby increasing the redshift range that the interaction acts over and ensuring a model-independent reconstruction. We also use the up-to-date Planck 2018 likelihood [61], instead of the 2015 likelihood used in the previous chapter. We study the constraining power of a theoretical prior acting across the bins and reconstruct the final interaction function. We then perform a Principal Component Analysis and calculate the Bayesian evidence for each case studied.

Parameter	Prior
$\Omega_b h^2$	$[0.005, 0.1]$
$\Omega_c h^2$	$[0.001, 0.99]$
H_0	$[50, 100]$
$\log 10^{10} A_s$	$[2.0, 4.0]$
n_s	$[0.8, 1.2]$
q_i	$[-6.0, 3.0]$

Table 7: Prior ranges of the parameters sampled in our analysis.

4.2 METHOD

In this section, we describe the numerical codes used and the modifications made to those codes, as well as the theoretical priors and data considered in our analysis.

4.2.1 *Modifying CAMB and CosmoMC*

The first step in our analysis is to constrain the coupling strength $q(a)$ with cosmological data. To this end we make use of modified versions of the CAMB [150, 151] and CosmoMC codes [162, 163]. We bin the interaction function $q(a)$ in terms of the cosmic scale factor, with q_i being the constant parameter value within the i^{th} bin.

We choose to extend our previous four bin analysis presented in Chapter 3 to seventeen bins, with $i = 1, ..., 17$; sixteen that are uniform in scale factor from $a = 1.0$ to $a = 0.14$, plus a single large bin that extends to $a \approx 0.0001$. We use CosmoMC to produce MCMC samples from the posterior distribution of the interaction parameter in each bin, plus the baryon and cold dark matter densities $\Omega_b h^2$ and $\Omega_c h^2$, the amplitude of the primordial power spectrum and the spectral index A_s and n_s, and the value of the Hubble parameter today, H_0. We use flat priors on these parameters, with the ranges specified in Table 7.

4.2.2 *Correlation prior*

Although we have no theoretically motivated model for the behaviour of the coupling as a function of scale factor (or, equivalently, time) we

do have one theoretical prejudice: we do not expect the coupling function to oscillate rapidly, as we consider very fast changes of sign in the coupling function to be unphysical. We therefore take the step of including a theoretical prior on the coupling parameter that actively suppresses high frequency oscillations, thereby allowing the low frequency modes that are potentially present in the data to dominate.

The theoretical prior takes the form of a scale-factor-dependent correlation between the values of the coupling function in each bin. Values of the function in neighbouring bins are correlated, with the correlation growing weaker for bins of greater separation. This *correlation prior* was first proposed in [227] and the method has been subsequently used in the reconstruction of the dark energy equation of state function $w(z)$ by [228, 190, 229]. The correlation prior method was also used by [230] to reconstruct the vacuum energy–cold dark matter interaction at low redshifts only, up to $z = 1.5$.

The correlation prior has further benefits in addition to suppressing high frequency oscillations. It tends to improve the convergence speed of MCMC chains, as the correlation can help to constrain the coupling parameter in bins where the data is sparse. Reconstruction bias, i.e. the dependence of results on the binning strategy chosen is also controlled by the prior, provided that the number of bins is sufficiently large, as we will describe below.

Following [227], we assume a correlation function that describes fluctuations around some fiducial model,

$$\xi(|a - a'|) \equiv \langle [q(a) - \bar{q}(a)][q(a') - \bar{q}(a')] \rangle, \tag{155}$$

and given a functional form for ξ, the corresponding covariance matrix can be found:

$$C_{ij} = \frac{1}{\Delta^2} \int_{a_i}^{a_i+\Delta} da \int_{a_j}^{a_j+\Delta} da' \xi(|a - a'|), \tag{156}$$

where Δ is the bin width, $\bar{q}$ is the fiducial model and a is the cosmic scale factor. The fiducial model can be set to ΛCDM (i.e. $\bar{q}(a_i) = 0$), but this may introduce an unwanted bias in favour of this model into our results, so for comparison we consider a case in which the fiducial model for each bin is calculated as the mean of that bin with its two neighbouring bins. We refer to these cases as *fixed fiducial* and *mean fiducial* respectively.

We use the Crittenden–Pogosian–Zhao (CPZ) form for the correlation function, as proposed in [227],

$$\xi(|a - a'|) = \xi(0)/[1 + (|a - a'|/a_c)^2], \tag{157}$$

where a_c is the correlation length.

The CPZ form implicitly assumes independence from translations in scale factor, which is good since we do not believe *a priori* that there is a preferred epoch for variations from the fiducial model. This choice of correlation function form is further motivated by the fact that in [228], three different forms of correlation function, including the CPZ, were used to reconstruct the dark energy equation of state. It was found that when looking at the eigenvalues of the different correlation priors, the CPZ form resulted in the most constrained high frequency modes. This makes the CPZ form, the simplest of those previously studied, a good choice. We will discuss the prior eigenvalues and vectors in our case in more detail in subsection 4.3.3.

As previously stated, we want to ensure that our results are independent of the number of bins used. To ensure that we eliminate this potential reconstruction bias, we require that

$$N > N_{\text{eff}}, \tag{158}$$

where N is the number of bins, and

$$N_{\text{eff}} = (a_{\text{max}} - a_{\text{min}})/a_c. \tag{159}$$

The parameters a_{max} and a_{min} are the limits of the scale factor range used in our analysis, $a = 1.0$ and $a = 0.0001$. Following the previous results of [183, 191], we choose $a_c = 0.06$. This means that $N_{\text{eff}} = 16.7$. Therefore, to ensure that $N > N_{\text{eff}}$, we choose $N = 17$.

The strength of the prior is determined by $\xi(0)$, but following [183], we use the variance of the mean instead, defined as $\sigma_q^2 \approx \pi\xi(0)a_c/(a_{\text{max}} - a_{\text{min}})$. We set $\sigma_q = 0.6$. We found that this choice is sufficient for the prior to provide some constraining power, but not so much that it completely dominates over the constraints from data in each bin. We discuss this point further in subsection 4.3.3.

4.2.3 *Observational data*

The data used in this chapter is a combination of the Planck 2018 measurements of the CMB temperature and polarisation [61], the BAO measurements from the 6dF Galaxy Survey [96] and the combined BAO and redshift space distortion (RSD) data from the SDSS DR12 consensus release [63], together with the Pantheon Type Ia supernovæ sample [49].

We note that some works in the literature that find a resolution to the H_0 tension in an interacting dark energy scenario do so by omitting the BAO data from their analyses (see e.g. [231]). This is because, without using BAO, the high redshift constraint on H_0 becomes weaker, and a late time solution to the tension is possible. If BAO are used in combination with supernovæ catalogues then late time solutions become disfavoured, and interacting dark energy models will therefore struggle to resolve the tension (see e.g. [232, 41]). However, this reasoning does not justify the exclusion of these datasets from model constraining analysis and we therefore make a point of including multiple BAO measurements in this work.

As previously mentioned, due to the coupling between the vacuum and cold dark matter in this scenario, RSD do not directly constrain the growth factor f as they do in ΛCDM [41, 193]. Instead, the RSD constrain what we denote as the interaction growth factor, f_i,

$$f_i = f - \frac{Q}{H\rho_c}, \tag{160}$$

where f is the usual growth factor for cold dark matter,

$$f = \frac{d\ln D}{d\ln a}, \tag{161}$$

with D being the amplitude of the linear growing mode.

4.3 RESULTS AND DISCUSSION

In this section, we describe and discuss the main results of our investigation, beginning with the results of the MCMC analysis, then moving to the reconstruction of the coupling function, the Principal Component Analysis performed and finally the findings of our Bayesian evidence calculation.

4.3.1 *MCMC parameter inference*

In Figure 18 we plot the 1D marginalised posteriors for the interaction parameter q_i in each of the seventeen bins, where $i = 1$ denotes the bin starting at $z = 0$, up to $i = 17$ for the wide bin at high redshift. The posterior distributions for q_i are generally broader in the mean fiducial case compared to the fixed fiducial case. This is to be expected, as the mean fiducial case essentially has one additional free

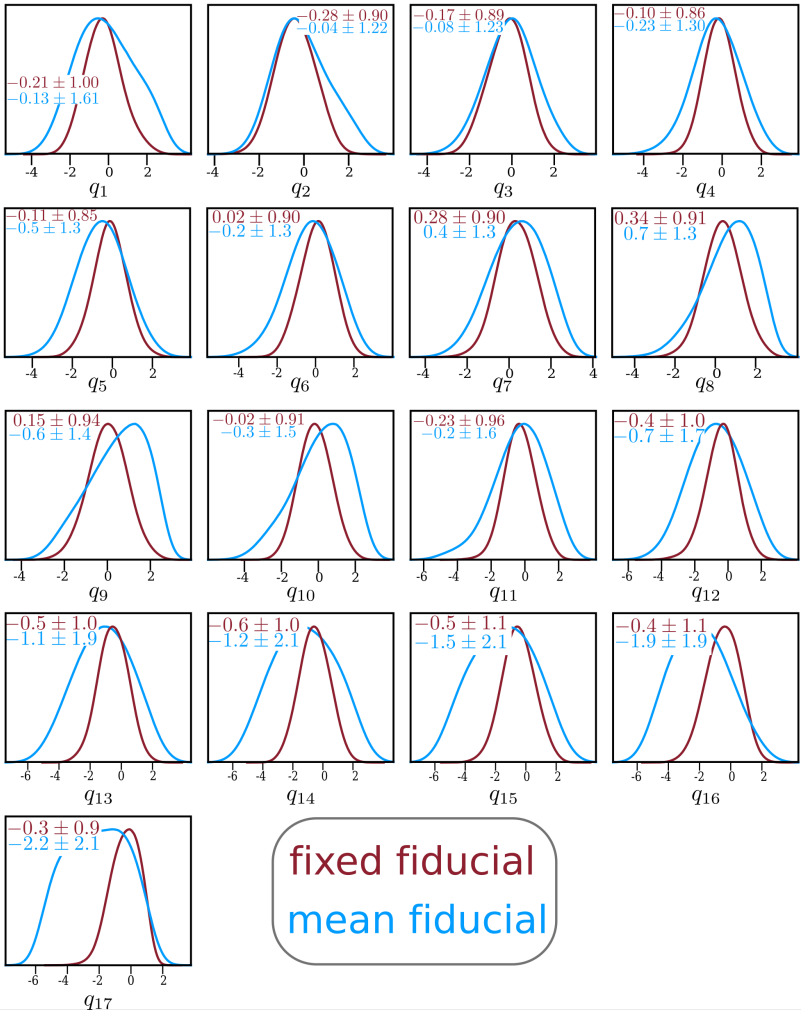

Figure 18: The 1D marginalised posteriors of the interaction parameter in each bin. In each panel we report the best fit value of the interaction parameters and their 68% confidence level bounds for the fixed fiducial (red) and mean fiducial (blue) case.

parameter with respect to the fixed fiducial, this being $\bar{q}$, the fiducial value for the correlation prior.

We find that the null interacting case ($q = 0$), coinciding with the ΛCDM limit of the model, is always within 1σ of the achieved constraints. However, the bounds found on the interaction parameter in every bin means the interacting scenario is still viable. It is clear from an Ockham's razor standpoint that the ΛCDM scenario should be favoured over both the interacting cases. We quantify this statement using the Bayes factor in subsection 4.3.4.

Table 8 shows the marginalised values of the standard cosmological parameters sampled in our MCMC analysis, while in Figure 19 we show the 2D marginalised joint distributions for the cosmological parameters H_0, Ω_m (the total matter density parameter) and σ_8. To preserve the readability of the plot, we choose to only show the results of the mean fiducial case in this figure. As can be inferred from Figure 18, the constraints on the cosmological parameters in the fixed fiducial case are almost identical to those in the mean fiducial case. In both cases we found the value of H_0 to be completely consistent with the Planck 2018 ΛCDM value of 67.4 ± 0.5 kms^{-1}Mpc^{-1}[61]. The value of σ_8 given by Planck is 0.81 ± 0.006, which is comfortably within 1σ of the values for σ_8 we find in both interacting cases.

As discussed in Chapter 1, the tensions in the values of H_0 and σ_8 are commonly used as motivations for alternative models of dark energy. However, as we also found in the previous chapter, the interacting vacuum fails to resolve the tensions when using the particular datasets chosen here. This can clearly be seen in the top panel of Figure 19, where the constraint on H_0 in the interacting scenario is shown in conjunction with both the Planck and local measurements. As we mentioned in subsection 4.2.3, for the case of the H_0 tension in particular, this is attributable to the fact that by including BAO and Type Ia supernovæ in the same analysis the tension is shifted to a discrepancy in the sound horizon scale that cannot be resolved with a late time solution [233, 234, 15].

The situation is slightly less clear with respect to the σ_8 tension. In ΛCDM, the tension appears between CMB measurements coming from Planck and large scale structure constraints on growth such as those from the Dark Energy Survey (DES) [235]. This mild tension can be seen in the bottom panel of Figure 19, with the ΛCDM constraints plotted in black, the filled contour corresponding to Planck and the open contour to DES. The DES constraint in the interacting scenario is plotted in the open blue contour – again, in the interests of legibility we only show the mean fiducial case.

Parameter	Fixed fiducial	Mean fiducial
$\Omega_b h^2$	0.022 ± 0.00015	0.022 ± 0.00013
$\Omega_c h^2$	0.11 ± 0.025	0.11 ± 0.030
$\log 10^{10} A_s$	3.05 ± 0.0058	3.05 ± 0.0064
n_s	0.97 ± 0.0040	0.97 ± 0.0048
H_0	68.22 ± 0.74	68.15 ± 0.80
σ_8	0.91 ± 0.18	0.91 ± 0.22

Table 8: Marginalised values of the cosmological parameters and their 68% confidence level bounds.

From this plot, we can see that the tension is relaxed in the interacting case, but only due to the increased size of the contours, which in turn is due to the additional free parameters in the interacting model with respect to ΛCDM. This should not be regarded as a true relaxation of the tension. Note that for the DES constraints presented here we implemented an aggressive cut of the non-linear scales in the data. Since we have no understanding of the non-linear regime in the interacting scenario we should not use this part of the data to obtain our constraints.

4.3.2 *Reconstructing the coupling function*

With the results of our MCMC analysis, we can reconstruct the coupling as a function of redshift. We show the results of using two different methods for the reconstruction: a simple cubic spline interpolation and a Gaussian process.

A Gaussian process is defined as a collection of random variables, any finite number of which have a joint Gaussian distribution [236]. It is completely specified by its mean and its covariance. In practice, the random variables represent the value of a given function $f(x)$ at a location x. There are a wide range of choices for the covariance function, or kernel, that is used to relate the function values at each point. In this work, we choose to use one of the simplest, the squared exponential kernel, given by

$$k(x, \tilde{x}) = \sigma^2 \exp\left(-\frac{(x-\tilde{x})^2}{2\ell^2}\right). \tag{162}$$

The hyperparameters ℓ and σ that appear in this kernel correspond to the approximate length scale over which the function varies, and the

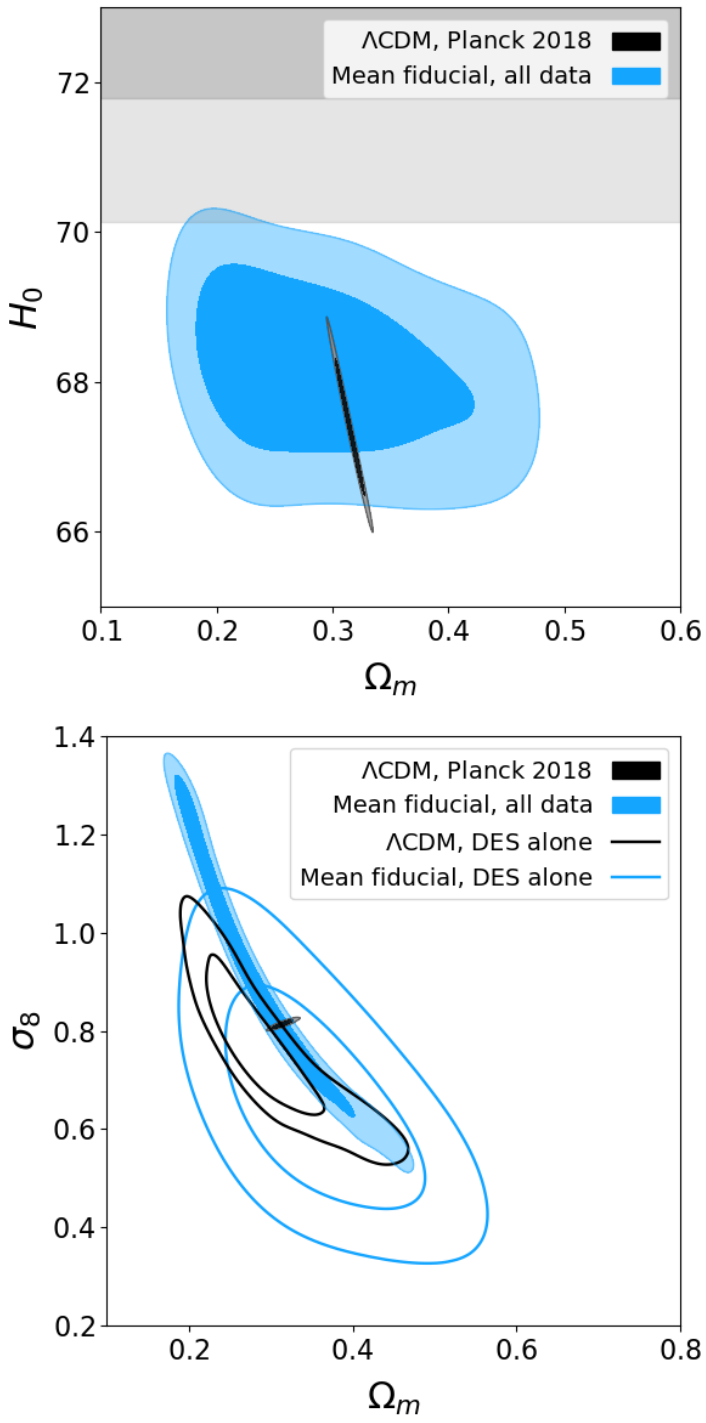

Figure 19: 68% and 95% confidence levels in the $H_0 - \Omega_m$ plane (top panel) and $\Omega_m - \sigma_8$ plane (bottom panel) for the mean fiducial case. The grey bands in the top panel denote the 68% and 95% confidence levels of the Riess et al. local measurement of $H_0 = 73.45 \pm 1.66$ $\mathrm{kms}^{-1}\mathrm{Mpc}^{-1}$ [211].

variance of the function at each point respectively. We optimise these by maximising the log-likelihood of the functions they produce.

In summary, the Gaussian process takes some given training data and constructs the best possible function that describes that data, given the kernel imposed. The training data passed to the Gaussian process in our case are the mean posterior values of the coupling parameter in each bin along with the corresponding 1σ errors given by our MCMC analysis, thereby allowing us to reconstruct the coupling function $q(z)$.

There are many packages and codes available to perform Gaussian process regression. In this work, we use the Gaussian process regressor available in the Python library `george`[1] [237].

The results of our reconstructions for the cubic spline and the Gaussian process are shown in Figure 20 and Figure 21 respectively. It is clear to see that the Gaussian process results in a smoother $q(z)$ function, but that the high redshift part of the reconstruction is biased towards the ΛCDM value of $q = 0$, due to the baseline that the Gaussian process is fixed to return to in the absence of information.

This is particularly obvious in the mean fiducial case, where the values of q themselves are very negative but the combination of the Gaussian process baseline and the large 1σ errors on q result in the reconstruction returning to zero. This is a problem that the cubic spline does not suffer from, hence the indication of a trend away from ΛCDM at high redshift in the mean fiducial case.

The most interesting features of the reconstruction are the points where $q(z)$ appears to peak or trough, for example, the peak at around $z = 1$, which is clear in both the spline and Gaussian process, or the trough at around $z = 3$, more obvious in the Gaussian process reconstruction. A promising line of enquiry would be to focus on the behaviour of the interaction at these points by using additional datasets in the analysis, but as $z = 3$ is beyond the upper limit of the commonly used low-redshift probes, such as Type Ia supernovæ, exploring the interaction in detail at this epoch may be more difficult.

A potential future constraint may come from the weak lensing of the Lyman-α forest in the spectra of high-redshift quasars, which probes the matter distribution at redshifts of 2 to 3.5 [238]. Furthermore, the Square Kilometre Array is predicted to be able to probe redshifts of between 3 and 25 using 21cm intensity mapping [239, 240]. Both of these new techniques could therefore be used to constrain any inter-

1 https://github.com/dfm/george

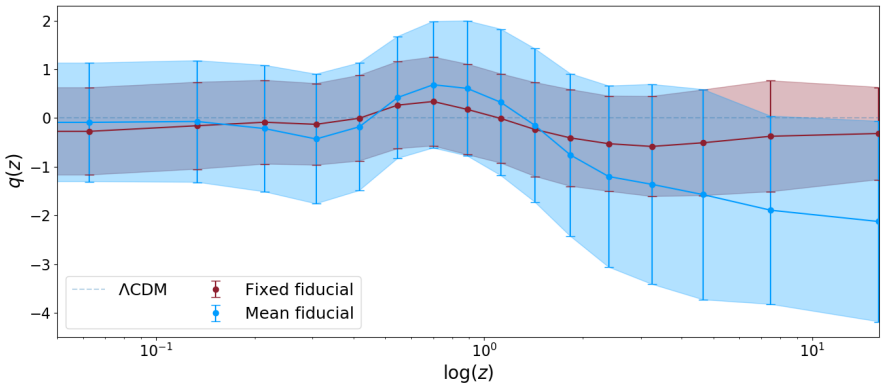

Figure 20: The results of the cubic spline reconstruction of the coupling function $q(z)$. Red and blue lines and areas refer to the fixed fiducial and mean fiducial cases respectively, and the shaded areas denote the 1σ confidence interval.

acting dark energy model which affects large scale structure growth or has other high redshift effects.

4.3.3 *Principal component analysis*

In this chapter, we have aimed to be agnostic when it comes to the reconstruction of the interaction function and so used a larger number of bins than in Chapter 3, i.e. the minimum number to satisfy the criterion given by equation (158). However, it is also possible to investigate how many modes in the result are informed by the observational data used and whether any are informed by the prior alone, and thus understand how many effective additional degrees of freedom our reconstruction has [241]. To do this, we perform a principal component analysis.

Principal component analysis can be thought of as finding the directions in the data that carry the most information. It also acts to decorrelate the errors on the interaction parameter in each bin. In practice, this involves computing the eigenvalues and eigenvectors of the inverse covariance matrix, or information matrix, of the data. In our case, the covariance matrix is one of the products obtained after running `GetDist`[2] [242] on our MCMC chains. We perform the principal component analysis on the information matrix for the q_i alone, after marginalising over the other cosmological and nuisance parameters.

2 https://github.com/cmbant/getdist

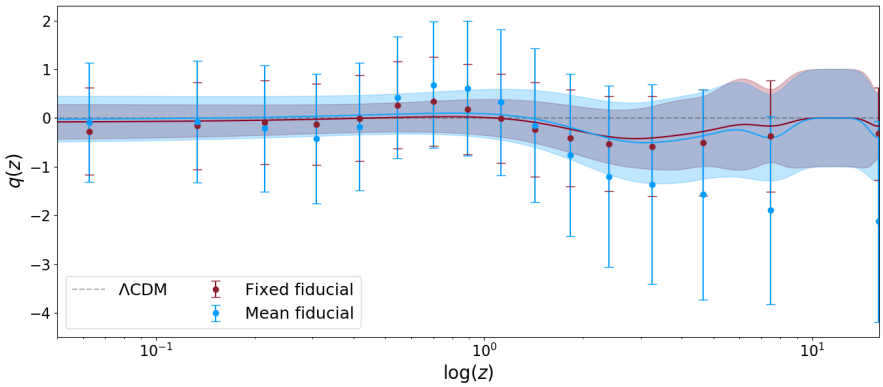

Figure 21: The results of the Gaussian process reconstruction of the coupling function $q(z)$. Red and blue lines and areas refer to the fixed fiducial and mean fiducial cases respectively, and the shaded areas denote the 1σ confidence interval.

The information matrix is given by

$$F = W^T \Lambda W, \tag{163}$$

where W is the decorrelation matrix and its rows define the eigenvectors; Λ is a diagonal matrix whose elements are the eigenvalues λ_i. The eigenvalues correspond to the amount of variance carried in each principal component and therefore determine how well q_i can be measured, i.e. $\sigma(q_i) = \lambda_i^{-1/2}$.

After finding the eigenvalues and eigenvectors of the covariance matrix, the eigenvectors are sorted according to decreasing value of their corresponding eigenvalues. The first eigenvector after this sort is performed corresponds to the first principal component, the second eigenvector corresponds to the second principal component and so on, until the N^{th} eigenvector for the N^{th} principal component is found (where the covariance matrix is $N \times N$).

We show the results of our principal component analysis in Figure 22 and Figure 23. From these plots we can see that in the fixed fiducial case around 15% of the total variance is in the first principal component, we reach around 50% with four principal components and 90% with 10. These results indicate that it would be unwise to reduce the effective degrees of freedom by discarding some of the principal components, as even the higher components contain a significant amount of information (above PC10 the remaining seven components together still contain approximately 11% of the variance). This is less true in the case of the mean fiducial, in which around 25% of the total variance is contained in the first principal component, rising

to nearly 50% with just two principal components and reaching 90% with seven. The final four principal components together contain just 1% of the variance.

To investigate whether the correlation prior dominates over the data, we also ran an MCMC chain without any data, using the prior alone to constrain the interaction. This prior alone case used $\bar{q} = 0$, as in the case of the fixed fiducial. We plot the eigenvalues of the fixed fiducial case and the prior alone case as a function of principal component number in Figure 24. This plot shows that the data permeates all the modes, meaning that the prior does not completely dominate over the data at any point and thus the selected prior strength was indeed sufficient to help constrain the interaction without washing out the information coming from the data. Note that we only show the result for the case of the fixed fiducial prior alone and the fixed fiducial prior plus data, as the result for the mean fiducial is extremely similar.

If we had found that the data dominated for say, the first three principal components and then the prior dominated over the rest, we would be able to conclude that our analysis effectively only had an additional three degrees of freedom compared to the ΛCDM case. However, this does not equate to doing an analysis using only three bins, as the principal components do not correspond to the bins themselves, but to the eigenvectors of the covariance matrix of the interaction parameter in each bin. We therefore conclude that the best strategy for an analysis such as this is to use as many bins as is computationally feasible, with the correlation prior being used to help constrain bins where data is scarce. The alternative is to increase the strength of the correlation prior, but this comes with its own pitfalls, as if the prior is too strong, it will completely wash out any contribution from the data. A balance can be achieved, but to ensure that the reconstruction remains independent of the number of bins used, the correlation length and therefore the prior strength should be determined by following equations (158) and (159).

4.3.4 *Bayesian evidence and* χ^2

Finally, we want to compare the results for each case in a Bayesian way, which, as we explained in Chapter 2 means making use of Bayes' theorem [160]:

$$P(\theta|D, M) = \frac{P(D|\theta, M)P(\theta|M)}{P(D|M)}, \tag{164}$$

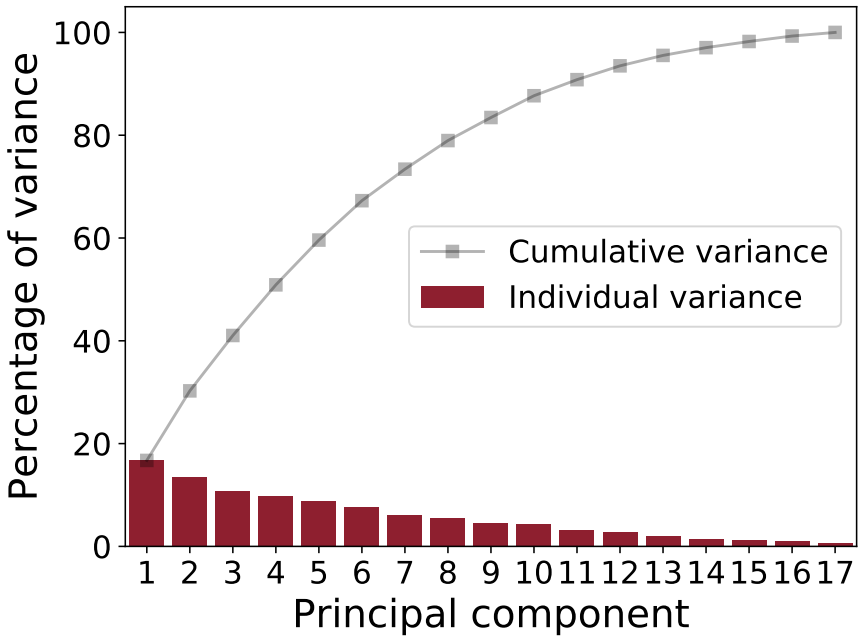

Figure 22: Percentage variance explained by each principal component in the fixed fiducial case.

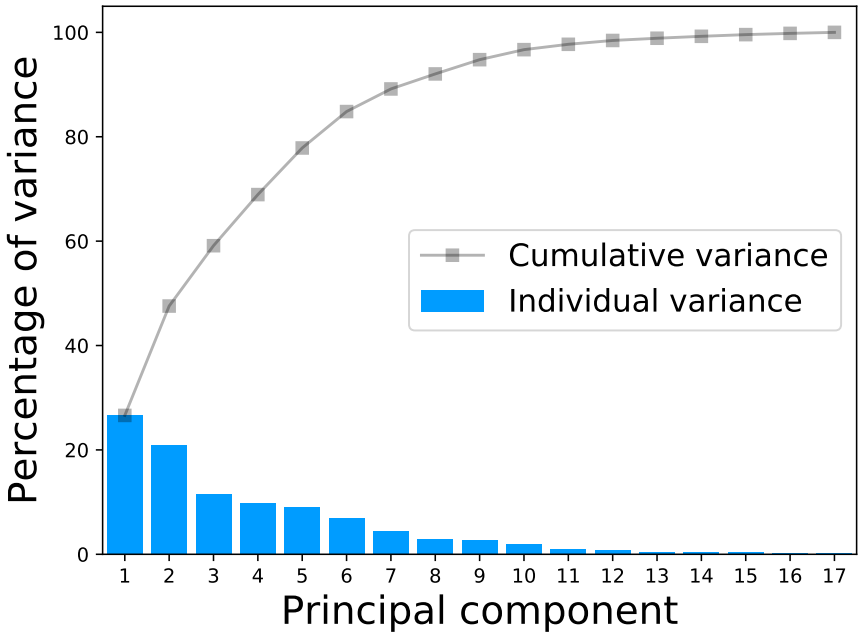

Figure 23: Percentage variance explained by each principal component in the mean fiducial case.

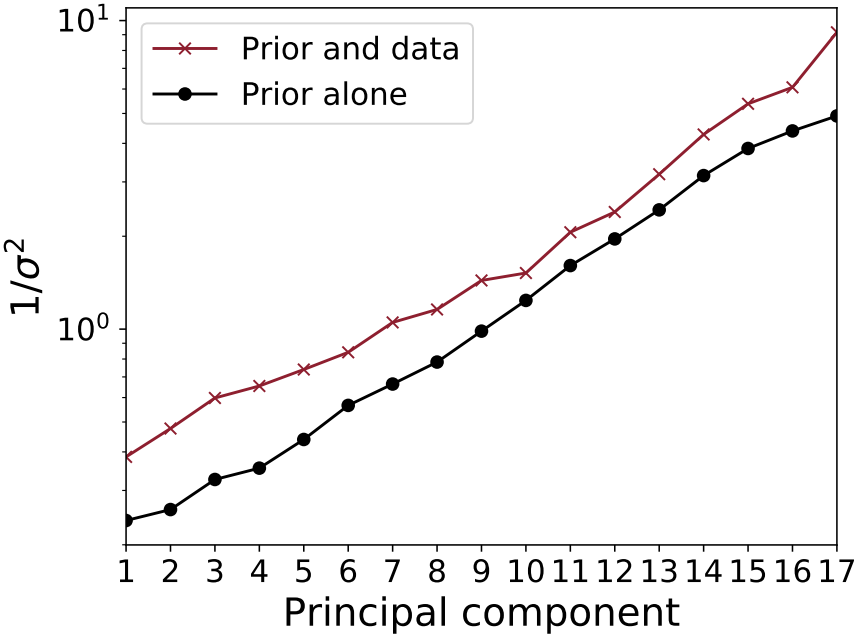

Figure 24: Showing that the data permeates all the modes.

where θ is the parameter vector, D is the data vector and M is the model. The numerator contains the likelihood and the prior, and the denominator is the evidence (sometimes known as the marginal likelihood). These combine to form the posterior probability distribution $P(\theta|D, M)$, which is the distribution sampled in our MCMC analysis.

As noted by [243] and discussed in Chapter 2, the use of model selection criteria such as the Bayesian Information Criterion (BIC), Akaike Information Criterion (AIC) and Deviance Information Criterion (DIC) are not strictly Bayesian as they do not take into account the prior information. We therefore use the Bayes factor as our model comparison tool, defined in the following way:

$$\log B_{12} = \log \left[\frac{P(D|M_1)}{P(D|M_2)} \right], \tag{165}$$

$$= \log[P(D|M_1)] - \log[P(D|M_2)], \tag{166}$$

where D is the data vector, M_1 and M_2 are the models to be compared, and $P(D|M)$ is the Bayesian evidence, the normalising factor in Bayes' theorem.

We calculate the Bayesian evidence from our MCMC chains for both of the two correlation prior cases studied to determine the support for each case over ΛCDM. This analysis was performed using the

Case	Bayes factor ($\log B_{12}$)	$\Delta\chi^2$
Fixed fiducial	1.64	-2.5
Mean fiducial	-0.52	-2.2

Table 9: The Bayes factor and $\Delta\chi^2$ for each case.

Bayes factor	Interpretation
$\lvert\log B_{12}\rvert < 1$	Not worth more than a bare mention
$1 < \lvert\log B_{12}\rvert < 2.5$	Weak
$2.5 < \lvert\log B_{12}\rvert < 5$	Significant
$5 < \lvert\log B_{12}\rvert$	Strong

Table 10: The Jeffreys scale, originally given in [177] and modified in [158].

`MCEvidence` code as presented in [176]. In each case, we use ΛCDM as model 1. We summarise our findings in Table 9.

To interpret these values, we make use of the Jeffreys scale, as shown in Table 10, which we also previously mentioned in Chapter 2. As pointed out in [158], the qualitative interpretations originally given by Jeffreys [177] are quite strong in the context of cosmology, where choosing suitable priors can often be an uncertain process. We therefore adopt the interpretations given in [158].

We find that the Bayes factor for the fixed fiducial case is 1.64. According to the Jeffreys scale, this reflects a weak preference for ΛCDM over the interacting case. The Bayes factor for the mean fiducial case is -0.52. In our evidence calculation, negative values indicate that model 2 is preferred over model 1, where model 1 is always ΛCDM. This result is therefore a slight indication for the mean fiducial case being favoured over ΛCDM. However, according to the Jeffreys scale, the very small absolute value of the Bayes factor means this is not worth more than a bare mention.

The fact that we find stronger evidence in favour of ΛCDM in the case where the fiducial is fixed as $q = 0$ could point to a slight bias in the results caused by the choice of fiducial model. However, the evidence in favour of the interaction when the fiducial is calculated as the mean of neighbouring bins is sufficiently small for us to confidently say that the choice of fiducial model does not drastically alter the result of a reconstruction.

However, it has been argued that the Bayesian evidence is not a good model comparison tool when there is uncertainty in the choice of pri-

ors [244]. We therefore also compute the $\Delta\chi^2$ for each case, removing the contribution of the priors to the χ^2 so that the values we compare come from the data only. We find $\Delta\chi^2 = -2.5$ in the fixed fiducial case and $\Delta\chi^2 = -2.2$ in the mean fiducial case, neither of which represents a significant improvement in fit over ΛCDM.

In summary, it is clear that we cannot conclusively state that ΛCDM is preferred over the interacting case, but the hints given by the evidence indicate that an interesting future direction would be to repeat this type of analysis with the newest datasets as they are released, to see if there is any strengthening in the evidence for or against ΛCDM. It is also worthwhile studying what possible improvements on current constraints can be made by future surveys.

4.4 SUMMARY

In this chapter we have reconstructed a dark matter – vacuum energy interaction, using a correlation prior to control the reconstruction bias. We implemented two different versions of the prior: a fiducial value for the prior that is fixed in each bin and a fiducial value that is computed as the mean of the neighbouring bins.

In our model comparison, we found evidence in favour of ΛCDM over the fixed fiducial model, but the Bayes factor in that case was small enough to classify the evidence on the Jeffreys scale as weak. In contrast, we found evidence for an interaction when comparing the ΛCDM case to the mean fiducial case, but the Jeffreys scale in that case classified the evidence as not worth more than a bare mention.

From our work, it is clear that a correlation prior, when effectively tuned so as not to drown out the constraining power of the data, can improve the convergence speed of high-dimensionality MCMC sampling. The prior also eliminates any potential reconstruction bias, making it a good choice for any form of reconstructive analysis.

In the next chapter, we conclude our analysis of interacting dark energy models with a study of a particular model which is constructed to mimic a fluid model of dark energy that obeys a Shan–Chen equation of state.

5

SHAN–CHEN DARK ENERGY

We have so much time and so little to see.
Wait a minute. Strike that. Reverse it.
GENE WILDER

In this chapter, we present the first observational constraints placed on the Shan–Chen dark energy model, cast as an interaction between the vacuum and cold dark matter. The Shan–Chen dark energy model is a fluid model of dark energy that behaves according to the Shan–Chen equation of state.

We firstly discuss the theory of the fluid model before incorporating it into our interacting vacuum scenario. We then use `CAMB` and `CosmoMC` to place constraints on the interacting vacuum Shan–Chen model and the cosmological parameters using observational data. We find weak evidence that this model is favoured over ΛCDM, but that the cosmological tensions previously discussed are still present in this model.

5.1 INTRODUCTION

As we have already seen, the validity of the cosmological constant's use as the dark energy has long been questioned, and many alternatives have been proposed. In the previous chapter, we aimed at reconstructing the coupling between the vacuum and cold dark matter in our familiar geodesic interacting vacuum scenario, employing a correlation prior to ensure that the reconstruction remained independent of the number of bins used.

This model-independent, "hands-off" approach can be taken one step further. Mathematicians and physicists alike have long been drawn to simple, minimalistic theories, motivated by the idea of mathematical beauty[1]. More formally, this can be seen as a facet of Ockham's razor, which, as we described in Chapter 2, urges us to select the simplest possible explanation of our observations. Finding a model of dark

1 This is particularly evident in the works of Dirac, to note one influential example [245].

energy which arises naturally from pre-existing physics is one way to satisfy this predisposition for elegant and simple models.

A promising approach along these lines is to consider dark energy and dark matter as a single cosmological fluid, which behaves according to some equation of state. This type of model has a long history, dating back to the introduction of the Chaplygin gas model in 2001 [246], in which the transition from cold dark matter to dark energy domination is achieved using a perfect fluid with a non-standard equation of state,

$$P = -\frac{A}{\rho}, \tag{167}$$

where, as in the standard equation of state we discussed in Chapter 1, P is the pressure of the fluid, ρ is the energy density and A is a positive constant. From the continuity equation, (5), this equation of state yields

$$\rho = \sqrt{A + \frac{B}{a^6}}, \tag{168}$$

where a is the cosmic scale factor and B is an integration constant. When B is positive and a is small (i.e. early times), this equation of state behaves like pressureless matter,

$$\rho \sim \frac{\sqrt{B}}{a^3}, \tag{169}$$

whereas when a is large,

$$\rho \sim \sqrt{A}, \tag{170}$$

it is akin to late time domination of a cosmological constant, here represented by $\sqrt{A}$.

The Chaplygin gas model was subsequently expanded in the *generalised* Chaplygin gas model [247], where the equation of state (167) was modified to

$$P = -\frac{A}{\rho^\alpha}, \tag{171}$$

where $0 < \alpha \leq 1$ allows the fluid described by (171) to interpolate between pressureless dust and a cosmological constant, as in the original Chaplygin gas model, but also allows for an intermediate stage of "soft" matter[2], described by

$$P = \alpha\rho. \tag{172}$$

2 The word "soft" here refers to the behaviour of the equation of state. Broadly speaking, a "stiff" or "hard" equation of state is one in which the pressure increases rapidly for a given density, e.g. for an equation of state given by $P \propto \rho^\alpha$, α is large. Conversely, a "soft" equation of state describes easily compressible matter, in which the pressure does not greatly increase with density (in this example, α is small).

This situation results in a density contrast that is more similar to the ΛCDM case than the original Chaplygin gas model where $\alpha = 1$ [247, 248]. Further constraints were placed on this model using the CMB [249] and Type Ia supernovæ [250, 251].

However, serious objections to the generalised Chaplygin gas model were raised when it was found that unified models[3] of this type result in oscillations or an exponential blow-up in the matter power spectrum, thus ruling out the vast majority of the viable Chaplygin gas model space [252].

To counter this, further models in which dark matter transitions to dark energy via a condensation mechanism have been proposed and studied [253, 254]. Interest in unified models as a possible solution to various problems in cosmology, such as the H_0 and σ_8 tensions and the coincidence problem, remains high – see, for example, [201, 255, 256, 202, 257, 258, 259, 260].

In this chapter, we consider a cosmological fluid with a Shan–Chen equation of state, albeit as a pure dark energy rather than a unified dark energy–dark matter fluid. This equation of state was first proposed by Shan and Chen in the context of lattice kinetic theory [261]. A fluid with this equation of state behaves as an ideal gas in the low and high density regimes, but has a liquid–gas coexistence curve (i.e. a region of temperature and pressure in which the fluid can be in both the liquid and gas state). Such an equation of state means that a phase transition can easily arise. Casting this into the language of cosmology, this means that the fluid can naturally model the evolution of the dark energy fluid, and the transition from matter to dark energy domination, without the need for a cosmological constant.

This model was successfully applied to the cosmological context in [262], with the result that a dark energy fluid with a Shan–Chen equation of state naturally evolves towards a Universe with a late time accelerating expansion without the presence of a cosmological constant. In that work, modifications made to the background by the Shan–Chen model were considered, and quantities such as the distance modulus in the Shan–Chen model were compared to Type Ia supernova data.

In this chapter, we build on the work presented in [262] and [263]. We firstly discuss various aspects of the behaviour of the Shan–Chen

3 Note that these so-called unified models are distinct from interacting dark energy models. Unified models seek to replicate the behaviour of both dark matter and dark energy using a single entity or fluid, whereas interacting models consider dark energy and dark matter to be separate but coupled components.

dark energy fluid model, before proceeding to our main analysis of the Shan–Chen model recast as a coupling between the vacuum and cold dark matter, in keeping with the models we have already studied in Chapters 3 and 4.

We implement both the background and the linear perturbations in this model in `CAMB` and `CosmoMC` and obtain constraints on the cosmological parameters in the Shan–Chen model using a full combination of cosmic microwave background, baryon acoustic oscillation and Type Ia supernova data before performing a model comparison and demonstrating the potential (albeit unfulfilled) that this type of model has to relax the H_0 tension.

5.2 THEORY

In this section, we give details on both the Shan–Chen model in the context of a dark energy fluid, and then in the context of our more familiar interacting vacuum scenario.

5.2.1 *The Shan–Chen dark energy fluid*

In the Shan–Chen model of dark energy introduced by [262], the matter–energy content of the Universe is assumed to be a perfect fluid which obeys a Shan–Chen equation of state [261],

$$P = w\rho_{\mathrm{crit},0}\left[\frac{\rho}{\rho_{\mathrm{crit},0}} + \frac{g}{2}\psi^2\right], \tag{173}$$

where

$$\psi = 1 - e^{-\alpha\frac{\rho}{\rho_{\mathrm{crit},0}}}, \tag{174}$$

and $\rho_{\mathrm{crit},0} = \frac{3H_0^2}{8\pi}$ is the critical density at redshift zero (H_0 being the value of the Hubble parameter at that redshift) and w, g and α are free (dimensionless) parameters of the model.

To better understand the qualitative behaviour of this equation of state, we can obtain a dimensionless effective equation of state from (173),

$$w_{\mathrm{eff}} = \frac{P}{\rho} = w + \frac{wg}{2}\frac{\rho_{\mathrm{crit},0}}{\rho}\left(1 - e^{-\alpha\frac{\rho}{\rho_{\mathrm{crit},0}}}\right)^2, \tag{175}$$

and, defining $x = \frac{\rho}{\rho_{\text{crit},0}}$, write

$$w_{\text{eff}} = w + \frac{wg}{2x}\left(1 - e^{-\alpha x}\right)^2 . \tag{176}$$

In Figures 25, 26 and 27, we plot the behaviour of the effective equation of state (176) for various different values of w, g and α respectively[4], keeping the other parameters fixed to the values quoted as best fits in [262]: $g = -8.0$, $\alpha = 2.7$ and $w = 1/3$. The orange curve in Figure 25 therefore represents the main case studied in [262].

In general, we can see from these figures that the choice of parameters in the Shan–Chen fluid model has a large effect on whether the resulting equation of state has an accelerating regime. In each figure, the point at which acceleration begins, $w_{\text{eff}} < -1/3$, is indicated by a dashed grey line.

In Figure 25, we can see that a negative w is never accelerating when $g < 0$, so this case is unsuitable for use as a dark energy model. When $w > 0$, we have a transition from the high energy regime at early times, i.e. $x > 1$, in which w_{eff} behaves as a constant, to the low energy regime at late times, i.e. $x < 1$. Depending on the value of w, the transition can cross into the phantom regime, i.e. $w_{\text{eff}} < -1$, indicated on the plot by a dot-dashed grey line.

Similarly, in Figure 26, we can see that the parameter g needs to be negative (in conjunction with a positive w) and at least $g = -3.0$ to reach the accelerating regime. Finally, in Figure 27, we can see that the best fit value of α found by [262], $\alpha = -2.7$, reaches the accelerating regime and very briefly crosses into the phantom regime (again, in conjunction with a positive w).

We conclude our discussion of the Shan–Chen dark energy fluid here. It is clear that this model provides many interesting possibilities for future study, but for the rest of this chapter we will analyse the Shan–Chen model in the context of the interacting vacuum, in alignment with the other studies of interacting dark energy presented in this thesis.

5.2.2 *The Shan–Chen interacting vacuum*

We now recast the Shan–Chen model as a parameterisation of the coupling Q between the vacuum and cold dark matter, thus intro-

4 The Python script used to create these plots was based on code provided by [264].

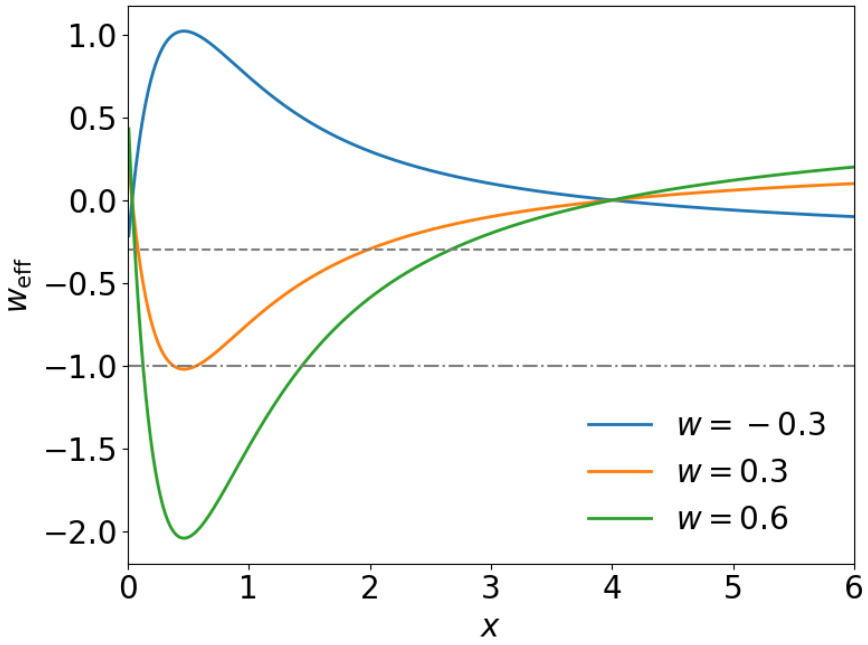

Figure 25: The behaviour of the effective equation of state for different values of w; in blue, $w = -0.3$, in orange, $w = 0.3$ and in green, $w = 0.6$. The other parameters are fixed to $g = -8.0$ and $\alpha = 2.7$. The dashed grey line indicates the transition to acceleration ($w_{\text{eff}} < -1/3$), while the dot-dashed grey line indicates the transition to the phantom regime ($w_{\text{eff}} < -1$).

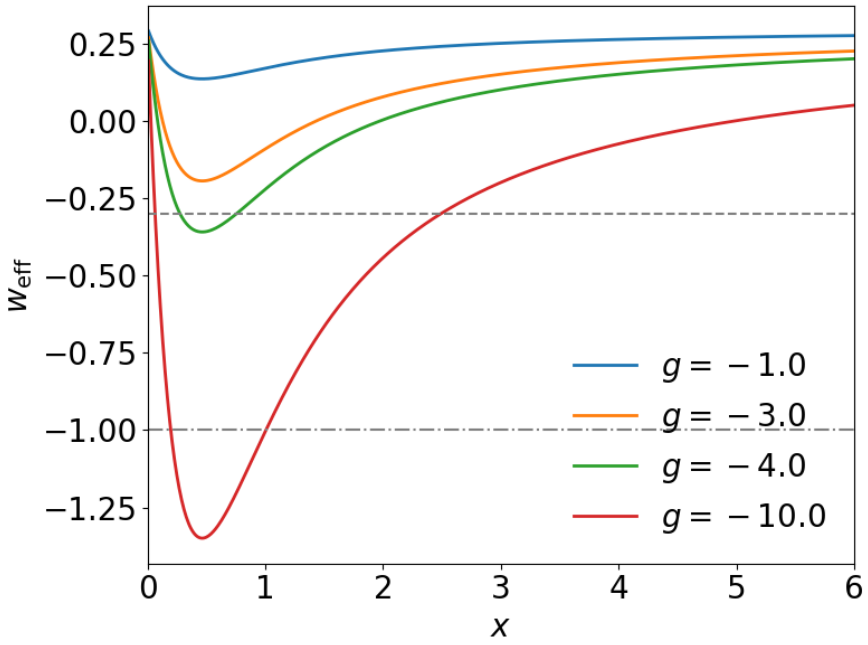

Figure 26: The behaviour of the effective equation of state for different values of g; in blue, $g = -1.0$, in orange, $g = -3.0$, in green, $g = -4.0$ and in red, $g = -10.0$. The other parameters are fixed to $\alpha = 2.7$ and $w = 1/3$. The dashed grey line indicates the transition to acceleration ($w_{\text{eff}} < -1/3$), while the dot-dashed grey line indicates the transition to the phantom regime ($w_{\text{eff}} < -1$).

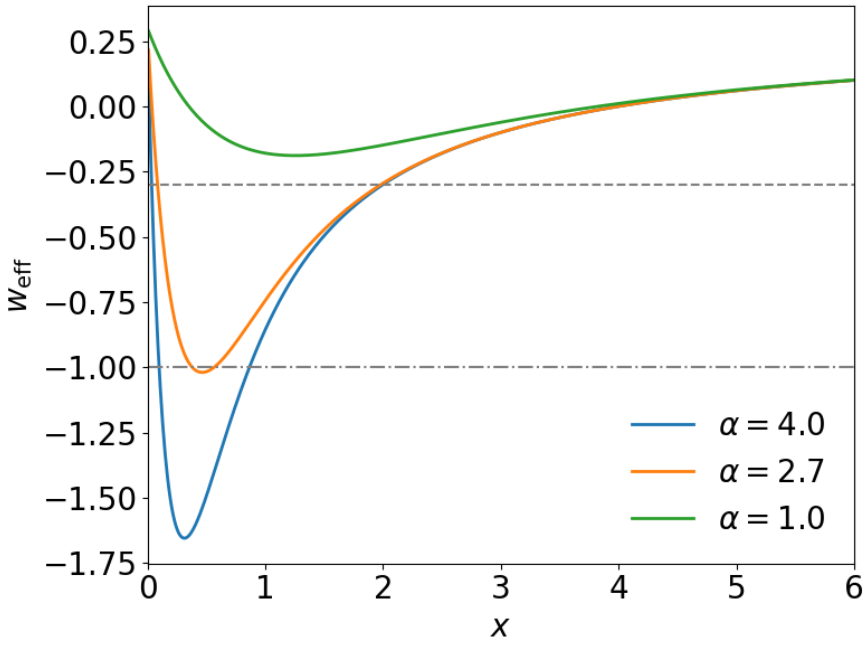

Figure 27: The behaviour of the effective equation of state for different values of α; in blue, $\alpha = 4.0$, in orange, $\alpha = 2.7$ and in green, $\alpha = 1.0$. The other parameters are fixed to $g = -8.0$ and $w = 1/3$. The dashed grey line indicates the transition to acceleration ($w_{\text{eff}} < -1/3$), while the dot-dashed grey line indicates the transition to the phantom regime ($w_{\text{eff}} < -1$).

ducing the Shan–Chen interacting vacuum model. We can write the equation of state a little more generally as

$$P = w\rho + \frac{wg}{2}\rho_* \left(1 - e^{-\alpha \frac{\rho}{\rho_*}}\right)^2, \tag{177}$$

where ρ_* is characteristic energy density scale. We will discuss choices for this scale below.

We maintain the same covariant theory for the general interacting vacuum model as previously described in Chapter 3, recalling that in a spatially flat Friedmann–Lemaître–Robertson–Walker (FLRW) background, the conservation of energy is given by

$$\dot{\rho} = -3H(\rho + P) \tag{178}$$

and we can substitute P from (177), and use our interacting vacuum notation in which $V \equiv \rho$ to find

$$\dot{V} = Q = -3Hq \left[(1+\beta)V + \frac{\beta g}{2}\rho_* \left(1 - e^{-\alpha \frac{V}{\rho_*}}\right)^2\right], \tag{179}$$

where we have also introduced the dimensionless parameter q which controls the overall strength of the interaction.

To avoid confusion, we have also renamed the parameter w as β, as we are now considering an interacting model rather than a dark energy fluid with a specific equation of state. We therefore remove the traditional equation of state parameter w from our notation and treat (179) as a coupling between the vacuum and cold dark matter.

However, as in the case of the Shan–Chen fluid, we can formally define an effective equation of state for the interacting case, so that we may better understand the behaviour of the vacuum energy density V with this interaction,

$$w_{\text{int}} = q(1+\beta) + \frac{q\beta g}{2x}\left(1 - e^{-\alpha x}\right)^2 - 1. \tag{180}$$

In Figure 28, we show the behaviour of (180) for two example values of the interaction strength q, keeping the values of the other parameters fixed to the best fit values shown in [262]. From this plot, we can see how the sign of q can affect whether the effective equation of state approaches the phantom limit from above or below. It is also clear that w_{int} is around -1 today, meaning that the vacuum energy density V is approximately constant. It is important to note here that this plot is obtained directly from the dimensionless effective equation of state (180) in order to show the general qualitative behaviour of the model. The full model, including the effects of the perturbations, are not taken into account in this plot.

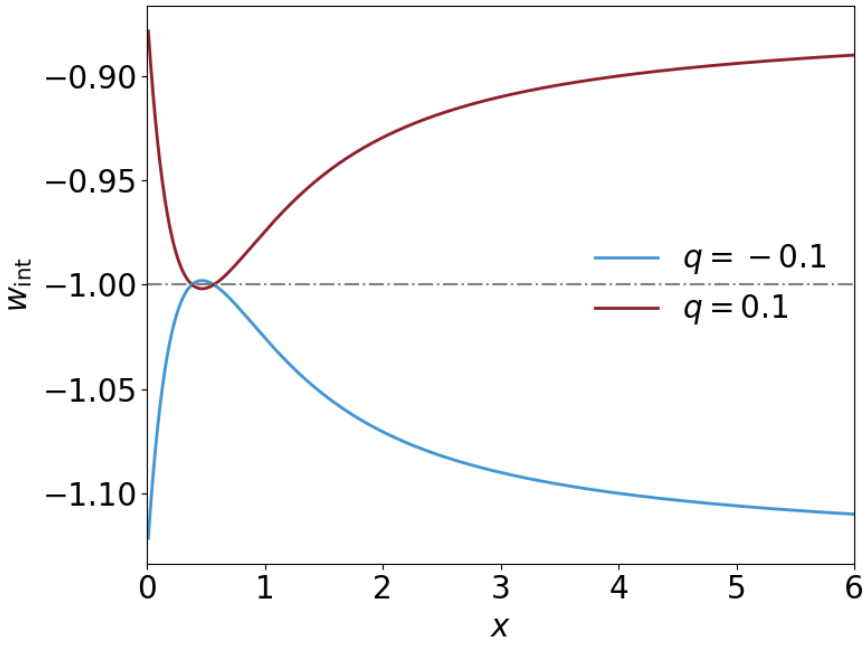

Figure 28: The behaviour of the effective equation of state for the interacting case for two different values of q; in blue, $q = -0.1$ and in red, $q = 0.1$. The dot-dashed grey line indicates the transition to the phantom regime ($w_{\rm int} < -1$).

5.2.3 *Choice of parameters*

We have a number of additional free parameters in the Shan–Chen interacting vacuum model with respect to ΛCDM: q, α, g, β and ρ_*. In order to simplify our analysis, we fix the values of some of these parameters. Specifically, we fix the characteristic energy scale to the value of the critical density today, i.e. $\rho_* = \rho_{\rm crit,0}$, as we are interested in the effect that the interaction may have at late times. Another choice for this energy scale could be, for example, the value of the matter density at matter–radiation equality, as this could result in an early dark energy-type behaviour (see [127] for an example of a successful early dark energy model).

We fix the saturation scale equal to one, i.e. $\alpha = 1$. In the course of our analysis, we explored some other choices for α but found that they had a negligible effect on the resulting constraints from data. For the same reason, we fix $g = -8.0$, as this was the best fit value found by [262].

This leaves us with β and the overall strength of the coupling, q. In the case of β, we firstly explore fixing it to a specific value, 0.3, before

sampling it as a free parameter. We do the same with q, fixing it to 0.1 and -0.1 before sampling over it. Overall, this means the final form of the interaction that we consider is given by

$$Q = -3Hq\left[(1+\beta)V - 4\beta\rho_{\text{crit},0}\left(1 - e^{-\frac{V}{\rho_{\text{crit},0}}}\right)^2\right]. \tag{181}$$

To demonstrate that the general effect is still that of an interacting vacuum, we plot the CMB temperature–temperature power spectrum and matter power spectrum for different values of q, with β fixed in Figure 29 and for different values of β, with q fixed in Figure 30. For the purposes of these plots, we keep the cosmological parameters fixed to the Planck 2018 best fits.

As expected, the presence of a coupling between the vacuum and cold dark matter acts to boost or suppress the peaks of the power spectrum, similar to the effect we have already seen in Chapter 3. When q is fixed, and different values of β chosen, there is a similar effect, although as we only show positive values of β, we only see a boost to the CMB peaks and a suppression in the matter power spectrum.

5.2.4 *Method and data*

In order to constrain the parameters of the Shan–Chen interacting vacuum model along with the cosmological parameters, we modify the publicly available Boltzmann code `CAMB` and its associated MCMC sampler `CosmoMC`. Using `CosmoMC`, we sample the posterior distributions of the baryon and cold dark matter densities $\Omega_b h^2$ and $\Omega_c h^2$, the amplitude of the primordial power spectrum and the spectral index A_s and n_s, the value of the Hubble parameter today, H_0, as well as the Shan–Chen parameters q and β. We list the priors we impose on the parameters in Table 11.

We use the Planck 2018 measurements of the CMB temperature and polarisation [61] together with the BAO measurements from the 6dF Galaxy Survey [96], the SDSS Main Galaxy Sample [97] and the SDSS DR12 consensus catalogue [63] and the Pantheon catalogue of Type Ia supernovæ [49].

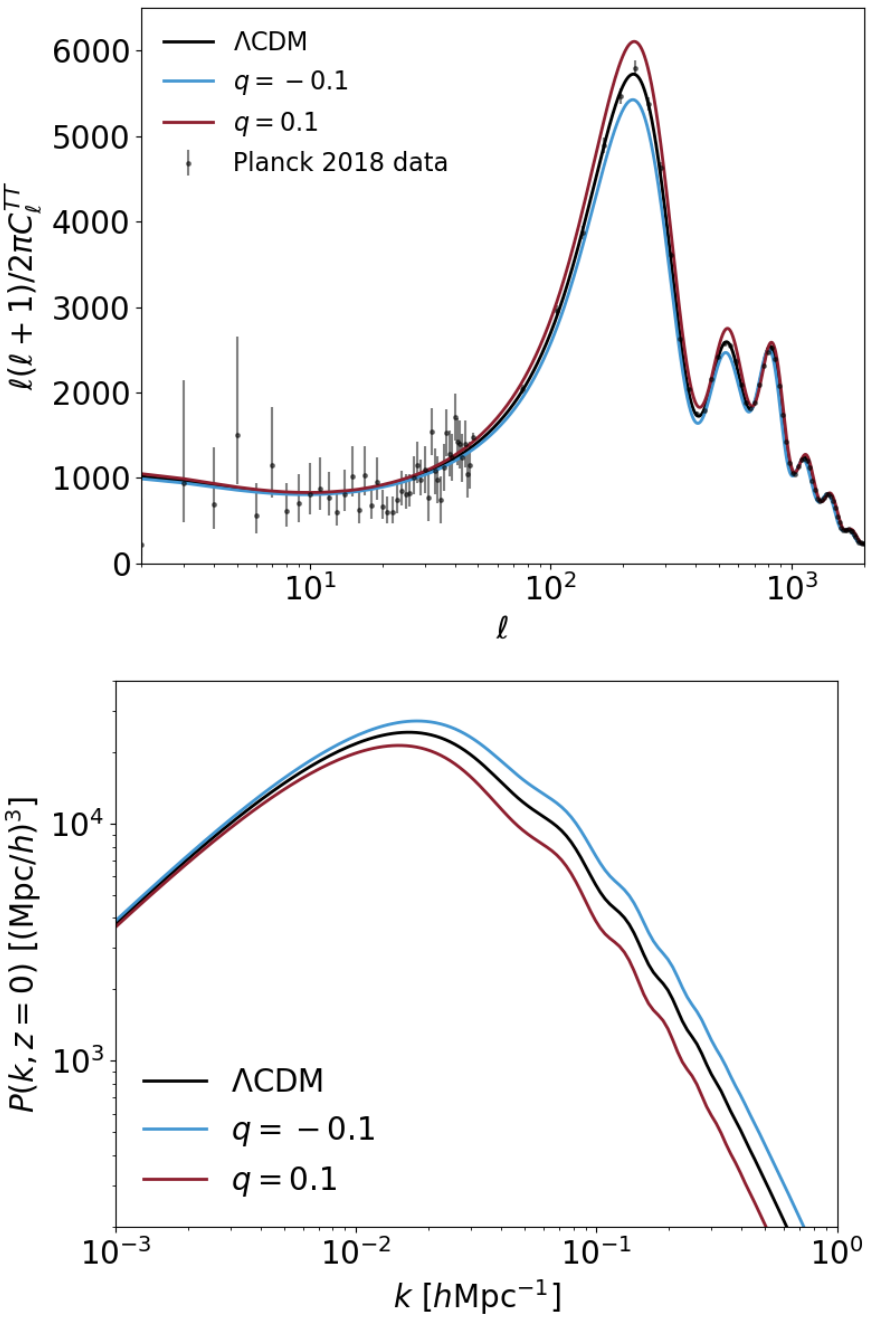

Figure 29: Top panel: CMB temperature–temperature power spectrum for different values of q. Bottom panel: matter power spectrum at $z = 0$ for different values of q. In all of these cases, $\beta = 0.3$.

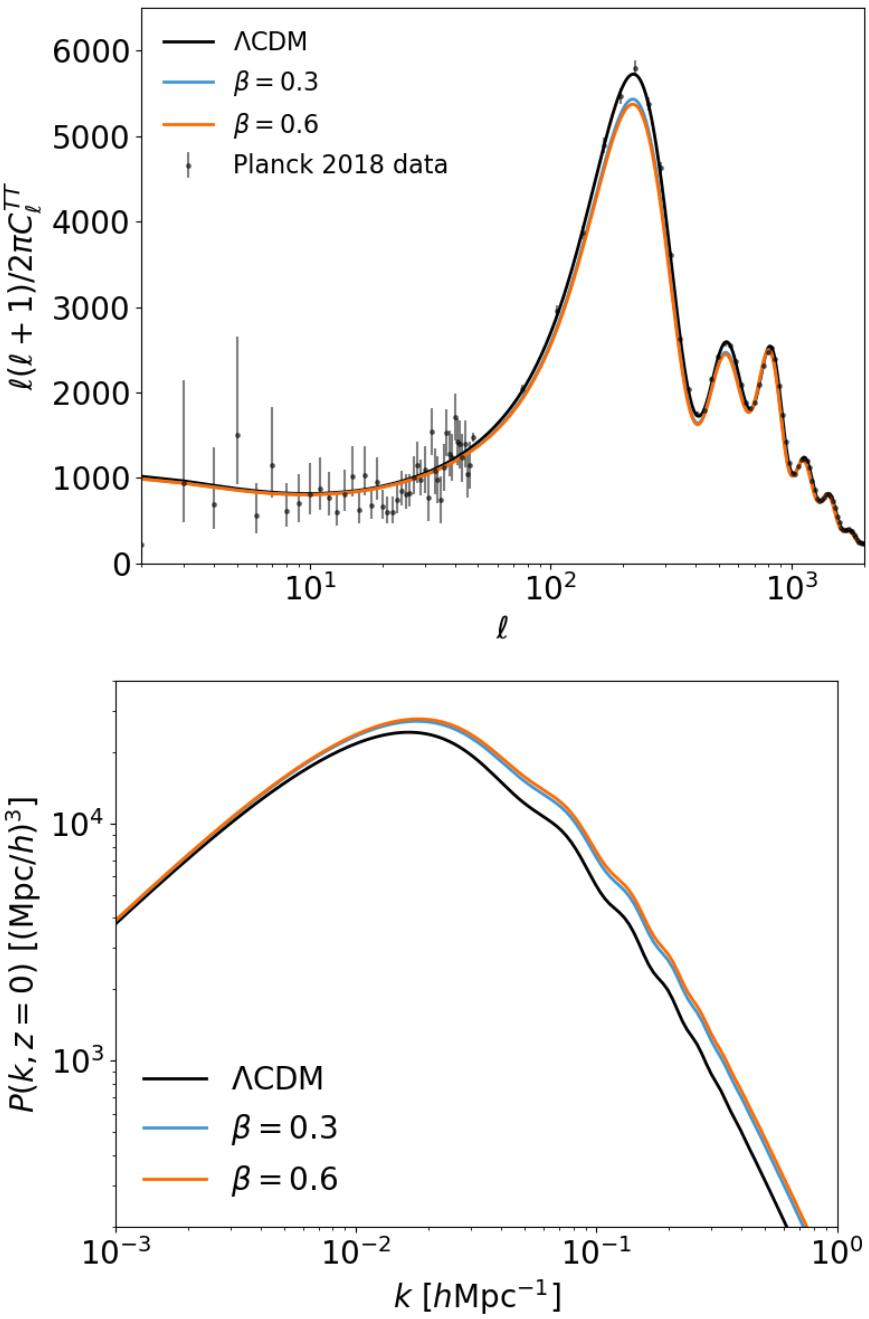

Figure 30: Top panel: CMB temperature–temperature power spectrum for different values of β. Bottom panel: matter power spectrum at $z = 0$ for different values of β. In all of these cases, $q = -0.1$.

Parameter	Prior
$\Omega_b h^2$	$[0.005, 0.1]$
$\Omega_c h^2$	$[0.001, 0.99]$
$\log 10^{10} A_s$	$[2.0, 4.0]$
n_s	$[0.8, 1.2]$
H_0	$[50, 100]$
q	$[-0.25, 0.25]$
β	$[0.0, 1.0]$

Table 11: Prior ranges of the parameters sampled in our analysis.

5.3 RESULTS AND DISCUSSION

In Figures 31 and 32, we firstly show the effect that different fixed values of the coupling strength q has on the constraints on the cosmological parameters of interest, i.e. H_0, Ω_m and σ_8, as well as the effect that different combinations of datasets can have on the constraints. In Figure 31, we show the parameter constraints obtained with the combination of CMB plus BAO data and Figure 32 we show the same parameter constraints but with the addition of the Pantheon supernova catalogue.

In Figure 31, i.e. CMB plus BAO, we see that when q is sampled over (yellow contours), it reveals degeneracies between the three cosmological parameters. When q is fixed to specific values (0.1, red contours; -0.1, blue contours; and 0 i.e. the ΛCDM limit, black contours), the constraints on the cosmological parameters are limited to moving along these lines of degeneracy. We can also see from this plot that negative values of q result in a higher value of H_0 being obtained from the CMB and BAO data than in ΛCDM, thus demonstrating how this type of interacting dark energy model can be invoked to relax the tension in that parameter.

However, in the same case ($q = -0.1$), we can see from the figure that, due to the direction of the degeneracy, this value of q results in a higher value of σ_8 also being obtained from the CMB plus BAO data. This has the effect of worsening the tension in σ_8. In all of the sub-cases shown here, β is fixed to 0.3.

Parameter	Case	Value
	Ia	0.02244 ± 0.00013
	Ib	0.02249 ± 0.00013

$\Omega_b h^2$	Ic	0.02237 ± 0.00013
	Id	0.02240 ± 0.00014
	IIa	0.02235 ± 0.00013
	IIb	0.02237 ± 0.00013
	III	0.02240 ± 0.00013
$\Omega_c h^2$	Ia	0.119 ± 0.0010
	Ib	0.132 ± 0.0010
	Ic	0.105 ± 0.0012
	Id	0.112 ± 0.0091
	IIa	0.102 ± 0.0013
	IIb	0.104 ± 0.0033
	III	0.0111 ± 0.0079
$\log 10^{10} A_s$	Ia	3.050 ± 0.005
	Ib	3.040 ± 0.006
	Ic	3.052 ± 0.006
	Id	3.051 ± 0.006
	IIa	3.052 ± 0.006
	IIb	3.051 ± 0.006
	III	3.052 ± 0.006
n_s	Ia	0.9667 ± 0.0035
	Ib	0.9694 ± 0.0037
	Ic	0.9655 ± 0.0036
	Id	0.9663 ± 0.0037
	IIa	0.9649 ± 0.0036
	IIb	0.9654 ± 0.0036
	III	0.9658 ± 0.0038
H_0	Ia	67.8 ± 0.4
	Ib	66.8 ± 0.4
	Ic	68.7 ± 0.4
	Id	68.2 ± 0.7
	IIa	68.9 ± 0.4
	IIb	68.8 ± 0.5
	III	68.2 ± 0.7
σ_8	Ia	0.8110 ± 0.0044
	Ib	0.7397 ± 0.0055
	Ic	0.9037 ± 0.0030

	Id	0.8602 ± 0.064
	IIa	0.9309 ± 0.0029
	IIb	0.9117 ± 0.023
	III	0.8664 ± 0.054
q	Ia	0.00
	Ib	0.1
	Ic	-0.1
	Id	-0.05 ± 0.06
	IIa	-0.1
	IIb	-0.1
	III	-0.06 ± 0.06
β	Ia	0.3
	Ib	0.3
	Ic	0.3
	Id	0.3
	IIa	0.6
	IIb	0.43 ± 0.28
	III	0.39 ± 0.328

Table 12: Marginalised values of the parameters and their 1σ confidence limits.

5.3.1 *Case I: different values of q*

In Figure 32, we show the constraints obtained using the full combination of CMB plus BAO plus supernovæ. For the purposes of our model comparison later on, we label the cases Ia ($q = 0$), Ib ($q = 0.1$), Ic ($q = -0.1$) and Id (q sampled). Since the supernovæ provide additional information on the matter density parameter Ω_m, the yellow contours of case Id are smaller, indicating that in this model, the supernovæ effectively break the degeneracy present in the $H_0 - \Omega_m$ plane, resulting in tighter constraints on these parameters.

We can also see from this plot that when sampling q, the data prefers values of the cosmological parameters that are very similar to ΛCDM. We quantify this in Table 12, where we report the mean posterior values and 1σ limits obtained using `GetDist` [242] for this and all subsequent cases studied. The value of q found in this case is $q =$

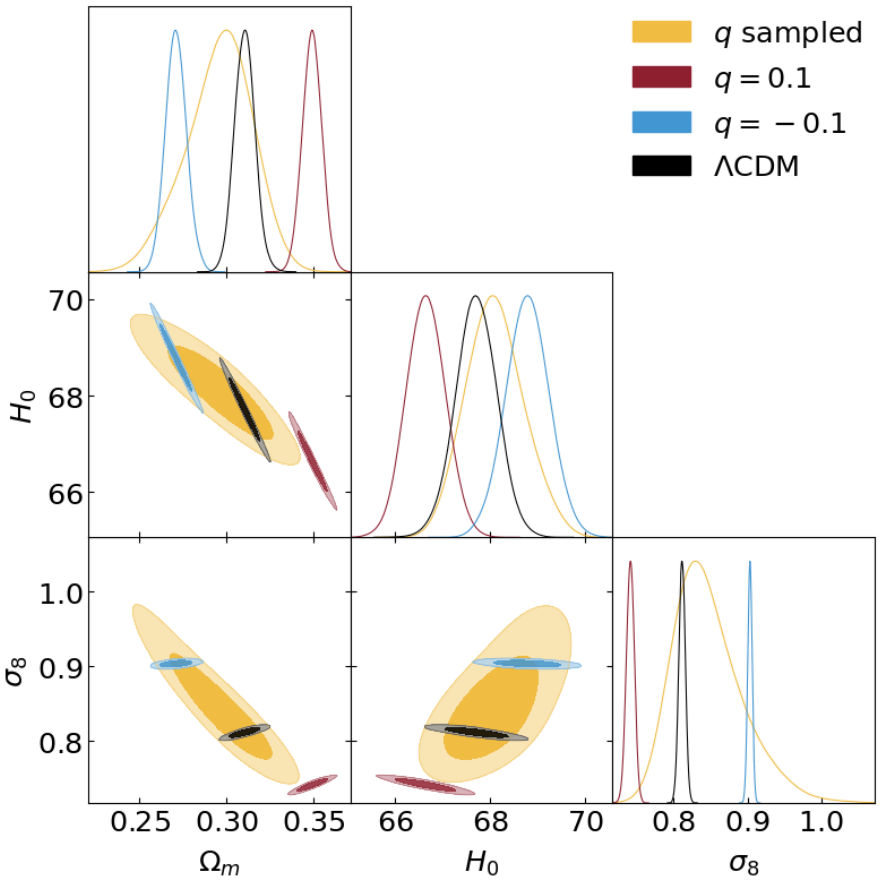

Figure 31: Constraints on Ω_m, H_0 and σ_8 for ΛCDM (black), and the Shan–Chen model with q fixed to 0.1 (red), -0.1 (blue) and sampled (yellow), using the Planck 2018 plus BAO datasets. Bottom panel: the same settings but with the addition of the Pantheon supernova catalogue. In all of these cases, $\beta = 0.3$.

-0.05 ± 0.06, which is completely consistent with the ΛCDM limit of $q = 0$.

5.3.2 *Case II: different values of β*

Next, in Figure 33, we show the result of fixing $q = -0.1$ and sampling β. We impose a flat prior of $[0.0, 1.0]$ on β, as it must have the opposite sign to g, which we have fixed to -8.0. In this plot, we see the same effect as in Figure 32, where the posterior distribution of β in the case which it is sampled over (purple contours, case IIb) describes the allowed range of the posterior distribution when β is fixed. The other two cases shown are $\beta = 0.3$ (blue contours; note that this

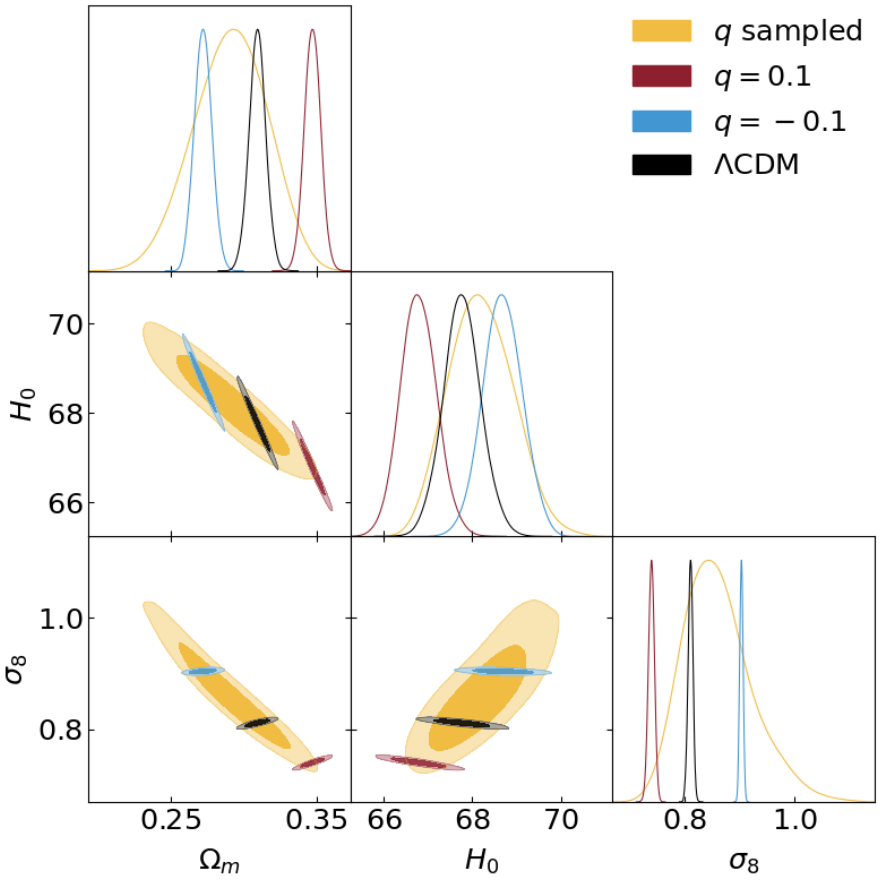

Figure 32: constraints on Ω_m, H_0 and σ_8 for ΛCDM (black), and the Shan–Chen model with q fixed to 0.1 (red), -0.1 (blue) and sampled (yellow), using the Planck 2018 plus BAO plus Pantheon supernova catalogue. In all of these cases, $\beta = 0.3$.

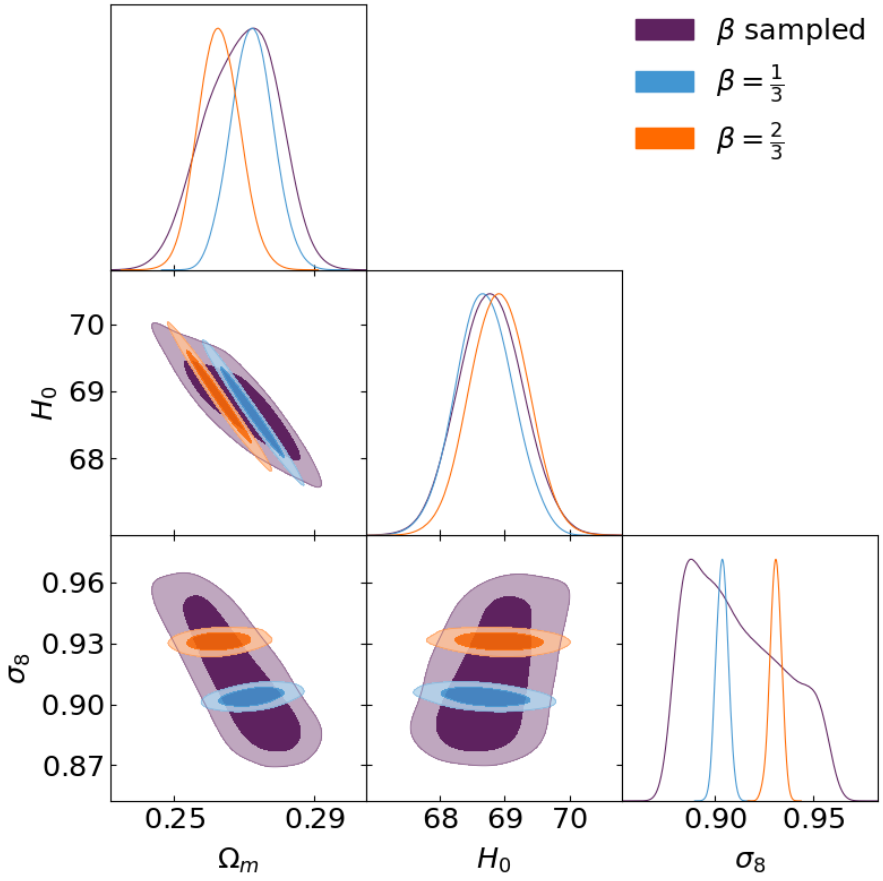

Figure 33: Constraints on Ω_m, H_0 and σ_8 for the Shan–Chen model with $q = -0.1$ and $\beta = 0.3$ (blue; note that this case is identical to the blue contour shown in Figure 32, $\beta = 0.6$ (orange) and β sampled (purple).

case is identical to case Ic) and $\beta = 0.6$ (orange contours, case IIa). The mean posterior values for all these cases are again shown in Table 12. We find that in this case, the value found for β is $\beta = 0.43 \pm 0.28$, showing that the data favours a non-zero β. However, $\beta = 0$ is not a ΛCDM limit of the model – in fact, $\beta = 0$ is equivalent to the *Cfix* case studied in Chapter 3.

5.3.3 *Case III: sampling q and β*

We finally consider the case in which we sample over both q and β. The constraints on the cosmological and model parameters in this case are shown in Figure 34. We can see that in this case, β is relatively unconstrained and q is once again consistent with the ΛCDM limit of

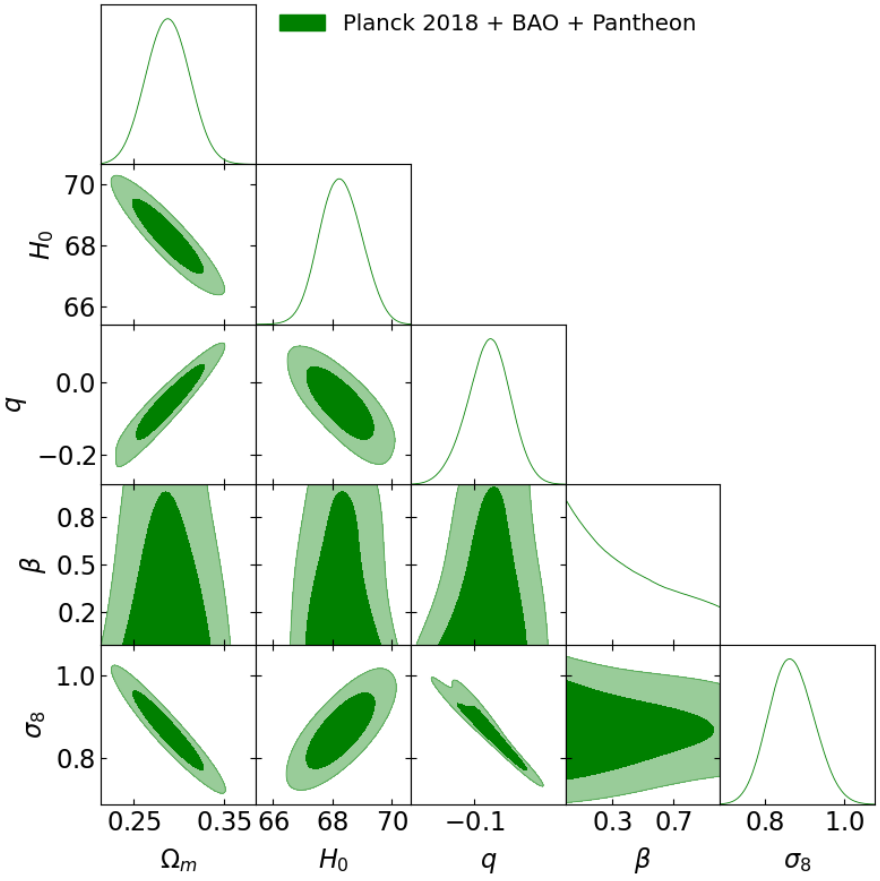

Figure 34: Constraints on Ω_m, H_0, q, β and σ_8 for the Shan–Chen model with both q and β sampled.

$q = 0$ (see Table 12). Accordingly, the constraints on the cosmological parameters are also in good agreement with their values in ΛCDM.

5.3.4 *Model comparison*

As we described in Chapter 2, there are a number of different ways to compare cosmological models. The most basic is to examine the χ^2 for each model, and for nested models a χ^2 difference test can be performed. However, the bare χ^2 does not take into account any effects of the prior, or any penalisation due to additional parameters.

To incorporate these factors, estimators such as the deviance information criterion, or DIC, are used [174, 175]. The DIC tends to be preferred over other information criteria such as the Akaike and Bayesian information criteria, as it is easy to calculate from the results of an

Case	χ^2	ΔDIC	Bayes factor
Ia (ΛCDM)	3831.75	0.0	n/a
Ib	3835.33	23.08	1.99
Ic	3832.26	4.58	0.01
Id	3832.36	4.95	-2.19
IIa	3833.03	1.88	0.20
IIb	3832.64	3.37	-1.04
III	3832.72	7.67	-2.04

Table 13: Model comparison results (Planck 2018 plus BAO plus Pantheon supernovæ).

MCMC parameter inference chain. Finally, a fully Bayesian model comparison can be achieved by computing the Bayesian evidence. The evidence is not a product of a typical MCMC sampler, but it can be estimated from MCMC chains using the `MCEvidence` [176]. This allows us to use the Bayes factor as our model comparison tool.

We report the χ^2, the ΔDIC and the Bayes factor for all the cases we consider in this chapter in Table 13. In summary, a smaller χ^2 indicates the model is a better fit to the data, a positive value of ΔDIC indicates that ΛCDM is favoured, as does a positive Bayes factor indicates that ΛCDM is favoured. A negative ΔDIC or Bayes factor indicates the alternative (i.e. the Shan–Chen model) is favoured. As in Chapter 3, we take $\Delta\text{DIC} = 5$ as the threshold for a moderate preference [210]. The Bayes factors values can be interpreted using the Jeffreys scale (see Table 2).

From the table, we can see that the case with the smallest χ^2 (excluding ΛCDM,) is Ic, i.e. $q = -0.1$ and $\beta = 0.3$ (blue contours). However, the ΔDIC in this case is positive and close to 5, showing a moderate preference for ΛCDM over this case. Furthermore, the Bayes factor in this case is inconclusive.

The case with the largest χ^2 and ΔDIC is Ib, i.e. $q = 0.1$ and $\beta = 0.3$ (red contours). This can be easily understood from Figure 32, as the red contours of case Ib are well separated from the ΛCDM case and almost in tension with the results of case Id (q sampled, yellow contours). Case Ib also has a positive Bayes factor, which indicates that ΛCDM is favoured over this particular alternative model.

Excluding ΛCDM, the case with the next smallest χ^2 is Id. Interestingly, this case also has a negative Bayes factor, indicating that it is favoured over ΛCDM. Overall, this result can be interpreted to mean

that the Shan–Chen model itself is not disfavoured by the data, but particular values of q are. When q is sampled over, slightly smaller values are inferred (i.e. around -0.05 and -0.06 – see cases Id and III in Table 12), which are acceptable to the data.

Using the Jeffreys scale to interpret the Bayes factor for case Id, we see that this corresponds to "weak" evidence in favour of the Shan–Chen model. The fact that we have uncovered even weak evidence in favour of a model with one (case Id) or two (case III) additional sampled parameters with respect to ΛCDM is very promising, and indicates that continued study of this model could be worthwhile.

In Figure 35, we show the CMB temperature–temperature power spectrum and matter power spectrum at $z = 0$ for case Id, calculated using not only the best fit model parameters, but also the best fit cosmological parameters from this case. From the figure we can see that this particular model results in a very good approximation to the CMB power spectrum, as can be expected from the model comparison result. However, the matter power spectrum reveals a small deviation from the ΛCDM case. This indicates that, in a future analysis, the inclusion of more datasets which probe the growth of structure, such as redshift space distortions, could provide a useful additional constraint on the model.

5.3.5 *Effect on the H_0 tension*

As we have previously mentioned, studies of alternative dark energy models such as the Shan–Chen model presented here can be motivated by their potential to relax the H_0 tension. As we found in subsection 5.3.4, case Id has the most competitive Bayes factor, so we plot the two dimensional marginalised contours in the H_0 – Ω_m plane in this case in Figure 36, along with the 1 and 2σ bands from the local constraint on H_0 as presented in [94], $H_0 = 74.03 \pm 1.42$ kms^{-1} Mpc^{-1}.

Note that this plot is similar to the top panel of Figure 19, but we use a more up-to-date local H_0 value, which is marginally larger, and therefore the tension between the value of H_0 in the interacting dark energy model and the local H_0 value appears larger. In fact, the 2σ contour in the Shan–Chen model shown in Figure 36 has its upper limit at $H_0 \approx 70$ kms^{-1} Mpc^{-1}, as does the 2σ contour in the mean fiducial model in Figure 19.

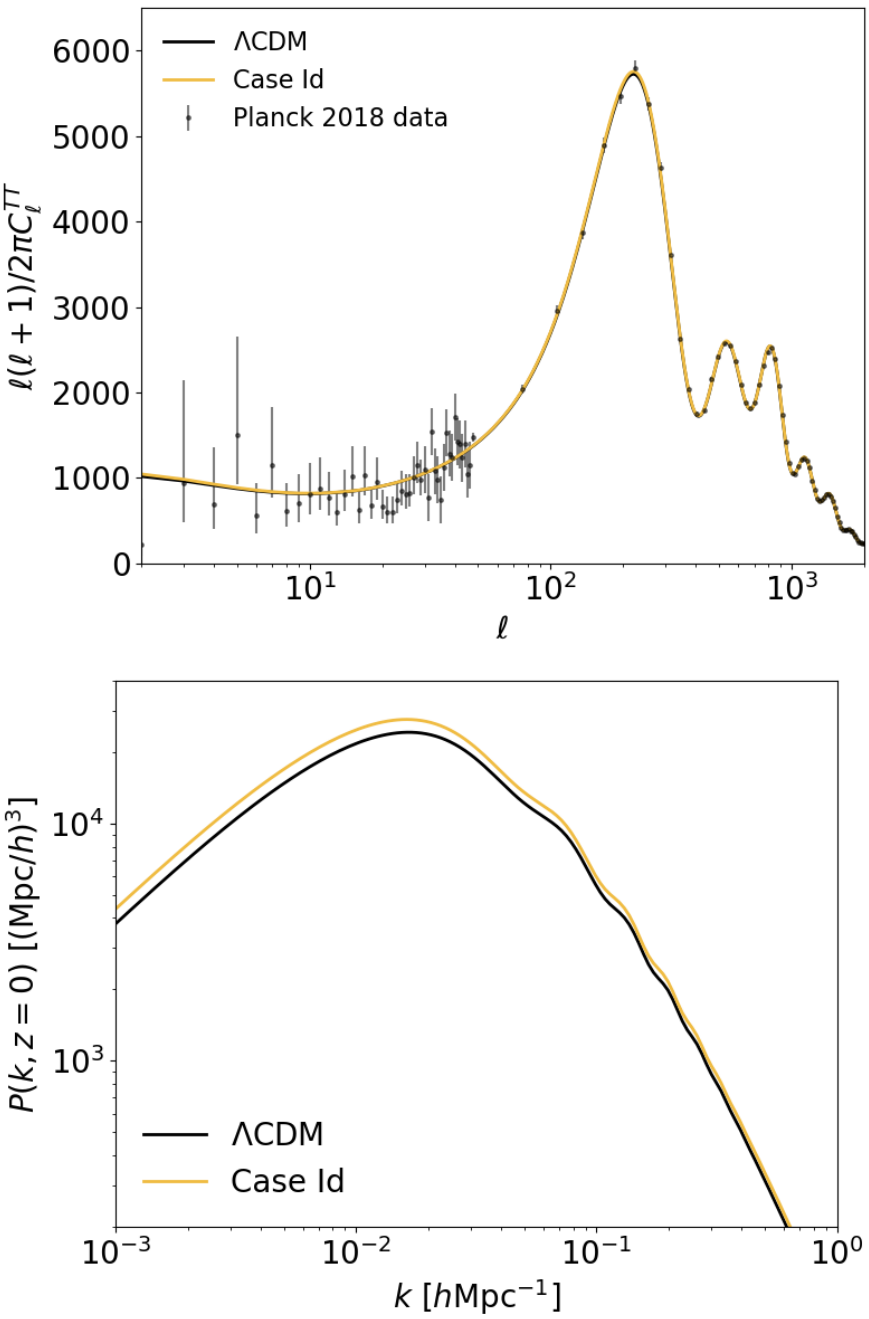

Figure 35: Top panel: CMB temperature–temperature power spectrum for case Id. Bottom panel: matter power spectrum at $z = 0$ for case Id.

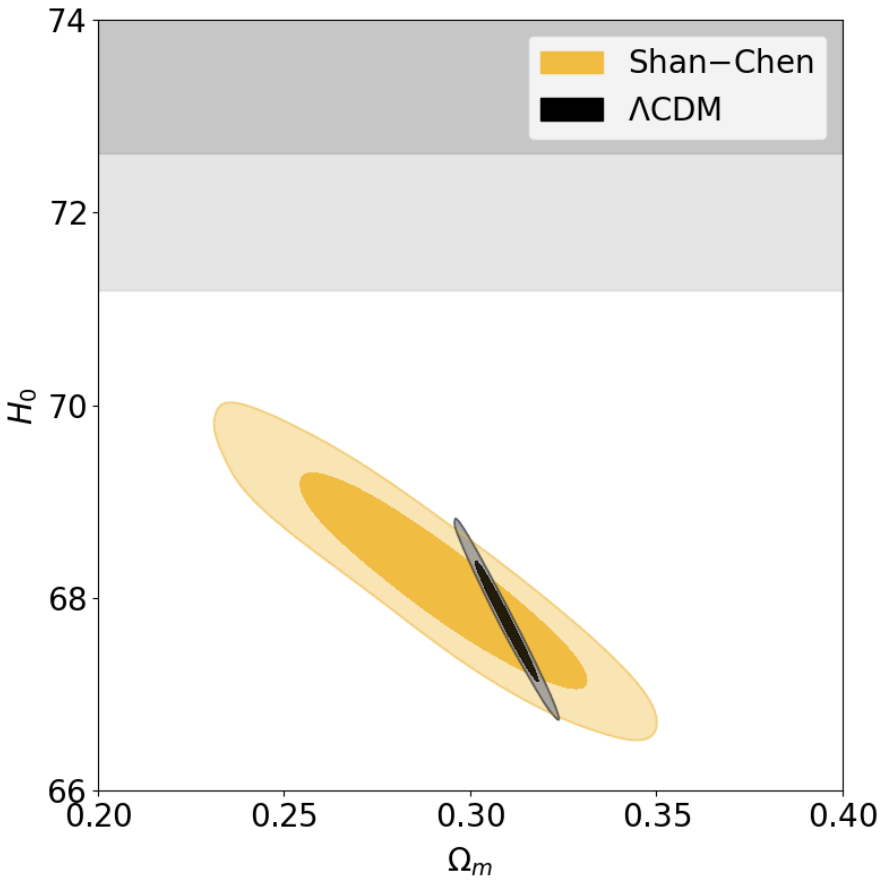

Figure 36: The constraints in the H_0 – Ω_m plane in case Id (yellow), compared to the ΛCDM constraint (black) and the local measurement of H_0 (grey bands denote the 1 and 2σ limits).

It is therefore clear that while the H_0 tension is somewhat relaxed, the various configurations of the Shan–Chen model studied in this chapter are not able to fully resolve it. Similarly, in this model, the direction of degeneracy between H_0 and σ_8 (as can be seen in Figure 32) is such that both tensions cannot simultaneously be resolved, as an increase in H_0 to match the local value corresponds to an increase in σ_8, whereas a smaller value of σ_8 is needed to resolve the tension in that parameter.

5.3.6 *Discussion*

The cases studied in this chapter are only a small subset of all possible models that exist under the umbrella of Shan–Chen dark energy. We have hardly given any consideration to the original dark energy fluid

as introduced in [262], focusing instead on the interacting vacuum scenario in line with the rest of this thesis. Even within the interacting vacuum Shan–Chen model, we have limited ourselves to fixing $\rho_* = \rho_{\mathrm{crit},0}$, when other possibilities exist, most obviously $\rho_* = \rho_{\mathrm{m}}(z_{\mathrm{eq}})$. All of these remain open to exploration in future works.

However, the repeated failures of the interacting vacuum models we have studied in this thesis to cure the H_0 tension point to the fact that perhaps this is the wrong line to continue down to try and achieve this particular goal. While it is beyond the scope of this thesis to explore these ideas, another type of dark energy such as the early dark energy presented in [127] could be a more fruitful avenue to explore, as could more complex modified gravity models (e.g. [265]).

At the start of this chapter, we partially motivated our repurposing of the Shan–Chen equation of state fluid dark energy model as an interacting model due to its basis in pre-existing physics rather than being a purely phenomenological model of a vacuum – cold dark matter interaction of the type we used in previous chapters. This opens up an interesting philosophical question: should this kind of argument be used more often when constructing alternative dark energy models?

On the one hand, more physically motivated models could yield interesting results, as we have seen in this chapter. On the other hand, it is important not to become dogmatic when using simplicity as a motivator, or when making arguments against fine-tuning. After all – invoking the anthropic principle once more – a Universe with a "natural" value for the cosmological constant would be inhospitable to life as we know it [266].

5.4 SUMMARY

In this chapter, we have placed the first observational constraints on the Shan–Chen model of dark energy, as introduced by [262], in the context of the interacting vacuum scenario. We found that certain cases within this model are competitive with ΛCDM when performing a model comparison using the results of our MCMC parameter inference, but the model still fails to resolve the H_0 tension.

The study presented here is a preliminary and non-exhaustive examination of the Shan-Chen model, and many unexplored combinations of parameters remain. However, as our analysis shows, it is generally difficult for these types of interacting dark energy models to be both

a better fit to the data than ΛCDM and simultaneously resolve the cosmological tensions.

In the next chapter, we leave behind our investigations of the interacting vacuum scenario to instead study future constraints on the distance duality relation both in the context of ΛCDM and in modified gravity, using mock datasets of Type Ia supernovæ, BAO and standard sirens.

6

STANDARD SIRENS AND THE DISTANCE DUALITY RELATION

The best thing that we're put here for's to see;
The strongest thing that's given us to see with's
A telescope.

ROBERT FROST

In this chapter, we move on from our studies of interacting dark energy to forecast constraints on the electromagnetic and gravitational distance duality relations using gravitational wave standard siren, Type Ia supernova and baryon acoustic oscillation (BAO) mock data. We make use of a parameterised approach based on a specific distance duality relation violation model, along with a machine learning reconstruction method based on the genetic algorithms. We find that gravitational waves provide an alternative to the use of BAO data to constrain violations of the distance duality relation, reaching 3% constraints on the violation parameter we consider when combined with supernovæ, which is only improved by a factor of ≈ 1.4 if we instead consider the combination of BAO and Type Ia supernovæ.

We also investigate the possibility that a neglected modification of gravity might lead to a false detection of distance duality relation violations, even when screening mechanisms are active. We find that such a false detection can be extremely significant, up to $\approx 10\sigma$ for very extreme modified gravity scenarios, although this reduces to $\approx 4\sigma$ in a more realistic case. False detections can also provide a smoking gun for the modified gravity mechanism at play, as a result of the tension introduced between the Type Ia supernovæ plus gravitational waves and Type Ia supernovæ plus BAO combinations. This chapter is based on [3].

6.1 INTRODUCTION

On the 11$^{\text{th}}$ February 2016, the Laser Interferometer Gravitational-Wave Observatory (LIGO) and Virgo collaborations announced the first direct detection of a gravitational wave signal, coming from the inspiral, merger and ringdown of a binary black hole system

(GW150914) [80]. The subsequent observation in 2017 of a binary neutron star merger concurrent with an electromagnetic counterpart (GW170817) heralded a new era of multi-messenger astronomy and the use of gravitational wave events as so-called "standard sirens" [267, 268, 269, 81].

These two groundbreaking observations had important repercussions for cosmology too. The first lent further support to Einstein's theory of general relativity by confirming the theory's prediction of gravitational waves; the second placed strong constraints on modified gravity theories that predicted a tensor speed different to that of light [270, 82, 83], as well as providing a new distance ladder independent measurement of the Hubble parameter H_0 [84].

Such a measurement of H_0 is still not competitive with those provided by other probes [271], but it highlights how future gravitational wave telescopes will be able to shed light on the cosmological tension problems faced by contemporary cosmology. Recent investigations have also shown how the observation of gravitational waves will provide new tests of general relativity, potentially constraining several still viable modified gravity theories (see e.g. [272, 273, 274]).

One example of a future gravitational wave observatory is the Einstein Telescope (ET), a proposed ground-based triangular interferometer that will be part of the third generation of gravitational wave detectors [275]. Current terrestrial detectors such as LIGO and Virgo are limited in the low frequency range by seismic and thermal noise; these factors will be mitigated especially in the case of the ET by its proposed underground construction and cryogenic cooling of the interferometer mirrors.

The reduced noise levels of the ET and other third generation detectors will therefore enable extremely sensitive measurements of gravitational wave signals to be made, bringing standard siren detections into the realm of precision cosmology [276].

As our measurements of cosmological parameters improve, the standard cosmological model of a spatially flat Universe dominated by a cosmological constant plus cold dark matter (ΛCDM) is still the most appealing to explain observations with respect to the most common alternatives (see e.g. [61, 277] for recent constraints obtained by the Planck and DES surveys). Therefore, it becomes necessary to consider how best to constrain more exotic deviations from the standard paradigms of general relativity and ΛCDM.

A feasible possibility is a violation of the distance duality relation, which relates angular diameter and luminosity distances, a possib-

ility for which several observational tests have been proposed [278, 279, 280, 281, 282, 283]. Deviations can occur in both the electromagnetic and gravitational wave sectors. However, these would be due to very different physical mechanisms, with the former related to a non-standard propagation of photons and the latter to an anomalous propagation of gravitational waves.

In this chapter, we focus on the first of these possibilities, studying a toy model in which the electromagnetic distance duality relation is broken as photons decay into axions while propagating through cosmic magnetic fields. Such deviations of the distance duality relation are commonly constrained using observations of Type Ia supernovæ alongside BAO measurements, since the latter are not sensitive to the violation mechanisms and can therefore break the degeneracies between distance duality relation violation and standard cosmological parameters.

We explore the possible use of future gravitational wave datasets as an alternative to BAO, or alongside them, to constrain the distance duality relation violation model under examination. We exemplify our method using mock datasets for future observations of Type Ia supernovæ, BAO and gravitational waves and, using an MCMC analysis, show the constraints that can be obtained on cosmological and model parameters.

However, this approach can lead to false detections of distance duality relation violations if mechanisms leading to anomalous gravitational wave propagation are also at play and are not considered in the analysis. Exploring this possibility, we attempt to highlight the signatures of such a scenario in the final results of the analysis pipeline, investigating the constraints one would obtain if both deviations from the standard behaviour are considered at the same time.

Finally, we also perform a machine learning reconstruction of the distance duality relations as functions of redshift, using genetic algorithms. Genetic algorithms are a stochastic optimisation approach that, given some data, can provide functional reconstructions that depend solely on the redshift z and are based on a minimal set of assumptions [284, 285].

The main advantage of this approach is that genetic algorithms are not susceptible to theoretical priors about the behaviour of the data under question and can detect hidden features in the data, that at first sight might be missed by traditional inference approaches. Genetic algorithms can also help avoid biases in the results and possible false

detections of distance duality relation violations, something which we explicitly test using mock data in order to validate our approach.

6.2 PHOTON DECAY AND DEVIATIONS FROM THE STANDARD DISTANCE DUALITY RELATION

The investigation of the homogeneous expansion of the Universe commonly relies on the observations of standard candles, which probe the luminosity distance $d_L(z)$, and standard rulers, through which we can measure the angular diameter distance $d_A(z)$. The general relation between these quantities, which holds under the two conditions that the number of photons is conserved and that they travel on null geodesics in a pseudo-Riemannian spacetime [32, 286], is given by

$$d_L(z) = (1+z)^2 d_A(z), \tag{182}$$

which is called the distance duality relation. Both the luminosity and angular diameter distance can be obtained in terms of the comoving distance $d_c(z)$ as

$$d_L(z) = (1+z) d_c(z)\,, \tag{183}$$

$$d_A(z) = \frac{d_c(z)}{1+z}\,. \tag{184}$$

Even though these relations hold for the minimal set of assumptions mentioned above, in this thesis we assume that the background expansion of the Universe is the one produced by a spatially flat ΛCDM model, which allows the comoving distance to be expressed as

$$d_c(z) = c \int_0^z \frac{dz'}{H(z')}\,, \tag{185}$$

where $H(z)$ is the Hubble parameter in units of km s^{-1} Mpc^{-1} and c is the speed of light in km s^{-1}.

In this chapter we focus on a violation of the first condition, photon number conservation, investigating mechanisms that lead photons to be converted into other particles, such as axions or other axion-like particles [287]. Axion models have received a spike in interest after the recent XENON1T observation of excess electronic recoil, which was attributed to solar axions with a significance of 3.5σ [144][1]. Here

1 It has been noted that astrophysical constraints on solar axions are incompatible with the XENON1T excess [145], and that the detection could be due to the previously unaccounted-for β decays of tritium in the detector [146]. The significance of the solar axion fit decreases to 2.1σ if this additional tritium component is considered.

we examine a specific mechanism that considers the possibility of novel scalar and pseudo-scalar particles inspired from beyond standard model physics coupling to the photons via the following interaction terms [279]

$$\mathcal{L}_{\rm int,scalar} = \frac{1}{4M} F_{\mu\nu} F^{\mu\nu} \phi \tag{186}$$

and

$$\mathcal{L}_{\rm int,pseudo} = \frac{1}{8M} \epsilon_{\mu\nu\lambda\rho} F^{\mu\nu} F^{\lambda\rho} \phi, \tag{187}$$

where M is the energy scale of the coupling, $\epsilon_{\mu\nu\lambda\rho}$ the antisymmetric Levi-Civita symbol, ϕ is the axion particle and $F^{\mu\nu}$ the electromagnetic field strength. In the presence of magnetic fields, photons have a non-vanishing probability of converting to axions via a see-saw-like mechanism after travelling a distance L. The probability is given by [288, 289]

$$P_{\gamma\to\phi} = \sin(2\theta)^2 \sin\left(\frac{\Delta}{\cos(2\theta)}\right)^2, \tag{188}$$

where the parameters in the previous equation are given by $\Delta = m_{\rm eff}^2 L/4\omega$, $\tan(2\theta) = 2B\omega/(M m_{\rm eff}^2)$. Here, B is the strength of the magnetic field, while $\omega = 2\pi f$ is the frequency of the photons and $m_{\rm eff}^2 = |m_\phi^2 - \omega_P^2|$, where $\omega_P^2 = 4\pi^2 \alpha n_e / m_e$ is the plasma frequency of the medium related to the effective mass of the photons and m_ϕ is the axion mass.

This probability of converting photons to axions means that the photon number is not conserved, hence the observed luminosity distance, $d_L^{\rm EM}(z)$, is different to the "bare" one, $d_L^{\rm bare}(z)$, which corresponds to a model where the photon number is conserved and can be computed using (182). Since we can only detect those photons along the line of sight, the observed and bare luminosity distances are related by a factor $\mathcal{P}(z)$ such that [279]

$$d_L^{\rm EM}(z) = \frac{d_L^{\rm bare}(z)}{\sqrt{\mathcal{P}(z)}}. \tag{189}$$

The redshift evolution of the function $\mathcal{P}(z)$ depends on the type of intervening magnetic field responsible for the photon decay. Following [279], we distinguish here between incoherent (inc) and coherent (coh) magnetic fields, leading to different redshift trends for the $\mathcal{P}(z)$ function:

$$\mathcal{P}_{\rm inc}(z) = A + (1-A)\exp\left(-\frac{3}{2}\frac{H_0}{c} d_c(z)\ \xi_0\right), \tag{190}$$

$$\mathcal{P}_{\rm coh}(z) = A + (1-A)\exp\left(-\frac{H(z) - H_0}{\Omega_{\rm m} H_0}\ \xi_0\right), \tag{191}$$

where $\Omega_{\rm m}$ is the energy density of matter at $z = 0$. The factor A sets the amplitude of the deviation from the standard distance duality relation, and it can be expressed in terms of the initial flux of the axions and photons at some initial redshift z_I, denoted by $I_\phi(z_I)$ and $I_\gamma(z_I)$ respectively, as [279]

$$A = \frac{2}{3}\left(1 + \frac{I_\phi(z_I)}{I_\gamma(z_I)}\right), \tag{192}$$

and the parameter ξ_0 is related to the transition probability $P_{\gamma\to\phi}$ of each domain of length L through

$$\xi_0 = \frac{c}{H_0}\frac{P_{\gamma\to\phi}}{L}. \tag{193}$$

Since we expect the photons to travel through several domains of intergalactic magnetic fields with coherence of at least ∼50 Mpc, then (190) and (191) can be considered as both an average over several domains and frequencies of the photons. Moreover, we may make a heuristic argument that the transition probability should be of the order of a few percent, which then implies from (193) that $\xi_0 = \mathcal{O}(1)$. Hence, throughout the rest of this chapter, we will assume that $\xi_0 = 1$.

Assuming the angular diameter distance $d_A(z)$ is not affected, we can then define the parameter $\eta_{\rm EM}(z)$ which characterises the deviation from the distance duality relation:

$$\eta_{\rm EM}(z) \equiv \frac{d_L^{\rm EM}(z)}{d_L^{\rm bare}(z)} = \frac{d_L^{\rm EM}(z)}{(1+z)^2 d_A(z)} = \frac{1}{\sqrt{\mathcal{P}(z)}}, \tag{194}$$

where $\mathcal{P}(z)$ is given by (190) and (191) in the incoherent and coherent regimes respectively. Previous literature investigating departures from the distance duality relation usually makes use of a simple parameterisation (see e.g. [290, 279])

$$d_L^{\rm EM} = (1+z)^{\epsilon_0} d_L^{\rm bare}(z), \tag{195}$$

which yields

$$\eta_{\rm EM}(z) = (1+z)^{\epsilon_0}. \tag{196}$$

Therefore, one can compare (194) and (196) to map current constraints on ϵ_0. From (192) we see that if $A > 1$, then this implies that at early times the intensity of the axions satisfies $I_\gamma(z_I) < 2I_\phi(z_I)$. Since we roughly expect the intensity of the particles to be proportional to their number n, then this also implies that approximately $n_\gamma(z_I) < 2n_\phi(z_I)$. Mapping current constraints on $\eta_{\rm EM}(z)$ [166] to the $\mathcal{P}(z)$ function through (194), we obtain, in the coherent regime, $A = \mathcal{O}(1)$, which

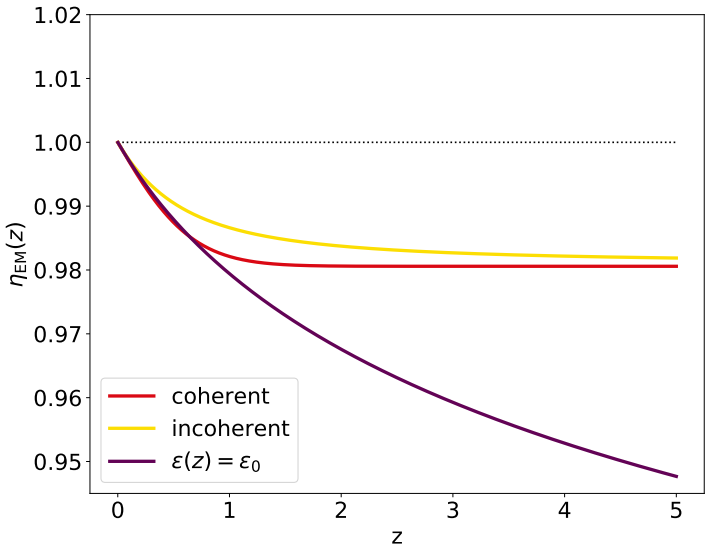

Figure 37: A comparison of the incoherent and coherent models, given by (190) and (191) respectively, versus the phenomenological expansion $\epsilon(z) = \epsilon_0$. We assumed $\Omega_m = 0.315$ and $\epsilon_0 = -0.03$.

implies that $n_\gamma(z_I) \simeq 1.881 n_\phi(z_I)$ and it is consistent with the fact that photons have two polarisations while axions have only one, and at early times they are all in a thermal equilibrium.

In Figure 37 we show a comparison of the duality parameter $\eta_{EM}(z)$ for the incoherent and coherent axion models, given by (190) and (191) respectively, versus the phenomenological parameterisation of (196). We assumed $\Omega_m = 0.315$ and $\epsilon_0 = -0.03$. Note that at $z = 0$, all models have $\eta_{EM}(z = 0) = 1$. Since the conversion of photons to axions is an integrated effect along the line of sight, at small distances away from the observer there are very few, if any, magnetic domains, and therefore the distance duality relation holds. It is worth pointing out here that models of the kind investigated here might also lead to the variation in time of fundamental constants such as the fine structure constant α (see e.g. [291]).

6.3 FORECAST DISTANCE DUALITY RELATION CONSTRAINTS: THE IMPACT OF STANDARD SIRENS

In this chapter, we are interested in quantifying the constraints on the possible deviations from the standard distance duality relation due to the mechanisms described in section 6.2. The crucial observations needed to constrain these effects are produced by Type Ia supernova

surveys, which will provide measurements of the distance modulus $\mu(z)$, connected to the luminosity distance through

$$\mu(z) \equiv m(z) - M = 5 \log_{10} d_L^{\rm EM}(z) + 25\,, \tag{197}$$

where m is the apparent magnitude of the supernova at redshift z and M its intrinsic magnitude. Such measurements are sensitive to the decay of photons through (189) and can therefore place constraints on the parameters that govern the coupling of photons to axions, A and ξ_0. However, it has been shown [166] that using the information from supernova surveys alone leads to strong degeneracies between the distance duality relation parameters and $\Omega_{\rm m}$, limiting the constraining power of this observable (more details on this degeneracy are shown in subsection 6.3.1 below).

For this reason, it is common to combine Type Ia supernovæ with BAO data; the latter are able to provide constraints on combinations of the angular diameter distance $d_A(z)$, the Hubble parameter $H(z)$ and the sound horizon at the drag epoch $r_{\rm drag}$. These measurements are not sensitive to the deviation from standard distance duality relation that we consider and can therefore be used to break the degeneracies and increase the constraining power of the data on A.

However, the BAO data come with their own issues. A fiducial cosmology must be assumed to obtain distances from the measured angular scale on the sky, thus possibly inducing some model bias in the data. Further uncertainties are introduced by the fact that non-linear effects damp and modify the locations of the BAO in the galaxy power spectrum, thus possibly introducing systematic errors in the estimation of the inferred cosmological parameters (see e.g. [292]).

Several techniques have been developed to standardise BAO distance measurements; however most of them rely on modelling of non-linear scales, which is not trivial if one abandons the ΛCDM model for extended theories. Alternatively one can rely on observables not affected by such non-linear effects [293, 294], paying the price of a reduced constraining power.

Given these caveats, it would be useful to have an extra observable to use alongside the routinely employed Type Ia supernovæ and BAO; such observables would need to be able to probe the cosmological parameters without suffering from the degeneracy with deviations from the distance duality relation that Type Ia supernovæ exhibit.

Recent detections of gravitational waves (e.g. [295, 296, 297]) have shown that these observations can provide a new way of testing the

fundamental physical mechanisms at play in the Universe. Gravitational waves are the propagation of perturbations in the tensor sector, which, in general relativity and in vacuum propagation (i.e. obtained by solving the linearised Einstein field equations with $T_{\mu\nu} = 0$) satisfy

$$h''_{\mathcal{A}}(\tau, k) + 2\mathcal{H}h'_{\mathcal{A}}(\tau, k) + k^2 h_{\mathcal{A}}(\tau, k) = 0 \tag{198}$$

with $h_{\mathcal{A}}(\tau, k)$ the Fourier modes of the gravitational wave amplitude, the prime representing the derivative with respect to conformal time $d\tau = dt/a(t)$, $\mathcal{H}$ the conformal Hubble parameter ($\mathcal{H} = aH$) and the index $\mathcal{A} = +, \times$ running over the two polarisations.

It can be shown [79] that $h_{\mathcal{A}}$ scales with the luminosity distance as

$$h_{\mathcal{A}} \propto \frac{1}{d_L^{\mathrm{GW}}(z)}\,, \tag{199}$$

and therefore distance measurements can be obtained by observing gravitational waves from merger events. If the redshift of the event is measured by observing an electromagnetic counterpart, we can construct a Hubble diagram using these as standard sirens.

The photon–axion coupling we consider in this chapter does not affect the luminosity distance measured through gravitational wave observations. These therefore probe the bare luminosity distance, assuming that no other physical mechanism is leading to deviations from the gravitational wave propagation predicted by general relativity, and in (199) $d_L^{\mathrm{GW}}(z) = d_L^{\mathrm{bare}}(z)$. This implies that, as with the BAO data, the observations of standard sirens by future surveys can be used in combination with Type Ia supernovæ to constrain deviations from the distance duality relation.

We therefore focus on these three observables: Type Ia supernovæ, BAO and gravitational waves, using them to quantify our future ability to constrain deviations from the distance duality relation. We create simulated data for:

- A Type Ia supernova survey based on what will be achievable with the Legacy Survey of Space and Time (LSST), performed by the Vera C. Rubin Observatory. LSST will survey approximately 18,000 square degrees of the sky and conservative estimates predict observations of 10,000 Type Ia supernovæ up to $z{\approx}1$ [298]. We provide more details of the LSST data we simulate in the Appendix, section A.1.
- A BAO survey based on forecast data for the Dark Energy Spectroscopic Instrument (DESI), a spectroscopic galaxy survey expected to be fully operational by the end of 2020 [299]. We

provide more details of the DESI data we simulate in section A.2.

- Gravitational wave data expected from the proposed Einstein Telescope (ET) [275], a future third generation terrestrial gravitational wave observatory. We consider here future observations of binary neutron star mergers; such events could provide a corresponding electromagnetic observation, allowing a redshift measurement, and in this chapter we assume that a counterpart will be available for $N_{\rm GW} = 1000$ observations performed by ET[2]. We follow the specifications and the noise calculation presented in [300, 301, 302]. A detailed description of the steps and assumptions made to obtain the simulated dataset for gravitational waves is shown in section A.3.

Note that the ET as an experiment is still in the proposal stage, as opposed to DESI, which has already seen first light, and LSST, which is currently under construction. This means that there is likely to be an approximately ten year gap between the final data releases from LSST and DESI and the first results from the ET. Nevertheless, forecasting the constraints that all three will jointly provide is still an interesting and useful endeavour.

Following the specifications for these experiments we assume a fiducial cosmology where no deviation from the standard distance duality relation is present ($A = 1$), and we take the fiducial values for the standard cosmological parameters from the Planck 2018 best fit, $\Omega_{\rm m} = 0.314$ and $H_0 = 67.36$ km s^{-1} Mpc^{-1} [61].

Throughout this thesis we assume a vanishing contribution to the total energy density from curvature ($\Omega_K = 0$) and we assume that the late time expansion of the Universe is dominated by a cosmological constant Λ with energy density $\Omega_\Lambda = 1 - \Omega_{\rm m}$. As the data we consider only probe the low redshift regime, we consider the contributions from the radiation energy density to be negligible.

We forecast the constraining power of these surveys, implementing a new likelihood module for the publicly available MCMC sampler `Cobaya` [303], obtaining the theoretical prediction for $d_A(z)$ from `CAMB` [150, 151] for each point in the parameter space, and computing the luminosity distances observed by Type Ia supernovæ ($d_L^{\rm EM}(z)$) and gravitational waves ($d_L^{\rm GW}(z)$) using (189) and (183) respectively.

2 Such an assumption could be seen as optimistic. If the number of events with an electromagnetic counterpart is reduced, one could infer the redshift of the mergers with alternative methods, paying the price of a larger uncertainty on the redshift estimation (see e.g. [271])

We sample the standard cosmological parameters Ω_m and H_0, alongside the distance duality relation parameter A, imposing flat priors on them. We obtained our constraints for both the incoherent and coherent axion models, finding no significant difference in the results for each. We thus choose to present only the incoherent model results.

When fitting the simulated supernova data we make use of the likelihood described in Appendix C of [304], which takes into account the complete degeneracy of H_0 and M that this probe suffers from, marginalising them out.

6.3.1 *Results*

Using the mock datasets introduced above, where no deviation from the distance duality relation occurs, we aim to forecast the constraints that will be achieved in the future using the three types of observations we consider here. We firstly focus on the results obtained using supernova observations alone. As we already discussed, these observations are not sensitive to H_0 and M individually, but rather only to their combination.

However, another strong degeneracy appears when we try to constrain deviations from the standard distance duality relation. As we show in Figure 38, the parameter A is strongly degenerate with Ω_m, and a variation of A allows the theoretical predictions we obtain to be compatible with the dataset for extreme values of the matter energy density.

Note that to obtain the results of Figure 38, we relied on a grid sampling of the bi-dimensional parameter space, rather than on MCMC method based on the Metropolis–Hastings algorithm [165], such as that implemented in `Cobaya`, that we use for the rest of the results. This is necessary due to the degeneracy itself, which results in the MCMC failing to properly sample the full posterior distribution. When sampling these parameters using the LSST mock dataset alone, the Metropolis–Hastings struggles to explore the full line of degeneracy between A and Ω_m, instead finding false peaks in the posterior distribution which it is unable to move away from.

As a further check, we exploited the method of nested sampling, using the `PolyChordLite` code [168, 169] implemented in `Cobaya`. This enabled us to properly explore the full extent of the degeneracy, as nested sampling is much better suited to sampling multi-modal and

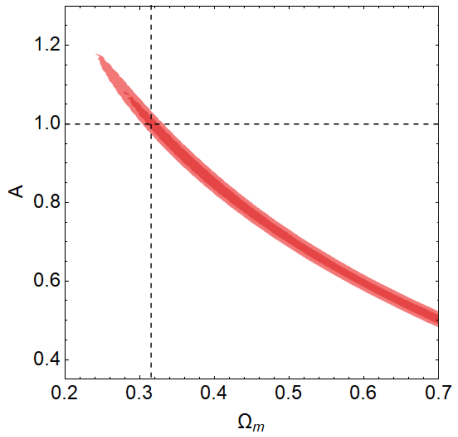

Figure 38: 2D constraints on the matter energy density Ω_m and the distance duality relation violation parameter A obtained analysing the LSST mock dataset for Type Ia supernovæ.

other complicated distributions than Metropolis–Hastings, and also allowed us to recover the results obtained with the grid approach.

We were further able to show that the addition of the BAO dataset is sufficient to break the degeneracy between Ω_m and A. We therefore urge caution when investigating degenerate models with simple sampling methods such as Metropolis–Hastings, and stress that checks with different sampling methods are always beneficial. Such a result highlights the necessity of using other observations which, unlike Type Ia supernovæ, are not sensitive to the parameter A and are therefore able to break this degeneracy by measuring Ω_m.

We therefore now focus on the combination of Type Ia supernovæ with BAO and gravitational wave observations. Our constraints on the cosmological parameters are reported in Table 14, while we show the marginalised posterior distributions and the two dimensional contours in Figure 39, combining LSST first with ET and DESI separately and then all together. The 68% confidence intervals of the constraints are all compatible with the ΛCDM fiducial cosmology, shown by the dashed lines.

These results show how a combination of Type Ia supernovæ and gravitational wave observations from the ET would be competitive with the combination of Type Ia supernovæ and BAO, with the constraints that improve only by a factor of $\approx$1.4 for the latter. The use of standard sirens is therefore able to break the degeneracy between A and Ω_m and to help in constraining deviations from the distance duality relation, thus allowing us to test whether or not the BAO results are affected by the possible issues we described above. Nevertheless,

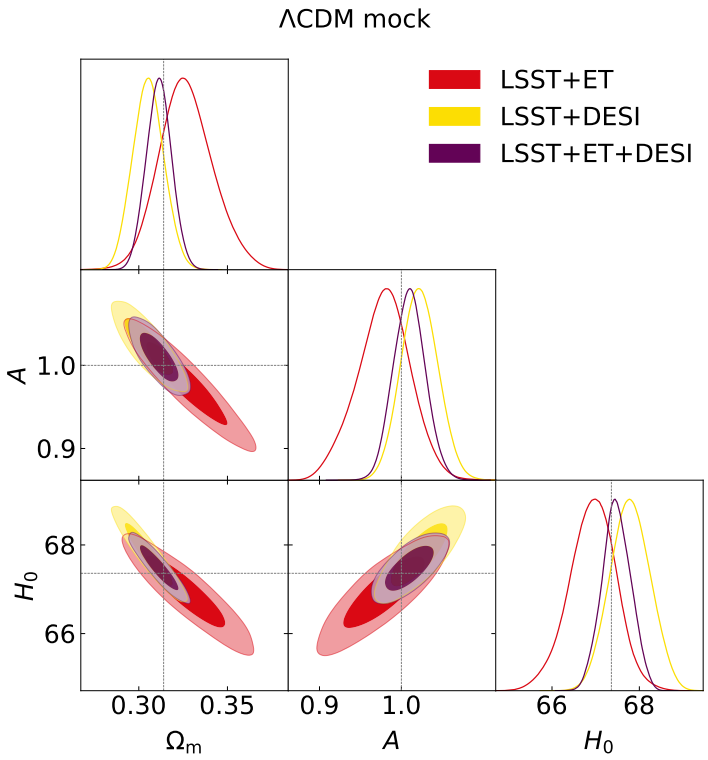

Figure 39: Constraints on H_0, Ω_m and the photon–axion decay model parameter A for electromagnetic distance duality relation breaking, using a mock obtained with a ΛCDM cosmology. The combinations of LSST+ET, LSST+DESI and LSST+ET+DESI are shown in red, yellow and purple respectively.

it is possible to notice in Figure 39 how the $A - \Omega_m$ degeneracy is not completely broken by the use of ET data, with the Ω_m posterior moving towards high values because of this effect.

Combining all datasets together the constraints on distance duality relation violations are improved with respect to the LSST+ET and LSST+DESI cases, and we achieve a 2% constraint on A.

6.4 MODIFIED GRAVITY EFFECTS ON THE LUMINOSITY DISTANCE

In section 6.3 we have shown how the use of gravitational wave observations alongside Type Ia supernovæ allows us to obtain results competitive with the use of BAO on violations of the distance duality relation, while at the same time avoiding the possible assumptions underlying the determination of the BAO data.

	LSST+ET	LSST+DESI	LSST+ET+DESI
H_0	66.87 ± 0.54	67.75 ± 0.47	67.44 ± 0.36
$\Omega_{\rm m}$	0.328 ± 0.015	0.3056 ± 0.0090	0.3116 ± 0.0077
A	0.977 ± 0.033	1.023 ± 0.023	1.010 ± 0.020

Table 14: Mean values and marginalised 68% confidence level errors for H_0, $\Omega_{\rm m}$ and A for the three combinations of mock datasets considered.

However, several effects can alter the propagation of gravitational waves leading to $d_L^{\rm GW}(z) \neq d_L^{\rm bare}(z)$. If such effects are not properly taken into account, the analysis we proposed above can lead to inaccurate results, with a bias introduced on the estimation of cosmological parameters.

In order to show this possible setback in the use of gravitational waves, in this chapter we focus on theories alternative to general relativity, such as theories that generalise the Einstein–Hilbert action by adding non-minimally coupled scalar fields or higher order covariant terms; in such cases, we expect modifications to the terms of (198). Changes to the $k^2 h_{\mathcal{A}}$ term cause the speed of propagation of gravitational waves (c_T) to vary and are therefore extremely constrained by the observations of the event GW170817 [81], which determined the relative difference between c_T and the speed of light to be $\mathcal{O}(10^{-15})$.

However, such constraints are obtained for $z \lesssim 0.1$, thus in principle a time-varying speed of the gravitational wave propagation could be allowed at higher redshifts. Changes to the friction term of gravitational wave propagation are also not excluded, so overall we can consider the modified propagation equation of the form [305, 306]

$$h''_{\mathcal{A}}(\tau,k) + 2\mathcal{H}[1-\delta(\tau)]h'_{\mathcal{A}}(\tau,k) + k^2 c_T(\tau)^2 h_{\mathcal{A}}(\tau,k) = 0, \qquad (200)$$

where $\delta(\tau)$ parameterises deviations from general relativity and is assumed to be scale independent. It can be shown that such a modification to the gravitational wave propagation leads to a departure of the gravitational wave luminosity distance from $d_L^{\rm bare}(z)$ [305, 307],

$$d_L^{\rm GW}(z) = \sqrt{\frac{c_T(z)}{c_T(z=0)}}\exp\left\{\left[-\int_0^z \frac{\delta(z')}{1+z'}dz'\right]\right\}(1+z)\int_0^z \frac{c_T(z')}{H(z')}dz\,, \qquad (201)$$

which reduces to the standard luminosity distance for $\delta(z) = 0$ and $c_T(z) = c$. In what follows we assume that the bound on c_T provided

by GW170817 holds at all redshifts, and therefore, setting $c_T(z) = c$, the previous equation reduces to

$$d_L^{\rm GW}(z) = \exp\left\{\left[-\int_0^z \frac{\delta(z')}{1+z'}dz'\right]\right\}(1+z)\int_0^z \frac{c}{H(z')}dz \tag{202}$$

$$= \exp\left\{\left[-\int_0^z \frac{\delta(z')}{1+z'}dz'\right]\right\} d_L^{\rm bare}(z). \tag{203}$$

To connect this expression to non-standard theories of gravity, we can use the relation between $\delta(\tau)$ and a time-varying effective Planck mass[3], $M_{\rm eff}$ [307],

$$\delta(\tau) = -\frac{d\ln M_{\rm eff}}{d\ln a}, \tag{204}$$

which means we can rewrite (202) as

$$\frac{d_L^{\rm GW}(z)}{d_L^{\rm bare}(z)} = \frac{M_{\rm eff}(0)}{M_{\rm eff}(z)}. \tag{205}$$

Since the effective Planck mass is related to the effective Newton's constant, $G_{\rm eff} \propto 1/M_{\rm eff}^2$, we can recast this as

$$\frac{d_L^{\rm GW}(z)}{d_L^{\rm bare}(z)} = \sqrt{\frac{G_{\rm eff}(z)}{G_{\rm eff}(0)}}. \tag{206}$$

An example of a non-standard theory that results in a time-varying Newton's constant can be found by examining the well-known Horndeski action, which describes the most general four dimensional Lorentz invariant scalar-tensor theory that produces second-order equations of motion[4] [139]. The action is given by

$$S = \int d^4x\sqrt{-g}\left[\sum_{i=2}^{5}\mathcal{L}_i + \mathcal{L}_m\right], \tag{207}$$

3 As noted by [307], this relation is not universally true for every theory of modified gravity and so a non-zero $\delta(\tau)$ should not be immediately associated with a time-varying Planck mass. However, for the purpose of our investigation, it is a suitable choice.

4 We note that it was very recently shown how a combination of Type Ia supernovæ and gravitational wave events would be able to probe dark energy fluctuations and a possible running of the Planck mass in the context of Degenerate Higher-Order Scalar-Tensor (DHOST) theories [308].

where the Lagrangian densities $\mathcal{L}_i$ are

$$\mathcal{L}_2 = G_2(\phi, X), \tag{208}$$
$$\mathcal{L}_3 = G_3(\phi, X)\Box\phi, \tag{209}$$
$$\mathcal{L}_4 = G_4(\phi, X)R + G_{4X}(\phi, X)[(\Box\phi)^2 - (\nabla_\mu\nabla_\nu\phi)^2], \tag{210}$$
$$\mathcal{L}_5 = G_5(\phi, X)G_{\mu\nu}\nabla^\mu\nabla^\nu\phi - \frac{1}{6}G_{5X}(\phi, X)[(\Box\phi)^3 - 3\Box\phi(\nabla_\mu\nabla_\nu\phi)^2 + 2(\nabla_\mu\nabla_\nu\phi)^3], \tag{211}$$

where $X = -\frac{1}{2}\partial_\mu\phi\partial^\mu\phi$ is the kinetic term, R is the Ricci scalar, $G_{\mu\nu}$ is the Einstein tensor, and ϕ is the additional scalar field of the Horndeski theory. Minimally coupled matter fields are contained in $\mathcal{L}_m$. The action is simplified by the binary neutron star merger constraint on the tensor speed, which implies that $G_{4X} = G_5 \approx 0$.

Theories with a surviving quartic Galileon term G_4 result in a time-varying Planck mass, $M(t) = M_P\sqrt{G_4(\phi)}$, which corresponds to an effective Newton's constant [309]

$$G_{\text{eff}}(t) = \frac{G_N}{G_4(\phi)}. \tag{212}$$

Note that here we focus on the effect of a time-varying Planck mass and not on the effective Newton's constant $G_{\text{eff}}(z, k)$ which has a k dependence and manifests as the effective gravitational constant between two test masses. This k dependence manifests itself for example in first-order perturbation theory of $f(R)$ and scalar-tensor models [310, 311, 312, 313, 314] and in generalised scalar-tensor models of the $f(R, \phi, X)$ type, where X is the kinetic term as above. In this case the effective Newton's constant $G_{\text{eff}}(z, k)$ is given by [310]

$$G_{\text{eff}}(z, k) = \frac{1}{F}\frac{f_{,X} + 4\left(f_{,X}\frac{k^2}{a^2}\frac{F_{,R}}{F} + \frac{F_{,\phi}^2}{F}\right)}{f_{,X} + 3\left(f_{,X}\frac{k^2}{a^2}\frac{F_{,R}}{F} + \frac{F_{,\phi}^2}{F}\right)}, \tag{213}$$

where $F = f'(R) = f_{,R}$ and $F_{,R} = F'(R)$. However, as mentioned earlier, we will not consider this k dependence here, only assuming a time dependence of the effective Newton's constant, which implies only a time-varying Planck mass, as in (212).

In theories where Newton's constant is associated with a time-varying Planck mass, the peak luminosity of Type Ia supernovæ will also exhibit a dependence on the time variation. This is due to the fact that the peak supernova luminosity is proportional to the mass of nickel synthesised in the supernova [315], which is a fixed fraction

of the Chandrasekhar mass $M_{\rm Ch}$. The latter varies as $M_{\rm Ch}{\sim}G_{\rm eff}^{-3/2}$, and as a result the supernova peak luminosity varies as $L{\sim}G_{\rm eff}^{-3/2}$. Thus, the absolute magnitude of the Type Ia supernovæ will acquire a correction of the form [316]

$$M(z) = M_0 + \frac{15}{4}\log_{10}\left[\frac{G_{\rm eff}(z)}{G_{\rm eff}(0)}\right], \tag{214}$$

where $G_{\rm eff}(0) \equiv G_N$ is the current value of Newton's constant as measured in a Cavendish experiment in a laboratory setting. This equation implies that the distance modulus now also acquires an extra correction of the form

$$\begin{aligned}\mu(z) &\equiv m(z) - M(z)\\ &= 5\log_{10} d_{\rm L}^{\rm EM}(z) + 25 - \frac{15}{4}\log_{10}\left(\frac{G_{\rm eff}(z)}{G_{\rm eff}(0)}\right).\end{aligned} \tag{215}$$

We note that the effect of modified gravity on the observables shows an interesting similarity with models in which the fine structure constant α is allowed to vary in redshift. In such models, there is also a dependency of the observables on the ratio of α taken at different redshifts (emission and observation). The similarity arises from the fact that in modified gravity theories falling into the class of scalar-tensor theories, the additional scalar degree of freedom produces a non-minimal coupling to the matter sector in the Einstein frame. This is similar to what happens in varying α models, where an additional scalar degree of freedom is coupled with the electromagnetic sector and impacts cosmological observables in a similar way [317].

Despite assuming a modified theory of gravity, we still fix the background expansion history in our model to that of a flat ΛCDM model, with fiducial parameters as discussed in section 6.3, and neglect possible deviations introduced by modifications of gravity. Such a choice is common in the investigation of modified gravity theories, see e.g. [61], and it arises from the tight constraints that current data place on most of these theories, making their background expansions almost identical to that of ΛCDM; as an example, current data constrain $f(R)$ theories, included in the Horndeski class described above, to a level in which any deviation from the standard behaviour needs to be in the perturbation sector, since the allowed parameter space produces a background that mimics that of ΛCDM [318, 319, 320].

We should point out that recent studies on the absolute magnitude dependency on $G_{\rm eff}$ have brought the relation of (214) and (215) into question. On the one hand it was proposed that even though

the Chandrasekhar mass varies as $M_{\rm Ch}\sim G_{\rm eff}^{-3/2}$, there are other effects that cause the effective luminosity of the Type Ia supernovæ to scale as $L\sim G_{\rm eff}^{3/2}$, and thus the $G_{\rm eff}$ term in the absolute magnitude would have the opposite sign [321]. On the other hand it was also suggested that the scaling of the Chandrasekhar mass in terms of $G_{\rm eff}$ needs to be revised completely, and a relation $M_{\rm Ch} \propto G_{\rm eff}^{-1}$ should be considered, resulting in an absolute magnitude given by $M(z) = M_0 + \frac{5}{2}\log_{10}\left[G_{\rm eff}(z)/G_{\rm eff}(0)\right]$ [309].

While the dependence on the specific parameterisation is important, we choose to use the standard expression as given by (214) since we are only interested in modelling the effects of the modified gravity model. Furthermore, we are only interested in demonstrating how big the effects of modified gravity can be, so we use the aforementioned parameterisation as it is representative of this class of models but also broad enough at the same time.

In order to parameterise the time evolution of Newton's constant, we consider a parameterisation for $G_{\rm eff}$ of the form [322]

$$\frac{G_{\rm eff}(z)}{G_N} = 1 + g_a\left(\frac{z}{1+z}\right)^n - g_a\left(\frac{z}{1+z}\right)^{2n}, \tag{216}$$

which is equal to unity at both early and late times, thus recovering the standard value of Newton's constant, but allowing it to vary in between. This parameterisation is actually a Taylor expansion of Newton's constant $G_{\rm eff}$ around $a = 1$ and then expressed in terms of redshift z via $a = \frac{1}{1+z}$. In [322], it was shown that this parameterisation can successfully fit the growth rate and CMB data, and due to its specific form it also allows us to avoid the stringent bounds imposed both at low redshift by Solar system tests [322] and at high redshifts by Big Bang nucleosynthesis [323].

In this chapter, we want to assess how neglecting modified gravity effects in gravitational wave propagation might lead to a false detection of distance duality relation violations. In order to quantify this effect we follow the same approach of section 6.3 to generate mock datasets, this time using a fiducial cosmology that assumes the presence of modifications of gravity, but no violations of the standard distance duality relation. Therefore, we set $A = 1$, $n = 2$ and generate two mocks with $g_a = 0.1$ and 0.5 that we call MG-low and MG-high respectively. The former value of g_a is consistent data, while the latter is not, as CMB lensing severely limits the available parameter space [322].

The value $g_a = 0.5$ is considered here as an extreme case, as an example that strongly highlights the degeneracy between the electro-

magnetic and gravitational wave sectors. Notice that while the BAO dataset is assumed to be unchanged, both the Type Ia supernovæ and gravitational wave observations are affected by the variation of $G_{\rm eff}$, according to (215) and (206) respectively.

6.4.1 *Modified gravity as a contaminant for distance duality relation constraints*

We now analyse the datasets obtained with a fiducial cosmology which includes a variation of Newton's constant, but still following the same procedure used in section 6.3, i.e. assuming (wrongly) that the only mechanism that enables a deviation from the ΛCDM expectations is the decay of photons into axions. We expect that this assumption will lead to a biased estimation of cosmological and distance duality relation parameters, and we therefore want to quantify the false detection of distance duality relation violation that might arise when analysing data.

We report the results of this analysis on both the MG-low and MG-high datasets in Table 15 with the contours of the free parameters $\Omega_{\rm m}$, H_0 and A shown in Figure 40, with the g_a parameter fixed to its standard value of 0, which means that in our analysis $G_{\rm eff}(z) = G_N$.

We find that the cosmological and distance duality relation parameters are significantly biased in the MG-high case when the underlying fiducial modified gravity cosmology is neglected, a bias that also appears in the MG-low case, albeit not as significant. For the latter, we find a false detection of distance duality relation violations reaching $\approx 4\sigma$, with the parameters $\Omega_{\rm m}$ and H_0 compatible with the fiducial cosmology within at most 2σ.

Instead, in the MG-high case, the LSST+DESI data still recovers the fiducial values of $\Omega_{\rm m}$ and H_0 within 2σ, but it now shows a striking false detection of $A \neq 1$ at $\approx 10\sigma$. Such a false detection is also present in the LSST+ET case, with similar significance, but in this case the cosmological parameters are also significantly biased away from their fiducial values ($\approx 4\sigma$ for $\Omega_{\rm m}$ and $\approx 2\sigma$ for H_0).

Therefore, the two results are in tension with each other, a hint that despite both cases showing a strong detection of distance duality relation violations, the mechanism considered is not sufficient to reproduce the observational data. We also report the combination of LSST+ET+DESI, even though such a combination is not very statistically sound, given the tension between the LSST+ET and LSST+DESI

	MG-low		
	LSST+ET	LSST+DESI	LSST+ET+DESI
H_0	$67.16^{+0.34}_{-0.38}$	67.88 ± 0.45	67.36 ± 0.26
Ω_m	0.308 ± 0.011	0.3001 ± 0.0087	0.3074 ± 0.0058
A	1.076 ± 0.028	1.093 ± 0.024	1.076 ± 0.019
	MG-high		
	LSST+ET	LSST+DESI	LSST+ET+DESI
H_0	66.50 ± 0.40	67.09 ± 0.47	66.39 ± 0.30
Ω_m	0.279 ± 0.011	0.3213 ± 0.0093	0.3228 ± 0.0069
A	1.419 ± 0.036	1.302 ± 0.029	1.299 ± 0.024

Table 15: Mean values and marginalised 68% confidence level errors for H_0, Ω_m and A for the three combinations of mock datasets considered, with the results for the MG-low and MG-high mocks shown separately.

results shown in Figure 40. We therefore make no further comment on this.

6.4.2 *Simultaneous modified gravity and distance duality relation constraints*

As a consequence of the false detection discussed in subsection 6.4.1, should a cosmological analysis find evidence for deviations from the distance duality relation, an analysis allowing for modifications of gravity should also be performed, as we have shown that its effects could be mistaken for violations of the distance duality relation.

Hence, we again analyse the MG-low and MG-high datasets, this time including g_a as a free parameter, thus allowing for a redshift evolving Newton's constant. Notice that here we fix the parameter n that enters into (216) to its fiducial value of 2, which is the minimum value allowed from Solar system tests [322].

Performing this analysis, we find a significant degeneracy between the A and g_a parameters, both in the LSST+DESI and LSST+ET combination, which make the posterior distributions very difficult to reconstruct through the Metropolis–Hastings MCMC approach we generally follow in this thesis. It is easy to see the degeneracy in the LSST+DESI case, as the distance modulus we compare with Type Ia

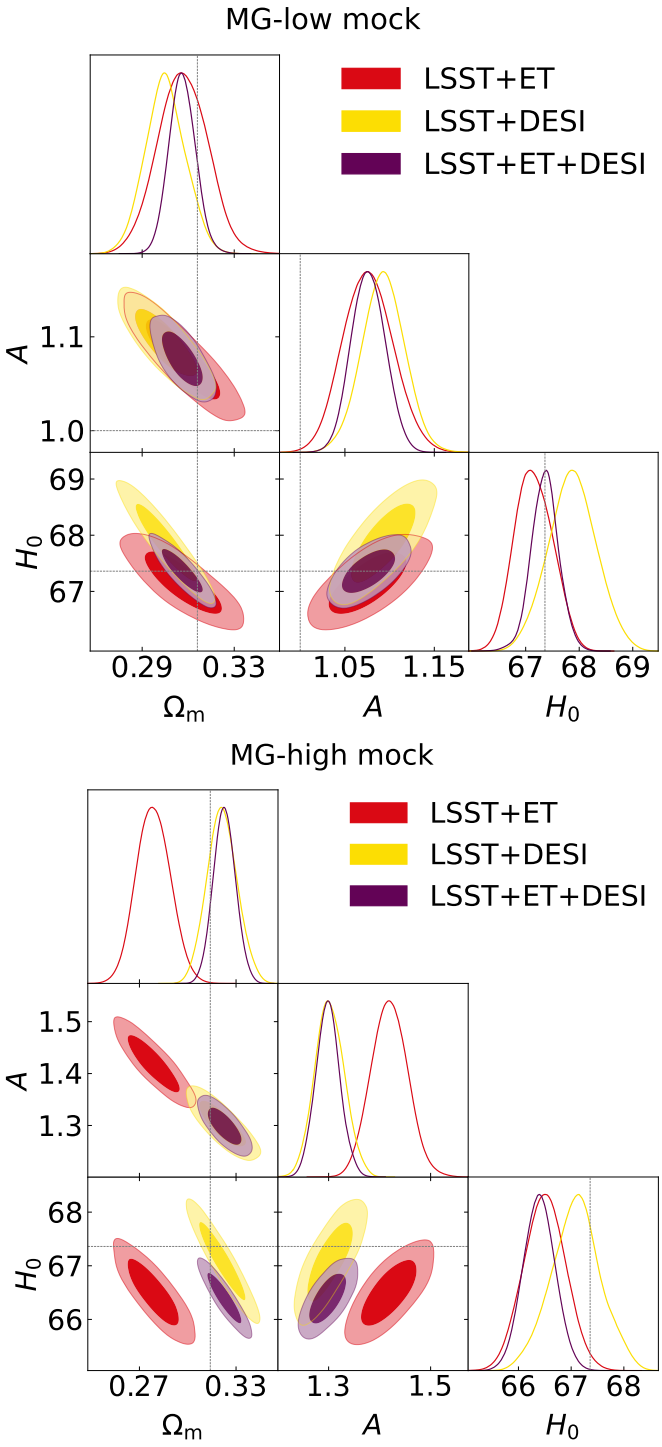

Figure 40: Constraints on H_0, Ω_m and the photon–axion decay model parameter A for electromagnetic distance duality relation breaking, using a mock obtained with a modified gravity cosmology (MG-low in the top panel, MG-high in the bottom panel). The combinations of LSST+ET, LSST+DESI and LSST+ET+DESI are shown in red, yellow and purple respectively.

supernovæ data is given by (215) which can also be written, substituting (183), as

$$\mu(z) = 5\log_{10} d_{\rm L}^{\rm bare}(z) + 25 - \frac{5}{2}\log_{10}\left[\mathcal{P}_{\rm inc}(z)\left(\frac{G_{\rm eff}(z)}{G_{\rm eff}(0)}\right)^{\frac{3}{2}}\right]. \quad (217)$$

It is clear how A, which enters into the expression of $\mathcal{P}_{\rm inc}(z)$, and g_a, which governs the deviations from G_N, can compensate each other to reproduce the mock data. As BAO are not sensitive to either of these parameters, this degeneracy will not be broken and the two parameters will be practically unconstrained.

One would expect the combination of LSST+ET not to suffer from this, as the gravitational waves are only sensitive to g_a and should therefore break such a degeneracy. However, a variation of g_a from its fiducial value can be partially compensated through a change in $\Omega_{\rm m}$ when analysing the ET datasets, since ET has less constraining power than DESI on this parameter. This means that the degeneracy between g_a and A is also present in this combination and the parameters remain unconstrained.

We show this degeneracy in Figure 41 for the MG-low analysis; this result highlights the importance of combining these three observables when one wants to analyse both possible deviations from standard cosmology. Indeed, the addition of DESI to the LSST+ET combination breaks the degeneracy between g_a and $\Omega_{\rm m}$ in the analysis of ET data and, consequently, also breaks the degeneracy between g_a and A, leading to strong constraints on both parameters.

We report these constraints in Table 16, where we find that when combining LSST+ET+DESI we can constrain A at the level of $\approx$3% even when the g_a parameter is allowed to vary, with constraints of $\approx$60% and $\approx$11% for the latter in the MG-low and MG-high cases respectively.

6.4.3 *Impact of modified gravity screening mechanisms*

Throughout this section we have included modified gravity effects in our analysis, implicitly assuming that for all the scales of interest these act in the same way. However, in modified gravity theories such as the well-known $f(R)$ [324], the equivalent scalar degree of freedom may develop an environment-dependent mass at small scales or when acting in a high density region. This dependence then makes the scalar field heavy enough that it screens the modifications of gravity, rendering them undetectable at those scales.

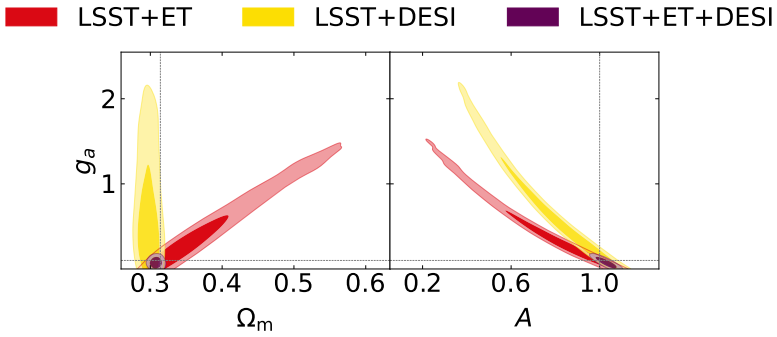

Figure 41: Constraints on Ω_m, the photon–axion decay model parameter A for electromagnetic distance duality relation breaking, and the Newton's constant variation amplitude g_a. The results are obtained using a mock obtained with the MG-low fiducial cosmology. The combinations of LSST+ET, LSST+DESI and LSST+ET+DESI are shown in red, yellow and purple respectively.

	MG-low	MG-high
	LSST+ET+DESI	LSST+ET+DESI
H_0	67.45 ± 0.26	67.29 ± 0.33
Ω_m	0.3079 ± 0.0058	$0.3174^{+0.0067}_{-0.0075}$
A	1.030 ± 0.033	1.002 ± 0.033
g_a	0.077 ± 0.046	0.482 ± 0.052

Table 16: Mean values and marginalised 68% confidence level errors for H_0, Ω_m, A and g_a for the full combination of our mock datasets LSST+ET+DESI.

A number of these screening mechanisms have been proposed, such as the chameleon screening [325] or the Vainshtein mechanism [326, 327] and it is clear that in the regimes of interest for our observables, i.e. the explosion of Type Ia supernovæ and the merging of binary neutron stars, one or other of these mechanisms might be active. The impact of screening on the observables we consider is rather difficult to predict, with the final result being strongly dependent on the specific mechanism at play.

Focusing on gravitational wave propagation, and assuming that screening is active at the density and energy scales of the binary merger, the chameleon and Vainshtein mechanisms lead to different results; in the latter modifications are screened at the merger but still impact the propagation of the waves (see e.g. [328]), in the former, any anomalous gravitational wave propagation might instead be completely screened away [309, 329].

Here, we take a phenomenological approach and simply look at the case in which screening completely removes any modification to our observables, either in the explosion of the Type Ia supernovæ or in the propagation of gravitational waves from the binary neutron star mergers. We do not consider the case in which the screening mechanism is active in both these astrophysical phenomena, as the resulting observations would be indistinguishable from the ΛCDM cosmology we assumed in section 6.3.

In order to investigate this scenario we consider our MG-high settings, i.e. a departure from G_N as parameterised in (216) with $g_a = 0.5$ and $n = 2$, but removing the modified gravity effects from either Type Ia supernovæ or gravitational waves. We analyse these datasets, again assuming that no modified gravity effect is taking place, in order to assess the false detection of a distance duality relation violation. The results are shown in Figure 42, with the top panel obtained assuming gravitational waves are screened and Type Ia supernovæ are not, and the bottom assuming the opposite.

We find that when gravitational waves are screened but Type Ia supernovæ are not, both the LSST+ET and LSST+DESI combinations find a false detection of distance duality relation violation, as the unscreened supernovæ dataset appears in all combinations.

If instead the supernovæ are not affected by modified gravity, while gravitational waves are, the modified gravity effects only enter in the ET dataset. The combinations including this dataset are therefore biased away from the fiducial cosmology, meaning only the LSST+DESI combination correctly recovers the fiducial. If such a situ-

ation were to arise in real data, it could provide potential smoking gun for the effects of a modified gravity model with this type of screening behaviour.

6.5 MACHINE LEARNING RECONSTRUCTIONS

We now consider a machine learning approach that can be used for non-parametric reconstruction of a given data set, called genetic algorithms. Genetic algorithms follow a stochastic approach based on the genetic operations of crossover and mutation, in order to express the notion of grammatical evolution of a population of test functions applied to data reconstruction.

In other words, genetic algorithms emulate the notion of evolution via natural selection; a given population changes and adapts to its environment under pressure from the stochastic operators of crossover, i.e. a random change in the chromosomes of an individual, and mutation, i.e. the merging of different individuals to form descendants, usually called offspring. Then, the probability that the members of the population will produce offspring, or equivalently their reproductive success, is assumed to be proportional to their fitness. The latter is a measure of how well the members of the population fit the data and in our analysis we take this to be a standard χ^2 statistic, as introduced in Chapter 2. For various applications to cosmology and more details on genetic algorithms see [330, 284, 285, 331, 332, 333, 334, 335, 336].

The process followed to fit the LSST, DESI and ET data using genetic algorithms is the following. First, an initial group of functions, called the initial population, is created based on a set of orthogonal polynomials which are called the grammar. This step is crucial, as the choice of the grammar has been shown to directly affect the rate at which the genetic algorithms code converges [284]. This initial population is then set up in such a manner that both the duality parameter $\eta(z)$ and $d_L(z)$ are encoded simultaneously by every member of the population.

At this point we may also demand that the targeted functions that are to be reconstructed, i.e. $\eta(z)$ and $d_L(z)$, satisfy a set of initial conditions or physical priors. For example, these priors might be that the duality parameter satisfies $\eta(z = 0) = 1$ or that the luminosity distance today is zero, i.e. $d_L(z = 0) = 0$, but in our analysis we remain completely agnostic with respect to the expansion history of the Uni-

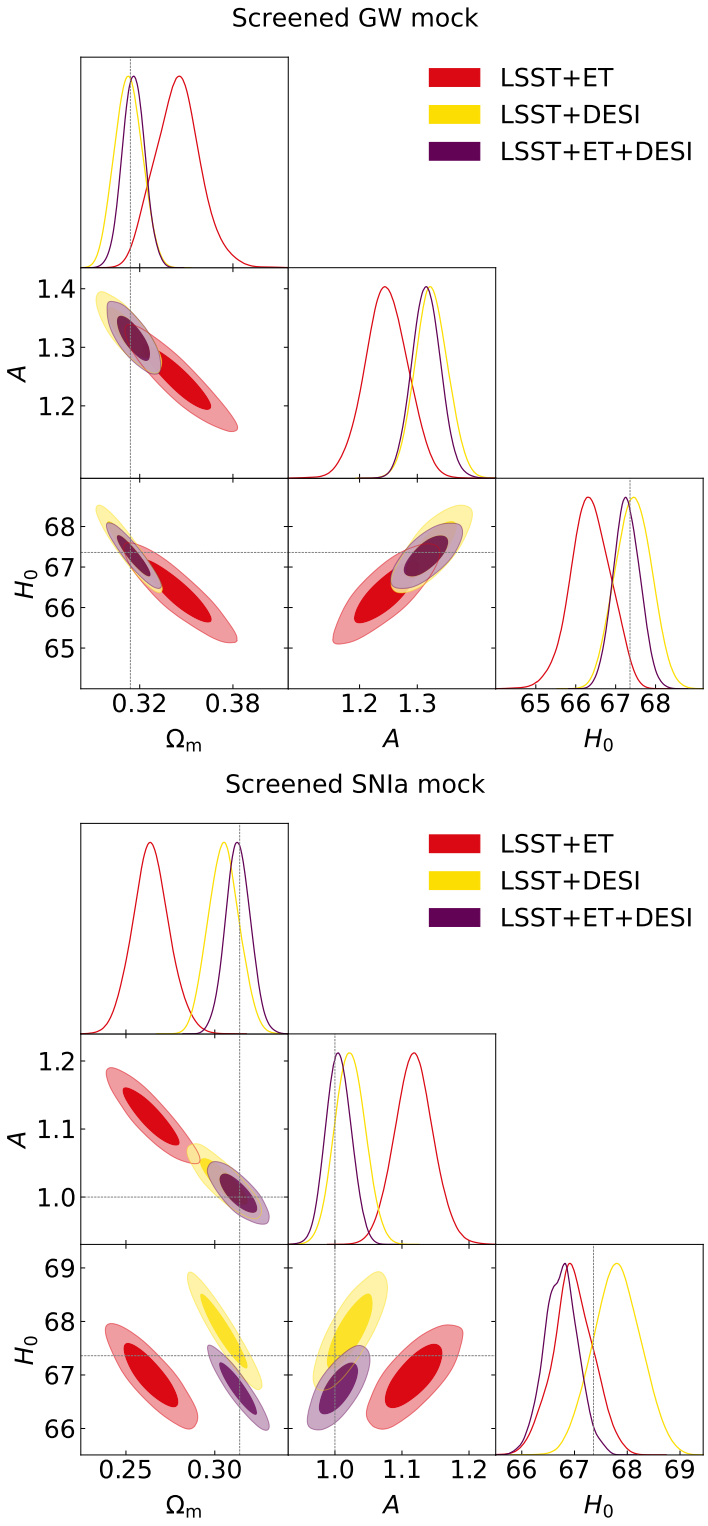

Figure 42: Constraints on H_0, Ω_m, and the photon–axion decay model parameter A for electromagnetic distance duality relation breaking. The results are obtained using a mock obtained the MG-high cosmology. In the top panel only the modified gravity effects on gravitational wave propagation are screened, while in the bottom panel the screening only acts on the Type Ia supernovæ. The combinations of LSST+ET, LSST+DESI and LSST+ET+DESI are shown in red, yellow and purple respectively.

verse and we do not assume any specific model for it, as well as for the distance duality relation deviation mechanism.

As mentioned earlier, the fitness of every member of the population is estimated with a χ^2 statistic, using the LSST, DESI and ET data. After that, the crossover and mutation stochastic operators are applied to a subset of the best fitting functions, which are chosen via tournament selection [284]. This procedure is subsequently repeated hundreds of times in order to ensure the convergence of the genetic algorithms code. We also repeat the analysis with several different random seeds, so as to avoid biasing the fit because of the choice of a specific random seed.

In order to provide error bounds on the reconstructions, we follow the approach of [285, 335], where the error regions are estimated using a path integral calculation over the functional space scanned by the genetic algorithms. This approach was compared against bootstrap Monte Carlo error estimates and its accuracy was thus validated [285]. The specific numerical implementation of the genetic algorithms we use in our analysis is based on the publicly available code `Genetic Algorithms`[5].

6.5.1 *Results*

In the genetic algorithms approach we reconstruct the quantities $d_L^{\rm bare}(z)$, $\eta_{\rm EM}(z)$ and $\eta_{\rm GW}(z)$, where the latter two are defined as

$$\eta_{\rm EM}(z) = \frac{d_L^{\rm EM}(z)}{d_L^{\rm bare}(z)}, \tag{218}$$

$$\eta_{\rm GW}(z) = \frac{d_L^{\rm GW}(z)}{d_L^{\rm bare}(z)}, \tag{219}$$

and $\eta_{\rm GW}(z)$ can also be related to the effective Newton's constant $G_{\rm eff}(z)$ via (205) as

$$\eta_{\rm GW}(z) = \sqrt{\frac{G_{\rm eff}(z)}{G_{\rm eff}(0)}}. \tag{220}$$

Note that in general relativity and the ΛCDM model, both $\eta_{\rm EM}(z)$ and $\eta_{\rm GW}(z)$ are exactly equal to unity, hence any deviation from that value would hint towards new physics, either in the electromagnetic or modified gravity sector respectively.

5 https://github.com/snesseris/Genetic-Algorithms

Having analysed the LSST, DESI and ET data with genetic algorithms, in what follows we now present the reconstructions of the two duality parameters. First, in Figure 43 we show the genetic algorithms reconstruction of $\eta_{\rm EM}(z)$ (left) and $\eta_{\rm GW}(z)$ (right) using the ΛCDM mock, while the orange shaded region corresponds to the 1σ errors. As expected, in both cases the reconstructions are in perfect agreement with unity within the errors and the mean value of the genetic algorithms result follows exactly the fiducial value of the mock.

Next, we examine the results from the MG-low and MG-high mocks. In particular, we show the results of the genetic algorithms reconstruction of $\eta_{\rm EM}(z)$ (left) and $\eta_{\rm GW}(z)$ (right) in Figure 44 and Figure 45 respectively for the two mocks. In these plots, we also show the theoretical value of the $\eta_{\rm GW}(z)$ with a dot-dashed black line, using the values $n = 2$ and $g_a = (0.1, 0.5)$ for the MG-low and MG-high mocks respectively, while the orange shaded region corresponds to the 1σ errors. As can be seen, while the $\eta_{\rm EM}(z)$ reconstructions are in agreement with unity, the mean value of $\eta_{\rm GW}(z)$ follows perfectly the fiducial model until $z{\sim}1$ where the supernovæ data end, albeit the parameter is consistent with unity within the errors in both cases.

Finally, in Figure 46 we show the genetic algorithms reconstruction of $\eta_{\rm EM}(z)$ using the LSST+DESI (left) and LSST+ET (right) combinations of the MG-high mock, while the orange shaded region corresponds to the 1σ errors. In both cases, we assume that any possible deviation from the distance duality relation is sourced from the EM sector, thus we assume that there are no modified gravity effects, i.e. $G_{\rm eff} = G_N$ and $\eta_{\rm GW}(z) = 1$, in order to examine any possible biases between the EM and modified gravity sectors.

As can be seen in the left panel of Figure 46, in the case of the LSST+DESI data combination, the genetic algorithms reconstruction shows a deviation of the mean $\eta_{\rm EM}(z)$ from unity as in the case of the supernovæ alone any effect of the modified gravity mocks can be reabsorbed in the luminosity distance, thus rescaling it and affecting the distance duality relation. We also observe a similar behaviour for the other data combination, LSST+ET. Hence, in both cases we also confirm the finding of the parameterised approach that neglecting the modified gravity effects in the likelihood leads to biases in the recovered quantities. While some deviation from the fiducial value of $\eta(z)$ is found in these plots at high redshifts ($z \geq 1.5$), and this is compatible with the results of the parameterised approach, there is no a priori widely accepted method on how to quantify it. In principle however, this could be done through a comparison of the χ^2 values obtained for the genetic algorithms and fiducial model functions.

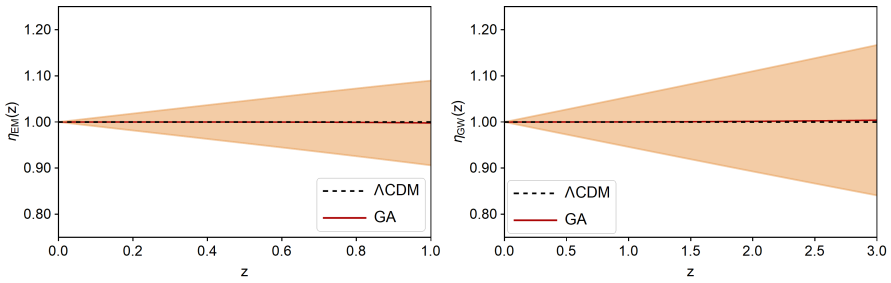

Figure 43: Reconstruction of $\eta_{\rm EM}(z)$ (left) and $\eta_{\rm GW}(z)$ (right) using the ΛCDM mock.

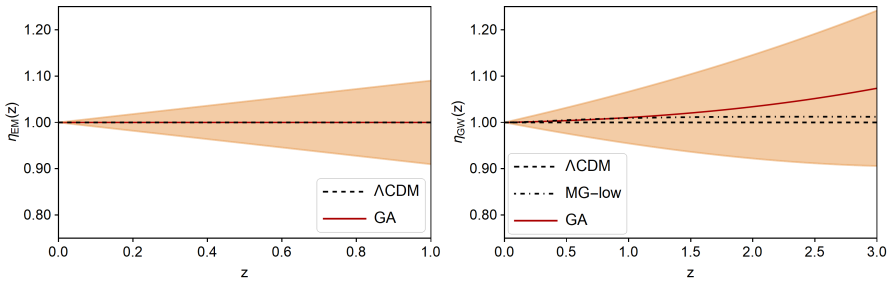

Figure 44: Reconstruction of $\eta_{\rm EM}(z)$ (left) and $\eta_{\rm GW}(z)$ (right) using the MG-low mock. The dot-dashed line corresponds to the fiducial model.

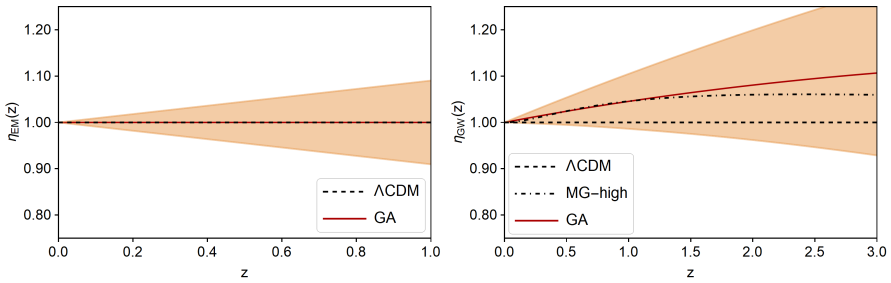

Figure 45: Reconstruction of $\eta_{\rm EM}(z)$ (left) and $\eta_{\rm GW}(z)$ (right) using the MG-high mock. The dot-dashed line corresponds to the fiducial model.

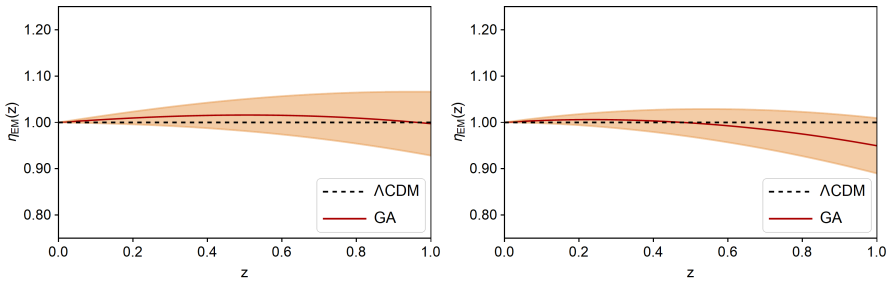

Figure 46: Reconstruction of $\eta_{\rm EM}(z)$ using the LSST+DESI (left) and LSST+ET (right) combinations of the MG-high mock. We assume no modified gravity effects in the likelihood.

6.6 SUMMARY

In this chapter, we assessed the capability of future gravitational wave observations to constrain the distance duality relation, alongside the commonly used observations of Type Ia supernovæ and BAO. Specifically, we investigated the constraining power of standard sirens both in combination with Type Ia supernovæ and BAO, and as an alternative to the latter, thus allowing us to overcome possible assumptions contained in the BAO data.

We firstly examined how the standard distance duality relation can be broken by a mechanism in which photons decay into axions in the presence of magnetic fields, demonstrating how standard sirens can break degeneracies between parameters, and improve the constraints on cosmological parameters as well as constraining the axion model parameter A, which encodes the amplitude of the deviation from the standard distance duality relation in this model.

We then explored how a generic toy model of modified gravity with a time-varying Newton's constant can alter the gravitational luminosity distance measured by standard sirens, while at the same time affecting the measurement of the distance modulus through Type Ia supernovæ observations. Using two mock datasets with different strengths of modified gravity, MG-low and MG-high, we showed how the distance duality relation breaking in the gravitational sector leads to a 4σ false detection of distance duality relation breaking in the electromagnetic regime via the photon–axion decay model in the case of the MG-low mock, if such modified gravity effects are not properly taken into account. The significance of the false detection rises to 10σ in the case of the MG-high mock.

This false detection demonstrates the powerful effect on the results of the parameter estimation pipeline of the assumptions made when running an MCMC analysis. Consequently, we showed that the effect can be mitigated by including the modified gravity parameter g_a in our analysis as a free parameter, although the strong degeneracy between this parameter, the axion model parameter A and the matter density parameter $\Omega_{\rm m}$ meant that reasonable constraints were only obtained by the full combination of the data, LSST+ET+DESI.

It is well known that many modified gravity models require a screening mechanism in order to evade stringent solar system constraints. We investigated the consequences of screening on our constraints, considering a case in which only the gravitational waves are screened, and a case in which only the Type Ia supernovæ are screened. In the

first case, we found yet another false detection of distance duality relation violation in the LSST+ET and LSST+DESI datasets, due to the presence of the unscreened supernovæ in both. In the case of screened supernovæ with unscreened gravitational waves, we found that any combination which includes the ET mock data was biased away from the fiducial cosmology, revealing a potential smoking gun for the presence of modified gravity, if such an effect were to be observed in real data.

Finally, we performed a non-parametric reconstruction of the distance duality parameter $\eta(z)$ using a specific machine learning approach, based on genetic algorithms. We showed that the genetic algorithms can correctly discriminate between the ΛCDM, MG-low and MG-high mocks, as in the case of the latter two the mean value of the $\eta_{\rm GW}(z)$ parameter found by the genetic algorithms shows deviations from unity and it follows the fiducial model perfectly in the range covered by the supernovæ (up to $z{\sim}1$). On the other hand, if we neglect the effects of modified gravity in the likelihood, then the reconstruction leads to biases as the genetic algorithms cannot discriminate the modified gravity from the electromagnetic effects, due to degeneracies in the parameters, something which is in agreement with the parameterised approach.

In conclusion, we have seen how mock datasets of standard siren events in combination with Type Ia supernovæ and baryon acoustic oscillations are an excellent way to understand the potential constraining power of future surveys when applied to the distance duality relation. However, as we have shown, rigorous checks of all possible degeneracies and biases should be carried out when using standard siren data in combination with other probes, to ensure that no false detections of beyond ΛCDM physics are accidentally made. With this important finding in mind, it becomes abundantly clear that, as our gravitational wave detectors continue to improve and the number of observed binary neutron star events begins to increase, standard sirens will become a vital part of future cosmological analyses.

7

DISCUSSION AND CONCLUSIONS

The story so far: in the beginning the Universe was created. This has made a lot of people very angry and been widely regarded as a bad move.

DOUGLAS ADAMS

The story so far: in this thesis, we have contended that the standard model of cosmology – or to be precise, the cosmological model in which gravity is described by general relativity with a spatially flat, homogeneous and isotropic background, in which the energy budget is dominated by a cosmological constant and cold dark matter – is under threat from both a theoretical and observational standpoint. The cosmological constant problem asserts that we either do not fully understand quantum physics or cosmology, and dilemmas like the H_0 tension cast doubt on the ability of ΛCDM to fully explain both low and high redshift cosmology.

We have therefore proposed that alternative models of dark energy should be considered and investigated, with the aim of resolving or relaxing one or more of these aforementioned problems. In particular, we focused on the concept of an interacting vacuum scenario, in which the vacuum is coupled to the dark matter, allowing for an exchange of energy between the two components. We further restricted the analysis of this scenario to the geodesic situation, in which there is no additional acceleration on the cold dark matter particles due to the interaction.

Such models could feasibly explain the H_0 tension by allowing for a growth of vacuum through the decay of dark matter at late times, thereby resulting in more acceleration and a higher value of H_0 at low redshift. To confront this scenario with observational data, we modified the public codes `CAMB` and `CosmoMC`, enabling exploration of the posterior distributions of the various model parameters and cosmological parameters of interest.

In the final part of the research work reported here, we expanded our scope to consider how observations of standard sirens could be used to probe violations of the distance duality relation, and highlighted the importance of understanding degeneracies and biases in the data

when testing the fundamental aspects of cosmology such as distance measurements.

7.1 SUMMARY OF RESULTS

In Chapter 3, we reported how we found little concrete evidence in favour of the interacting vacuum scenario in its most basic form, and furthermore, that (since the data generally prefers ΛCDM) it struggles to relax any cosmological tension in a meaningful or significant way.

In Chapter 4, we extended the analysis of the interacting vacuum scenario to reconstruct the interaction as a function of redshift, making use of a correlation prior to control the reconstruction. We also performed a Bayesian model comparison, again finding no conclusive evidence that the interacting vacuum scenario is preferred over ΛCDM by the data.

In Chapter 5, we explored a more complex version of the interacting vacuum scenario, in which a Shan–Chen equation of state is repurposed as the form of the coupling between the vacuum and cold dark matter. We found that two cases of this more complex and physically motivated form of the interaction were weakly favoured over ΛCDM, but that the constraints on the cosmological parameters in this model were still sufficiently tight that the H_0 tension was only slightly relaxed rather than completely resolved.

Finally, in Chapter 6, we shifted our investigation away from specific dark energy models to examine the implications of fundamental precision cosmology in greater detail. We considered the relationship between angular diameter and luminosity distances, a relationship that should remain unaltered provided spacetime is Riemannian and photon number is conserved. By considering a model of photon–axion decay, we used mock datasets to forecast future constraints on the distance duality relation, finding that standard sirens are an excellent alternative to the use of baryon acoustic oscillations, achieving a 3% constraint on the distance duality violation parameter in combination with Type Ia supernovæ.

We also found that a hidden modification of gravity that has different effects on the gravitational and electromagnetic luminosity distances can bias the results in this type of analysis, resulting in a false detection of a violation of the distance duality relation. Finally, by using this concept of false detections, we uncovered a new smoking gun

for modified gravity with a particular phenomenological screening behaviour.

7.2 METHODOLOGICAL PHILOSOPHY

The common methodological thread in this thesis was the use of the Boltzmann solver `CAMB` and the MCMC sampler `CosmoMC`. It is important to consider the effects on the results that the choice of code, and more fundamentally, the choice of sampling method could have had.

`CAMB` is now approaching its second decade of use as a tool in cosmology and has thus been robustly tested in many situations. Since the models studied in this thesis all have well-defined ΛCDM limits (and indeed, cannot depart from that standard model too far, otherwise they would not fit the data at all), it is unlikely that we ran the risk of falling foul of unknown numerical errors. Furthermore, if unphysical combinations of parameters are accidentally used, the programme will generally abort. Further fail-safes of this type can be written into the code by the user, as was done when implementing our alternative models.

The use of the Metropolis–Hastings MCMC method for sampling posterior distributions is a little more fraught with problems. By introducing new models that have never been studied before, setting reasonable priors can be challenging, and unforeseen parameter degeneracies may arise. Quite apart from any pathological problems that the choice of sampling method may produce, the computational time alone required to achieve a good level of convergence in the MCMC chains discourages any attempts to reproduce such results. This is not good for the general scientific well-being of the field.

The alternatives to using Metropolis–Hastings MCMC are few and far between when it comes to cosmological applications. There are a number of different Python implementations of MCMC algorithms, but these are generally far too cumbersome to use with a Boltzmann code (that could already run slowly due to the implementation of beyond ΛCDM models) and a likelihood with as many nuisance parameters as `plik18`, for example. This rules out samplers such as `emcee` [170] from being used for this type of investigation.

A different approach comes with using nested sampling, rather than Metropolis–Hastings MCMC. As previously mentioned, there is a cosmology-adapted code for this purpose called `CosmoChord`, which is an adaptation of `polychord`. Nested sampling deals much better

with multimodal distributions than Metropolis–Hastings MCMC but this can result in an increased computation time.

Since nested sampling essentially begins in the tails of the distribution, it can be somewhat unstable when used with `CAMB`, as the initial points chosen in the sampling will consequently be the most unphysical values of the parameters (if flat priors are used). This can be somewhat alleviated by imposing very tight priors, but this in turn may lead to an exclusion of areas of parameter space which are of interest.

We note that a new MCMC method, ensemble slice sampling, has recently been developed, which has excellent potential for cosmological applications [337]. A Python implementation of this method is publicly available as the `zeus` package [338], and an implementation that is designed for easy parallelisation and hence use on a cluster is under development[1].

Another tool we used in this thesis was the machine learning reconstruction method of Gaussian processes. As with any reconstruction, an increased number of data points will improve the result. This difference can be seen by comparing Figure 16 with Figure 21. The latter has four times as many data points, allowing finer details in the variation of the coupling function to be seen. The Gaussian process reconstruction can also learn from the errors on the data points that are given to it, resulting in a smaller error on the reconstruction in comparison to the cubic spline reconstruction shown in Figure 20.

The reconstruction that results from using Gaussian processes can depend fairly strongly on the kernel being used. This is highlighted in Figure 17. In this work, we have focused on using the most basic kernels that are provided in all Gaussian process or machine learning packages. However, it can be beneficial to combine these basic kernels, along with others, such as a white noise kernel, to better approximate the physical result or model that is being reconstructed.

This is difficult in the case of an interacting dark energy scenario, where we have little idea of how such an interaction might behave at intermediate redshifts, but it can be done successfully, for example when reconstructing the distance duality relation, (218). In this case, there is a hard physical prior on the reconstruction, as the luminosity and angular distances must exactly coincide at redshift zero. In [4], it was shown how a custom kernel can be used to almost exactly recover different fiducial models of distance duality violation using constraints from future observations of strongly lensed Type Ia su-

1 This package, `cronus`, is available at https://github.com/minaskar/cronus.

pernovæ. This emphasises the need to consider how tools can be best applied to the problem at hand, rather than used immediately out of the box.

The other machine learning tool used in this thesis was genetic algorithms, as discussed in Chapter 6. Genetic algorithms share some of the same pitfalls of Gaussian processes, in that the final result can be somewhat dependent on the hyperparameters chosen, such as the initial population size and the number of generations the algorithm evolves for. Furthermore, while the genetic algorithm method is good at finding a range of good fits or solutions, it may struggle to find the single most optimal solution, as the full extent of the parameter space is never explored. Again, this drives home the point that tools and methods should be carefully chosen according to the problem at hand, rather than indiscriminately deployed with the expectation of consistently useful and interpretable results.

7.3 WIDER IMPLICATIONS

Optimisation of computer programmes has been recognised as crucial since the days of Babbage and Lovelace [339]. The modern day ubiquity of personal computers, the rapid increase of processing power in laptops and desktop computers and the race to the bottom in the production and release of software have all led to computer programmes becoming generally less efficient. This is further exacerbated by the popularity of interpreted languages such as Python, which generally require little optimisation on the part of the casual user to run programmes successfully.

All of the work reported in this thesis required running computationally intensive jobs on a large high performance computing cluster. Depending on how the cluster is configured, and how well the programmes being run are optimised for parallelisation, such high performance computing can be as bad for the environment as telescope operations or aviation [340, 341, 342].

All of this combined leads to cosmology research of the type presented here having a heavy environmental footprint. Going forward, it is important that the field considers how computing power is used, and in particular, how programmes are written and optimised, especially for use on clusters. A focus on compiled languages in undergraduate teaching could also go some way to mitigating the environmental effects of inefficient programmes.

It is also important to note that not every researcher, potential researcher or student has access to a computing cluster, or even a basic personal computer. Arguably, the most important tenet of the scientific method is that experiments should be replicable by other parties, but if results are obtained using resources available to only a very small subset of all researchers, this infringes on the reproducibility of those results. Little can be done to change this in the short term, as widening access to resources naturally has many economic implications.

7.4 FUTURE DIRECTIONS

> *That which is in locomotion must arrive at the halfway stage before it arrives at the goal*[2].
>
> ZENO

At the beginning of this thesis, we asked three questions: is the cosmological constant the best explanation for dark energy? what is the reason for the H_0 tension? and how can we ensure our data are both precise and accurate?

We have proposed and extensively tested the interacting vacuum dark energy scenario as an attempt to address the first two questions, and investigated bias that could be induced by modified gravity in future standard siren observations in the context of constraints on the distance duality relation. Nevertheless, and fortunately for the health of the field of cosmology, concrete answers to all three questions still elude us.

Further research in the field of dark energy would do well to understand the behaviour of structure formation on non-linear scales in beyond ΛCDM models. While rather difficult and again, computationally expensive (as it would require running N-body simulations), this opens up far more observational data that could be used to constrain, or even completely rule out these types of models. This point was exemplified in Chapter 4, in which the DES data had to be aggressively cut to remove the non-linear scales before it could be used to obtain constraints on the interacting vacuum scenario.

Similarly, the discovery of potential observational signatures that can only be due to the specific model in question (i.e. smoking guns) is particularly desirable, as it would allow alternative models to be definitively ruled out, rather than churning out ever tighter con-

2 Attributed to Zeno by Aristotle, in *Physics* VI:9, 239b10.

straints on the model parameters in question as new and better data becomes available.

Another interesting avenue of related research would be an investigation into the question of Type Ia supernova standardisability. It was found in [41] that accounting for the effects of redshift-dependent luminosity in supernovæ can go some way to alleviating the H_0 and σ_8 tensions. However, the supernovæ catalogues themselves are not well able to constrain the parameters used to describe these systematic effects. An important next step will be to consider how another probe of the luminosity distance could be used to constrain these systematics and hence as a calibrator for supernovæ luminosities. Standard sirens are one such probe.

In conclusion, theory and observation in cosmology enjoy a productive symbiosis, in which observations generate new theories and theories point the way to future observational goals. The only thing that remains persistently clear is the vast amount we have left to learn about the physics of the cosmos. As cosmologists, our fate is akin to that of Zeno: we will always be halfway towards an answer to the many and varied questions about the Universe which our theories and observations continue to inspire.

A

MOCK DATASET CREATION

In this Appendix, we explain the procedure followed to create the mock datasets used in Chapter 6.

A.1 TYPE IA SUPERNOVÆ

Here we present the details of the Type Ia supernovæ mocks used in our analysis. In particular, we simulate Type Ia supernovæ observations based on the specifications of the Legacy Survey of Space and Time (LSST), performed by the Vera C. Rubin Observatory [298]. The LSST deep-drilling fields will observe $N_{\rm SNIa} = 8800$ Type Ia supernovæ in the redshift range $z \in [0.1, 1.0]$, for which we use the redshift distributions of [343]. Regarding the error budget of the observations, we follow [343] and for every event i we assign an observational error $\sigma_{{\rm tot},i}$ given by

$$\sigma^2_{{\rm tot},i} = \delta\mu^2_i + \sigma^2_{\rm flux} + \sigma^2_{\rm scat} + \sigma^2_{\rm intr}\,. \tag{221}$$

We have assumed that the contributions to the error due to the flux, scatter, and intrinsic uncertainties described in the previous equation are given by $\sigma_{\rm flux} = 0.01$, $\sigma_{\rm scat} = 0.025$, and $\sigma_{\rm intr} = 0.12$ respectively and are the same for all events. However, we also include an error on the distance modulus $\mu(z) = m(z) - M$,

$$\delta\mu_i = e_M\, z_i, \tag{222}$$

which evolves linearly in redshift, but now the parameter e_M is normally distributed with standard deviation $\sigma(e_M) = 0.01$ and vanishing mean [344, 343].

In Figure 47 we show the distance modulus of the LSST ΛCDM Type Ia supernovæ mock, along with the 1σ error bars of each point for the mock. The data points are in red, while the fiducial is in yellow. The error bars correspond to 1σ errors.

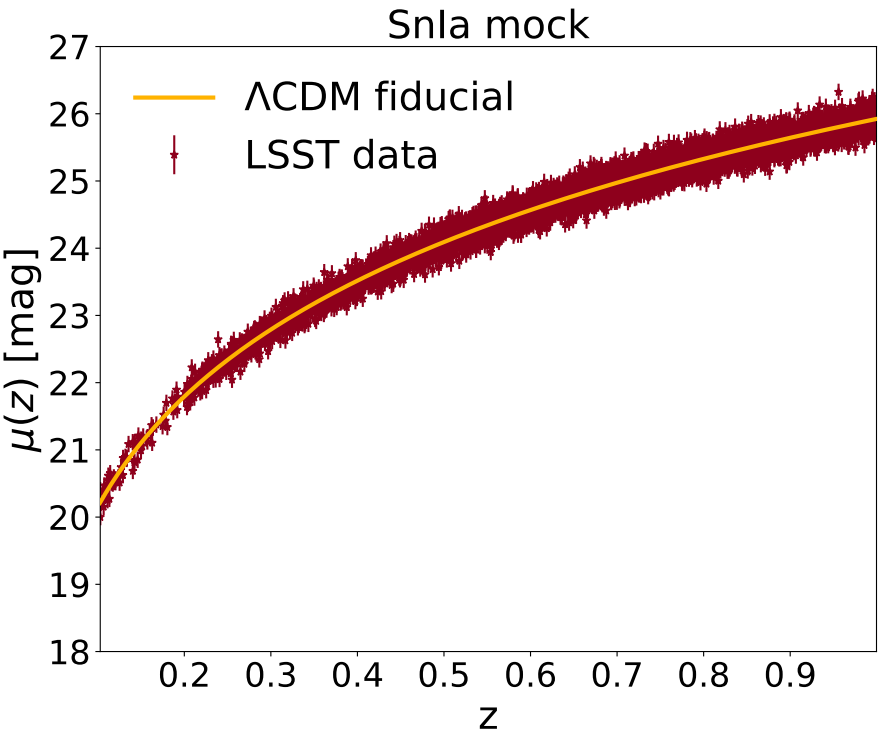

Figure 47: The distance modulus for the LSST ΛCDM Type Ia supernovæ mock as a function of redshift. The data points are in red, while the fiducial is in yellow. The error bars correspond to 1σ errors.

A.2 BARYON ACOUSTIC OSCILLATIONS

For the baryon acoustic oscillation mocks, we make use of the extended redshift range of the Dark Energy Spectroscopic Instrument [299], which will probe the large scale structure and expansion rate of the Universe. The DESI survey will measure the optical spectra of tens of millions of quasars and galaxies up to $z \sim 4$, so as to enable redshift space distortion and BAO analyses. Here we base our mock DESI data on the official forecasts for both the angular diameter distance $d_{\rm A}(z)$ and the Hubble parameter $H(z)$ [299].

The DESI survey will have a coverage of approximately 14,000 deg^2 and the main types of DESI targets will be quasars, emission line galaxies, luminous red galaxies and bright galaxies. The main DESI forecast measurements will cover the range $z \in [0.05, 3.55]$, with a precision that may depend on the target population. In particular, the DESI bright galaxies will be in the redshift range $z \in [0.05, 0.45]$ in five equispaced redshift bins, while the Lyα forest quasars will be in the range $z \in [1.96, 3.55]$ with eleven equispaced redshift bins. On the other hand, the luminous red galaxies and emission line galaxies will be in $z \in [0.65, 1.85]$ with thirteen equispaced redshift bins. Finally, we also assume that the aforementioned measurements will be uncorrelated.

In our analysis in particular, we simulate measurements of the angular diameter distance $d_A(z)$ and the Hubble parameter $H(z)$ in the redshift range $z \in [0.05, 3.55]$. In the top and bottom panels of Figure 48 we show the DESI ΛCDM BAO mocks for the angular diameter distance $d_A(z)$ (top) and the Hubble parameter $H(z)$ (bottom). The data points are in red, the fiducial model in each case is in yellow, while the error bars correspond to 1σ errors.

A.3 STANDARD SIRENS

The inspirals and mergers of compact objects cause gravitational waves to propagate through spacetime. These waves can be detected by the strain $h(t)$ they produce in interferometers. This strain is expressed in the transverse traceless gauge as [79]

$$h(t) = F_+(\theta, \phi, \psi) h_+(t) + F_\times(\theta, \phi, \psi) h_\times(t), \tag{223}$$

where $h_{+,\times}$ are the two independent components of the gravitational wave tensor $h_{\alpha\beta}$, $F_{+,\times}$ are the corresponding antenna pattern func-

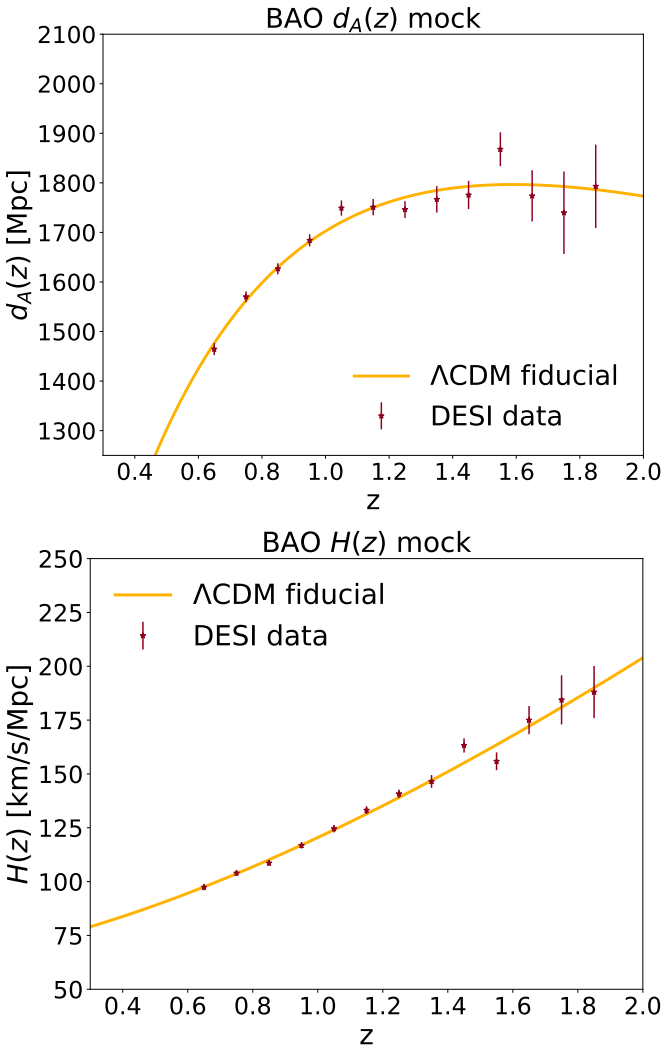

Figure 48: The DESI ΛCDM BAO mocks for the angular diameter distance $d_A(z)$ (top) and the Hubble parameter $H(z)$ (bottom). The data points are in red, while the fiducial in each case is in yellow. The error bars correspond to 1σ errors.

tions, ψ is the polarisation angle, and (θ, ϕ) is the angular position of the wave source on the sky with respect to the detector.

During an inspiral, there is negligible change in the orbital frequency over a single period. We can therefore compute the Fourier transform of the strain $h(t)$ in the stationary phase approximation [345, 300, 301],

$$\mathcal{H}(\mathrm{f}) = \mathcal{A}\mathrm{f}^{-\frac{7}{6}} \exp\Big\{\Big[i(2\pi \mathrm{f} t_0 - \frac{\pi}{4} + 2\Psi(\mathrm{f}/2) - \varphi_{(2,0)})\Big]\Big\}, \tag{224}$$

where t_0 is a constant giving the fiducial epoch of the merger, which for the purposes of our analysis we set to zero.

The Fourier amplitude $\mathcal{A}$ is given by

$$\mathcal{A} = \frac{1}{d_L^{\mathrm{GW}}(z)} \sqrt{F_+^2[1+\cos^2(\omega)]^2 + 4F_\times^2 \cos^2(\omega)} \sqrt{\frac{5\pi}{96}} \pi^{-\frac{7}{6}} \mathcal{M}_c^{\frac{5}{6}}, \tag{225}$$

where ω is the inclination of the orbital angular momentum with respect to the line of sight, and $\mathcal{M}_c = M\eta^{3/5}$ is the chirp mass, related to the masses[1] of the two binary components (m_1 and m_2) through the symmetric mass ratio $\eta = m_1 m_2 / M^2$ and the total mass $M = m_1 + m_2$.

The phase $\Psi(\mathrm{f})$ is given by

$$\Psi(\mathrm{f}) = \psi_0 + \frac{3}{256\eta} \sum_{i=0}^{7} \psi_i (2\pi M \mathrm{f})^{(i/3)}, \tag{226}$$

where ψ_0 is the phase at the fiducial epoch and ψ_i are the coefficients of the post-Newtonian expansion [346] (see Equation 129 of [300] for the specific form used here). On the other hand, the function $\varphi_{(2,0)}$ is given by

$$\varphi_{(2,0)} = \tan^{-1}\left(-\frac{2\cos(\omega)F_\times}{(1+\cos^2(\omega)F_+}\right). \tag{227}$$

We can see from (225) that measuring the amplitude of gravitational wave signals allows estimates of the luminosity distances of the associated mergers to be obtained. However, in order to create a mock dataset of these mergers, we need to propagate the observational error to the luminosity distance. We focus here on the expected error for the Einstein Telescope, and following [347, 302] we approximate the instrumental error on $d_L^{GW}(z)$ as

$$\sigma_{\mathrm{inst}}(d_L^{\mathrm{GW}}(z)) \approx \frac{2 d_L^{GW}(z)}{\rho}, \tag{228}$$

1 Notice that the masses considered here are the observed masses, obtained from the intrinsic ones as $M_{\mathrm{obs}} = (1+z)M_{\mathrm{int}}$.

where ρ is the combined signal-to-noise ratio of the three interferometers of the ET, with $\rho^2 = \sum_i \rho_i^2$, and ρ_i obtained as

$$\rho_i = \sqrt{\langle \mathcal{H}_i, \mathcal{H}_i \rangle} = \left[4 \int_{\mathrm{f_{lower}}}^{\mathrm{f_{upper}}} \mathcal{H}(\mathrm{f}) \mathcal{H}^*(\mathrm{f}) \frac{d\mathrm{f}}{S_h(\mathrm{f})} \right]^{\frac{1}{2}}. \tag{229}$$

There is a correlation at play between the gravitational wave luminosity distance and the inclination of the source to the observer. For a single detector, $d_L^{\mathrm{GW}}(z)$ and ω are completely degenerate with each other and the antenna patterns $F_{+,\times}$. However, with more than one detector, and sensitivity to both polarisations, this degeneracy can be broken. The maximum effect of this degeneracy on the signal to noise ratio is a factor of two, between the source being face on (inclination $\omega = 0$) and edge on ($\omega = \pi/2$); this is the source of the factor of two that appears in (228) [348].

In (229), the function S_h is the noise power spectral density; this function is provided for the ET in [301], where the antenna pattern functions for the three interferometers are given by

$$\begin{aligned}
F_+^{(1)}(\theta, \phi, \psi) =& \frac{\sqrt{3}}{2} \left[\frac{1}{2}(1 + \cos^2(\theta)) \cos(2\phi) \cos(2\psi) \right. \\
& \left. - \cos(\theta) \sin(2\phi) \sin(2\psi) \right] \\
F_\times^{(1)}(\theta, \phi, \psi) =& \frac{\sqrt{3}}{2} \left[\frac{1}{2}(1 + \cos^2(\theta)) \cos(2\phi) \cos(2\psi) \right. \\
& \left. + \cos(\theta) \sin(2\phi) \sin(2\psi) \right] \\
F_{+,\times}^{(2)}(\theta, \phi, \psi) =& F_{+,\times}^{(1)}(\theta, \phi + \frac{2\pi}{3}, \psi) \\
F_{+,\times}^{(3)}(\theta, \phi, \psi) =& F_{+,\times}^{(1)}(\theta, \phi + \frac{4\pi}{3}, \psi).
\end{aligned} \tag{230}$$

The frequency boundaries of (229) represent the cut-off frequencies of the observation. The upper one is connected to the last stable orbit (LSO) and is given by

$$\mathrm{f_{upper}} = 2\mathrm{f_{LSO}} = \frac{2}{6^{3/2} 2\pi M_{\mathrm{obs}}}. \tag{231}$$

The lower cut-off frequency is dictated by the experimental configuration, as well as the location of the detector (for example, seismic noise affects ground-based detectors, raising this frequency in comparison to space-based detectors). We take the lower cut-off frequency to be 1 Hz [300, 301].

We now have all the equations needed to obtain the error $\sigma_{\rm inst}$ on the fiducial $d_L^{\rm GW}(z)$ we computed. It is expected that the Einstein Telescope will be able to observe on the order of 10^5 binary neutron star and neutron star–black hole mergers per year [300]. However, only a small fraction of these will be accompanied by the visible optical counterpart necessary for cosmological parameter estimation. We therefore make the realistic assumption that 1000 binary neutron star sources with an optical counterpart will be detected over a three year period. This allows us to make some other important simplifications:

- We assume that these 1000 events are the subset of observations for which we can observe an electromagnetic counterpart in the form of short γ-ray bursts. This allows us to assume that we have a precise determination of the redshift for each event;
- As discussed in [302, 349], the detection of short γ-ray bursts implies that the systems are oriented approximately face on, which allows us to assume that the inclination $\omega \approx 0$. It is noted in [348, 350] that the maximum inclination angle is around 20°, but if the information matrix is averaged over the inclination and polarisation ψ with the condition $\omega < 20°$ this is the same as fixing the inclination to zero;
- We can assume the same masses of the binaries for all observed systems, with $m_1 = m_2 = 1.4\ M_\odot$.

With these assumptions in mind we generate our N events assuming a uniform distribution for their position (θ, ϕ) in the sky, while for their distribution in redshift we use [301]

$$P(z) \propto \frac{4\pi d_c^2(z) R(z)}{H(z)(1+z)}, \tag{232}$$

where $d_c(z)$ is the comoving distance and $R(z)$ is the merger rate of the binary systems, given by [351]

$$R(z) = \begin{cases} 1+2z & \text{if } z \leq 1, \\ \frac{3}{4}(5-z) & \text{if } 1 < z < 5, \\ 0 & \text{if } z \geq 5. \end{cases} \tag{233}$$

With the equations and the assumptions reported here, we are able to simulate our data points using the fiducial values of $d_L^{\rm GW}(z_i)$ at each sampled redshift z_i and a total error on the observation given by

$$\sigma(d_L^{\rm GW}(z)) = \sqrt{\sigma_{\rm inst}^2 + \sigma_{\rm lens}^2}, \tag{234}$$

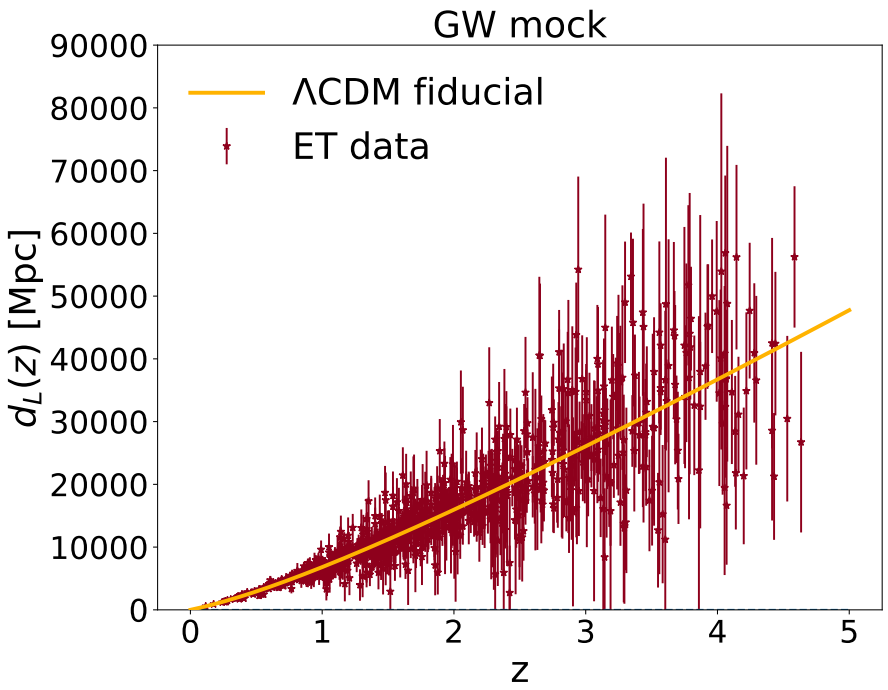

Figure 49: Luminosity distance for the ET ΛCDM gravitational wave mock as a function of redshift. The data points are in red, while the fiducial is in yellow. The error bars correspond to 1σ errors.

where $\sigma_{\rm lens} \approx 0.05z$ is an extra error contribution given by weak lensing effects on the luminosity distance [300]. Finally we simulate a spread of $d_L^{\rm GW}(z_i)$ with respect to the fiducial values, as it is given by observational noise, and therefore our final data points are obtained for each redshift from a Gaussian distribution with mean $d_L^{\rm GW}(z_i)$ and standard deviation $\sigma(d_L^{\rm GW}(z_i))$. The final result is shown in Figure 49.

BIBLIOGRAPHY

[1] M. Martinelli, N. B. Hogg, S. Peirone, M. Bruni and D. Wands. "Constraints on the interacting vacuum–geodesic CDM scenario". In: *Monthly Notices of the Royal Astronomical Society* 488.3 (2019), pp. 3423–3438. DOI: 10.1093/mnras/stz1915. arXiv: 1902.10694 [astro-ph.CO] (cit. on pp. xv, 53, 65).

[2] N. B. Hogg, M. Bruni, R. Crittenden, M. Martinelli and S. Peirone. "Latest evidence for a late time vacuum–geodesic CDM interaction". In: *Physics of the Dark Universe* 29 (2020), p. 100583. DOI: 10.1016/j.dark.2020.100583. arXiv: 2002.10449 [astro-ph.CO] (cit. on pp. xv, 95).

[3] N. B. Hogg, M. Martinelli and S. Nesseris. "Constraints on the distance duality relation with standard sirens". In: *Journal of Cosmology and Astroparticle Physics* 12.019 (2020). DOI: 10.1088/1475-7516/2020/12/019. arXiv: 2007.14335 [astro-ph.CO] (cit. on pp. xv, 139).

[4] F. Renzi, N. B. Hogg, M. Martinelli and S. Nesseris. "Strongly lensed supernovæ as a self-sufficient probe of the distance duality relation" (2020). arXiv: 2010.04155 [astro-ph.CO] (cit. on pp. xv, 23, 174).

[5] M. Rappenglück. "The Pleiades in the Salle des Taureaux, grotte de Lascaux". In: *Actas del IV Congreso de la Seac* (1997), pp. 217–225 (cit. on p. 1).

[6] A. Einstein. "Die Grundlage der allgemeinen Relativitätstheorie". In: *Annalen der Physik* 354 (1916), pp. 769–822 (cit. on pp. 1, 6).

[7] E. Hubble. "A relation between distance and radial velocity among extra-galactic nebulæ". In: *Proceedings of the National Academy of Sciences* 15.3 (1929), pp. 168–173. DOI: 10.1073/pnas.15.3.168 (cit. on p. 1).

[8] G. Lemaître. "The Beginning of the World from the Point of View of Quantum Theory". In: *Nature* 127 (1931), p. 706. DOI: 10.1038/127706b0 (cit. on pp. 1, 53, 55).

[9] G. Lemaître. "Expansion of the universe, a homogeneous universe of constant mass and increasing radius accounting for the radial velocity of extra-galactic nebulæ". In: *Monthly Notices of the Royal Astronomical Society* 91 (1931), pp. 483–490. DOI: 10.1093/mnras/91.5.483 (cit. on p. 1).

[10] G. Lemaître. "Evolution of the Expanding Universe". In: *Proceedings of the National Academy of Sciences* 20.1 (1934), pp. 12–17. DOI: 10.1073/pnas.20.1.12 (cit. on pp. 1, 53, 55).

[11] A. Penzias and R. Wilson. "A Measurement of Excess Antenna Temperature at 4080 Mc/s." In: *The Astrophysical Journal* 142 (1965), pp. 419–421 (cit. on pp. 1, 16).

[12] Y. Akrami et al. "Planck 2018 results. I. Overview and the cosmological legacy of Planck". In: *Astronomy & Astrophysics* 641 (2020), A1. DOI: 10.1051/0004-6361/201833880. arXiv: 1807.06205 [astro-ph.CO] (cit. on pp. 1, 16, 18, 19).

[13] A. G. Riess et al. "Observational Evidence from Supernovæ for an Accelerating Universe and a Cosmological Constant". In: *The Astronomical Journal* 116 (1998), pp. 1009–1038. DOI: 10.1086/300499. arXiv: astro-ph/9805201 (cit. on pp. 1, 9, 14).

[14] S. Perlmutter et al. "Measurements of Ω and Λ from 42 High-Redshift Supernovæ". In: *The Astrophysical Journal* 517 (1999), pp. 565–586. DOI: 10.1086/307221. arXiv: astro-ph/9812133 (cit. on pp. 1, 9, 14, 15).

[15] L. Knox and M. Millea. "Hubble constant hunter's guide". In: *Physical Review D* 101 (4 2020), p. 043533. DOI: 10.1103/PhysRevD.101.043533. arXiv: 1908.03663 [astro-ph.CO] (cit. on pp. 2, 31, 101).

[16] A. H. Guth. "Inflationary universe: A possible solution to the horizon and flatness problems". In: *Physical Review D* 23 (2 1981), pp. 347–356. DOI: 10.1103/PhysRevD.23.347 (cit. on p. 5).

[17] D. Baumann and H. V. Peiris. "Cosmological Inflation: Theory and Observations". In: *Advanced Science Letters* 2 (2009), pp. 105–120. DOI: 10.1166/asl.2009.1019. arXiv: 0810.3022 [astro-ph] (cit. on p. 5).

[18] A. R. Liddle and D. H. Lyth. *Cosmological Inflation and Large Scale Structure*. Cambridge University Press, 2000 (cit. on pp. 7, 22).

[19] B. A. Bassett, S. Tsujikawa and D. Wands. "Inflation dynamics and reheating". In: *Reviews of Modern Physics* 78 (2006), pp. 537–589. DOI: 10.1103/RevModPhys.78.537. arXiv: astro-ph/0507632 (cit. on p. 7).

[20] L. Kofman, A. D. Linde and A. A. Starobinsky. "Reheating after inflation". In: *Physical Review Letters* 73 (1994), pp. 3195–3198. DOI: 10.1103/PhysRevLett.73.3195. arXiv: hep-th/9405187 (cit. on p. 7).

[21] R. A. Alpher, H. Bethe and G. Gamow. "The Origin of Chemical Elements". In: *Physical Review* 73.7 (1948), pp. 803–804. DOI: 10.1103/PhysRev.73.803 (cit. on p. 7).

[22] F. Zwicky. "Die Rotverschiebung von extragalaktischen Nebeln". In: *Helvetica Physica Acta* 6 (1933), pp. 110–127 (cit. on p. 8).

[23] Y. Sofue and V. Rubin. "Rotation curves of spiral galaxies". In: *Annual Review of Astronomy and Astrophysics* 39 (2001), pp. 137–174. DOI: 10.1146/annurev.astro.39.1.137. arXiv: astro-ph/0010594 (cit. on p. 8).

[24] V. R. Eke, J. F. Navarro and C. S. Frenk. "The Evolution of X-Ray Clusters in a Low-Density Universe". In: *The Astrophysical Journal* 503.2 (1998), pp. 569–592. DOI: 10.1086/306008 (cit. on p. 8).

[25] C. Frenk and S. D. White. "Dark matter and cosmic structure". In: *Annalen der Physik* 524 (2012), pp. 507–534. DOI: 10.1002/andp.201200212. arXiv: 1210.0544 [astro-ph.CO] (cit. on p. 8).

[26] M. Kunz, S. Nesseris and I. Sawicki. "Constraints on dark-matter properties from large-scale structure". In: *Physical Review D* 94.2 (2016), p. 023510. DOI: 10.1103/PhysRevD.94.023510. arXiv: 1604.05701 [astro-ph.CO] (cit. on p. 8).

[27] D. B. Thomas, M. Kopp and C. Skordis. "Constraining the Properties of Dark Matter with Observations of the Cosmic Microwave Background". In: *The Astrophysical Journal* 830.2 (2016), p. 155. DOI: 10.3847/0004-637X/830/2/155. arXiv: 1601.05097 [astro-ph.CO] (cit. on p. 8).

[28] M. Viel, G. D. Becker, J. S. Bolton and M. G. Haehnelt. "Warm dark matter as a solution to the small scale crisis: New constraints from high redshift Lyα forest data". In: *Physical Review D* 88 (2013), p. 043502. DOI: 10.1103/PhysRevD.88.043502. arXiv: 1306.2314 [astro-ph.CO] (cit. on p. 8).

[29] M. Markevitch, A. H. Gonzalez, D. Clowe, A. Vikhlinin, L. David, W. Forman, C. Jones, S. Murray and W. Tucker. "Direct constraints on the dark matter self-interaction cross-section from the merging galaxy cluster 1E0657-56". In: *The Astrophysical Journal* 606 (2004), pp. 819–824. DOI: 10.1086/383178. arXiv: astro-ph/0309303 (cit. on p. 8).

[30] A. Robertson, R. Massey and V. Eke. "What does the Bullet Cluster tell us about self-interacting dark matter?" In: *Monthly Notices of the Royal Astronomical Society* 465.1 (2017), pp. 569–587. DOI: 10.1093/mnras/stw2670. arXiv: 1605.04307 [astro-ph.CO] (cit. on p. 8).

[31] I. M. H. Etherington. "The Definition of Distance in General Relativity". In: *Philosophical Magazine* 15 (1933), pp. 761–773. DOI: 10.1080/14786443309462220 (cit. on p. 11).

[32] G. F. R. Ellis. "On the definition of distance in general relativity: I. M. H. Etherington (Philosophical Magazine ser. 7, vol. 15, 761 (1933))". In: *General Relativity and Gravitation* 39.7 (2007), pp. 1047–1052. DOI: 10.1007/s10714-006-0355-5 (cit. on pp. 11, 142).

[33] L. Amendola and S. Tsujikawa. *Dark Energy: Theory and Observations*. Cambridge University Press, 2010 (cit. on pp. 12, 16, 17, 20).

[34] D. A. Vandenberg, K. Brogaard, R. Leaman and L. Casagrande. "The Ages of 55 Globular Clusters as Determined Using an Improved Delta V HB TO Method along with Color-Magnitude Diagram Constraints, and Their Implications for Broader Issues". In: *The Astrophysical Journal* 775.2, 134 (2013), p. 134. DOI: 10.1088/0004-637X/775/2/134. arXiv: 1308.2257 [astro-ph.GA] (cit. on p. 12).

[35] A. W. Alsabti and P. Murdin, eds. *Handbook of Supernovæ*. Springer International Publishing, 2017. DOI: 10.1007/978-3-319-20794-0 (cit. on p. 13).

[36] M. Turatto. "Classification of supernovæ". In: *Lecture Notes in Physics* 598 (2003), p. 21. DOI: 10.1007/3-540-45863-8_3. arXiv: astro-ph/0301107 (cit. on p. 13).

[37] E. Cappellaro and M. Turatto. "Supernova types and rates". In: *Astrophysics and Space Science Library* 264 (2001), p. 199. DOI: 10.1007/978-94-015-9723-4_16. arXiv: astro-ph/0012455 (cit. on p. 13).

[38] B. Wang and Z. Han. "Progenitors of type Ia supernovæ". In: *New Astronomy Reviews* 56.4 (2012), pp. 122–141. DOI: 10.1016/j.newar.2012.04.001. arXiv: 1204.1155 [astro-ph.SR] (cit. on p. 13).

[39] K. Maeda and Y. Terada. "Progenitors of type Ia supernovæ". In: *International Journal of Modern Physics D* 25 (2016), p. 1630024. DOI: 10.1142/S021827181630024X. arXiv: 1609.03639 [astro-ph.SR] (cit. on p. 13).

[40] R. Tripp. "A two-parameter luminosity correction for Type Ia supernovæ". In: *Astronomy & Astrophysics* 331 (1998), pp. 815–820 (cit. on p. 13).

[41] M. Martinelli and I. Tutusaus. "CMB tensions with low-redshift H_0 and S_8 measurements: impact of a redshift-dependent type-Ia supernovæ intrinsic luminosity". In: *Symmetry* 11.8 (2019), p. 986. DOI: 10.3390/sym11080986. arXiv: 1906.09189 [astro-ph.CO] (cit. on pp. 13, 99, 177).

[42] M. Sullivan et al. "SNLS3: Constraints on Dark Energy Combining the Supernova Legacy Survey Three-year Data with Other Probes". In: *The Astrophysical Journal* 737.2, 102 (2011),

p. 102. DOI: 10.1088/0004-637X/737/2/102. arXiv: 1104.1444 [astro-ph.CO] (cit. on p. 13).

[43] J. Johansson et al. "SN Ia host galaxy properties from Sloan Digital Sky Survey-II spectroscopy". In: *Monthly Notices of the Royal Astronomical Society* 435.2 (2013), pp. 1680–1700. DOI: 10.1093/mnras/stt1408. arXiv: 1211.1386 [astro-ph.CO] (cit. on p. 13).

[44] M. Betoule et al. "Improved cosmological constraints from a joint analysis of the SDSS-II and SNLS supernova samples". In: *Astronomy & Astrophysics* 568 (2014), A22. DOI: 10.1051/0004-6361/201423413. arXiv: 1401.4064 [astro-ph.CO] (cit. on pp. 13, 70).

[45] M. Rigault et al. "Evidence of Environmental Dependencies of Type Ia Supernovæ from the Nearby Supernova Factory indicated by Local Hα". In: *Astronomy & Astrophysics* 560 (2013), A66. DOI: 10.1051/0004-6361/201322104. arXiv: 1309.1182 [astro-ph.CO] (cit. on p. 14).

[46] M. J. Childress, C. Wolf and H. J. Zahid. "Ages of Type Ia Supernovæ Over Cosmic Time". In: *Monthly Notices of the Royal Astronomical Society* 445.2 (2014), pp. 1898–1911. DOI: 10.1093/mnras/stu1892. arXiv: 1409.2951 [astro-ph.CO] (cit. on p. 14).

[47] P. Podsiadlowski, P. A. Mazzali, P. Lesaffre, C. Wolf and F. Forster. "Cosmological Implications of the Second Parameter of Type Ia Supernovæ" (2006). arXiv: astro-ph/0608324 (cit. on p. 14).

[48] M. Santander-Garcia et al. "The double-degenerate, super-Chandrasekhar nucleus of the planetary nebula Henize 2-428". In: *Nature* 519.7541 (2015), pp. 63–65. DOI: 10.1038/nature14124. arXiv: 1609.00178 [astro-ph.SR] (cit. on p. 14).

[49] D. M. Scolnic et al. "The Complete Light-curve Sample of Spectroscopically Confirmed SNe Ia from Pan-STARRS1 and Cosmological Constraints from the Combined Pantheon Sample". In: *The Astrophysical Journal* 859.2 (2018), p. 101. DOI: 10.3847/1538-4357/aab9bb. arXiv: 1710.00845 [astro-ph.CO] (cit. on pp. 14, 98, 123).

[50] J. C. Mather et al. "Measurement of the cosmic microwave background spectrum by the COBE FIRAS instrument". In: *The Astrophysical Journal* 420 (1994), pp. 439–444. DOI: 10.1086/173574 (cit. on p. 16).

[51] P. de Bernardis et al. "A flat universe from high resolution maps of the cosmic microwave background radiation". In: *Nature* 404 (2000), pp. 955–959. DOI: 10.1038/35010035. arXiv: astro-ph/0004404 [astro-ph] (cit. on p. 16).

[52] A. Balbi et al. "Constraints on cosmological parameters from MAXIMA-1". In: *The Astrophysical Journal Letters* 545 (2000), pp. L1–L4. DOI: 10.1086/323608. arXiv: astro-ph/0005124 (cit. on p. 16).

[53] G. Hinshaw et al. "Five–Year Wilkinson Microwave Anisotropy Probe Observations: Data Processing, Sky Maps, and Basic Results". In: *The Astrophysical Journal Supplement* 180 (2009), pp. 225–245 (cit. on p. 16).

[54] R. K. Sachs and A. M. Wolfe. "Perturbations of a Cosmological Model and Angular Variations of the Microwave Background". In: *The Astrophysical Journal* 147 (1967), p. 73. DOI: 10.1086/148982 (cit. on p. 16).

[55] N. Wiener. "Generalized harmonic analysis". In: *Acta Mathematica* 55 (1930), pp. 117–258. DOI: 10.1007/BF02546511 (cit. on p. 16).

[56] A. Khinchin. "Korrelationstheorie der stationären stochastischen Prozesse". In: *Mathematische Annalen* 109 (1934), pp. 604–615 (cit. on p. 16).

[57] M. Kamionkowski, A. Kosowsky and A. Stebbins. "A Probe of primordial gravity waves and vorticity". In: *Physical Review Letters* 78 (1997), pp. 2058–2061. DOI: 10.1103/PhysRevLett.78.2058. arXiv: astro-ph/9609132 (cit. on p. 17).

[58] U. Seljak and M. Zaldarriaga. "Signature of gravity waves in polarization of the microwave background". In: *Physical Review Letters* 78 (1997), pp. 2054–2057. DOI: 10.1103/PhysRevLett.78.2054. arXiv: astro-ph/9609169 (cit. on p. 17).

[59] P. A. R. Ade et al. "A measurement of the cosmic microwave background B–mode polarization power spectrum at subdegree scales with POLARBEAR". In: *The Astrophysical Journal* 794.2 (2014), p. 171. DOI: 10.1088/0004-637x/794/2/171 (cit. on p. 17).

[60] O. H. Philcox, B. D. Sherwin and A. van Engelen. "Detection and Removal of B-mode Dust Foregrounds with Signatures of Statistical Anisotropy". In: *Monthly Notices of the Royal Astronomical Society* 479.4 (2018), pp. 5577–5595. DOI: 10.1093/mnras/sty1769. arXiv: 1805.09177 [astro-ph.CO] (cit. on p. 17).

[61] N. Aghanim et al. "Planck 2018 results. VI. Cosmological parameters". In: *Astronomy & Astrophysics* 641 (2020), A6. DOI: 10.1051/0004-6361/201833910. arXiv: 1807.06209 (cit. on pp. 18, 19, 27, 31, 65, 95, 98, 101, 123, 140, 148, 155).

[62] D. J. Eisenstein et al. "Detection of the Baryon Acoustic Peak in the Large-Scale Correlation Function of SDSS Luminous Red

Galaxies". In: *The Astrophysical Journal* 633 (2005), pp. 560–574. DOI: 10.1086/466512. arXiv: astro-ph/0501171 (cit. on p. 20).

[63] S. Alam et al. "The clustering of galaxies in the completed SDSS-III Baryon Oscillation Spectroscopic Survey: cosmological analysis of the DR12 galaxy sample". In: *Monthly Notices of the Royal Astronomical Society* 470.3 (2017), pp. 2617–2652. DOI: 10.1093/mnras/stx721. arXiv: 1607.03155 [astro-ph.CO] (cit. on pp. 21, 27, 70, 98, 123).

[64] M. Ata et al. "The clustering of the SDSS-IV extended Baryon Oscillation Spectroscopic Survey DR14 quasar sample: first measurement of baryon acoustic oscillations between redshift 0.8 and 2.2". In: *Monthly Notices of the Royal Astronomical Society* 473.4 (2018), pp. 4773–4794. DOI: 10.1093/mnras/stx2630. arXiv: 1705.06373 [astro-ph.CO] (cit. on pp. 21, 27).

[65] N. Kaiser. "Clustering in real space and in redshift space". In: *Monthly Notices of the Royal Astronomical Society* 227 (1987), pp. 1–21. DOI: 10.1093/mnras/227.1.1 (cit. on p. 21).

[66] A. Hamilton. "Linear redshift distortions: A Review". *Ringberg Workshop on Large Scale Structure*. 1997. DOI: 10.1007/978-94-011-4960-0_17. arXiv: astro-ph/9708102 (cit. on p. 21).

[67] A. J. S. Hamilton. "Formulae for growth factors in expanding universes containing matter and a cosmological constant". In: *Monthly Notices of the Royal Astronomical Society* 322.2 (2001), pp. 419–425. DOI: 10.1046/j.1365-8711.2001.04137.x (cit. on pp. 21, 59).

[68] S. Alam et al. "The Completed SDSS-IV extended Baryon Oscillation Spectroscopic Survey: Cosmological Implications from two Decades of Spectroscopic Surveys at the Apache Point observatory" (2020). arXiv: 2007.08991 [astro-ph.CO] (cit. on p. 21).

[69] P. Schneider, J. Ehlers and E. Falco. *Gravitational Lenses*. Springer, 1992 (cit. on p. 22).

[70] P. Schneider, C. S. Kochanek and J. Wambsganss. *Gravitational Lensing: Strong, Weak and Micro*. Springer, 2006 (cit. on p. 22).

[71] S. Refsdal. "On the Possibility of Determining Hubble's Parameter and the Masses of Galaxies from the Gravitational Lens Effect". In: *Monthly Notices of the Royal Astronomical Society* 128.4 (1964), pp. 307–310. ISSN: 0035-8711. DOI: 10.1093/mnras/128.4.307 (cit. on p. 23).

[72] K. C. Wong et al. "HoLiCOW – IV. Lens mass model of HE 0435−1223 and blind measurement of its time-delay distance for cosmology". In: *Monthly Notices of the Royal Astronomical Society* 465.4 (2017), pp. 4895–4913. DOI: 10.1093/mnras/stw3077. arXiv: 1607.01403 [astro-ph.CO] (cit. on p. 23).

[73] V. Bonvin et al. "HoLiCOW – V. New COSMOGRAIL time delays of HE 0435−1223: H_0 to 3.8 per cent precision from strong lensing in a flat ΛCDM model". In: *Monthly Notices of the Royal Astronomical Society* 465.4 (2017), pp. 4914–4930. DOI: 10.1093/mnras/stw3006. arXiv: 1607.01790 [astro-ph.CO] (cit. on p. 23).

[74] O. Tihhonova et al. "HoLiCOW VIII. A weak-lensing measurement of the external convergence in the field of the lensed quasar HE 0435−1223". In: *Monthly Notices of the Royal Astronomical Society* 477.4 (2018), pp. 5657–5669. DOI: 10.1093/mnras/sty1040. arXiv: 1711.08804 [astro-ph.CO] (cit. on p. 23).

[75] S. Birrer et al. "HoLiCOW - IX. Cosmographic analysis of the doubly imaged quasar SDSS 1206+4332 and a new measurement of the Hubble constant". In: *Monthly Notices of the Royal Astronomical Society* 484 (2019), p. 4726. DOI: 10.1093/mnras/stz200. arXiv: 1809.01274 [astro-ph.CO] (cit. on p. 23).

[76] K. C. Wong et al. "HoLiCOW XIII. A 2.4% measurement of H_0 from lensed quasars: 5.3σ tension between early and late-Universe probes". In: *Monthly Notices of the Royal Astronomical Society* 498.1 (2020). DOI: 10.1093/mnras/stz3094. arXiv: 1907.04869 [astro-ph.CO] (cit. on pp. 23, 30).

[77] J. A. Peacock. *Cosmological Physics*. Cambridge University Press, 1999. ISBN: 0521422701 (cit. on pp. 23, 41).

[78] T. Abbott et al. "Dark Energy Survey Year 1 Results: Cosmological constraints from cluster abundances and weak lensing". In: *Physical Review D* 102.2 (2020), p. 023509. DOI: 10.1103/PhysRevD.102.023509. arXiv: 2002.11124 [astro-ph.CO] (cit. on pp. 23, 31).

[79] M. Maggiore. *Gravitational Waves: Volume 1: Theory and Experiments*. Oxford University Press, 2007 (cit. on pp. 23, 24, 147, 181).

[80] B. P. Abbott et al. "Observation of Gravitational Waves from a Binary Black Hole Merger". In: *Physical Review Letters* 116 (2016), p. 061102. DOI: 10.1103/PhysRevLett.116.061102 (cit. on pp. 23, 140).

[81] B. P. Abbott et al. "GW170817: Observation of Gravitational Waves from a Binary Neutron Star Inspiral". In: *Physical Review Letters* 119 (2017), p. 161101. DOI: 10.1103/PhysRevLett.119.161101 (cit. on pp. 24, 140, 152).

[82] J. M. Ezquiaga and M. Zumalacárregui. "Dark Energy After GW170817: Dead Ends and the Road Ahead". In: *Physical Review Letters* 119.25, 251304 (2017), p. 251304. DOI: 10.1103/

PhysRevLett.119.251304. arXiv: 1710.05901 [astro-ph.CO] (cit. on pp. 24, 140).

[83] P. Creminelli and F. Vernizzi. "Dark Energy after GW170817 and GRB170817A". In: *Physical Review Letters* 119.25 (2017), p. 251302. DOI: 10.1103/PhysRevLett.119.251302. arXiv: 1710.05877 [astro-ph.CO] (cit. on pp. 24, 140).

[84] B. P. Abbott et al. "A gravitational-wave standard siren measurement of the Hubble constant". In: *Nature* 551.7678 (2017), pp. 85–88. DOI: 10.1038/nature24471. arXiv: 1710.05835 [astro-ph.CO] (cit. on pp. 24, 30, 140).

[85] S. Weinberg. "The cosmological constant problem". In: *Reviews of Modern Physics* 61 (1 1989), pp. 1–23 (cit. on p. 25).

[86] R. J. Adler, B. Casey and O. C. Jacob. "Vacuum catastrophe: An elementary exposition of the cosmological constant problem". In: *American Journal of Physics* 63 (1995), pp. 620–626. DOI: 10.1119/1.17850 (cit. on p. 25).

[87] S. M. Carroll. "The Cosmological Constant". In: *Living Reviews in Relativity* 4 (2001), p. 1. DOI: 10.12942/lrr-2001-1. arXiv: astro-ph/0004075 [astro-ph] (cit. on p. 25).

[88] J. Martin. "Everything you always wanted to know about the cosmological constant problem (but were afraid to ask)". In: *Comptes Rendus Physique* 13.6-7 (2012), pp. 566–665. DOI: 10.1016/j.crhy.2012.04.008. arXiv: 1205.3365 [astro-ph.CO] (cit. on p. 25).

[89] E. Bianchi and C. Rovelli. "Why all these prejudices against a constant?" (2010). arXiv: 1002.3966 [astro-ph.CO] (cit. on p. 26).

[90] N. Sivanandam. "Is the Cosmological Coincidence a Problem?" In: *Physical Review D* 87.8 (2013), p. 083514. DOI: 10.1103/PhysRevD.87.083514. arXiv: 1203.4197 [astro-ph.CO] (cit. on p. 26).

[91] H. E. S. Velten, R. F. vom Marttens and W. Zimdahl. "Aspects of the cosmological "coincidence problem"". In: *European Physical Journal C* 74.11 (2014), p. 3160. DOI: 10.1140/epjc/s10052-014-3160-4. arXiv: 1410.2509 [astro-ph.CO] (cit. on p. 26).

[92] J. D. Barrow and F. J. Tipler. *The Anthropic Cosmological Principle*. Oxford University Press, 1988 (cit. on p. 26).

[93] B. Carter. "Large number coincidences and the anthropic principle in cosmology." *Confrontation of Cosmological Theories with Observational Data*. Ed. by M. S. Longair. Vol. 63. 1974, pp. 291–298 (cit. on p. 26).

[94] A. G. Riess et al. "Large Magellanic Cloud Cepheid Standards Provide a 1% Foundation for the Determination of the Hubble Constant and Stronger Evidence for Physics beyond ΛCDM".

In: *The Astrophysical Journal* 876.1, 85 (2019), p. 85. DOI: 10.3847/1538-4357/ab1422. arXiv: 1903.07603 [astro-ph.CO] (cit. on pp. 27, 134).

[95] L. Verde, T. Treu and A. G. Riess. "Tensions between the early and late Universe". In: *Nature Astronomy* 3 (2019), pp. 891–895. DOI: 10.1038/s41550-019-0902-0. arXiv: 1907.10625 [astro-ph.CO] (cit. on pp. 28, 30, 31).

[96] F. Beutler et al. "The 6dF Galaxy Survey: baryon acoustic oscillations and the local Hubble constant". In: *Monthly Notices of the Royal Astronomical Society* 416 (2011), pp. 3017–3032. DOI: 10.1111/j.1365-2966.2011.19250.x. arXiv: 1106.3366 (cit. on pp. 27, 70, 98, 123).

[97] A. J. Ross, L. Samushia, C. Howlett, W. J. Percival, A. Burden and M. Manera. "The clustering of the SDSS DR7 main Galaxy sample – I. A 4% distance measure at $z = 0.15$". In: *Monthly Notices of the Royal Astronomical Society* 449.1 (2015), pp. 835–847. DOI: 10.1093/mnras/stv154. arXiv: 1409.3242 [astro-ph.CO] (cit. on pp. 27, 70, 123).

[98] T. M. C. Abbott et al. "Dark Energy Survey Year 1 Results: A Precise H_0 Estimate from DES Y1, BAO, and D/H Data". In: *Monthly Notices of the Royal Astronomical Society* 480.3 (2018), pp. 3879–3888. DOI: 10.1093/mnras/sty1939 (cit. on p. 27).

[99] S. Nadathur, P. M. Carter, W. J. Percival, H. A. Winther and J. Bautista. "Beyond BAO: Improving cosmological constraints from BOSS data with measurement of the void-galaxy cross-correlation". In: *Physical Review D* 100.2 (2019), p. 023504. DOI: 10.1103/PhysRevD.100.023504. arXiv: 1904.01030 [astro-ph.CO] (cit. on p. 27).

[100] V. de Sainte Agathe et al. "Baryon acoustic oscillations at $z = 2.34$ from the correlations of Lyα absorption in eBOSS DR14". In: *Astronomy & Astrophysics* 629 (2019), A85. DOI: 10.1051/0004-6361/201935638. arXiv: 1904.03400 [astro-ph.CO] (cit. on p. 27).

[101] M. Blomqvist et al. "Baryon acoustic oscillations from the cross-correlation of Lyα absorption and quasars in eBOSS DR14". In: *Astronomy & Astrophysics* 629 (2019), A86. DOI: 10.1051/0004-6361/201935641. arXiv: 1904.03430 [astro-ph.CO] (cit. on p. 27).

[102] S. Nadathur, W. J. Percival, F. Beutler and H. Winther. "Testing Low-Redshift Cosmic Acceleration with Large-Scale Structure". In: *Physical Review Letters* 124.22 (2020), p. 221301. DOI: 10.1103/PhysRevLett.124.221301. arXiv: 2001.11044 [astro-ph.CO] (cit. on pp. 27, 29).

[103] A. Cuceu, J. Farr, P. Lemos and A. Font-Ribera. "Baryon Acoustic Oscillations and the Hubble Constant: Past, Present and Future". In: *Journal of Cosmology and Astroparticle Physics* 10 (2019), p. 044. DOI: 10.1088/1475-7516/2019/10/044. arXiv: 1906.11628 [astro-ph.CO] (cit. on p. 29).

[104] C. D. Huang et al. "A Near-infrared Period–Luminosity Relation for Miras in NGC 4258, an Anchor for a New Distance Ladder". In: *The Astrophysical Journal* 857.1 (2018), p. 67. DOI: 10.3847/1538-4357/aab6b3. arXiv: 1801.02711 [astro-ph.CO] (cit. on p. 29).

[105] C. D. Huang et al. "Hubble Space Telescope Observations of Mira Variables in the Type Ia Supernova Host NGC 1559: An Alternative Candle to Measure the Hubble Constant". In: *The Astrophysical Journal* 889.1 (2020), p. 5. DOI: 10.3847/1538-4357/ab5dbd. arXiv: 1908.10883 [astro-ph.CO] (cit. on p. 29).

[106] S. Sakai. "The Tip of the Red Giant Branch as a Population II Distance Indicator". *Cosmological Parameters and the Evolution of the Universe*. Ed. by K. Sato. Vol. 183. 1999, p. 48 (cit. on p. 29).

[107] W. L. Freedman et al. "The Carnegie-Chicago Hubble Program. VIII. An Independent Determination of the Hubble Constant Based on the Tip of the Red Giant Branch". In: *The Astrophysical Journal* 882.1 (2019), p. 34. DOI: 10.3847/1538-4357/ab2f73. arXiv: 1907.05922 [astro-ph.CO] (cit. on p. 29).

[108] C. Potter, J. B. Jensen, J. Blakeslee, P. Milne, P. M. Garnavich and P. Brown. "Calibrating the Type Ia Supernova Distance Scale Using Surface Brightness Fluctuations". *American Astronomical Society Meeting Abstracts*. Vol. 232. 2018, p. 319.02 (cit. on p. 29).

[109] J. L. Tonry, J. P. Blakeslee, E. A. Ajhar and A. Dressler. "The SBF survey of galaxy distances. I. Sample selection, photometric calibration, and the Hubble constant". In: *The Astrophysical Journal* 475 (1997), pp. 399–413. DOI: 10.1086/303576. arXiv: astro-ph/9609113 (cit. on p. 30).

[110] J. B. Jensen et al. "The infrared surface brightness fluctuation Hubble constant". In: *The Astrophysical Journal* 550 (2001), p. 503. DOI: 10.1086/319819. arXiv: astro-ph/0011288 (cit. on p. 30).

[111] N. Khetan et al. "A new measurement of the Hubble constant using Type Ia supernovæ calibrated with surface brightness fluctuations" (2020). arXiv: 2008.07754 [astro-ph.CO] (cit. on p. 30).

[112] E. Macaulay et al. "First cosmological results using Type Ia supernovæ from the Dark Energy Survey: measurement of the Hubble constant". In: *Monthly Notices of the Royal Astronom-*

ical Society 486.2 (2019), pp. 2184–2196. DOI: 10.1093/mnras/stz978. arXiv: 1811.02376 [astro-ph.CO] (cit. on p. 30).

[113] D. Pesce et al. "The Megamaser Cosmology Project. XIII. Combined Hubble constant constraints". In: *The Astrophysical Journal Letters* 891.1 (2020), p. L1. DOI: 10.3847/2041-8213/ab75f0. arXiv: 2001.09213 [astro-ph.CO] (cit. on p. 30).

[114] S. Nadathur and S. Sarkar. "Reconciling the local void with the CMB". In: *Physical Review D* 83.6, 063506 (2011), p. 063506. DOI: 10.1103/PhysRevD.83.063506. arXiv: 1012.3460 [astro-ph.CO] (cit. on p. 31).

[115] R. A. Battye, T. Charnock and A. Moss. "Tension between the power spectrum of density perturbations measured on large and small scales". In: *Physical Review D* 91.10 (2015), p. 103508. DOI: 10.1103/PhysRevD.91.103508. arXiv: 1409.2769 [astro-ph.CO] (cit. on p. 31).

[116] C. Heymans et al. "KiDS-1000 Cosmology: Multi-probe weak gravitational lensing and spectroscopic galaxy clustering constraints" (2020). arXiv: 2007.15632 [astro-ph.CO] (cit. on p. 31).

[117] R. Bousso. "The Cosmological Constant Problem, Dark Energy, and the Landscape of String Theory". In: *International Symposium on Subnuclear Physics: past, present and future Vatican City, October 30-November 2, 2011*. Vol. 119. 2011, pp. 129–151. arXiv: 1203.0307 [astro-ph.CO] (cit. on p. 32).

[118] C. Wetterich. "An asymptotically vanishing time-dependent cosmological "constant"." In: *Astronomy & Astrophysics* 301 (1995), p. 321. eprint: hep-th/9408025 (cit. on p. 32).

[119] B. Ratra and P. J. E. Peebles. "Cosmological consequences of a rolling homogeneous scalar field". In: *Physical Review D* 37 (12 1988), pp. 3406–3427 (cit. on p. 32).

[120] R. Caldwell, R. Dave and P. J. Steinhardt. "Cosmological imprint of an energy component with general equation of state". In: *Physical Review Letters* 80 (1998), pp. 1582–1585. DOI: 10.1103/PhysRevLett.80.1582. arXiv: astro-ph/9708069 (cit. on p. 32).

[121] L. Amendola. "Coupled quintessence". In: *Physical Review D* 62 (2000), p. 043511. DOI: 10.1103/PhysRevD.62.043511. arXiv: astro-ph/9908023 [astro-ph] (cit. on p. 32).

[122] S. Tsujikawa. "Quintessence: A Review". In: *Classical and Quantum Gravity* 30 (2013), p. 214003. DOI: 10.1088/0264-9381/30/21/214003. arXiv: 1304.1961 [gr-qc] (cit. on p. 32).

[123] C. Armendariz-Picon, V. F. Mukhanov and P. J. Steinhardt. "A Dynamical solution to the problem of a small cosmological constant and late time cosmic acceleration". In: *Physical Review*

Letters 85 (2000), pp. 4438–4441. DOI: 10.1103/PhysRevLett.85.4438. arXiv: astro-ph/0004134 [astro-ph] (cit. on p. 32).

[124] J. Grande, A. Pelinson and J. Solà. "Dark energy perturbations and cosmic coincidence". In: *Physical Review D* 79 (2009), p. 043006. DOI: 10.1103/PhysRevD.79.043006. arXiv: 0809.3462 [astro-ph] (cit. on p. 32).

[125] E. J. Copeland, M. Sami and S. Tsujikawa. "Dynamics of Dark Energy". In: *International Journal of Modern Physics D* 15.11 (2006), pp. 1753–1935. DOI: 10.1142/S021827180600942X. arXiv: hep-th/0603057 [hep-th] (cit. on p. 32).

[126] A. R. Liddle, P. Parsons and J. D. Barrow. "Formalizing the slow roll approximation in inflation". In: *Physical Review D* 50 (1994), pp. 7222–7232. DOI: 10.1103/PhysRevD.50.7222. arXiv: astro-ph/9408015 (cit. on p. 33).

[127] V. Poulin, T. L. Smith, T. Karwal and M. Kamionkowski. "Early Dark Energy Can Resolve The Hubble Tension". In: *Physical Review Letters* 122.22 (2019), p. 221301. DOI: 10.1103/PhysRevLett.122.221301. arXiv: 1811.04083 [astro-ph.CO] (cit. on pp. 33, 85, 122, 137).

[128] C. M. Will. "The Confrontation between General Relativity and Experiment". In: *Living Reviews in Relativity* 17 (2014), p. 4. DOI: 10.12942/lrr-2014-4. arXiv: 1403.7377 [gr-qc] (cit. on p. 34).

[129] J. Khoury and A. Weltman. "Chameleon Cosmology". In: *Physical Review D* 69 (2003) (cit. on p. 34).

[130] J. Khoury and A. Weltman. "Chameleon Fields: Awaiting Surprises for Tests of Gravity in Space". In: *Physical Review Letters* 93 (2003) (cit. on p. 34).

[131] E. Babichev, C. Deffayet and R. Ziour. "k-Mouflage gravity". In: *International Journal of Modern Physics D* 18 (2009), pp. 2147–2154. DOI: 10.1142/S0218271809016107. arXiv: 0905.2943 [hep-th] (cit. on p. 34).

[132] A. Vainshtein. "To the problem of nonvanishing gravitation mass". In: *Physical Letters B* 39 (1972), pp. 393–394. DOI: 10.1016/0370-2693(72)90147-5 (cit. on p. 34).

[133] A. Joyce, L. Lombriser and F. Schmidt. "Dark Energy Versus Modified Gravity". In: *Annual Review of Nuclear and Particle Science* 66.1 (2016), pp. 95–122. DOI: 10.1146/annurev-nucl-102115-044553. arXiv: 1601.06133 [astro-ph.CO] (cit. on p. 34).

[134] D. Wands, J. De-Santiago and Y. Wang. "Inhomogeneous vacuum energy". In: *Classical and Quantum Gravity* 29 (2012), p. 145017. DOI: 10.1088/0264-9381/29/14/145017. arXiv: 1203.6776 [astro-ph.CO] (cit. on pp. 34, 53).

[135] V. Salvatelli, N. Said, M. Bruni, A. Melchiorri and D. Wands. "Indications of a Late-Time Interaction in the Dark Sector". In: *Physical Review Letters* 113.18 (2014), p. 181301. DOI: 10.1103/PhysRevLett.113.181301 (cit. on pp. 34, 53, 54, 56, 71, 75, 76, 80, 92).

[136] E. Di Valentino, E. V. Linder and A. Melchiorri. "Vacuum phase transition solves the H_0 tension". In: *Physical Review D* 97.4 (2018), p. 043528. DOI: 10.1103/PhysRevD.97.043528. arXiv: 1710.02153 [astro-ph.CO] (cit. on p. 34).

[137] M. Ostrogradsky. "Mémoires sur les équations différentielles, relatives au problème des isopérimètres". In: *Mémoires de l'Académie impériale des sciences de St. Pétersbourg* 6.4 (1850), pp. 385–517 (cit. on p. 35).

[138] R. P. Woodard. "Ostrogradsky's theorem on Hamiltonian instability". In: *Scholarpedia* 10.8 (2015), p. 32243. DOI: 10.4249/scholarpedia.32243. arXiv: 1506.02210 [hep-th] (cit. on p. 35).

[139] G. W. Horndeski. "Second-Order Scalar-Tensor Field Equations in a Four-Dimensional Space". In: *International Journal of Theoretical Physics* 10.6 (1974), pp. 363–384. DOI: 10.1007/BF01807638 (cit. on pp. 35, 153).

[140] Y. B. Zel'dovich and I. D. Novikov. "The Hypothesis of Cores Retarded during Expansion and the Hot Cosmological Model". In: *Astronomicheskii Zhurnal* 43 (1966), p. 758 (cit. on p. 36).

[141] R. D. Peccei and H. R. Quinn. "CP conservation in the presence of pseudoparticles". In: *Physical Review Letters* 38.25 (1977), pp. 1440–1443. DOI: 10.1103/PhysRevLett.38.1440 (cit. on p. 36).

[142] R. D. Peccei and H. R. Quinn. "Constraints imposed by CP conservation in the presence of pseudoparticles". In: *Physical Review D* 16.6 (1977), pp. 1791–1797. DOI: 10.1103/PhysRevD.16.1791 (cit. on p. 36).

[143] G. Sato-Polito, E. D. Kovetz and M. Kamionkowski. "Constraints on the primordial curvature power spectrum from primordial black holes". In: *Physical Review D* 100.6 (2019), p. 063521. DOI: 10.1103/PhysRevD.100.063521. arXiv: 1904.10971 [astro-ph.CO] (cit. on p. 36).

[144] E. Aprile et al. "Observation of Excess Electronic Recoil Events in XENON1T" (2020). arXiv: 2006.09721 [hep-ex] (cit. on pp. 36, 142).

[145] L. Di Luzio, M. Fedele, M. Giannotti, F. Mescia and E. Nardi. "Solar axions cannot explain the XENON1T excess" (2020). arXiv: 2006.12487 [hep-ph] (cit. on pp. 36, 142).

[146] A. E. Robinson. "XENON1T observes tritium" (2020). arXiv: 2006.13278 [hep-ex] (cit. on pp. 36, 142).

[147] E. Bertschinger. "COSMICS: cosmological initial conditions and microwave anisotropy codes" (1995). arXiv: astro-ph/9506070 (cit. on p. 37).

[148] U. Seljak and M. Zaldarriaga. "A Line of sight integration approach to cosmic microwave background anisotropies". In: *The Astrophysical Journal* 469 (1996), pp. 437–444. DOI: 10.1086/177793. arXiv: astro-ph/9603033 (cit. on p. 37).

[149] M. Doran. "CMBEASY: an object oriented code for the cosmic microwave background". In: *Journal of Cosmology and Astrophysics* 10 (2005), p. 011. DOI: 10.1088/1475-7516/2005/10/011. arXiv: astro-ph/0302138 (cit. on p. 37).

[150] A. Lewis, A. Challinor and A. Lasenby. "Efficient computation of CMB anisotropies in closed FRW models". In: *The Astrophysical Journal* 538 (2000), pp. 473–476. DOI: 10.1086/309179. arXiv: astro-ph/9911177 [astro-ph] (cit. on pp. 37, 58, 96, 148).

[151] C. Howlett, A. Lewis, A. Hall and A. Challinor. "CMB power spectrum parameter degeneracies in the era of precision cosmology". In: *Journal of Cosmology and Astroparticle Physics* 1204 (2012), p. 027. DOI: 10.1088/1475-7516/2012/04/027. arXiv: 1201.3654 [astro-ph.CO] (cit. on pp. 37, 58, 96, 148).

[152] J. Lesgourgues. "The Cosmic Linear Anisotropy Solving System (CLASS) I: Overview" (2011). arXiv: 1104.2932 [astro-ph.IM] (cit. on p. 37).

[153] D. Blas, J. Lesgourgues and T. Tram. "The Cosmic Linear Anisotropy Solving System (CLASS). Part II: Approximation schemes". In: *Journal of Cosmology and Astroparticle Physics* 2011.7, 034 (2011), p. 034. DOI: 10.1088/1475-7516/2011/07/034. arXiv: 1104.2933 [astro-ph.CO] (cit. on p. 37).

[154] Antony Lewis. *CAMB Notes*. https://cosmologist.info/notes/CAMB.pdf. 2014 (cit. on p. 38).

[155] C.-P. Ma and E. Bertschinger. "Cosmological perturbation theory in the synchronous and conformal Newtonian gauges". In: *The Astrophysical Journal* 455 (1995), pp. 7–25. DOI: 10.1086/176550. arXiv: astro-ph/9506072 (cit. on pp. 38–41).

[156] A. M. Lewis. "Geometric algebra and covariant methods in physics and cosmology". PhD thesis. University of Cambridge, 2000 (cit. on p. 42).

[157] L. Wasserman. *All of Statistics*. Springer, 2004 (cit. on p. 43).

[158] M. P. Hobson, A. H. Jaffe, A. R. Liddle, P. Mukherjee and D. Parkinson. *Bayesian Methods in Cosmology*. Cambridge University Press, 2010 (cit. on pp. 43–47, 50, 110).

[159] S. Joudaki, P. G. Ferreira, N. A. Lima and H. A. Winther. "Testing Gravity on Cosmic Scales: A Case Study of Jordan-Brans-Dicke Theory" (2020). arXiv: 2010.15278 [astro-ph.CO] (cit. on p. 43).

[160] T. Bayes. "LII. An essay towards solving a problem in the doctrine of chances. By the late Rev. Mr. Bayes, F. R. S. communicated by Mr. Price, in a letter to John Canton, A. M. F. R. S". In: *Philosophical Transactions of the Royal Society of London* 53 (1763), pp. 370–418. DOI: 10.1098/rstl.1763.0053 (cit. on pp. 43, 107).

[161] N. Metropolis. "The beginning of the Monte Carlo method". In: *Los Alamos Science* (1987). URL: https://permalink.lanl.gov/object/tr?what=info:lanl-repo/lareport/LA-UR-88-9067 (cit. on p. 45).

[162] A. Lewis and S. Bridle. "Cosmological parameters from CMB and other data: A Monte Carlo approach". In: *Physical Review D* 66 (2002), p. 103511. DOI: 10.1103/PhysRevD.66.103511. arXiv: astro-ph/0205436 [astro-ph] (cit. on pp. 46, 71, 96).

[163] A. Lewis. "Efficient sampling of fast and slow cosmological parameters". In: *Physical Review D* 87 (2013), p. 103529. DOI: 10.1103/PhysRevD.87.103529. arXiv: 1304.4473 [astro-ph.CO] (cit. on pp. 46, 71, 96).

[164] N. Metropolis, A. W. Rosenbluth, M. N. Rosenbluth, A. H. Teller and E. Teller. "Equation of State Calculations by Fast Computing Machines". In: *Journal of Chemical Physics* 21.6 (1953), pp. 1087–1092. DOI: 10.1063/1.1699114 (cit. on p. 46).

[165] W. K. Hastings. "Monte Carlo Sampling Methods using Markov Chains and their Applications". In: *Biometrika* 57.1 (1970), pp. 97–109. DOI: 10.1093/biomet/57.1.97 (cit. on pp. 46, 149).

[166] M. Martinelli et al. "Euclid: Forecast constraints on the cosmic distance duality relation with complementary external probes". In: *Astronomy & Astrophysics* 644 (2020), A80. DOI: 10.1051/0004-6361/202039078. arXiv: 2007.16153 [astro-ph.CO] (cit. on pp. 47, 144, 146).

[167] J. Skilling. "Nested Sampling". In: *AIP Conference Proceedings* 735.1 (2004), pp. 395–405 (cit. on p. 47).

[168] W. J. Handley et al. "PolyChord: nested sampling for cosmology". In: *Monthly Notices of the Royal Astronomical Society* 450.1 (2015), pp. L61–L65 (cit. on pp. 47, 149).

[169] W. J. Handley et al. "POLYCHORD: next-generation nested sampling". In: *Monthly Notices of the Royal Astronomical Society* 453 (2015), pp. 4384–4398 (cit. on pp. 47, 149).

[170] D. Foreman-Mackey, D. W. Hogg, D. Lang and J. Goodman. "emcee: The MCMC Hammer". In: *Publications of the Astronomical Society of the Pacific* 125.925 (2013), p. 306. DOI: 10.1086/670067. arXiv: 1202.3665 [astro-ph.IM] (cit. on pp. 47, 173).

[171] R. Allison and J. Dunkley. "Comparison of sampling techniques for Bayesian parameter estimation". In: *Monthly Notices of the Royal Astronomical Society* 437.4 (2013), pp. 3918–3928. ISSN: 0035-8711. DOI: 10.1093/mnras/stt2190 (cit. on p. 47).

[172] H. Akaike. "A new look at the statistical model identification". In: *IEEE Transactions on Automatic Control* 19.6 (1974), pp. 716–723 (cit. on p. 49).

[173] G. Schwarz. "Estimating the Dimension of a Model". In: *Annals of Statistics* 6 (1978), pp. 461–464 (cit. on p. 49).

[174] D. J. Spiegelhalter, N. G. Best, B. P. Carlin and A. Van Der Linde. "Bayesian measures of model complexity and fit". In: *Journal of the Royal Statistical Society: Series B (Statistical Methodology)* 64.4 (2002), pp. 583–639. DOI: https://doi.org/10.1111/1467-9868.00353 (cit. on pp. 49, 132).

[175] D. J. Spiegelhalter, N. G. Best, B. P. Carlin and A. van der Linde. "The deviance information criterion: 12 years on". In: *Journal of the Royal Statistical Society: Series B (Statistical Methodology)* 76.3 (2014), pp. 485–493. ISSN: 1467-9868. DOI: 10.1111/rssb.12062 (cit. on pp. 49, 84, 132).

[176] A. Heavens, Y. Fantaye, A. Mootoovaloo, H. Eggers, Z. Hosenie, S. Kroon and E. Sellentin. "Marginal Likelihoods from Monte Carlo Markov Chains" (2017). arXiv: 1704.03472 [stat.CO] (cit. on pp. 50, 110, 133).

[177] H. Jeffreys. *Theory of Probability*. Clarendon Press, Oxford, 1961 (cit. on pp. 50, 110).

[178] O. Bertolami. "Time-dependent cosmological term". In: *Il Nuovo Cimento B (1971-1996)* 93.1 (1986), pp. 36–42. ISSN: 1826-9877. DOI: 10.1007/BF02728301 (cit. on p. 53).

[179] D. Pavón. "Nonequilibrium fluctuations in cosmic vacuum decay". In: *Physical Review D* 43 (2 1991), pp. 375–378. DOI: 10.1103/PhysRevD.43.375 (cit. on p. 53).

[180] A. Al-Rawaf and M. Taha. "A resolution of the cosmological age puzzle". In: *Physics Letters B* 366.1 (1996), pp. 69–71. ISSN: 0370-2693. DOI: https://doi.org/10.1016/0370-2693(95)01145-5 (cit. on p. 53).

[181] I. L. Shapiro and J. Solà. "Scaling behavior of the cosmological constant: Interface between quantum field theory and cosmology". In: *JHEP* 02 (2002), p. 006. DOI: 10.1088/1126-6708/2002/02/006. arXiv: hep-th/0012227 [hep-th] (cit. on p. 53).

[182] J. Solà. "Cosmologies with a time dependent vacuum". In: *Journal of Physics Conference Series* 283 (2011), p. 012033. DOI: 10.1088/1742-6596/283/1/012033. arXiv: 1102.1815 [astro-ph.CO] (cit. on p. 53).

[183] Y. Wang, G.-B. Zhao, D. Wands, L. Pogosian and R. G. Crittenden. "Reconstruction of the dark matter–vacuum energy interaction". In: *Physical Review D* 92 (2015), p. 103005. DOI: 10.1103/PhysRevD.92.103005. arXiv: 1505.01373 [astro-ph.CO] (cit. on pp. 53, 98).

[184] G.-B. Zhao et al. "Dynamical dark energy in light of the latest observations". In: *Nature Astronomy* 1.9 (2017), pp. 627–632. DOI: 10.1038/s41550-017-0216-z. arXiv: 1701.08165 [astro-ph.CO] (cit. on p. 53).

[185] J. Solà, A. Gómez-Valent and J. de Cruz Pérez. "Vacuum dynamics in the Universe versus a rigid Λ = const". In: *International Journal of Modern Physics A* 32.19-20 (2017), p. 1730014. DOI: 10.1142/S0217751X17300149. arXiv: 1709.07451 [astro-ph.CO] (cit. on p. 53).

[186] E. Di Valentino, A. Melchiorri and O. Mena. "Can interacting dark energy solve the H_0 tension?" In: *Physical Review D* 96.4 (2017), p. 043503. DOI: 10.1103/PhysRevD.96.043503. arXiv: 1704.08342 [astro-ph.CO] (cit. on p. 53).

[187] S. Kumar and R. C. Nunes. "Echo of interactions in the dark sector". In: *Physical Review D* 96.10 (2017), p. 103511. DOI: 10.1103/PhysRevD.96.103511. arXiv: 1702.02143 [astro-ph.CO] (cit. on pp. 53, 89, 91).

[188] J. Solà, A. Gómez-Valent and J. de Cruz Pérez. "Signs of Dynamical Dark Energy in Current Observations". In: *Physics of the Dark Universe* 25 (2019), p. 100311. DOI: 10.1016/j.dark.2019.100311. arXiv: 1811.03505 [astro-ph.CO] (cit. on pp. 53, 91).

[189] W. Yang, S. Pan, E. Di Valentino, E. N. Saridakis and S. Chakraborty. "Observational constraints on one-parameter dynamical dark-energy parametrizations and the H_0 tension". In: *Physical Review D* 99.4 (2019), p. 043543. DOI: 10.1103/PhysRevD.99.043543. arXiv: 1810.05141 [astro-ph.CO] (cit. on p. 53).

[190] Y. Wang, L. Pogosian, G.-B. Zhao and A. Zucca. "Evolution of dark energy reconstructed from the latest observations". In: *The Astrophysical Journal* 869 (2018), p. L8. DOI: 10.3847/2041-8213/aaf238. arXiv: 1807.03772 [astro-ph.CO] (cit. on pp. 53, 97).

[191] Y. Wang, D. Wands, G.-B. Zhao and L. Xu. "Post-*Planck* constraints on interacting vacuum energy". In: *Physical Review D*

90.2 (2014), p. 023502. DOI: 10.1103/PhysRevD.90.023502. arXiv: 1404.5706 [astro-ph.CO] (cit. on pp. 56, 98).

[192] Y. Wang, D. Wands, L. Xu, J. De-Santiago and A. Hojjati. "Cosmological constraints on a decomposed Chaplygin gas". In: *Physical Review D* 87 (8 2013), p. 083503. DOI: 10.1103/PhysRevD.87.083503 (cit. on p. 56).

[193] H. A. Borges and D. Wands. "Growth of structure in interacting vacuum cosmologies". In: *Physical Review D* 101.10 (2020), p. 103519. DOI: 10.1103/PhysRevD.101.103519. arXiv: 1709.08933 [astro-ph.CO] (cit. on pp. 56, 60, 91, 99).

[194] M. Bruni, D. B. Thomas and D. Wands. "Computing General Relativistic effects from Newtonian N-body simulations: Frame dragging in the post-Friedmann approach". In: *Physical Review D* 89.4 (2014), p. 044010. DOI: 10.1103/PhysRevD.89.044010. arXiv: 1306.1562 [astro-ph.CO] (cit. on p. 56).

[195] I. Sawicki, V. Marra and W. Valkenburg. "Seeding supermassive black holes with a nonvortical dark-matter subcomponent". In: *Physical Review D* 88 (8 2013), p. 083520. DOI: 10.1103/PhysRevD.88.083520 (cit. on p. 56).

[196] H. Kodama and M. Sasaki. "Cosmological Perturbation Theory". In: *Progress of Theoretical Physics Supplement* 78 (1984) (cit. on pp. 58, 59).

[197] K. A. Malik and D. Wands. "Cosmological perturbations". In: *Physics Reports* 475 (2009), pp. 1–51. DOI: 10.1016/j.physrep.2009.03.001. arXiv: 0809.4944 [astro-ph] (cit. on pp. 58, 59).

[198] R. Kimura, T. Suyama, M. Yamaguchi, D. Yamauchi and S. Yokoyama. "Are redshift-space distortions actually a probe of growth of structure?" In: *Publications of the Astronomical Society of Japan* 70.5 (2018). DOI: 10.1093/pasj/psy083. arXiv: 1709.09371 [astro-ph.CO] (cit. on p. 60).

[199] P. A. R. Ade et al. "Planck 2015 results. XIII. Cosmological parameters". In: *Astronomy & Astrophysics* 594 (2016), A13. DOI: 10.1051/0004-6361/201525830. arXiv: 1502.01589 [astro-ph.CO] (cit. on pp. 60, 64, 65).

[200] C. Quercellini, M. Bruni, A. Balbi and D. Pietrobon. "Late universe dynamics with scale-independent linear couplings in the dark sector". In: *Physical Review D* 78 (2008), p. 063527. DOI: 10.1103/PhysRevD.78.063527. arXiv: 0803.1976 [astro-ph] (cit. on p. 62).

[201] O. F. Piattella, D. Bertacca, M. Bruni and D. Pietrobon. "Unified Dark Matter models with fast transition". In: *Journal of Cosmology and Astroparticle Physics* 1001 (2010), p. 014. DOI: 10.1088/1475-7516/2010/01/014. arXiv: 0911.2664 [astro-ph.CO] (cit. on pp. 64, 115).

[202] D. Bertacca, M. Bruni, O. F. Piattella and D. Pietrobon. "Unified Dark Matter scalar field models with fast transition". In: *Journal of Cosmology and Astroparticle Physics* 1102 (2011), p. 018. DOI: 10.1088/1475-7516/2011/02/018. arXiv: 1011.6669 [astro-ph.CO] (cit. on pp. 64, 115).

[203] N. Aghanim et al. "Planck 2015 results. XI. CMB power spectra, likelihoods, and robustness of parameters". In: *Astronomy & Astrophysics* 594 (2016), A11. DOI: 10.1051/0004-6361/201526926. arXiv: 1507.02704 [astro-ph.CO] (cit. on p. 65).

[204] W. J. Percival et al. "The 2dF Galaxy Redshift Survey: spherical harmonics analysis of fluctuations in the final catalogue". In: *Monthly Notices of the Royal Astronomical Society* 353 (2004), pp. 1201–1218. DOI: 10.1111/j.1365-2966.2004.08146.x. arXiv: astro-ph/0406513 (cit. on p. 82).

[205] F. Beutler, C. Blake, M. Colless, D. H. Jones, L. Staveley-Smith, G. B. Poole, L. Campbell, Q. Parker, W. Saunders and F. Watson. "The 6dF Galaxy Survey: $z \approx 0$ measurements of the growth rate and σ_8". In: *Monthly Notices of the Royal Astronomical Society* 423 (2012), pp. 3430–3444. DOI: 10.1111/j.1365-2966.2012.21136.x. arXiv: 1204.4725 [astro-ph.CO] (cit. on p. 82).

[206] C. Blake et al. "The WiggleZ Dark Energy Survey: the growth rate of cosmic structure since redshift $z = 0.9$". In: *Monthly Notices of the Royal Astronomical Society* 415 (2011), pp. 2876–2891. DOI: 10.1111/j.1365-2966.2011.18903.x. arXiv: 1104.2948 (cit. on p. 82).

[207] L. Samushia, W. J. Percival and A. Raccanelli. "Interpreting large-scale redshift-space distortion measurements". In: *Monthly Notices of the Royal Astronomical Society* 420 (2012), pp. 2102–2119. DOI: 10.1111/j.1365-2966.2011.20169.x. arXiv: 1102.1014 [astro-ph.CO] (cit. on p. 82).

[208] B. A. Reid et al. "The clustering of galaxies in the SDSS-III Baryon Oscillation Spectroscopic Survey: measurements of the growth of structure and expansion rate at $z = 0.57$ from anisotropic clustering". In: *Monthly Notices of the Royal Astronomical Society* 426 (2012), pp. 2719–2737. DOI: 10.1111/j.1365-2966.2012.21779.x. arXiv: 1203.6641 [astro-ph.CO] (cit. on p. 82).

[209] S. de la Torre et al. "The VIMOS Public Extragalactic Redshift Survey (VIPERS) . Galaxy clustering and redshift-space distortions at $z \approx 0.8$ in the first data release". In: *Astronomy & Astrophysics* 557, A54 (2013), A54. DOI: 10.1051/0004-6361/201321463. arXiv: 1303.2622 [astro-ph.CO] (cit. on p. 82).

[210] S. Joudaki et al. "KiDS-450: Testing extensions to the standard cosmological model". In: *Monthly Notices of the Royal Astronomical Society* 471.2 (2017), pp. 1259–1279. DOI: 10.1093/mnras/stx998. arXiv: 1610.04606 [astro-ph.CO] (cit. on pp. 84, 133).

[211] A. G. Riess et al. "New Parallaxes of Galactic Cepheids from Spatially Scanning the Hubble Space Telescope: Implications for the Hubble Constant". In: *The Astrophysical Journal* 855, 136 (2018), p. 136. DOI: 10.3847/1538-4357/aaadb7. arXiv: 1801.01120 [astro-ph.SR] (cit. on pp. 87, 103).

[212] M. Seikel, C. Clarkson and M. Smith. "Reconstruction of dark energy and expansion dynamics using Gaussian processes". In: *Journal of Cosmology and Astroparticle Physics* 6, 036 (2012), p. 036. DOI: 10.1088/1475-7516/2012/06/036. arXiv: 1204.2832 (cit. on p. 86).

[213] A. Shafieloo, A. G. Kim and E. V. Linder. "Gaussian process cosmography". In: *Physical Review D* 85.12, 123530 (2012), p. 123530. DOI: 10.1103/PhysRevD.85.123530. arXiv: 1204.2272 [astro-ph.CO] (cit. on p. 86).

[214] T. Yang, Z.-K. Guo and R.-G. Cai. "Reconstructing the interaction between dark energy and dark matter using Gaussian Processes". In: *Physical Review D* 91.12 (2015), p. 123533. DOI: 10.1103/PhysRevD.91.123533. arXiv: 1505.04443 [astro-ph.CO] (cit. on p. 86).

[215] M.-J. Zhang and H. Li. "Gaussian processes reconstruction of dark energy from observational data". In: *European Physical Journal C* 78, 460 (2018), p. 460. DOI: 10.1140/epjc/s10052-018-5953-3. arXiv: 1806.02981 (cit. on p. 86).

[216] M. Seikel and C. Clarkson. "Optimising Gaussian processes for reconstructing dark energy dynamics from supernovæ" (2013). arXiv: 1311.6678 [astro-ph.CO] (cit. on p. 86).

[217] J. Solà, A. Gómez-Valent and J. de Cruz Pérez. "The H_0 tension in light of vacuum dynamics in the Universe". In: *Physics Letters* 774 (2017), pp. 317–324. DOI: 10.1016/j.physletb.2017.09.073. arXiv: 1705.06723 [astro-ph.CO] (cit. on pp. 89, 91).

[218] J. Solà, J. de Cruz Pérez and A. Gómez-Valent. "Possible signals of vacuum dynamics in the Universe". In: *Monthly Notices of the Royal Astronomical Society* 478.4 (2018), pp. 4357–4373. DOI: 10.1093/mnras/sty1253. arXiv: 1703.08218 [astro-ph.CO] (cit. on pp. 89, 91).

[219] P. Tsiapi and S. Basilakos. "Testing dynamical vacuum models with CMB power spectrum from Planck". In: *Monthly Notices of the Royal Astronomical Society* 485.2 (2019), pp. 2505–2510. DOI: 10.1093/mnras/stz540. arXiv: 1810.12902 [astro-ph.CO] (cit. on pp. 89, 91).

[220] S. Kumar, R. C. Nunes and S. K. Yadav. "Dark sector interaction: a remedy of the tensions between CMB and LSS data". In: *European Physical Journal C* 79.7 (2019), p. 576. DOI: 10.1140/epjc/s10052-019-7087-7. arXiv: 1903.04865 [astro-ph.CO] (cit. on pp. 89, 91).

[221] P. A. R. Ade et al. "Planck 2015 results. XXIV. Cosmology from Sunyaev-Zeldovich cluster counts". In: *Astronomy & Astrophysics* 594 (2016), A24. DOI: 10.1051/0004-6361/201525833. arXiv: 1502.01597 [astro-ph.CO] (cit. on p. 91).

[222] C. Heymans et al. "CFHTLenS tomographic weak lensing cosmological parameter constraints: Mitigating the impact of intrinsic galaxy alignments". In: *Monthly Notices of the Royal Astronomical Society* 432 (2013), p. 2433. DOI: 10.1093/mnras/stt601. arXiv: 1303.1808 [astro-ph.CO] (cit. on p. 91).

[223] F. Köhlinger et al. "KiDS-450: the tomographic weak lensing power spectrum and constraints on cosmological parameters". In: *Monthly Notices of the Royal Astronomical Society* 471.4 (2017), pp. 4412–4435. ISSN: 0035-8711. DOI: 10.1093/mnras/stx1820 (cit. on p. 91).

[224] A. G. Riess et al. "A 2.4% Determination of the Local Value of the Hubble Constant". In: *The Astrophysical Journal* 826.1, 56 (2016), p. 56. DOI: 10.3847/0004-637X/826/1/56. arXiv: 1604.01424 [astro-ph.CO] (cit. on p. 91).

[225] W. Yang, N. Banerjee, A. Paliathanasis and S. Pan. "Reconstructing the dark matter and dark energy interaction scenarios from observations". In: *Physics of the Dark Universe* 26 (2019), p. 100383. DOI: 10.1016/j.dark.2019.100383. arXiv: 1812.06854 [astro-ph.CO] (cit. on p. 92).

[226] J. He, L. Guzzo, B. Li and C. M. Baugh. "No evidence for modifications of gravity from galaxy motions on cosmological scales". In: *Nature Astronomy* 2.12 (2018), pp. 967–972. DOI: 10.1038/s41550-018-0573-2. arXiv: 1809.09019 [astro-ph.CO] (cit. on p. 93).

[227] R. G. Crittenden, L. Pogosian and G.-B. Zhao. "Investigating dark energy experiments with principal components". In: *Journal of Cosmology and Astroparticle Physics* 0912 (2009), p. 025. DOI: 10.1088/1475-7516/2009/12/025. arXiv: astro-ph/0510293 [astro-ph] (cit. on p. 97).

[228] R. G. Crittenden, G.-B. Zhao, L. Pogosian, L. Samushia and X. Zhang. "Fables of reconstruction: controlling bias in the dark energy equation of state". In: *Journal of Cosmology and Astroparticle Physics* 2, 048 (2012), p. 048. DOI: 10.1088/1475-7516/2012/02/048. arXiv: 1112.1693 (cit. on pp. 97, 98).

[229] F. Gerardi, M. Martinelli and A. Silvestri. "Reconstruction of the Dark Energy equation of state from latest data: the impact of theoretical priors". In: *Journal of Cosmology and Astroparticle Physics* 1907 (2019), p. 042. DOI: 10.1088/1475-7516/2019/07/042. arXiv: 1902.09423 [astro-ph.CO] (cit. on p. 97).

[230] L. Dam, K. Bolejko and G. F. Lewis. "Probing the independence within the dark sector in the fluid approximation". In: *Journal of Cosmology and Astroparticle Physics* 1912.12 (2019), p. 030. DOI: 10.1088/1475-7516/2019/12/030. arXiv: 1908.01953 [astro-ph.CO] (cit. on p. 97).

[231] E. Di Valentino, A. Melchiorri, O. Mena and S. Vagnozzi. "Interacting dark energy in the early 2020s: A promising solution to the H_0 and cosmic shear tensions". In: *Physics of the Dark Universe* 30 (2020), p. 100666. DOI: 10.1016/j.dark.2020.100666. arXiv: 1908.04281 [astro-ph.CO] (cit. on p. 99).

[232] V. Poulin, K. K. Boddy, S. Bird and M. Kamionkowski. "Implications of an extended dark energy cosmology with massive neutrinos for cosmological tensions". In: *Physical Review D* 97.12 (2018), p. 123504. DOI: 10.1103/PhysRevD.97.123504. arXiv: 1803.02474 [astro-ph.CO] (cit. on p. 99).

[233] K. Aylor, M. Joy, L. Knox, M. Millea, S. Raghunathan and W. L. K. Wu. "Sounds Discordant: Classical Distance Ladder & ΛCDM -based Determinations of the Cosmological Sound Horizon". In: *The Astrophysical Journal* 874.1 (2019), p. 4. DOI: 10.3847/1538-4357/ab0898. arXiv: 1811.00537 [astro-ph.CO] (cit. on p. 101).

[234] N. Arendse et al. "Cosmic dissonance: new physics or systematics behind a short sound horizon?" (2019). arXiv: 1909.07986 [astro-ph.CO] (cit. on p. 101).

[235] T. Abbott et al. "Dark Energy Survey year 1 results: Cosmological constraints from galaxy clustering and weak lensing". In: *Physical Review D* 98.4 (2018), p. 043526. DOI: 10.1103/PhysRevD.98.043526. arXiv: 1708.01530 [astro-ph.CO] (cit. on p. 101).

[236] C. E. Rasmussen and C. K. I. Williams. *Gaussian Processes for Machine Learning*. MIT Press, 2006 (cit. on p. 102).

[237] S. Ambikasaran, D. Foreman-Mackey, L. Greengard, D. W. Hogg and M. O'Neil. "Fast Direct Methods for Gaussian Processes". In: *IEEE Transactions on Pattern Analysis and Machine Intelligence* 38 (2015). DOI: 10.1109/TPAMI.2015.2448083. arXiv: 1403.6015 [math.NA] (cit. on p. 104).

[238] R. A. C. Croft, A. Romeo and R. B. Metcalf. "Weak lensing of the Lyα forest". In: *Monthly Notices of the Royal Astronomical So-*

ciety 477.2 (2018), pp. 1814–1821. DOI: 10.1093/mnras/sty650. arXiv: 1706.07870 [astro-ph.CO] (cit. on p. 104).

[239] R. Braun, T. Bourke, J. A. Green, E. Keane and J. Wagg. "Advancing Astrophysics with the Square Kilometre Array". In: *Proceedings of Science (AASKA14)*, 174 (2015), p. 174 (cit. on p. 104).

[240] D. J. Bacon et al. "Cosmology with Phase 1 of the Square Kilometre Array; Red Book 2018: Technical specifications and performance forecasts" (2018). arXiv: 1811.02743 [astro-ph.CO] (cit. on p. 104).

[241] D. Huterer and G. Starkman. "Parameterization of dark-energy properties: A Principal-component approach". In: *Physical Review Letters* 90 (2003), p. 031301. DOI: 10.1103/PhysRevLett.90.031301. arXiv: astro-ph/0207517 [astro-ph] (cit. on p. 105).

[242] A. Lewis. "GetDist: a Python package for analysing Monte Carlo samples" (2019). arXiv: 1910.13970 [astro-ph.IM]. URL: https://getdist.readthedocs.io (cit. on pp. 105, 128).

[243] F. X. Linares Cedeño, A. Montiel, J. C. Hidalgo and G. Germán. "Bayesian evidence for α-attractor dark energy models". In: *Journal of Cosmology and Astroparticle Physics* 1908.08 (2019), p. 002. DOI: 10.1088/1475-7516/2019/08/002. arXiv: 1905.00834 [gr-qc] (cit. on p. 109).

[244] G. Efstathiou. "Limitations of Bayesian Evidence applied to cosmology". In: *Monthly Notices of the Royal Astronomical Society* 388.3 (2008), pp. 1314–1320. DOI: 10.1111/j.1365-2966.2008.13498.x. arXiv: 0802.3185 [astro-ph] (cit. on p. 111).

[245] H. S. Kragh. *Dirac: A Scientific Biography*. Cambridge University Press, 1990 (cit. on p. 113).

[246] A. Y. Kamenshchik, U. Moschella and V. Pasquier. "An alternative to quintessence". In: *Physics Letters B* 511 (2001), pp. 265–268. DOI: 10.1016/S0370-2693(01)00571-8. arXiv: gr-qc/0103004 (cit. on p. 114).

[247] M. Bento, O. Bertolami and A. Sen. "Generalized Chaplygin gas, accelerated expansion and dark energy matter unification". In: *Physical Review D* 66 (2002), p. 043507. DOI: 10.1103/PhysRevD.66.043507. arXiv: gr-qc/0202064 (cit. on pp. 114, 115).

[248] J. Fabris, S. Goncalves and P. de Souza. "Density perturbations in a universe dominated by the Chaplygin gas". In: *General Relativity and Gravity* 34 (2002), pp. 53–63. DOI: 10.1023/A:1015266421750. arXiv: gr-qc/0103083 (cit. on p. 115).

[249] M. d. C. Bento, O. Bertolami and A. Sen. "Generalized Chaplygin gas and CMBR constraints". In: *Physical Review D* 67 (2003),

p. 063003. DOI: 10.1103/PhysRevD.67.063003. arXiv: astro-ph/0210468 (cit. on p. 115).

[250] J. C. Fabris, S. Goncalves and P. Souza. "Fitting the supernova type Ia data with the Chaplygin gas" (2002). arXiv: astro-ph/0207430 (cit. on p. 115).

[251] M. Makler, S. Quinet de Oliveira and I. Waga. "Constraints on the generalized Chaplygin gas from supernovae observations". In: *Physics Letters B* 555 (2003), p. 1. DOI: 10.1016/S0370-2693(03)00038-8. arXiv: astro-ph/0209486 (cit. on p. 115).

[252] H. Sandvik, M. Tegmark, M. Zaldarriaga and I. Waga. "The end of unified dark matter?" In: *Physical Review D* 69 (2004), p. 123524. DOI: 10.1103/PhysRevD.69.123524. arXiv: astro-ph/0212114 (cit. on p. 115).

[253] B. A. Bassett, M. Kunz, D. Parkinson and C. Ungarelli. "Condensate cosmology - Dark energy from dark matter". In: *Physical Review D* 68 (2003), p. 043504. DOI: 10.1103/PhysRevD.68.043504. arXiv: astro-ph/0211303 (cit. on p. 115).

[254] B. A. Bassett, M. Kunz, J. Silk and C. Ungarelli. "A late-time transition in the cosmic dark energy?" In: *Monthly Notices of the Royal Astronomical Society* 336 (2002), pp. 1217–1222. DOI: 10.1046/j.1365-8711.2002.05887.x. arXiv: astro-ph/0203383 (cit. on p. 115).

[255] O. F. Piattella. "The extreme limit of the generalized Chaplygin gas". In: *Journal of Cosmology and Astroparticle Physics* 03 (2010), p. 012. DOI: 10.1088/1475-7516/2010/03/012. arXiv: 0906.4430 [astro-ph.CO] (cit. on p. 115).

[256] C. Gao, M. Kunz, A. R. Liddle and D. Parkinson. "Unified dark energy and dark matter from a scalar field different from quintessence". In: *Physical Review D* 81 (2010), p. 043520. DOI: 10.1103/PhysRevD.81.043520. arXiv: 0912.0949 [astro-ph.CO] (cit. on p. 115).

[257] A. De Felice, S. Nesseris and S. Tsujikawa. "Observational constraints on dark energy with a fast varying equation of state". In: *Journal of Cosmology and Astroparticle Physics* 05 (2012), p. 029. DOI: 10.1088/1475-7516/2012/05/029. arXiv: 1203.6760 [astro-ph.CO] (cit. on p. 115).

[258] Y. Wang, D. Wands, L. Xu, J. De-Santiago and A. Hojjati. "Cosmological constraints on a decomposed Chaplygin gas". In: *Physical Review D* 87.8 (2013), p. 083503. DOI: 10.1103/PhysRevD.87.083503. arXiv: 1301.5315 [astro-ph.CO] (cit. on p. 115).

[259] H. Li, W. Yang and Y. Wu. "Constraint on the generalized Chaplygin gas as an unified dark fluid model after Planck

2015". In: *Physics of the Dark Universe* 22 (2018), pp. 60–66. DOI: 10.1016/j.dark.2018.09.001 (cit. on p. 115).

[260] H. Li, W. Yang and L. Gai. "Astronomical bounds on the modified Chaplygin gas as a unified dark fluid model". In: *Astronomy & Astrophysics* 623 (2019), A28. DOI: 10.1051/0004-6361/201833836 (cit. on p. 115).

[261] X. Shan and H. Chen. "Lattice Boltzmann model for simulating flows with multiple phases and components". In: *Physical Review E* 47 (3 1993), pp. 1815–1819. DOI: 10.1103/PhysRevE.47.1815 (cit. on pp. 115, 116).

[262] D. Bini, A. Geralico, D. Gregoris and S. Succi. "Dark energy from cosmological fluids obeying a Shan-Chen nonideal equation of state". In: *Physical Review D* 88.6 (2013), p. 063007. DOI: 10.1103/PhysRevD.88.063007. arXiv: 1408.5483 [gr-qc] (cit. on pp. 115–117, 121, 122, 137).

[263] D. Bini, G. Esposito and A. Geralico. "Late-time evolution of cosmological models with fluids obeying a Shan-Chen-like equation of state". In: *Physical Review D* 93.2 (2016), p. 023511. DOI: 10.1103/PhysRevD.93.023511. arXiv: 1601.04177 [gr-qc] (cit. on p. 115).

[264] A. Hashemi and F. Maron. Private communication. 2020 (cit. on p. 117).

[265] N. Frusciante, S. Peirone, L. Atayde and A. De Felice. "Phenomenology of the generalized cubic covariant Galileon model and cosmological bounds". In: *Physical Review D* 101.6 (2020), p. 064001. DOI: 10.1103/PhysRevD.101.064001. arXiv: 1912.07586 [astro-ph.CO] (cit. on p. 137).

[266] C. D. Dijkstra. "Naturalness as a reasonable scientific principle in fundamental physics". MA thesis. University of Groningen, 2019. URL: https://arxiv.org/abs/1906.03036 (cit. on p. 137).

[267] B. F. Schutz. "Determining the Hubble constant from gravitational wave observations". In: *Nature* 323.6086 (1986), pp. 310–311. DOI: 10.1038/323310a0 (cit. on p. 140).

[268] D. E. Holz and S. A. Hughes. "Using gravitational-wave standard sirens". In: *The Astrophysical Journal* 629 (2005), pp. 15–22. DOI: 10.1086/431341. arXiv: astro-ph/0504616 (cit. on p. 140).

[269] N. Dalal, D. E. Holz, S. A. Hughes and B. Jain. "Short GRB and binary black hole standard sirens as a probe of dark energy". In: *Physical Review D* 74 (2006), p. 063006. DOI: 10.1103/PhysRevD.74.063006. arXiv: astro-ph/0601275 (cit. on p. 140).

[270] B. Abbott et al. "Gravitational Waves and Gamma-rays from a Binary Neutron Star Merger: GW170817 and GRB 170817A". In: *The Astrophysical Journal Letters* 848.2 (2017), p. L13. DOI: 10.3847/2041-8213/aa920c. arXiv: 1710.05834 [astro-ph.HE] (cit. on p. 140).

[271] H.-Y. Chen, M. Fishbach and D. E. Holz. "A two per cent Hubble constant measurement from standard sirens within five years". In: *Nature* 562.7728 (2018), pp. 545–547. DOI: 10.1038/s41586-018-0606-0. arXiv: 1712.06531 [astro-ph.CO] (cit. on pp. 140, 148).

[272] S. Mukherjee, B. D. Wandelt and J. Silk. "Probing the theory of gravity with gravitational lensing of gravitational waves and galaxy surveys". In: *Monthly Notices of the Royal Astronomical Society* 494.2 (2020), pp. 1956–1970. DOI: 10.1093/mnras/staa827. arXiv: 1908.08951 [astro-ph.CO] (cit. on p. 140).

[273] S. Mukherjee, B. D. Wandelt and J. Silk. "Multimessenger tests of gravity with weakly lensed gravitational waves". In: *Physical Review D* 101.10 (2020), p. 103509. DOI: 10.1103/PhysRevD.101.103509. arXiv: 1908.08950 [astro-ph.CO] (cit. on p. 140).

[274] S. Mukherjee, B. D. Wandelt, S. M. Nissanke and A. Silvestri. "Accurate and precision Cosmology with redshift unknown gravitational wave sources" (2020). arXiv: 2007.02943 [astro-ph.CO] (cit. on p. 140).

[275] M. Maggiore et al. "Science Case for the Einstein Telescope". In: *Journal of Cosmology and Astroparticle Physics* 03.03 (2020), p. 050. DOI: 10.1088/1475-7516/2020/03/050. arXiv: 1912.02622 [astro-ph.CO] (cit. on pp. 140, 148).

[276] S. Hild et al. "Sensitivity Studies for Third-Generation Gravitational Wave Observatories". In: *Classical and Quantum Gravity* 28 (2011), p. 094013. DOI: 10.1088/0264-9381/28/9/094013. arXiv: 1012.0908 [gr-qc] (cit. on p. 140).

[277] T. M. C. Abbott et al. "Dark Energy Survey Year 1 Results: Constraints on Extended Cosmological Models from Galaxy Clustering and Weak Lensing". In: *Physical Review D* 99.12 (2019), p. 123505. DOI: 10.1103/PhysRevD.99.123505. arXiv: 1810.02499 [astro-ph.CO] (cit. on p. 140).

[278] R. Holanda, J. Lima and M. Ribeiro. "Testing the Distance-Duality Relation with Galaxy Clusters and Type Ia Supernovæ". In: *The Astrophysical Journal Letters* 722 (2010), pp. L233–L237. DOI: 10.1088/2041-8205/722/2/L233. arXiv: 1005.4458 [astro-ph.CO] (cit. on p. 141).

[279] A. Avgoustidis, C. Burrage, J. Redondo, L. Verde and R. Jimenez. "Constraints on cosmic opacity and beyond the standard model physics from cosmological distance measurements". In:

Journal of Cosmology and Astroparticle Physics 10 (2010), p. 024. DOI: 10.1088/1475-7516/2010/10/024. arXiv: 1004.2053 [astro-ph.CO] (cit. on pp. 141, 143, 144).

[280] R. Holanda, R. Gonçalves and J. Alcaniz. "A test for cosmic distance duality". In: *Journal of Cosmology and Astroparticle Physics* 06 (2012), p. 022. DOI: 10.1088/1475-7516/2012/06/022. arXiv: 1201.2378 [astro-ph.CO] (cit. on p. 141).

[281] K. Liao, A. Avgoustidis and Z. Li. "Is the Universe Transparent?" In: *Physical Review D* 92.12 (2015), p. 123539. DOI: 10.1103/PhysRevD.92.123539. arXiv: 1512.01861 [astro-ph.CO] (cit. on p. 141).

[282] K. Liao, Z. Li, S. Cao, M. Biesiada, X. Zheng and Z.-H. Zhu. "The Distance Duality Relation From Strong Gravitational Lensing". In: *The Astrophysical Journal* 822.2 (2016), p. 74. DOI: 10.3847/0004-637X/822/2/74. arXiv: 1511.01318 [astro-ph.CO] (cit. on p. 141).

[283] K. Liao. "The cosmic distance duality relation with strong lensing and gravitational waves: an opacity-free test". In: *The Astrophysical Journal* 885 (2019), p. 70. DOI: 10.3847/1538-4357/ab4819. arXiv: 1906.09588 [astro-ph.CO] (cit. on p. 141).

[284] C. Bogdanos and S. Nesseris. "Genetic Algorithms and Supernovæ Type Ia Analysis". In: *Journal of Cosmology and Astroparticle Physics* 05 (2009), p. 006. DOI: 10.1088/1475-7516/2009/05/006. arXiv: 0903.2805 [astro-ph.CO] (cit. on pp. 141, 163, 165).

[285] S. Nesseris and J. Garcia-Bellido. "A new perspective on Dark Energy modeling via Genetic Algorithms". In: *Journal of Cosmology and Astroparticle Physics* 1211 (2012), p. 033. DOI: 10.1088/1475-7516/2012/11/033. arXiv: 1205.0364 [astro-ph.CO] (cit. on pp. 141, 163, 165).

[286] B. A. Bassett and M. Kunz. "Cosmic distance-duality as a probe of exotic physics and acceleration". In: *Physical Review D* 69 (2004), p. 101305. DOI: 10.1103/PhysRevD.69.101305. arXiv: astro-ph/0312443 (cit. on p. 142).

[287] P. Tiwari. "Constraining axionlike particles using the distance-duality relation". In: *Physical Review D* 95.2 (2017), p. 023005. DOI: 10.1103/PhysRevD.95.023005. arXiv: 1610.06583 [astro-ph.CO] (cit. on p. 142).

[288] C. Csaki, N. Kaloper and J. Terning. "Dimming supernovæ without cosmic acceleration". In: *Physical Review Letters* 88 (2002), p. 161302. DOI: 10.1103/PhysRevLett.88.161302. arXiv: hep-ph/0111311 (cit. on p. 143).

[289] C. Deffayet, D. Harari, J.-P. Uzan and M. Zaldarriaga. "Dimming of supernovæ by photon pseudoscalar conversion and

the intergalactic plasma". In: *Physical Review D* 66 (2002), p. 043517. DOI: 10.1103/PhysRevD.66.043517. arXiv: hep-ph/0112118 (cit. on p. 143).

[290] A. Avgoustidis, L. Verde and R. Jimenez. "Consistency among distance measurements: transparency, BAO scale and accelerated expansion". In: *Journal of Cosmology and Astroparticle Physics* 2009.06, 012 (2009). DOI: 10.1088/1475-7516/2009/06/012. arXiv: 0902.2006 [astro-ph.CO] (cit. on p. 144).

[291] A. Hees, O. Minazzoli and J. Larena. "Breaking of the equivalence principle in the electromagnetic sector and its cosmological signatures". In: *Physical Review D* 90 (2014), p. 124064. DOI: 10.1103/PhysRevD.90.124064. arXiv: 1406.6187 [astro-ph.CO] (cit. on p. 145).

[292] R. Angulo, C. Baugh, C. Frenk and C. Lacey. "The detectability of baryonic acoustic oscillations in future galaxy surveys". In: *Monthly Notices of the Royal Astronomical Society* 383 (2008), p. 755. DOI: 10.1111/j.1365-2966.2007.12587.x. arXiv: astro-ph/0702543 (cit. on p. 146).

[293] S. Anselmi, G. D. Starkman, P.-S. Corasaniti, R. K. Sheth and I. Zehavi. "Galaxy Correlation Functions Provide a More Robust Cosmological Standard Ruler". In: *Physical Review Letters* 121.2 (2018), p. 021302. DOI: 10.1103/PhysRevLett.121.021302. arXiv: 1703.01275 [astro-ph.CO] (cit. on p. 146).

[294] S. Anselmi, P.-S. Corasaniti, G. D. Starkman, R. K. Sheth and I. Zehavi. "Linear point standard ruler for galaxy survey data: Validation with mock catalogs". In: *Physical Review D* 98.2 (2018), p. 023527. DOI: 10.1103/PhysRevD.98.023527. arXiv: 1711.09063 [astro-ph.CO] (cit. on p. 146).

[295] Abbott, B.P. and others. "GWTC-1: A Gravitational-Wave Transient Catalog of Compact Binary Mergers Observed by LIGO and Virgo during the First and Second Observing Runs". In: *Physical Review X* 9.3 (2019), p. 031040. DOI: 10.1103/PhysRevX.9.031040. arXiv: 1811.12907 [astro-ph.HE] (cit. on p. 146).

[296] Abbott, B.P. and others. "GW190425: Observation of a Compact Binary Coalescence with Total Mass $\sim 3.4 M_{\odot}$". In: *The Astrophysical Journal Letters* 892 (2020), p. L3. DOI: 10.3847/2041-8213/ab75f5. arXiv: 2001.01761 [astro-ph.HE] (cit. on p. 146).

[297] R. Abbott et al. "GW190412: Observation of a Binary-Black-Hole Coalescence with Asymmetric Masses". In: *Physical Review D* 102.4 (2020), p. 043015. DOI: 10.1103/PhysRevD.102.043015. arXiv: 2004.08342 [astro-ph.HE] (cit. on p. 146).

[298] P. A. Abell, J. Allison, S. F. Anderson, J. R. Andrew and J. R. P. Angel. "LSST Science Book, Version 2.0", arXiv:0912.0201 (2009). arXiv: 0912.0201 [astro-ph.IM] (cit. on pp. 147, 179).

[299] A. Aghamousa et al. "The DESI Experiment Part I: Science,Targeting, and Survey Design", arXiv:1611.00036 (2016). arXiv: 1611.00036 [astro-ph.IM] (cit. on pp. 147, 181).

[300] B. S. Sathyaprakash, B. F. Schutz and C. Van Den Broeck. "Cosmography with the Einstein Telescope". In: *Classical and Quantum Gravity* 27 (2010), p. 215006. DOI: 10.1088/0264-9381/27/21/215006. arXiv: 0906.4151 [astro-ph.CO] (cit. on pp. 148, 183–186).

[301] W. Zhao, C. Van Den Broeck, D. Baskaran and T. G. F. Li. "Determination of Dark Energy by the Einstein Telescope: Comparing with CMB, BAO and SNIa Observations". In: *Physical Review D* 83 (2011), p. 023005. DOI: 10.1103/PhysRevD.83.023005. arXiv: 1009.0206 [astro-ph.CO] (cit. on pp. 148, 183–185).

[302] M. Du, W. Yang, L. Xu, S. Pan and D. F. Mota. "Future constraints on dynamical dark-energy using gravitational-wave standard sirens". In: *Physical Review D* 100.4 (2019), p. 043535. DOI: 10.1103/PhysRevD.100.043535. arXiv: 1812.01440 [astro-ph.CO] (cit. on pp. 148, 183, 185).

[303] J. Torrado and A. Lewis. "Cobaya: Code for Bayesian Analysis of hierarchical physical models" (2020). arXiv: 2005.05290 [astro-ph.IM] (cit. on p. 148).

[304] A. Conley et al. "Supernova Constraints and Systematic Uncertainties from the First 3 Years of the Supernova Legacy Survey". In: *The Astrophysical Journal Supplement* 192 (2011), p. 1. DOI: 10.1088/0067-0049/192/1/1. arXiv: 1104.1443 [astro-ph.CO] (cit. on p. 149).

[305] E. Belgacem, Y. Dirian, S. Foffa and M. Maggiore. "Gravitational-wave luminosity distance in modified gravity theories". In: *Physical Review D* 97.10 (2018), p. 104066. DOI: 10.1103/PhysRevD.97.104066. arXiv: 1712.08108 [astro-ph.CO] (cit. on p. 152).

[306] E. Belgacem, Y. Dirian, S. Foffa and M. Maggiore. "Modified gravitational-wave propagation and standard sirens". In: *Physical Review D* 98.2 (2018), p. 023510. DOI: 10.1103/PhysRevD.98.023510. arXiv: 1805.08731 [gr-qc] (cit. on p. 152).

[307] E. Belgacem et al. "Testing modified gravity at cosmological distances with LISA standard sirens". In: *Journal of Cosmology and Astroparticle Physics* 07 (2019), p. 024. DOI: 10.1088/1475-7516/2019/07/024. arXiv: 1906.01593 [astro-ph.CO] (cit. on pp. 152, 153).

[308] A. Garoffolo, M. Raveri, A. Silvestri, G. Tasinato, C. Carbone, D. Bertacca and S. Matarrese. "Detecting Dark Energy Fluctuations with Gravitational Waves" (2020). arXiv: 2007.13722 [astro-ph.CO] (cit. on p. 153).

[309] C. Dalang and L. Lombriser. "Limitations on Standard Sirens tests of gravity from screening". In: *Journal of Cosmology and Astroparticle Physics* 10 (2019), p. 013. DOI: 10.1088/1475-7516/2019/10/013. arXiv: 1906.12333 [astro-ph.CO] (cit. on pp. 154, 156, 162).

[310] S. Tsujikawa. "Matter density perturbations and effective gravitational constant in modified gravity models of dark energy". In: *Physical Review D* 76 (2007), p. 023514. DOI: 10.1103/PhysRevD.76.023514. arXiv: 0705.1032 [astro-ph] (cit. on p. 154).

[311] S. Nesseris. "Matter density perturbations in modified gravity models with arbitrary coupling between matter and geometry". In: *Physical Review D* 79 (2009), p. 044015. DOI: 10.1103/PhysRevD.79.044015. arXiv: 0811.4292 [astro-ph] (cit. on p. 154).

[312] S. Nesseris and A. Mazumdar. "Newton's constant in $f(R, R_{\mu\nu}R^{\mu\nu}, \Box R)$ theories of gravity and constraints from BBN". In: *Physical Review D* 79 (2009), p. 104006. DOI: 10.1103/PhysRevD.79.104006. arXiv: 0902.1185 [astro-ph.CO] (cit. on p. 154).

[313] R. Arjona, W. Cardona and S. Nesseris. "Unraveling the effective fluid approach for $f(R)$ models in the subhorizon approximation". In: *Physical Review D* 99.4 (2019), p. 043516. DOI: 10.1103/PhysRevD.99.043516. arXiv: 1811.02469 [astro-ph.CO] (cit. on p. 154).

[314] R. Arjona, W. Cardona and S. Nesseris. "Designing Horndeski and the effective fluid approach". In: *Physical Review D* 100.6 (2019), p. 063526. DOI: 10.1103/PhysRevD.100.063526. arXiv: 1904.06294 [astro-ph.CO] (cit. on p. 154).

[315] E. Gaztanaga, E. Garcia-Berro, J. Isern, E. Bravo and I. Dominguez. "Bounds on the possible evolution of the gravitational constant from cosmological type Ia supernovæ". In: *Physical Review D* 65 (2002), p. 023506. DOI: 10.1103/PhysRevD.65.023506. arXiv: astro-ph/0109299 (cit. on p. 154).

[316] S. Nesseris and L. Perivolaropoulos. "Evolving Newton's constant, extended gravity theories and SNIa data analysis". In: *Physical Review D* 73 (2006), p. 103511. DOI: 10.1103/PhysRevD.73.103511. arXiv: astro-ph/0602053 (cit. on p. 155).

[317] E. Calabrese, M. Martinelli, S. Pandolfi, V. Cardone, C. Martins, S. Spiro and P. Vielzeuf. "Dark Energy coupling with electro-

magnetism as seen from future low-medium redshift probes". In: *Physical Review D* 89.8 (2014), p. 083509. DOI: 10.1103/PhysRevD.89.083509. arXiv: 1311.5841 [astro-ph.CO] (cit. on p. 155).

[318] L. Lombriser. "Constraining chameleon models with cosmology". In: *Annalen der Physik* 526 (2014), pp. 259–282. DOI: 10.1002/andp.201400058. arXiv: 1403.4268 [astro-ph.CO] (cit. on p. 155).

[319] T. Baker et al. "The Novel Probes Project – Tests of Gravity on Astrophysical Scales" (2019). arXiv: 1908.03430 [astro-ph.CO] (cit. on p. 155).

[320] H. Desmond and P. G. Ferreira. "Galaxy morphology rules out astrophysically interesting $f(R)$" (2020). arXiv: 2009.08743 [astro-ph.CO] (cit. on p. 155).

[321] B. S. Wright and B. Li. "Type Ia supernovæ, standardizable candles, and gravity". In: *Physical Review D* 97.8 (2018), p. 083505. DOI: 10.1103/PhysRevD.97.083505. arXiv: 1710.07018 [astro-ph.CO] (cit. on p. 156).

[322] S. Nesseris, G. Pantazis and L. Perivolaropoulos. "Tension and constraints on modified gravity parametrizations of $G_{\rm eff}(z)$ from growth rate and Planck data". In: *Physical Review D* 96.2 (2017), p. 023542. DOI: 10.1103/PhysRevD.96.023542. arXiv: 1703.10538 [astro-ph.CO] (cit. on pp. 156, 158).

[323] C. Bambi, M. Giannotti and F. Villante. "The Response of primordial abundances to a general modification of G(N) and/or of the early Universe expansion rate". In: *Physical Review D* 71 (2005), p. 123524. DOI: 10.1103/PhysRevD.71.123524. arXiv: astro-ph/0503502 (cit. on p. 156).

[324] T. P. Sotiriou and V. Faraoni. "f(R) Theories Of Gravity". In: *Reviews of Modern Physics* 82 (2010), pp. 451–497. DOI: 10.1103/RevModPhys.82.451. arXiv: 0805.1726 [gr-qc] (cit. on p. 160).

[325] P. Brax, C. van de Bruck, A.-C. Davis and D. J. Shaw. "f(R) Gravity and Chameleon Theories". In: *Physical Review D* 78 (2008), p. 104021. DOI: 10.1103/PhysRevD.78.104021. arXiv: 0806.3415 [astro-ph] (cit. on p. 162).

[326] A. Vainshtein. "To the problem of nonvanishing gravitation mass". In: *Physics Letters B* 39.3 (1972), pp. 393–394. ISSN: 0370-2693. DOI: https://doi.org/10.1016/0370-2693(72)90147-5 (cit. on p. 162).

[327] C. Deffayet, G. Dvali, G. Gabadadze and A. Vainshtein. "Nonperturbative continuity in graviton mass versus perturbative discontinuity". In: *Physical Review D* 65.4 (2002). ISSN: 1089-4918. DOI: 10.1103/physrevd.65.044026 (cit. on p. 162).

[328] J. Beltran Jimenez, F. Piazza and H. Velten. "Evading the Vainshtein Mechanism with Anomalous Gravitational Wave Speed: Constraints on Modified Gravity from Binary Pulsars". In: *Physical Review Letters* 116.6 (2016), p. 061101. DOI: 10.1103/PhysRevLett.116.061101. arXiv: 1507.05047 [gr-qc] (cit. on p. 162).

[329] C. Dalang, P. Fleury and L. Lombriser. "Horndeski gravity and standard sirens". In: *Physical Review D* 102.4 (2020), p. 044036. DOI: 10.1103/PhysRevD.102.044036. arXiv: 1912.06117 [gr-qc] (cit. on p. 162).

[330] Y. Akrami, P. Scott, J. Edsjo, J. Conrad and L. Bergstrom. "A Profile Likelihood Analysis of the Constrained MSSM with Genetic Algorithms". In: *Journal of High Energy Physics* 04 (2010), p. 057. DOI: 10.1007/JHEP04(2010)057. arXiv: 0910.3950 [hep-ph] (cit. on p. 163).

[331] R. Arjona and S. Nesseris. "What can Machine Learning tell us about the background expansion of the Universe?" In: *Physical Review D* 101.12 (2020), p. 123525. DOI: 10.1103/PhysRevD.101.123525. arXiv: 1910.01529 [astro-ph.CO] (cit. on p. 163).

[332] R. Arjona and S. Nesseris. "Hints of dark energy anisotropic stress using Machine Learning", arXiv:2001.11420 (2020). arXiv: 2001.11420 [astro-ph.CO] (cit. on p. 163).

[333] R. Arjona. "Machine Learning meets the redshift evolution of the CMB Temperature" (2020). arXiv: 2002.12700 [astro-ph.CO] (cit. on p. 163).

[334] S. Nesseris and A. Shafieloo. "A model independent null test on the cosmological constant". In: *Monthly Notices of the Royal Astronomical Society* 408 (2010), pp. 1879–1885. DOI: 10.1111/j.1365-2966.2010.17254.x. arXiv: 1004.0960 [astro-ph.CO] (cit. on p. 163).

[335] S. Nesseris and J. Garcia-Bellido. "Comparative analysis of model-independent methods for exploring the nature of dark energy". In: *Physical Review D* 88.6 (2013), p. 063521. DOI: 10.1103/PhysRevD.88.063521. arXiv: 1306.4885 [astro-ph.CO] (cit. on pp. 163, 165).

[336] D. Sapone, E. Majerotto and S. Nesseris. "Curvature versus distances: Testing the FLRW cosmology". In: *Physical Review D* 90.2 (2014), p. 023012. DOI: 10.1103/PhysRevD.90.023012. arXiv: 1402.2236 [astro-ph.CO] (cit. on p. 163).

[337] M. Karamanis and F. Beutler. "Ensemble Slice Sampling" (2020). arXiv: 2002.06212 [stat.ML] (cit. on p. 174).

[338] M. Karamanis and F. Beutler. *zeus: Lightning Fast MCMC*. 2020. ascl: 2008.010 (cit. on p. 174).

[339] L. Menebrea. "Sketch of the Analytical Engine invented by Charles Babbage, Esq." Trans. by A. A. B. King. In: *Scientific Memoirs* 3 (1843), pp. 666–731 (cit. on p. 175).

[340] M. Avgerinou, P. Bertoldi and L. Castellazzi. "Trends in Data Centre Energy Consumption under the European Code of Conduct for Data Centre Energy Efficiency". In: *Energies* 10.10 (2017), p. 1470. ISSN: 1996-1073. DOI: 10.3390/en10101470 (cit. on p. 175).

[341] A. Cocaña-Fernández, E. San José Guiote, L. Sánchez and J. Ranilla. "Eco-Efficient Resource Management in HPC Clusters through Computer Intelligence Techniques". In: *Energies* 12.11 (2019), p. 2129. ISSN: 1996-1073. DOI: 10.3390/en12112129 (cit. on p. 175).

[342] S. Portegies Zwart. "The Ecological Impact of High-performance Computing in Astrophysics". 2020. DOI: 10.1038/s41550-020-1208-y. arXiv: 2009.11295 [astro-ph.IM] (cit. on p. 175).

[343] P. Astier et al. "Extending the supernova Hubble diagram to $z\sim1.5$ with the Euclid space mission". In: *Astronomy & Astrophysics* 572 (2014), A80. DOI: 10.1051/0004-6361/201423551. arXiv: 1409.8562 [astro-ph.CO] (cit. on p. 179).

[344] Y. Gong, A. Cooray and X. Chen. "Cosmology with Photometric Surveys of Type Ia Supernovæ". In: *The Astrophysical Journal* 709 (2010), pp. 1420–1428. DOI: 10.1088/0004-637X/709/2/1420. arXiv: 0909.2692 [astro-ph.CO] (cit. on p. 179).

[345] E. Poisson and C. M. Will. "Gravitational waves from inspiraling compact binaries: Parameter estimation using second-post-Newtonian waveforms". In: *Physical Review D* 52 (2 1995), pp. 848–855. DOI: 10.1103/PhysRevD.52.848 (cit. on p. 183).

[346] L. Blanchet. "Gravitational Radiation from Post-Newtonian Sources and Inspiralling Compact Binaries". In: *Living Reviews in Relativity* 17 (2014), p. 2. DOI: 10.12942/lrr-2014-2. arXiv: 1310.1528 [gr-qc] (cit. on p. 183).

[347] R.-G. Cai and T. Yang. "Estimating cosmological parameters by the simulated data of gravitational waves from the Einstein Telescope". In: *Physical Review D* 95.4 (2017), p. 044024. DOI: 10.1103/PhysRevD.95.044024. arXiv: 1608.08008 [astro-ph.CO] (cit. on p. 183).

[348] T. G. F. Li. "Extracting Physics from Gravitational Waves: Testing the Strong-field Dynamics of General Relativity and Inferring the Large-scale Structure of the Universe". PhD thesis. Vrije U., Amsterdam, 2013 (cit. on pp. 184, 185).

[349] S.-J. Jin, D.-Z. He, Y. Xu, J.-F. Zhang and X. Zhang. "Forecast for cosmological parameter estimation with gravitational-

wave standard siren observation from the Cosmic Explorer" (2020). arXiv: 2001.05393 [astro-ph.CO] (cit. on p. 185).

[350] T. Yang, R. Holanda and B. Hu. "Constraints on the cosmic distance duality relation with simulated data of gravitational waves from the Einstein Telescope". In: *Astroparticle Physics* 108 (2019), pp. 57–62. DOI: 10.1016/j.astropartphys.2019.01.005. arXiv: 1710.10929 [astro-ph.CO] (cit. on p. 185).

[351] C. Cutler and D. E. Holz. "Ultra-high precision cosmology from gravitational waves". In: *Physical Review D* 80 (2009), p. 104009. DOI: 10.1103/PhysRevD.80.104009. arXiv: 0906.3752 [astro-ph.CO] (cit. on p. 185).

This thesis was typeset using the `classicthesis` LaTeX template developed by André Miede: https://ctan.org/tex-archive/macros/latex/contrib/classicthesis/.